University of South-Eastern Norway
Faculty of Technology, Natural Sciences and Maritime Studies

Doctoral dissertation no. 41
2019

Prasanna Welahettige

Transient drilling fluid flow in Venturi channels: comparing 3D and 1D models to experimental data

Prasanna Welahettige

Transient drilling fluid flow in Venturi channels: comparing 3D and 1D models to experimental data

A PhD dissertation in
Process, Energy and Automation Engineering

© 2019 Prasanna Welahettige

Faculty of Technology, Natural Sciences and Maritime Studies
University of South-Eastern Norway
Porsgrunn, 2019

Doctoral dissertations at the University of South-Eastern Norway no. 41

ISSN: 2535-5244 (print)
ISSN: 2535-5252 (online)

ISBN: 978-82-7206-535-4 (print)
ISBN: 978-82-7206-536-1 (online)

This publication is, except otherwise stated, licenced under Creative Commons. You may copy and redistribute the material in any medium or format. You must give appropriate credit provide a link to the license, and indicate if changes were made.
http://creativecommons.org/licenses/by-nc-sa/4.0/deed.en

Print: University of South-Eastern Norway

To,

Ayesha and Sisira.

Preface

This thesis is submitted in partial fulfillment of the requirements for the degree of Doctor of Philosophy at the Faculty of Technology, Natural Sciences, and Maritime Sciences, The University of South-Eastern Norway. The dissertation presents a collection of my publications published in journal and conference proceedings. I hope this study will be useful to advanced fluid dynamics studies, and that the thesis will add new knowledge to the world. Financial support has been provided by The Research Council of Norway and Equinor ASA through project no. 255348/E30 ‘‘Sensors and models for improved kick/loss detection in drilling (Semi-kidd)’’ which I gratefully acknowledge.

I want to thank my main supervisor Professor Knut Vaagsaether selecting me as the most suitable candidate when the Ph.D. started in 2016 and for believing in me all the way to thesis submission. His excellent guidance, support, and motivation allowed me to develop myself throughout the Ph.D. period, academically and personally. His expert CFD knowledge in particular leading me to acquire wisdom and understanding complex fluid mechanics concepts. Thank you also for introducing me to the research group. The group helped me solve the many technical questions during the group’s morning meeting every working day and without any pre-scheduling being required. Many thanks also to my co-supervisor Professor Bernt Lie for showing me the direction and opportunities. His experienced academic background helped me to learn “How to communicate with the scientific community”. Moreover, I would like to thank him for correcting my research papers, presentations, and thesis.

My sincere gratitude also goes to the research group at USN: Professor Dag Bjerketvedt, Dr. Joachim Lundberg, Dr. Andre Verner Gaathaug, Dr. Per Morten Hansen, Mathias Henriksen, Professor Ole Marius Lysaker, Samee Maharjan and Agnieszka Lach for valuable technical and non-technical discussions. I would like to thank Christian Berg, Professor Britt E. Moldestad, Asanthi Jinasena, Morten Hansen Jondahl, Dr. Håkon Viumdal, Dr. Khim Chhantyal, Sumudhu Karunarathna, and all the Semi-kidd members for their collaboration work in the Ph.D. period. I would also like to thank my fellow

Ph.D. students, my lecturers, the technical and non-technical staff at USN-TNM for their continuous encouragement throughout the project.

I would like to thank Geir Elseth for laying the path for me to join as a PhD-intern at Equinor. I would also like to thank Åsmund Hjulstad for supervising me as a PhD-intern at Equinor. Your sound technical knowledge helped me to understand the real industrial problems well. I also appreciate the dedication of your time, even during your vacation.

My dear "*Telemark Sri Lankan*" and "*Sri Lankan in Norway*," you all became my big family in Norway. Many thanks for all your support.

I would like to thank my parents, Sumathipala Welahettige and Gunawahi Vitharana for their hard work and dedication to make a strong man of me in the world. I thank my eldest brother Dr. Sisira Welahettige who changed my entire life from one world to another world. I would also like to thank my elder brother Indika Welahettige and my sister Thilni Welahettige for being with me in all the hard situations in my life unconditionally. Moreover, I thank all the people who helped me directly or indirectly since I was born into the world.

Finally, I thank my loving wife Ayesha Madhumali for your enormous love, dedication, support, understanding, and encouragement in these exciting years I have spent as a Ph.D. student.

Porsgrunn, March 2019
Prasanna Welahettige

Abstract

Keywords: open channel flow, CFD, TVD scheme, Non-Newtonian, 1D model, FVM

In well drilling operations, bottom hole pressure control within a narrow pressure margin has a high risk of influx (*kick*) and outflux (*loss*) at greater depths. *Kick* occurs when the formation pressure is higher than hydrostatic pressure on the borehole. As a consequence of poor bottom hole pressure control, the following adverse effects can happen in the drilling operation: increase of non-productive time, fracturing of the wellbore, loss of drilling fluid, and in a worst-case scenario: blowout. Monitoring the active pit volume and measuring the return flow using a flow paddle in the open channel running to the active pit are the standard kick monitoring methods. These methods have low accuracy, which limits the resolution of *kick/loss* detection. As a low cost and accurate solution for the return flow measurement, a Venturi flume method was studied in this thesis work. The thesis presents the results of modeling return channel flow under two aspects: 3D computational fluid dynamics (CFD) modeling and 1D numerical modeling. The flow modeling results were validated with experimental laboratory results. The experiments were carried out in a laboratory Venturi rig for water and drilling fluids. Measurement were taken from ultrasonic level sensors, a Coriolis mass flow meter, an Anton Paar rheometer and a density meter, and the channel inclination was measured and taken into account. The model drilling fluid used in the experiment is a water-based drilling fluid, which contains potassium carbonate as a densifying agent and xanthan gum as a viscosifier.

The CFD models are based on the volume of fluid (VOF) model and the Eulerian multi-fluid VOF method. 3D and 2D CFD open channel flow *always* can be considered as a multiphase flow because it has an interface (free surface) between the flowing fluid and air above the flowing fluid. The non-Newtonian behavior of drilling fluid, the effect of drill cuttings, gravity flow, hydraulic jump, turbulence, wall and boundary conditions, and unsteady flow were the main factors analyzed from the CFD simulations.

The 1D model, which is a version of the shallow water equations, was developed from the fundamental conservation laws by application to a non-Newtonian *open Venturi channel* flow. The flow depth and mean flow velocity (or flow rate) are the state variables of the developed 1D model. The momentum equation was modified with additional friction slopes for the non-Newtonian drilling fluid. High resolution well balanced numerical schemes were used to solve the developed 1D model because of unsteady hydraulic jumps propagation. The second order accurate total variation diminishing (TVD), flux limiter centered (FLIC) scheme and the fourth-order Runge-Kutta scheme were used to solve the 1D numerical model. The cell interface fluxes, discretized with the finite volume method (FVM), is calculated with a higher order flux and a lower order flux combined with a flux limiter function, still keeping the second order accuracy.

A hydraulic jump, depending on the channel inclination, stands between the inlet and the Venturi contraction. Flow regimes, when there is a standing hydraulic jump, changes supercritical to critical, and critical to subcritical until the Venturi throat; after the Venturi throat, subcritical to critical, and critical to supercritical. An oblique jump propagates, when the flow state is at supercritical flow condition, at the Venturi throat. The wall-reflection pressure-force from the contraction walls significantly changes the flow regimes in open Venturi channel flow. The conventional shallow water equations must be modified to capture the wall-reflection pressure-force effect in irregular geometry. The strictly hyperbolic requirement can be violated in the FLIC scheme, which allows adding additional friction slopes to the Saint-Venant equations. Two friction slopes in the 1D open channel model can be correlated for drilling fluid flow: external friction slope and internal friction slope. The external friction slope covers the wall friction and turbulence behavior, and the internal friction slope covers the non-Newtonian surface friction and laminar behavior. The developed 1D model of the TVD Runge-Kutta scheme can be used for real-time flow measuring in the well return flow using a single level sensor. Drill cuttings effect on the flow depth might be insignificant for low concentrations of drill cuttings, especially in short length open channels.

List of papers

Paper 1

Welahettige, P., Lie, B., & Vaagsaether, K. (2017). Flow regime changes at hydraulic jumps in an open Venturi channel for Newtonian fluid. The Journal of Computational Multiphase Flows, 9(4), 169-179. doi: 10.1177/1757482X17722890

Paper 2

Welahettige, P. K., Lie, B., & Vaagsaether, K. (2017). Computational fluid dynamics study of flow depth in an open Venturi channel for Newtonian fluid. In: Proceedings of the 58th SIMS. Reykjavik: Linköping University Electronic Press, pp. 29–34. doi:10.3384/ecp1713829

Paper 3

Welahettige, P., Lie, B., & Vaagsaether, K. (2018). A solution method for 1D shallow water equations using FLIC scheme for open Venturi channels. The Journal of Computational Multiphase Flows, 10(4), 228-238. doi: 10.1177/1757482X18791895

Paper 4

Welahettige, P., Lie, B., Vaagsaether, K. (2019): Computational Fluid Dynamics Study of Shear Thinning Fluid (Drilling Fluid) Viscosity Models in an Open Venturi Channel. International Journal of Petroleum Science and Technology, 13(1):9–20

Paper 5

Welahettige, P., Lundberg J., Bjerketvedt D., Lie, B., Vaagsaether, K. (2018): 1-Dimensional Non-Newtonian (drilling mud) turbulent modelling for non-prismatic channels. Journal of Petroleum Exploration and Production Technology. doi.org/10.1007/s13202-019-00772-9

Paper 6

Welahettige P, Lie B, Vaagsaether K (2019) A Real-Time Flow-Measuring Algorithm for Open Venturi Channel Non-Newtonian Flow. International Journal of Petroleum Science and Technology, 13:1–7

Paper 7

Welahettige P, Berg C, Lundberg J, Lie B, Vaagseather K (2019) Computational fluid dynamics study of the effects of drill cuttings on the open channel flow. International Journal of Chemical Engineering. doi.org/10.1155/2019/6309261

Paper 8

Welahettige, P., Lie, B., Vaagsaether, K., Moldestad, B.M.E. (2017): Study of Fluidization Regimes using OpenFOAM Computational Fluid Dynamics. In: Proceedings of the 58th SIMS. pp. 128–136. Linköping University Electronic Press, Reykjavik. doi:10.3384/ecp17138128

List of tables

List of figures

Abbreviations

CFD Computational fluids dynamics

CFL Courant–Friedrichs–Lewy number

CICSAM Compressive interface capturing scheme for arbitrary meshes

CPU central processing unit

CV Control volume

FLIC Flux limiter centered

FORCE First order centered

FDM Finite difference method

FVM Finite volume method

HB Herschel-Bulkley

HO Higher order

HRIC High resolution interface capturing

KDV Kick detection volume

KRT Kick response time

LF Lax–Friedrichs

LO Lower order

MUSCL Monotonic Upwind Scheme for Conservation Laws

NPT Non-productive time

ODE Ordinary differential equation

PC Pierre Carreau

PDE Partial differential equations

PISO Pressure-Implicit with Splitting of Operators

PL Power law

PRESTO Pressure Staggering Option

QUICK Quadratic Upstream Interpolation for Convective Kinematics

RI Richtmyer

ROP Rate of penetration

RNG Re-Normalization Group

SIMPLE Semi-Implicit Method for Pressure Linked Equations

TVD Total variation diminishing

VOF Volume of fluid

List of symbols

A Cross sectional area (m^2)

a Constant (-)

b Bottom width (m), constant (-)

F Force (N)

Fr Froude number (-)

g Specific gravity (m/s^2)

h Flow depth (m)

h_c Critical flow depth (m)

H Vertical elevation of platform

k Fluid consistency index ($Pa \cdot s^n$), turbulent kinetic energy (m^2/s^2)

L Characteristic length (m)

l Characteristic length (m)

m Mass (kg)

n Flow behavior index (-)

Q Mean volume flow rate (m^3/s)

q Phase (-)

R_e Reynolds number (-)

R_h Hydraulic radius (m)

S Source term, friction slope (-)

T	Temperature (K)
t	Time (s)
U	Average velocity (m/s)
U_w	Wave speed (m/s)
u	x-directional velocity (m/s)
u'	Turbulent fluctuation (m/s)
v	y-directional velocity (m/s)
X	Eigenvector
α	Volume fraction (-), channel inclination angle (degree)
$\dot{\gamma}$	Shear rate (1/s)
η	Apparent viscosity (Pa·s)
θ	Pitch angle (degree), channel trapezoidal angle (degree)
μ	Viscosity (Pa·s)
ν	Kinematic viscosity (m^2/s)
ξ	Non-dimensional length scale (-)
ρ	Density (kg/m^3)
σ	Stain rate (1/s), surface tension (N/m)
τ	Shear stress (Pa)
ω	Angular frequency (rad/s)
ε	Phase shift (rad), rate of dissipation of turbulence energy (m^2/s^3)

ϕ Displacement due to roll motion (degree), flux limiter function

Table of contents

Part I

Overview

1 Introduction

Oil and gas well drilling has, due to the increase in world energy demand, become a wider research area in the last few decades. Kick and loss are the primary pressure control problems in the well drilling process. When formation pressure is much higher than the hydrostatic pressure in the annulus, formation fluid enters the well. This is called a *kick*. A kick can lead to a blowout. The Macondo incident represents a worst-case scenario of a blowout due to poor kick detection (Graham et al., 2011). When the formation pressure is lower than the hydrostatic pressure in the annulus, drilling fluid enters the cavities and is called a *loss*. Kick and loss increase non-productive time (NPT) in drilling operation and lead to significant production loss. Key performance indicators of kick detection are kick detection volume (KDV) and kick response time (KRT) (Fraser et al., 2014). Risk of kick can be reduced by reducing KDV and KRT values. Flow meters are an efficient way of reducing KDV and KRT. Flow meters should be easy to install in the return line, and cuttings should not block the flow measuring line.

Early kick detection can minimize the influx of formation fluid into the wellbore and reduce risk. Primary indicators of kicks are an increase in return flow rate and pit volume. Advanced early kick detection techniques have, in recent decades, been used in industries to minimize kick, and show considerable improvement. The following methods are used for kick detection and monitoring (Nayeem et al., 2016): mudlogging, flow meters, delta flow method, influx detection using standpipe pressure (SPP), influx detection using down-hole pressure, influx detection using the micro flux control method, and the kick detection system developed by Weatherford, Schlumberger, and MezurX (Nayeem et al., 2016). The managed pressure drilling (MPD) method, a new technology, is widely used for accurate control of annular downhole pressure during drilling operations (Hauge et al., 2013; Stamnes et al., 2008; Wilson, 2014). Studies show that measurement of delta flow (the difference between in and out fluxes) is one the best methods for identifying the kick and loss while drilling (Orban et al., 1987; Steine et al., 1995).

Changes in the composition of the drilling fluid while drilling mean that it is more difficult to measure return line flow than inflow. Water, formation fluid, gas, and drill cuttings can be mixed with the drilling fluid inside the wellbore, the density and viscosity of the drilling fluid potentially being significantly changed where mixed with the inert materials. Coriolis mass flow meters have, in the past 20 years, been widely used in real time flow measurement in drilling operation. In most cases, kick is confirmed or identified by Coriolis flowmeters much faster than by the conventional method (Reitsma, 2010). Two Coriolis flow meters are used in well drilling, one mounted in-line between the active mud pit and the mud pumps for inflow measurement, the other mounted in the return line (Norman, 2011). Coriolis meters can measure density, volume flow rate, and mass flow rate for selected drilling fluids. The Coriolis flow meter has some tolerance of gas (Fraser et al., 2014; Reitsma, 2010). A shallow flow occurs where the return line is not choked. The Coriolis flowmeter can record large disturbances due to the air enrichment of shallow flow in the return line. Space on an offshore rig is limited. Considerable space is, however, required to install the Coriolis meters. The Coriolis meters also need to be properly maintained to keep them in good working order. They are also very expensive.

1.1 Semi-kidd project

The “Sensors and models for improved kick/loss detection in drilling” (*Semi-kidd*) project is funded by the research council of Norway and Equinor ASA, project no. 255348/E30. The primary objective of the *Semi-kidd* project is to develop cost effective and automated kick/loss detection sensor technology for drilling operations, see Figure 1-1. This thesis is part of the *Semi-kidd* project.

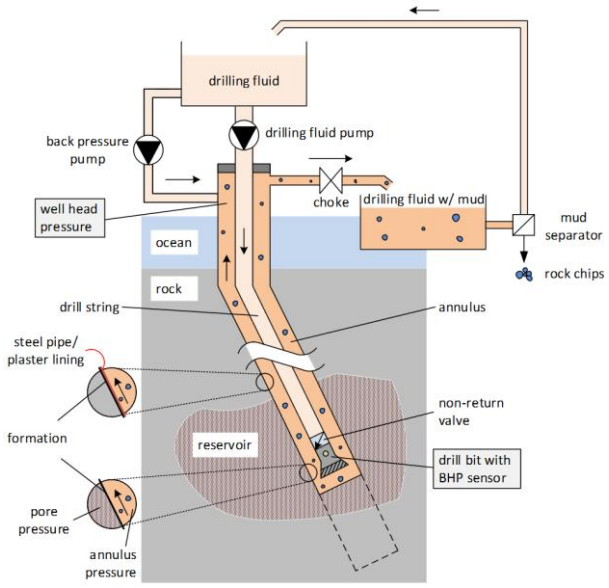

Figure 1-1. Illustration of the drilling process (Semi-kidd, 2016)

1.2 Objectives and methods of the thesis

The delta-flow method does not consider the dynamic hydraulic processes occurring inside the well. The method is generally used for steady state hydraulic conditions (Cayeux and Daireaux, 2013). In this study, return line transient behavior in open channel flow is considered. The open channel can be located just after the choke valve in the return line and before the mud pit tank. The variation of the return flow rate due to kick and loss is considered in the study. Hydraulic waves might give more information on the transient behavior of the return flow than pipe flow. Open Venturi channel flow measurement in the return line might, however, provide a solution. It will furthermore become a low-cost and more accurate method. The thesis work is divided into the three following aspects,

1. Detailed computational fluid dynamics (CFD) study of open Venturi channel flow in steady and transient conditions.

   The work starts with Newtonian fluid simulation in an open Venturi channel using the ANSYS Fluent simulation tool. 3D geometries and 3D mesh are required to capture flow depth in relation to sidewall effects. The CFD simulation aids a basic understanding of flow behavior and hydraulic jumps in an open Venturi

channel. The simulations are to be further extended to a Non-Newtonian fluid similar to the drilling fluid. The behavior of a non-Newtonian drilling fluid in an open channel and the effect of non-Newtonian properties will be focused on. Multiphase flow simulations of drilling fluid and drill cuttings will be the final step of the CFD simulations. The significance of drill cuttings on the open channel flow depth and velocity are to be analyzed. Simulation results will be validated by experimental results.

2. Development of a simplified 1D model for non-Newtonian drilling fluid flow in open channels.

   A simplified 1D model is to be developed for the drill mudflow in the open Venturi channel. Friction, turbulence, and waves are to be taken into consideration through suitable modification of the momentum balance. The 1D model development is to be based on the shallow water equations. The partial differential equations (PDEs) are to be solved using high-resolution numerical schemes. The numerical schemes are expected to have the following features: well-balanced, positivity preserving, high accuracy, and good resolution for discontinuities. The friction slopes of the shallow water equations are expected to be modified by taking into consideration non-Newtonian effects and particle effects. The 1D model is to consider the following aspects: transient and steady state conditions and real time suitability. The momentum balance is to be extended with forces from the oscillatory wave movement of the platform.

3. Open channel experiments and models validations.

   Experiment results are used to validate the results of the 3D CFD and 1D model. The experiments are to be conducted in a laboratory scale mudflow loop, see Figure 1-2. Experimental research is to be performed at a unique test facility for open channel flow and is primarily designed to carry out realistic tests of flow and density sensors on drilling fluids.

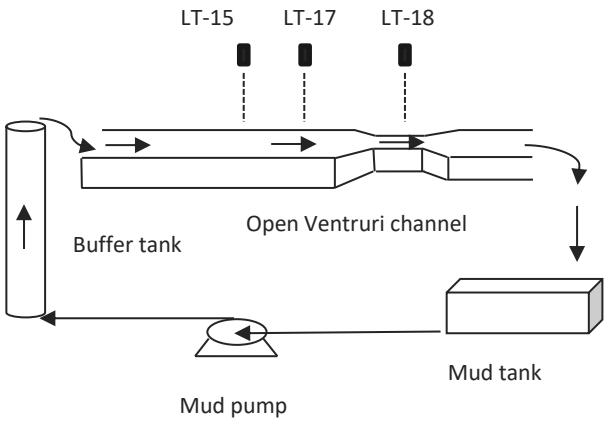

Figure 1-2. Flow loop of the experimental setup: The Coriolis flow meter is located between pump outlet and buffer tank. Three level sensors LT-15, LT-17 and LT-18 are located along the channel central axis.

The results from the presented work have been described in nine publications: six journal articles and two conference papers. All the publications are at or above the scientific level-1 as defined by the Norwegian center for research data (NSD).

1.3 Thesis structure

Chapter 1 is the introduction to the thesis. This is followed by Chapter 2, the literature review, which presents studies relevant to open channel flow regimes, open channel flow measurements, non-Newtonian behavior of drilling fluids, and higher order numerical schemes for solving shallow water equations. Chapter 3 includes the volume of fluid (VOF) computational scheme used for the CFD simulations. The CFD model contains the iteration methods, interface capturing method, turbulence models, non-Newtonian rheological models, and multiphase models. Chapter 4 introduces the 1D model and the numerical scheme used to solve it. The FLIC scheme, a *source term splitting* method for solving the PDEs and a dam-break problem numerical experiment are presented. Chapter 5 presents the experimental setup and methods. Chapter 6 summarizes and discusses the main findings and the contribution of the thesis publications. Chapter 7 concludes the thesis and presents recommendations. Part II contains the journal articles and conference papers.

2 Literature study on open channel flow

2.1 Open channel flow

Open channels and river flows are well-known hydrodynamics concepts. Numerous studies on open channel flow have been published over the last one hundred years. Most of the open channel flow models are derived from the pipe flow models. The Froude number, $\mathrm{Fr} = U/\sqrt{lg}$, describes the state of flow in open channel flow, and is the ratio between inertia force and hydrostatic force (Akan, 2006; Chow, 1959). The Reynolds number $\mathrm{R}_e = Ul/\nu$, which is the ratio between inertia force and viscous force, similarly describes flow patterns in the flow field. The average wave speed is defined as $U_w = U \pm \sqrt{lg}$, the wave propagation speed here being $\sqrt{lg}$ and l being the characteristic length. There are three main states, which depend on the value of the Froude number.

- Subcritical flow: $\mathrm{Fr} < 1$, $U < \sqrt{lg}$, $U_w < 0$ or $U_w > 0$, disturbances (waves) can travel upstream or downstream.
- Critical flow: $\mathrm{Fr} = 1$, $U_w = 0$ disturbances remain stationary.
- Supercritical flow: $\mathrm{Fr} > 1$, $U > \sqrt{lg}$, $U_w > 0$, disturbances (waves) cannot travel upstream.

Open channel flow regimes can, depending on the turbulence condition, be further categorized into subcritical-laminar, subcritical-turbulent, supercritical-laminar and supercritical-turbulent (Chow, 1959). The studies of the turbulence characteristic of open channel can be found in (Bonakdari et al., 2008; Christian et al., 2014; Nezu, 2005; Pu, 2015). The fully developed turbulence velocity profiles in an open channel are described in (Bonakdari et al., 2008; Christian et al., 2014; Guo et al., 2015; Iehisa and Ryoukei, 2004; Nezu et al., 1994). Their studies indicate that the turbulent boundary layer is composed of an inner and outer region. According to laser-Doppler anemometer (LDA) data in the literature, the inner region is 10-20% of the entire boundary thickness.

Open channel turbulence can also be described by eddy viscosity, mixing length, and the Prandtl model (Nezu, 2005).

Figure 2-1 shows a hydraulic jump in open channel flow. It is primarily made up of a supercritical flow, a transition region and a subcritical region (Chanson and Brattberg, 2000; M. and Hanif, 1991).

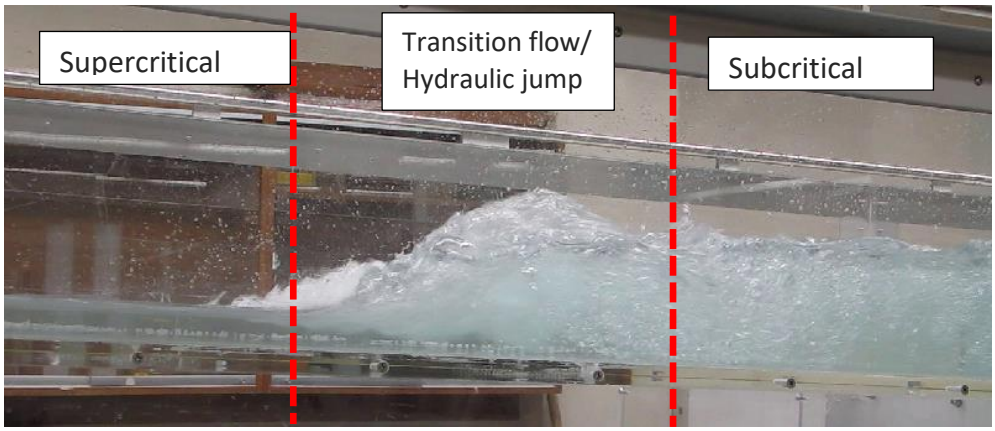

Figure 2-1. A hydraulic jump in an open channel. Supercritical flow converts, through critical flow to subcritical flow. Fluid flows left to right (Hotchkiss and Kern, 2012).

Maximum velocity in the open channel velocity profile occurs below the free surface and is due to secondary motion. This is called the dip-phenomena (Absi, 2011; Bonakdari et al., 2008; Nezu et al., 1994; Sarma et al., 1983; Stearns, 1883; Yang et al., 2004). According to experiment results of Christian et al. (2014), the strength of the secondary currents vanish where aspect ratio $>$ 4-5 (Yang et al., 2004). The aspect ratio is defined as being the ratio between free surface width and flow depth. More secondary currents are generated at the bends of open channel by the counter-rotating circulation cells near the outer bank (Blanckaert and De Vriend, 2004; Patel and Gill, 2006). Open channel friction parameters have been derived and studied for Newtonian and non-Newtonian fluids in the following literature (Alderman and Haldenwang, 2007; Burger et al., 2010a; Haldenwang, 2003; Haldenwang and Slatter, 2006; Jin and Fread, 1997, n.d.; Nezu, 2005). Most of the open channel friction models have been derived from the pipe flow friction models. Burger et al. (2010b) found that the linear relationship between the Fanning friction factor and the Reynolds number changes with the shape of the cross section for a non-Newtonian laminar open channel flow. Turbulent friction

models are crucial at industrial scale, for example in oil well return flow, due to the variation of flow rates and flow properties in real time.

The effect of lateral channel contraction has been studied in the following literature (Abdo et al., 2018; Akers and Bokhove, 2008; Datta and Debnath, 2014; Hsu et al., 1998; Kocaman and Ozmen-Cagatay, 2012; Murty Bhallamudi and Hanif Chaudhry, 1992; Rahman and Chaudhry, 1997; Sanders and Iahr, 2001). Datta and Debnath (2014) used the VOF method to compute open channel contraction flow. Turbulent intensity increases as contraction ratio decreases. Surface roughness increases in the wake of the velocity profile and with turbulence intensity level (Tachie et al., 2003). Akers and Bokhove (2008) found steady upstream jumps, supercritical weak oblique waves, and subcritical smooth flow in a hydraulic flow through a channel contraction. A standing hydraulic jump is common in supercritical flow that passes through a contraction or an overtopping. According to Abdo et al. (2018), a large flow depth occurs along the channel at a reduced flow rate, with maximum depth occurring in the contraction region. Kocaman and Ozmen-Cagatay (2012) found that when a dam break flood wave encounters an open channel contraction, part of the wave passes through the opening, the other part reflecting against the contraction. The reflected part forms a negative bore traveling in the upstream direction. According to the Khandelwal et al. (2015) study of laminar flow of a non-Newtonian shear-thinning fluid in a channel, the flow disturbance in shear-thinning fluid is much more dominant and exists for a much greater distance in the side branches than for a Newtonian fluid.

2.2 Open channel flow models

Orban et al. (1987) developed a return line flow meter for open channel flow through combining the readings from an ultrasonic level sensor and an ultrasonic Doppler velocity probe. Flow rate is calculated by multiplying the cross-sectional area with the average velocity using a friction factor. The local flow rate of open channel Q can be integrated from the local fluid height h and local mean streamwise velocity u, $Q = \int_0^h u(z)dz$ (Fernández-Nieto et al., 2010). However, finding the precise local velocity

profile is not an easy task. An Irish engineer Robert Manning (Manning et al., 1890) derived an empirical equation which can estimate the open channel water flow rate, and it is a function of flow area, hydraulic radius and channel slope (Chow, 1959). The recommended conditions for Manning's equation are channel minimum straight length greater than 60 m, uniform cross section, uniform slope, uniform roughness, no sudden contraction or expansion, and no backflow. Under the ideal conditions, the accuracy of the equation is ± 10-20 %, potentially rising to ± 50 % depending on flow conditions (Openchannelflow, 2018). Haldenwang (Haldenwang, 2003) derived a flow model based on the Slatter's (Slatter, 1995) model, for Herschel-Bulkley fluid in open channels. The model was based on semi-empirical data.

The international standard ISO 4359 (International Standard-ISO 4359, 2013) introduced a set of equations to estimate flow rate in flumes based on critical flow depth. Critical flow location has also shown to change with flow conditions (Chhantyal, 2018). These equations might be challenging to use with different flow conditions. Berg et al. (Berg et al., 2015) conducted a feasibility study on a cost-effective flow measurement in an open Venturi channel. Agu et al. (Agu et al., 2017) introduced a flow measuring method in open channel flow based on the hydraulic structure and slope-hydraulic radius method. Chhantyal (2018) analyzed three types of flow models for an open channel with Venturi constriction. The three models were upstream-throat level based, upstream level based, and critical level based. Rheological parameter changes in each circulation while drilling mean the flow models are not reliable for return flow estimations, without the tuning of correction factors (Chhantyal, 2018).

Pipe flow Venturi flow meters are available in oil and gas industries. However, to the best of our knowledge, open channel Venturi flow meters are rarely used. In pipe flow, Venturi flow generates a differential pressure signal to calculate the flow rate through using empirical correlations (Lindsay et al., 2001; Ünalmis and Raul, 2016). A free surface gravity flow is, unlike pipe Venturi flow, included in open Venturi flow.

2.3 Non-Newtonian drilling fluid flow

The functions of drilling fluid are transportation of the drill cuttings from drill bit to the top surface, cooling and cleaning of the bit, lubricating the drill string, and maintaining well stability (Caenn et al., 2011). Drilling fluid properties can create severe problems in drilling operations, including bridging of the hole, reduced penetration rate, filling the bottom of the hole with drill cuttings, stuck pipe, hole enlargement, loss of circulation, and blowout (Zamora and Roy, 2000). Water-based drilling fluid and oil-based drilling fluid are the most popular types of drilling muds used in the oil and gas industries. A drilling fluid should have a gel strength that is sufficient to hold cuttings in suspension when fluid circulation stops (N. Alderman et al., 1988). Drilling fluids should have shear thinning and yield properties that fulfill the above requirement. Yield stress is used to evaluate the ability of mud to lift cuttings out of the annulus. Water-based drilling fluids are commonly suspensions of bentonite clay (N. J. Alderman et al., 1988). Water-based drilling fluid uses polymers such as Xanthan gum, Guar gum, and tamarind gum to achieve higher viscosity ranges (Wan et al., 2011). Drilling fluid generally shows non-Newtonian properties, the properties under certain conditions, being of a liquid, a solid or a semisolid.

Gucuyener (1983) tested the Bingham model, the power law model, the Herschel-Bulkley model, the Casson model and the Robertson-Stiff model for various drilling fluids. A difficulty of non-Newtonian fluid models is finding the shear stress at the zero shear rate. A challenge with yield stress rheological models is the experimental determination of the yield stress value (Møller et al., 2006). Techniques used for finding yield stress by non-linear regression may give negative values for the yield stress in the Herschel-Bulkley model (Kelessidis et al., 2006). The Herschel-Bulkley model can also give substantial viscosity at very small shear rates. The Carreau viscosity model is a good fit for shear-thinning fluids and is capable of catching rheological behavior at small and large shear rates (Picchi et al., 2017). The Carreau model gives a finite viscosity at zero shear rate, which the Herschel-Bulkley model cannot achieve. The Carreau model has four parameters, which increases the complexity of the equations.

2.3.1 Power-law model

The power-law model has two model parameters. The laminar sublayer is thinner for a shear thinning fluid $0 < n < 1$ than for the Newtonian case $n = 1$. This is because a pseudoplastic fluid has lower viscosities at high shear rates than its related Newtonian case. The viscous effect near the wall might therefore be neglected for some shear thinning fluids (Dodge and Metzner, 1959). Drilling fluid must have a yield stress as explained above. It is therefore practically difficult to use the power-law model for drilling fluids. Yield-power law rheological models are therefore suitable for mud rheology (Hemphill et al., 1993).

$$\eta = k\dot{\gamma}^{n-1} \tag{2.1}$$

Here, η is the apparent viscosity. The model parameters k and n are known as the fluid consistency index and flow behavior index, respectively.

2.3.2 Herschel-Bulkley model

The Herschel-Bulkley model combines the properties of Bingham and power-law models. It has one more unknown parameter than the power-law model. This parameter is yield stress τ_y. The Herschel-Bulkley model is widely used in the oil field industry. According to the Herschel-Bulkley model, material starts to flow when stress exceeds the yield stress. A Herschel-Bulkley fluid can, according to Longo et al. (2016), have motionless regions in steady uniform flow in an open channel. The motionless regions occur in the upper region of the cross section beside the plug flow. Plug flow propagates above the shear region, the shear region being at or near the bottom wall. The motionless region might disappear in unsteady flow.

$$\tau = \begin{cases} \tau_y, \tau \leq \tau_y \\ \tau_y + k\dot{\gamma}^n, \tau \geq \tau_y \end{cases} \tag{2.2}$$

2.3.3 Pierre Carreau model

The Pierre Carreau (or Carreau) viscosity model is recommended for shear-thinning fluids, due to its capacity to capture rheological behavior at low and large shear rates (Carreau, 1972; Picchi et al., 2017). The power-law model, in contrast, has some limitations; the governing equations become highly non-linear at low values of the power-law index (D'Alessio and Pascal, 1996; Khandelwal et al., 2015; Picchi et al., 2017). Shear-thinning fluids can be modeled using the power-law model, the Herschel-Bulkley model, the Carreau viscosity model, the Cross viscosity model, and the Ellis model (Chhabra and Richardson, 2011). Paper 4 further describes other available rheological models for shear thinning fluids.

$$\eta = \eta_\infty + (\eta_0 - \eta_\infty)(1 + (\lambda\dot{\gamma})^2)^{\frac{n-1}{2}} \tag{2.3}$$

Figure 2-2 shows a comparison of different rheological models.

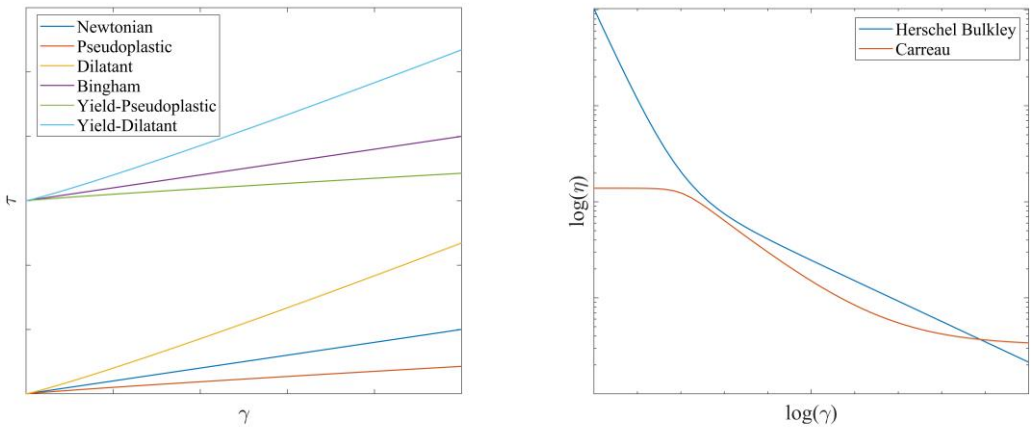

(a) (b)

Figure 2-2. A comparison of rheological models: (a) Shear stress vs shear rate, (b) Viscosity vs shear rate

2.4 Typical drilling flow parameters industrial scale

Some key drilling parameters which would affect bottom hole pressure are controllable at the surface. Some are not controllable (Paknejad et al., 2009). The uncontrollable

parameters are the amount of formation water, cuttings size, and cuttings concentration. Typical drilling parameters that are important in this study are summarized in Table 2-1.

Table 2-1. Typical drilling flow parameters used in industries

Parameters	**Value**	**Sources**
Hole diameter (m)	0.12 m – 1 m	(Mitchell and Miska, 2011)
Drill mud density (kg/m^3)	1000 – 2160	(Orban et al., 1987)
Drill mud apparent viscosity (Pas)	0.001 – 0.2	(Orban et al., 1987)
Drill cutting sizes	1 µm – 4 cm	(Neff, 2010)
ROP	1 m/h – 22 m/h	(Keshavarz Moraveji and Naderi, 2016)
Cuttings concentration	4-5 % v/v	(Paknejad et al., 2009; Pigott, 1941)

2.5 Numerical schemes for solving Saint-Venant PDEs

Free surface flows are considered to be *shallow flow* when the horizontal length scale is higher than the vertical length scale (Cea et al., 2007). The shallow water equations are a well-known set of hyperbolic equations, which can be used for hydrodynamic applications. The Saint-Venant equations are the unidirectional approach to the shallow water equations. The basics assumptions of the Saint-Venant equations are as follows (Aldrighetti, 2007): flow is in 1D, the free surface is horizontal in a cross-section, the velocity is uniform over the cross-section, vertical direction acceleration is negligible,

and pressure can be considered to be hydrostatic. Equation (2.4) and (2.5) shows the Saint-Venant equations for a prismatic channel (same cross sectional shape).

$$\underbrace{\frac{\partial h}{\partial t}}_{(a)} = \underbrace{-\frac{\partial (hu)}{\partial x}}_{(b)}, \tag{2.4}$$

$$\underbrace{\frac{\partial (hu)}{\partial t}}_{(c)} = \underbrace{-\frac{\partial (hu^2)}{\partial x}}_{(d)} \underbrace{- gh\frac{\partial h}{\partial x}}_{(e)} \underbrace{+ hg\sin\alpha}_{(f)} \underbrace{- hgS_f}_{(g)}. \tag{2.5}$$

The terms (a) and (c) represent the rate of increase of mass (or height) and momentum (or flow rate) in the control volume. The terms (b) and (d) represent the net rate of mass and momentum out from the control volume. The term (e) represents the hydrostatic pressure acting on the control volume. The term (f) represents the gravity effect, and the term (g) represents the source term effect. The Saint-Venant equation can be presented in the form of the Cauchy momentum equation, $\mathbf{U}_j^{m+1} = \mathbf{U}_j^m - \frac{\Delta t}{\Delta x}\left[\mathbf{F}(\mathbf{U})_{j+\frac{1}{2}}^m - \mathbf{F}(\mathbf{U})_{j-\frac{1}{2}}^m\right] + \Delta t\, \mathbf{S}$. Chapter 4 describes the discretized equation in more detail.

High resolution well balanced numerical schemes are required to solve the shallow water equations for the following reasons: the unsteady hydraulic jumps (discontinuities), preservation of non-negative flow depths, maintaining stability at dry or near dry conditions, and satisfying the entropy inequality (Kurganov and Petrova, 2007; Perthame and Simeoni, 2001; Sanders and Iahr, 2001). TVD (total variation diminishing), TVB (total variation bounded) and ENO (essential non-oscillatory) schemes have proven to be very important for the discontinuous solutions of hyperbolic conservation laws (Shu and Osher, 1988). Higher order Godunov type numerical

schemes are used to solve the Saint-Venant equations (Kurganov and Petrova, 2007; LeVeque, 1998). One of the main difficulties in the solving of the Saint-Venant equations is to find accurate fluxes in control volumes. Higher order well balanced finite volume or finite difference schemes have been used in recent decades to calculate the fluxes. These schemes are the essentially non-oscillatory (ENO) scheme (Vukovic and Sopta, 2002), the weighted essentially non-oscillatory (WENO) scheme (Xing and Shu, 2006), the central-upwind scheme (Kurganov and Levy, 2002) and Roe's approximate Riemann solvers (Castro et al., 2009). Kelly (2017) suggested a second order accurate fluid-in-cell method for a 2D shallow water equations solving method. The fourth order WENO method estimates the interface fluxes. High-resolution shock-capturing methods used in gas dynamics can be applied to the shallow water equation even though this uses an inhomogeneous source term (Toro, 2009; Tseng, 2004). The total variation diminishing (TVD) method is widely used for solving the shallow water equations (Bradford and Sanders, 2002; Kelly, 2017; Liang and Marche, 2009; Song et al., 2011; Tseng, 2004; Vukovic and Sopta, 2002; Xing and Shu, 2011, 2006). The operator-splitting approach, the eigenvector-projection approach, and other improved methods can be applied to the solving of complex source terms (Tseng, 2004).

Depth-averaged equations can be derived for the open channel flow by integrating the Navier-Stokes equations (Aldrighetti, 2007; Thomas and Hanif, 1995). The 1D form of the depth-averaged equations is equal to the Saint-Venant form. Tomas et al. (1995) used a constant eddy viscosity model to approximate the turbulent Reynolds stresses in the 2D depth-averaged equations. 2D turbulent shallow water equations were derived by Pu (Pu, 2015) by adapting the Kolmogorov scaling into the k- ε model. According to the numerical investigation of Park et al. (2012), the effect of turbulent intensity on friction drag cannot be neglected in the dam break problem, especially in the wave front.

2.6 Open channel drill cuttings flow

Cuttings are generated at the drill bit and transported along the wellbore to the top surface through the annulus. Specific transport mechanics such as the rolling mechanism, the lifting mechanism, and particle settling apply at high, intermediate, and

near-vertical angles of the wellbore; the actual transport mechanics depends on the wellbore angle (Clark and Bickham, 1994). The static forces on the cuttings are gravity force, buoyancy force and plastic force (due to the yield stress of the mud). The dynamic forces are drag force, lift force, and pressure gradient force (Akhshik et al., 2015). Cuttings rolling occurs when the dynamic force exceeds the static force. Dynamic forces are high at high mud velocities. Drag force is, in general, in the flow direction, and lift force is normal to the flow direction (Ramadan et al., 2003). Lift acts on the particle due to asymmetry in the flow field (or velocity gradient), which leads to particle rotation (Crowe et al., 1998). A no-slip condition at the wall may create high flow field asymmetry.

Extensive studies have been carried out on drill cutting flow in pipe flow. However, only minor studies have been conducted in open channel drill cutting flow. Open channel solid particle transport has been studied for particle size up to 0.5 mm in the following studies: (Jha, 2017; Kiger and Pan, 2002). According to Loisel et al. (2013), the particle volume fraction is homogeneously distributed in the channel cross-section. However, particle concentration becomes higher near-wall due to inertia driven migration at steady state. The mean streamwise particle velocity is lower than the fluid velocity. The fluid, however, only instantaneously lags by a small amount (Kidanemariam et al., 2013). Kiger and Pan (2002) found that particles increased wall friction velocity, and the normal and shear Reynolds stresses in the outer flow.

Two-layer and three-layer formulas are available for 1D solid transport modeling for conduits (Aarsnes and Busch, 2018; Doron and Barnea, 1993). The three-layer model contains a homogeneous layer, a moving bed layer, and a stationary layer. The two-layer model neglects the moving bed layer of the three-layer model. Stationary beds are unable to be predicted by the two-layer model at low flow rates (Doron and Barnea, 1993). Each layer has two components: a liquid and a solid component. The three-layer model consists of six equations. Solving six equations might, however, be time-consuming in real time flow estimations.

3 Computational Fluid Dynamics (CFD) models

A CFD model was developed in the commercial simulation tool ANSYS Fluent 16.2 and 18.2. The CFD model was used to validate the 1D model. The CFD model was validated using the experimental data. The CFD modeling work was divided, in this study, into three categories: Newtonian fluid, non-Newtonian fluid, and drilling fluid with drill cuttings. Free surface flow, inlet and outlet boundaries, wall friction, particle, non-Newtonian effect, and wave motion effects in an open Venturi channel were emphasized in the CFD study.

3.1 Volume of fluid (VOF) model

3D open channel flow contains minimum two fluids: fluid flowing in the channel and fluid above the flowing fluid (air). The volume of fluid (VOF) method has been specialized for capturing the interface between two or more immiscible fluids (Hirt and Nichols, 1981). The VOF model belongs to the Eulerian class of methods. A single set of momentum equations solves the fluid domain by tracking the volume fraction of each control volume (ANSYS Fluent, 2009). At the interface of the q^{th} phase, $0 < \alpha_q < 1$ is surrounded by the other phases. The total volume fraction is equal to unity. In this study, the maximum number of phases are two, for example air, and drilling fluid or water; $\sum_{q=1}^{2} \alpha_q = 1$. The fluids are assumed to be incompressible and immiscible, and the system is considered to be isothermal. All control volumes must be filled with either a single phase or a combination of phases (ANSYS Fluent, 2009). The continuity equation and the momentum equations are:

$$\frac{\partial \rho}{\partial t} = -\nabla.(\rho \mathbf{u}), \tag{3.1}$$

$$\frac{\partial \rho \mathbf{u}}{\partial t} + \nabla.(\rho \mathbf{u}\mathbf{u}) = -\nabla \mathrm{p} + \nabla.\mu_{eff}(\nabla \mathbf{u} + \nabla \mathbf{u}') + \rho \mathbf{g} + \mathbf{F}_s. \tag{3.2}$$

Here $\mathbf{F}_s$ is the surface tension force. The effective viscosity $\mu_{eff} = \mu + \mu_t$ is the sum of the molecular dynamic viscosity μ, and turbulent eddy viscosity μ_t. The interface between the liquid (l) and air (g) is tracked by solving the volume fraction equation:

$$\frac{\partial \alpha_l}{\partial t} = -\nabla.(\alpha_l \mathbf{u}), \tag{3.3}$$

$$\rho = \alpha_l \rho_l + (1 - \alpha_l)\rho_g, \tag{3.4}$$

$$\mu = \alpha_l \mu_l + (1 - \alpha_l)\mu_g. \tag{3.5}$$

The volume fraction equation can be solved either through implicit or explicit time discretization. Qian and Lawal (Qian and Lawal, 2006) described three challenges that might arise while implementing the VOF model:

- Mixture properties ρ and μ vary within the flow domain in Equation (3.1) and (3.2). Mixture properties are a function of volume fraction. The volume fraction is computed from Equation (3.3). The energy equation is used to calculate the density of air, even though heat transfer is very small. Fluid viscosity is not a constant in this study due to the non-Newtonian rheology. Equation (2.1) or (2.2) or (2.3) computes the viscosity of fluid as a function of shear rate. The k-ε model computes the turbulence velocity fluctuation $\mathbf{u}'$ in Equation (3.2).
- The interface has to be constructed based on the calculated volume fractions and the application of interpolation schemes.
- Surface tension between each pair of phases, and adhesion between phases and walls become very crucial. These effects might, however, be insignificant when the gravity effect predominates.

The continuum surface force (CSF) formulation describes surface tension force $\mathbf{F}_s$ (Brackbill et al., 1992; Ubbink and Issa, 1999), $\mathbf{F}_s = -(\sigma \nabla \alpha_l)\nabla \cdot \left(\frac{\nabla \alpha_l}{|\alpha_l|}\right)$, where σ is surface tension, σ being set in this study to 0.072 N/m and as a water-air interface.

3.2 Turbulence modeling

Time-averaged convective divergence terms in the momentum equation produce the product of fluctuating velocity terms, $\overline{\nabla.(\mathbf{uu})} = \nabla.(\overline{\mathbf{u}}\,\overline{\mathbf{u}}) + \nabla.(\overline{\mathbf{u}'\mathbf{u}'})$. The Reynolds stresses using Boussinesq's isotropic eddy viscosity approximation are:

$$\tau_{xy} = -\rho\overline{u_x' u_y'} = \mu_t\left(\frac{\partial \bar{u}}{\partial y} + \frac{\partial \bar{v}}{\partial x}\right) - \frac{2}{3}\rho k \delta_{ij} \tag{3.6}$$

Here $\mathbf{u}'$ is the turbulence fluctuation of three dimensional velocity component, k is the turbulent kinetic energy $k = \overline{u'^2} + \overline{v'^2} + \overline{w'^2}$, μ_t is the turbulent eddy viscosity, $\mu_t = \rho C_\mu k^2/\varepsilon$, δ_{ij} is the Kronecker delta. The two equation turbulence closure model, the k-ε model, calculates the turbulent kinetic energy and the dissipation rate of turbulent kinetic energy (ANSYS Fluent, 2009; Versteeg and Malalasekera, 2007).

$$\frac{\partial(\rho k)}{\partial t} + \nabla.(\rho k \mathbf{u}) = \nabla.\left[\left(\mu + \frac{\mu_t}{\sigma_k}\right)\nabla k\right] + G_k + \rho\varepsilon, \tag{3.7}$$

$$\frac{\partial(\rho \varepsilon)}{\partial t} + \nabla.(\rho \varepsilon \mathbf{u}) = \nabla.\left[\left(\mu + \frac{\mu_t}{\sigma_k}\right)\nabla \varepsilon\right] + C_{1\varepsilon}\frac{\varepsilon}{k}G_k - C_{2\varepsilon}\rho\frac{\varepsilon^2}{k}. \tag{3.8}$$

G_k here represents the generation of turbulent kinetic energy due to the mean velocity gradient, which is consistent with the Boussinesq hypothesis, $G_k = \mu_t\left(\frac{\partial \bar{u}}{\partial y} + \frac{\partial \bar{v}}{\partial x}\right)\frac{\partial \bar{u}}{\partial y}$. The standard k-ε model parameters $C_\mu = 0.09$, $\sigma_k = 1.00$, $C_{1\varepsilon} = 1.44$ and $C_{2\varepsilon} = 1.92$ are used in the simulation. Amanna and Khorsand Movaghar (2016) also used these parameter values. The non-Newtonian fluid based k-ε model parameters might, however, be more accurate. The VOF model can couple with the standard k-ε, k-ε RNG, k-ε realizable, k-ω , Reynolds stress (Patel and Gill, 2006) and LES (Li et al., 2015) turbulent models. The standard k-ε model assumes an isotropic eddy viscosity, and can therefore not predict secondary currents (Nezu, 2005). We have not focused on secondary currents in this study. Fully developed turbulent flow has two boundary layers: the inner and outer regions. The log-wake-law might provide a wake strength analysis solution (Guo, 2014).

Near-wall treatment is highly important to turbulence properties capture from an Eulerian mesh. The *law of the wall* is generally described using dimensionless analysis, $u^+ = U/u_\tau$ and $y^+ = \rho u_\tau y/\mu$, here, $u_\tau = \sqrt{\tau_w/\rho}$. For smooth walls, the inner region can be divided into viscous sublayer, buffer layer, and log-law layer. The viscous sublayer predominates, there being viscous stresses where $y^+ \leq 5$ and $U^+ = y^+$. For a viscous

fluid, the *no-slip* wall condition implies that fluid sticks to the wall. The viscous sublayer is important to the definition of the no-slip condition. The viscous sub-layer is, however, quite small and difficult to measure experimentally. Turbulent stresses are dominant in the log-law layer, where $30 < y^+$ and $U^+ = \frac{1}{\kappa}\ln y^+ + A$. Here, A is an integration constant, and, κ is the von Karman constant. According to Nikuradse's (1950) experiments, $A = 5.5$ and $\kappa = 0.4$. In this study, the rough wall condition applies to the wall boundaries and the *law of the wall* modifies with the roughness function as (Versteeg and Malalasekera, 2007):

$$U^+ = \frac{1}{\kappa}\ln y^+ + \Delta B \tag{3.9}$$

ΔB depends on the type and size of roughness (ANSYS Fluent, 2009). Three wall regimes are defined based on the non-dimensional roughness height ${K_s}^+$. These are hydrodynamic smooth at $K_s^+ \leq 2.25$, transitional at $2.25 < K_s^+ \leq 90$, and fully rough at $K_s^+ > 90$ for the hydrodynamic smooth region $\Delta B = 0$ and for the fully rough regime $\Delta B = \frac{1}{\kappa}\ln\left(1 + C_s {K_s}^+\right)$. Here ${K_s}^+ = \rho K_s u^*/\mu$, K_s is the physical roughness height, $u^* = C_\mu^{1/4}\kappa^{1/2}$, and C_s is the roughness constant. In this study, channel walls are fabricated of stainless steel. Therefore, by assuming uniform sand-grain roughness, $K_s = 15$ µm and $C_s = 0.5$ (Nikuradse, 1950).

3.3 Interphase capturing

A free surface always occurs between the flowing fluid and the atmosphere in open channel flow. Interface-tracking methods are required to track the interface for space and time in a fixed mesh. There are two main interface-tracking techniques available, VOF (Hirt and Nichols, 1981) and level-set methods. Chapter 3.1 describes the VOF method. The interface construction has to be based on the calculated volume fractions and the application of interpolation schemes. The face flux can be interpolated from an interface reconstruction method or a finite volume discretization method (ANSYS Fluent, 2009). The interface can be reconstructed using the geometry-reconstruct method or donor-acceptor method. Ubbink (1997) introduced the *compressive interface*

capturing scheme for arbitrary meshes (CICSAM). The CICSAM method is suitable for high ratios of viscosity between the phases. According to the *donor-acceptor* method, the donor cell is the center cell, and the two neighbor cells are the acceptor cell and upwind cell, see Figure 3-1. In the *donor-acceptor* method, the volume fraction flux over the cell face is calculated from the volume fraction values of both the donor and the accepter cell (Hirt and Nichols, 1981). ANSYS Fluent has a *compressive* and *modified HRIC* method for volume fraction discretization. The *compressive* scheme is an explicit implementation of the CICSAM scheme.

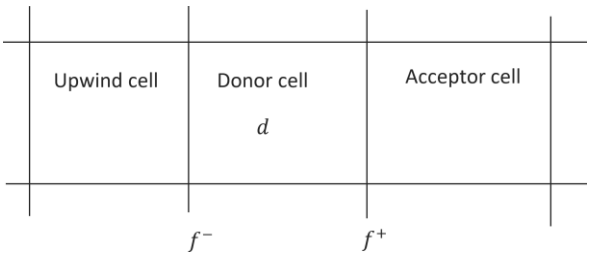

Figure 3-1. 1D control volume to explain donor and acceptor cells (Hirt and Nichols, 1981).

The *compressive* scheme is:

$$\varphi_f = \varphi_d + \beta \nabla \varphi_d. \tag{3.10}$$

Here, φ is VOF values (flow quantities), and can be either a vector or scalar. Furthermore, φ_f is the face VOF value, φ_d is the donor cell VOF value, and β is the slope limiter value. When $\beta = 0$, $\beta = 1$ and $\beta = 2$ the discretization scheme represents respectively fist order upwind, second order upwind, and compressive scheme (ANSYS Fluent, 2009). In this study, the slope limiter is set as *cell to face limiter.* The *minmod* based limiter function is used. Heat transfer between two phases through the interface is neglected in this study.

3.4 Boundary conditions

In transient problems, the initial values of all the solution points must be defined before the simulations are started. In the finite volume method, *ghost cells* are defined out from the physical boundaries, this generally being in the *staggered grid, see* Figure 3-2.

The numbers of ghost cells are decided for each boundary, the number depending on the discretization scheme.

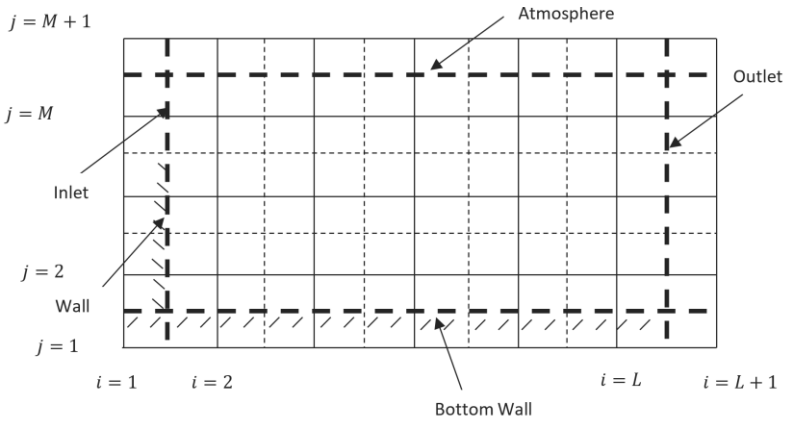

Figure 3-2. 2D staggered grid shows ghost cells in boundaries such as inlet, outlet, wall, bottom wall, and atmosphere for an open channel.

The inlet boundary flux is perpendicular to the cell face (or x-direction). It is defined as being the *mass-flow-inlet*. The inlet mass flow rate for all species is defined as *fixed values* based on the Dirichlet boundary condition (Rusche, 2003). At the inlet, the convective flux is fixed and the diffusion gradient is neglected. The atmosphere boundary is defined as being a *pressure-outlet,* where pressure is specified from the neighboring cell. The free surface in a control volume is assumed to be horizontal and normal to the direction of gravity (ANSYS Fluent, 2009). The outlet is considered to be a *pressure-outlet.* Velocity and pressure are unknown prior to solving the flow problem at the outlet. An assumption at the outlet is that a fully developed state occurs in the flow direction, the gradient of all variables except pressure being set to zero (Versteeg and Malalasekera, 2007). This assumption is more accurate where the outlet is far from the inlet (Ferziger and Peric, 2002). The gauge pressure at the outlet, which is open to the atmosphere, is set to zero. The boundary turbulent behavior is described by turbulent intensity and length scale. The *backflow* direction is normal to the boundary, and backflow pressure is taken from the total pressure. The wall boundary condition is described in Chapter 3.2.

3.5 Non-Newtonian rheological models

No single equation has yet been developed that can explain the relationship between shear stress and shear rate for all fluids. Viscous force is a surface force. Viscous stress can be formulated as a function of local deformation rate or strain rate. Local deformation is a combination of the linear elongation deformation and linear shear deformation. The linear elongation deformation is also called the volumetric deformation. There are, in a cubic control volume, three linear elongation deformations (similar to σ_{xx}) and six linear shear deformations (similar to σ_{xy}). The volumetric deformation can be neglected for an incompressible fluid, $\nabla . \mathbf{u} = 0$, (Versteeg and Malalasekera, 2007). The relationship between shear stress and shear rate is linear for a Newtonian fluid at constant viscosity. Non-Newtonian fluid viscosity, however, depends on shear rate.

$$\bar{\sigma}_{xx} = \frac{\partial \bar{u}}{\partial x}, \bar{\sigma}_{xy} = \frac{1}{2}\left(\frac{\partial \bar{u}}{\partial y} + \frac{\partial \bar{v}}{\partial x}\right). \tag{3.11}$$

These strain rates (shear rates) are used to calculate the non-Newtonian viscosity from the non-Newtonian models described in Chapter 2.3. The momentum equation, Equation (3.2), combines the above mentioned viscosities and turbulence models.

3.6 Iteration method

The numerical integrations are based on the finite volume method (FVM). In the finite volume method, the divergence theorem is applied to the divergence terms and converts these into surface integral terms. The transport equations are discretized according to the staggered grid method. The staggered grid stores velocities at the boundary faces, and the pressure field at the center of the control volume. The staggered grid avoids a highly non-uniform pressure field acting as a uniform pressure field (Versteeg and Malalasekera, 2007). Table 3-1 shows the discretization schemes, which are available in the ANSYS Fluent tool. They are compatible with the VOF model.

Table 3-1. The spatial and time discretization scheme can be used for the VOF method in ANSYS Fluent

Variable/concept	**Discretization scheme/scheme**
Pressure-velocity coupling	SIMPLE, SIMPLEC, PISO, and Coupled
Gradient	Least-square cell based, Green-Gauss cell based, Green-Gauss Node based
Pressure	PRESTO, Body Force Weighted
Momentum, Turbulent kinetic energy, Turbulent dissipation rate, Energy	First order upwind, second order upwind, Power law, QUICK, Third-order MUSCL
Volume fraction	Compressive
Interpolation near the scheme	The geometry construction , The donor-acceptor , CICSAM
Transient (time)	First order implicit, Second order implicit, Bounded second order implicit

Figure 3-3 shows the VOF method computing cycle in a transient condition for two-phase flow. The discretized momentum equation is solved using a guessed pressure field in the initial step (the previous iteration result being used after this), to yield the velocity field. The pressure correction terms can be found from the calculated velocity field and the continuity equation. The corrected pressure and velocity fields can be calculated from the calculated pressure correction and velocity correction terms. An assumption in the SIMPLE algorithm is that the velocity corrections for the neighboring cells are omitted in each iteration cycle. However, the omission terms do not affect the final

solution, because the correction factors become zero in a converged result (Versteeg and Malalasekera, 2007).

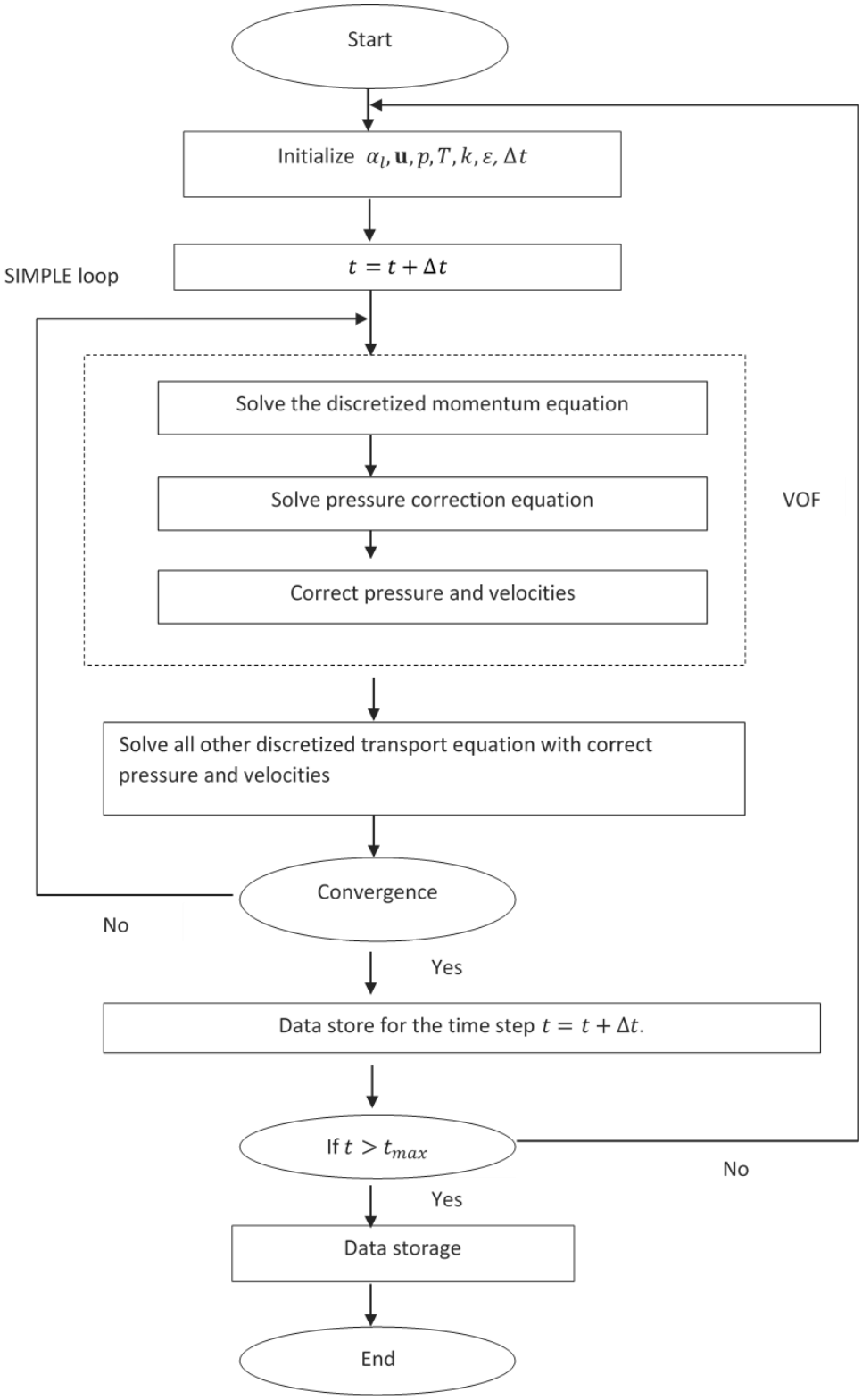

Figure 3-3 Computing cycle of transient VOF model for two-phase flow.

3.7 Eulerian multi-fluid VOF model

A three-phase flow must be considered in drilling fluids with drill cuttings flow in open channels. There are separate equations for each phase in the multi-fluid VOF model (Murthy and Ghadge, 2007). An explicit VOF option can capture sharp interface in the Euler-Granular multiphase flow model in ANSYS Fluent 18.2. The multi-fluid VOF model provides anisotropic drag for free surface flow. The anisotropic drag force applies in the tangential and normal directions to the interface (ANSYS Fluent, 2009). However, the sharp and disperse interface method is also compatible with the other drag models. According to Jing et al. (2016), OpenFOAM solves VOF continuity equations first and then the updated fluid cell condition is used to initialize the PISO loop. Figure 3-4 shows the multi-fluid VOF method computation cycle for transient calculations.

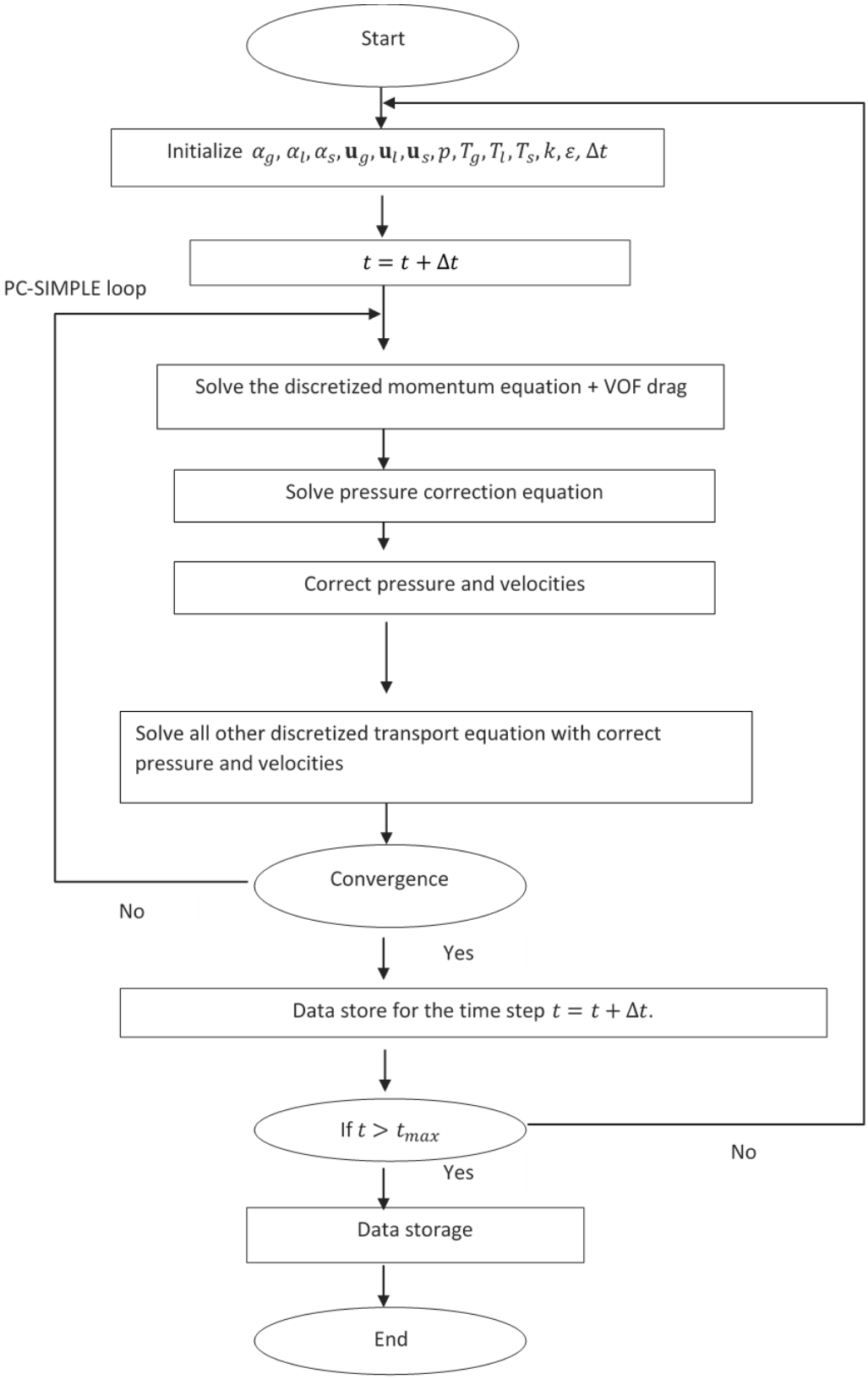

Figure 3-4 Computing cycle of transient Euler-Granular VOF model for three-phase flow.

4 1D model for open channel flow

One-dimensional (1D) hydrodynamics models are used extensively for river flow models, channel flow models, tailing flow models, flood models, blood models and other applications. The cost of simulation for the 1D model is comparatively low, as it has a lower computational power demand than the 3D and 2D models. 1D models can achieve significant improvements in speed of calculation in real-time flow measuring applications. It might even be possible to achieve speeds that are faster real-time. The primary challenge of 1D models in relation to higher dimensional models is achieving the required accuracy.

4.1 Model developments

The objective of the 1D model is to calculate the transient flow rate in open Venturi channels. The area averaged flow depth and the mean flow velocity are essential to flow rate calculation. Model development contains the following three main steps. The first step introduces the fundamental laws, the continuity equation and momentum equation. The second step relates the external quantities to the fundamental laws. The third step manipulates the model into the desired form, which form depending on the computational language used.

The domain is discretized based on the finite volume method (FVM). The finite difference method (FDM) can be expected to break down near the discontinuities, where the differential equation does not hold (LeVeque, 2002). The fluid domain was divided into control volumes (grid cells) and total integral or cell average is considered in each control volume. The divergence terms were converted into fluxes at the edges by integrating over the control volume using Gauss's theorem. The numerical fluxes through the boundaries of the control volumes were calculated using high-resolution numerical flux functions. The spatial discretization was based on a Cartesian grid as shown in Figure 4-1.

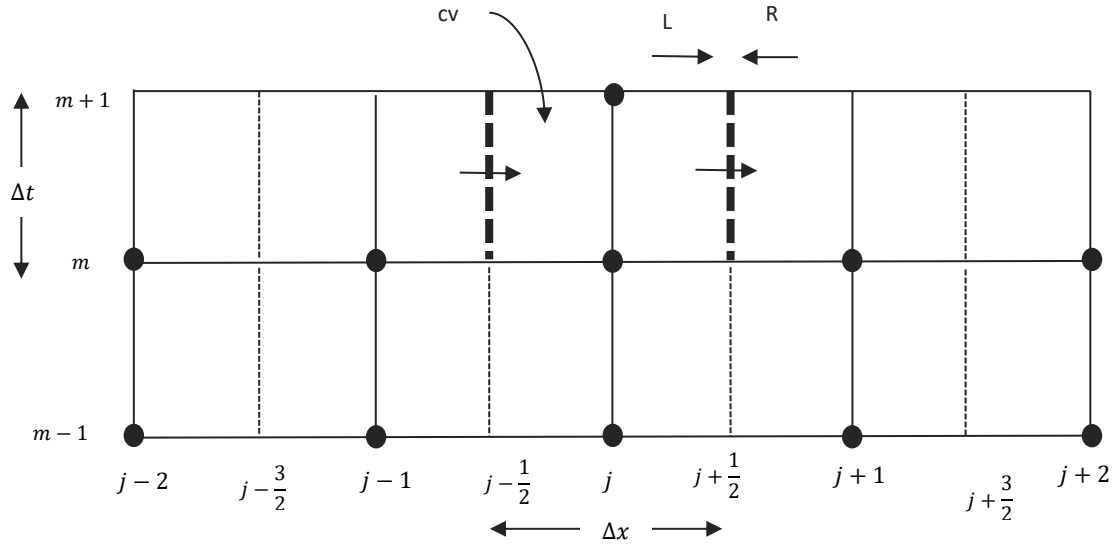

Figure 4-1. 1D grid: j is the node index in the spatial grid, $j \in \{1, 2, \dots, l\}$. m is the time index, $m \in \{1, 2, \dots, N\}$.

The total mass balance and x-directional momentum balance for a control volume are:

$$\frac{\partial m_j}{\partial t} = \dot{m}_{j-\frac{1}{2}} - \dot{m}_{j+\frac{1}{2}}, \tag{4.1}$$

$$\frac{\partial (mu)_j}{\partial t} = (\dot{m}u)_{j-\frac{1}{2}} - \ (\dot{m}u)_{j+\frac{1}{2}} + \sum_j F_j. \tag{4.2}$$

Considering the mean velocity to be $u \approx \bar{u}$, and the mean cross-sectional area to be $A \approx \bar{A}$, then $m = \ \rho \, \Delta x A$, $\dot{m}u = \rho A u^2$. The forces acting on the control volume are $\sum_i F_i = F_p + F_R + F_g + F_e + F_i$. The open channel flow cross-sectional area is a state variable. It is a function of flow depth and the shape of the channel. The cross-sectional areas for rectangular and trapezoidal shape channels are $A = bh$ and $A = h(b + k_1 h)$. h is the flow depth, b is the bottom width $k_1 = \cot\theta$, and θ is the trapezoidal angle. The forces $\sum_i F_i$ that apply to the control volume are pressure force F_p, wall-reflection pressure-force F_R, gravity force F_g, external friction force F_e, and internal friction force F_i. The wall-reflection pressure-force is due to the wall contraction or expansion effect. Paper 3 describes the non-prismatic (not same channel cross-section shape) impact on open channel flow. The friction forces are due to the wall friction and non-Newtonian viscous effect. Paper 5 describes the friction forces.

$$F_p = k_g \left((Ah)_{j-\frac{1}{2}} - (Ah)_{j+\frac{1}{2}} \right) \rho g$$

$$F_R = -2k_g \Delta x h_j^2 \rho g \, tan \, \beta$$

$$F_g = \rho \, \Delta x \, \bar{A} \, g \sin \alpha$$

$$F_e = \rho S_e g \bar{A} \Delta x$$

$$F_i = \rho S_i g \bar{A} \Delta x$$

The 1D shallow water equations can be derived for locally trapezoidal channels and for a non-Newtonian fluid from Equation (4.1) and (4.2) in Saint-Venant's form:

$$\frac{\partial A}{\partial t} = -\frac{\partial (Au)}{\partial x}, \tag{4.3}$$

$$\frac{\partial (Au)}{\partial t} = -\frac{\partial (Au^2)}{\partial x} - \frac{\partial \left(k_{g_1} Ah\right)}{\partial x} g + k_{g_2} h^2 g \frac{\partial b}{\partial x} + Ag \sin \alpha - AgS_e - AgS_i. \tag{4.4}$$

The external friction slope, S_e, is based on Manning's formula, which describes wall friction and turbulent behavior. The internal friction slope, S_i, is based on the rheological model. There are two main velocity regions in open channel flow: laminar and turbulent. Turbulent flow can easily propagate in industrial applications such as well return open channel flow, due to the unsteady flow variation, wall friction, short length of channel, impurities, and flow properties. The external friction slope is:

$$S_e = \frac{k_{\mathrm{M}}^2}{k_n^2 R_h^{4/3}} |u| \mathrm{u}.$$

The internal friction slope, based on the Pierre Carreau (PC) model for a trapezoidal shape channel, is:

$S_i = \rho f_i,$

$$f_{i_{\mathrm{PC}}} = \frac{(b+2k_2k_{g_1}h)}{\rho}\left(\frac{2V}{R_h}\left(\eta_\infty + (\eta_0 - \eta_\infty)\left(1+\left(\lambda\frac{2V}{R_h}\right)^2\right)^{\frac{n-1}{2}}\right)\right).$$

The modified partial differential equations (PDEs) are a set of non-linear equations.

4.2 FLIC scheme

Toro (2009) introduced a second order accurate total variation diminishing (TVD), flux limiter centered (FLIC) scheme, which can be used for solving Equations (4.2) and (4.3). Simplicity and high computational speed are the main advantages. The disadvantage of is that it smooths the shocks over more computation cells than the upwind scheme (Vaagsaether et al., 2007). The strictly hyperbolic condition does not need to be met to solve the second order centered TVD scheme. The source terms due to gravity force, external friction, and internal friction are non-zero values. The wall reflection effect can therefore be considered to be a flux term in the FLIC scheme without limiting the hyperbolic condition. The source term splitting method handles the source terms.

4.2.1 FLIC-TVD scheme

Equations (4.3) and (4.4) without source terms can be presented after the discretization and integration steps in the compact form:

$$\mathbf{U}_j^{m+1} = \mathbf{U}_j^m - \frac{\Delta t}{\Delta x}\left[\mathbf{F}(\mathbf{U})_{j+\frac{1}{2}}^m - \mathbf{F}(\mathbf{U})_{j-\frac{1}{2}}^m\right]. \tag{4.5}$$

Here, $\mathbf{U} = \begin{pmatrix} A \\ AV \end{pmatrix} = \begin{pmatrix} u_1 \\ u_2 \end{pmatrix}$, $\mathbf{F}(\mathbf{U}) = \begin{pmatrix} AV \\ AV^2 + k_{g_1}Ahg \end{pmatrix} = \begin{pmatrix} u_2 \\ \frac{{u_2}^2}{u_1} + k_{g_1}u_1hg \end{pmatrix}$.

The FLIC scheme calculates the cell interface flux $\mathbf{F}(\mathbf{U})_{j+\frac{1}{2}}^m$. The FLIC scheme is a combination of the first-order accurate FORCE scheme and the second-order accurate Richtmyer version of the Lax-Wendroff scheme.

$$\boldsymbol{F}(\boldsymbol{U})_{j+\frac{1}{2}}^{m} = \boldsymbol{F}(\boldsymbol{U})_{j+\frac{1}{2}}^{m,LO} + \phi_{j+\frac{1}{2}}\left[\boldsymbol{F}(\boldsymbol{U})_{j+\frac{1}{2}}^{m,HO} - \boldsymbol{F}(\boldsymbol{U})_{j+\frac{1}{2}}^{m,LO}\right]. \tag{4.6}$$

The higher order (HO) and the lower order (LO) fluxes are combined with a flux limiter function ϕ in the FLIC scheme. The Richtmyer (RI) scheme calculates the higher order flux. A Taylor series expansion goes up to second order in the Lax-Wendroff method. The Richtmyer scheme therefore has second-order accuracy.

$$\begin{aligned} \boldsymbol{F}(\boldsymbol{U})_{j+\frac{1}{2}}^{m,HO} &= \boldsymbol{F}\left(\boldsymbol{U}_{j+\frac{1}{2}}^{m,RI}\right) \\ \boldsymbol{U}_{j+\frac{1}{2}}^{m,RI} &= \frac{1}{2}\left[\boldsymbol{U}_{j}^{m} + \boldsymbol{U}_{j+1}^{m}\right] + \frac{\Delta t}{2\Delta x}\left[\boldsymbol{F}\left(\boldsymbol{U}_{j}^{m}\right) - \boldsymbol{F}\left(\boldsymbol{U}_{j+1}^{m}\right)\right]. \end{aligned} \tag{4.7}$$

The FORCE scheme calculates low order flux. The FORCE flux is the average of the Lax-Friedrichs (LF) flux and Richtmyer flux. The Lax-Friedrichs method is only first-order accurate. The method is, however, stable up to where the Courant number (CFL number) reaches one for a linear hyperbolic equation (LeVeque, 2002). The Lax-Friedrichs scheme typically introduces high diffusion.

$$\begin{aligned} \boldsymbol{F}(\boldsymbol{U})_{j+\frac{1}{2}}^{n,LO} &= \boldsymbol{F}(\boldsymbol{U})_{j+\frac{1}{2}}^{n,FORCE} \\ &= \frac{1}{2}\left[\boldsymbol{F}(\boldsymbol{U})_{j+\frac{1}{2}}^{n,LF} + \boldsymbol{F}\left(\boldsymbol{U}_{j+\frac{1}{2}}^{n,RI}\right)\right]. \end{aligned} \tag{4.8}$$

$$\boldsymbol{F}(\boldsymbol{U})_{j+\frac{1}{2}}^{n,LF} = \frac{1}{2}\left[\boldsymbol{F}\left(\boldsymbol{U}_{j}^{n}\right) + \boldsymbol{F}\left(\boldsymbol{U}_{j+1}^{n}\right)\right] + \frac{\Delta x}{2\Delta t}\left[\boldsymbol{U}_{j}^{n} - \boldsymbol{U}_{j+1}^{n}\right]. \tag{4.9}$$

High-resolution flux limiter functions ensure a non-oscillatory nature. There are several high-resolution flux limiter functions ϕ, for example minmod, superbee, MC-limiter. The superbee flux limiter ϕ_{SB} lies along the upper boundary of the TVD region. The superbee flux limiter is the least diffusive limiter and gives small oscillations around a strong gradient (Vaagsaether et al., 2007). A disadvantage of the superbee is the steepening of a smooth transition near the inflection points (LeVeque, 2002). It does, however, keep second-order accuracy.

$$\phi_{SB}(r) = \begin{cases} 0, & r < 0, \\ 2r, & 0 \le r \le \frac{1}{2}, \\ 1, & \frac{1}{2} \le r \le 1, \\ min\{2,\ \phi_g + (1-\phi_g)r\}, & r > 1. \end{cases} \tag{4.10}$$

$$\phi_g = \frac{1 - c_{max}}{1 + c_{max}}$$

Here c_{max} is the CFL number, which can vary from zero to one. r is the ratio of upwind change to local change, which is considered to be a flow parameter. A specific energy q based method is used to calculate the upwind and local changes. Here we use q in a way that it can capture the hydraulic jumps, as hydraulic jumps represent a significant energy loss. The minimum flow parameter value from the left (L) side and the right (R) side of a cell interface is considered to be a flow parameter for each interface. The flux limiter function obtains information for the j-th cell interfaces flux calculation from five cells, where $j-2$, $j-1$, j, $j+1$, and $j+2$.

$$r^n_{j+\frac{1}{2}} = min\left(r^{n,L}_{j+\frac{1}{2}},\ r^{n,R}_{j+\frac{1}{2}}\right),$$

$$r^{n,L}_{j+\frac{1}{2}} = \frac{\Delta q_{j-\frac{1}{2}}}{\Delta q_{j+\frac{1}{2}}} = \frac{q^n_j - q^n_{j-1}}{q^n_{j+1} - q^n_j}, \tag{4.11}$$

$$r^{n,R}_{j+\frac{1}{2}} = \frac{\Delta q_{j+\frac{3}{2}}}{\Delta q_{j+\frac{1}{2}}} = \frac{q^n_{j+2} - q^n_{j+1}}{q^n_{j+1} - q^n_j},$$

$$q = \frac{1}{2}hg + \frac{1}{2}u^2.$$

The time step Δt is a variable function of wave speed and CFL number, as described in Paper 3. The wave speed is calculated from the Froude number. To improve the stability, maximum wave speed is used to calculate the minimum time step value for the fluid domain.

$$\Delta t = \frac{c_{max}\,\Delta x}{max\left(abs\left(u_j + \sqrt{h_j g}\right)\right)}, \forall \text{ j.} \tag{4.12}$$

The Courant-Friedrichs-Lewy (CFL) criterion preserves numerical stability in the scheme: the wave travel distance is less than the mesh element size for a time step length. The maximum wave speed from the total domain is used to calculate the time step. The non-staggered *fully-discrete* FLIC scheme is naturally reduced to a particularly simple *semi-discrete* form, when considering time step in this way (Kurganov et al., 2001).

4.2.2 Dam-Break problem

The dam-break problem is a well-known solution of verifying a TVD scheme using the Riemann problem. The shallow water equations without source terms are solved using the FLIC scheme for the dam-break problem. In the example, a dam separating two levels of water bursts and determines the flow depth (h) and the velocity (u) over time. In this example, non-dimensional flow depth and non-dimensional mean velocity are considered. The initial conditions are:

$$h(x,0) = \begin{cases} h_1 = 1 \text{ if } x < 0.5, \\ h_2 = 0 \text{ if } x > 0.5, \end{cases} u(x,0) = 0.$$

Figure 4-2 shows the dam break problem result at $t = 0$ s (*blue*) and $t = 0.1$ s (*orange*). The results are well matched with the Leveque (2002) results. The Riemann solution contains two waves in the shallow water equations: a shock wave and a rarefaction wave. The shock wave travels to the right side, and accelerates the fluid abruptly. The rarefaction wave goes to the left side, and accelerates the fluid smoothly.

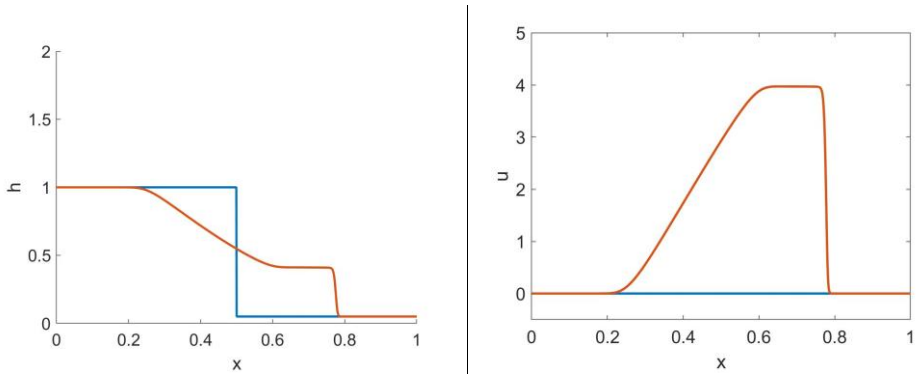

(a) (b)

Figure 4-2. Solution of the dam-break Riemann problem for the shallow water equation without source term. The blue lines are $t = 0$ and orange lines are $t = 0.1$ s: (a) Non-dimensional flow depth (h), (b) Non-dimensional velocity (u).

4.2.3 Treatment of source terms

The non-linear shallow water equations are solved in two steps: the first step solves the pure advection terms and the second step solves the source terms. This method is called a fractional-step or operator splitting or source term splitting method. The first step is described in Chapter 4.2.1. ODE solvers are used to solve the second step, and the Runge-Kutta fourth order method is used in this study.

Step-1: $\mathbf{U}_j^* = \mathbf{U}_j^m - \frac{\Delta t}{\Delta x}\left[\mathbf{F}(\mathbf{U})_{j+\frac{1}{2}}^m - \mathbf{F}(\mathbf{U})_{j-\frac{1}{2}}^m\right]$,

Step-2: $\mathbf{U}_j^{m+1} = \mathbf{U}_j^* + \frac{1}{6}(\mathbf{K_1} + 2\mathbf{K_2} + 2\mathbf{K_3} + \mathbf{K_4})$.

The explicit Runge-Kutta fourth order method parameters are $\mathbf{K_1} = \Delta t\ \mathbf{S}\left(t^n, \mathbf{U}_j^*\right)$, $\mathbf{K_2} = \Delta t\ \mathbf{S}\left(t^n + \Delta t/2, \mathbf{U}_j^* + \mathbf{K_1}/2\right)$, $\mathbf{K_3} = \Delta t\ \mathbf{S}\left(t^n + \Delta t/2, \mathbf{U}_j^* + \mathbf{K_2}/2\right)$, and $\mathbf{K_4} = \Delta t\ \mathbf{S}\left(t^n + \Delta t, \mathbf{U}_j^* + \mathbf{K_3}\right)$. Here, $\mathbf{S}(\mathbf{U}) = \begin{pmatrix} 0 \\ u_1 g \sin\alpha + \mathrm{S}_R - u_1 g \mathrm{S}_e - u_1 g \mathrm{S}_i \end{pmatrix}$.

4.3 Stability of the numerical scheme

In some cases, spatial grid refinement and a time step size reduction improve the stability of a solution. This method is, however, not reliable in general cases of flow over rough, irregular beds (Burguete et al., 2007). The CFL condition is only a necessary condition for stability. It is not always sufficient to guarantee stability, because every

point can affect the solution in the domain (LeVeque, 2002). The CFL condition ensures the correct physical speeds, as determined by the eigenvalues of the flux Jacobian. The flux Jacobian and diagonal matrices are (Tseng, 2004):

$$\mathbf{J} = \frac{\partial \mathbf{F}}{\partial \mathbf{U}} = \begin{bmatrix} 0 & 1 \\ -u^2 + gh & 2u \end{bmatrix},$$

$$\mathbf{\Lambda} = \begin{bmatrix} u + \sqrt{gh} & 0 \\ 0 & u - \sqrt{gh} \end{bmatrix}, \mathbf{X} = \begin{bmatrix} 1 & 1 \\ u + \sqrt{gh} & u - \sqrt{gh} \end{bmatrix}, \mathbf{J} = \mathbf{X\Lambda X^{-1}}.$$

Here, X is the eigenvector matrix. The eigenvalues of the Jacobian are $u \pm \sqrt{gh}$. There exist two real eigenvalues for $h > 0$ (not dry bed or near dry bed). The eigenvalues can be presented as a diagonal matrix, because it has linearly independent eigenvectors (Strang, 2016). Equations (4.3) and (4.4) constitute a *hyperbolic* system, and are for a rectangular channel without source terms. When $u \ll \sqrt{gh}$, the flow is strictly subcritical and the characteristic speed is in the opposite direction, this potentially reducing the stability of the system. The celerity $\sqrt{gh}$ becomes independent when the derivatives are discretized implicitly (Aldrighetti, 2007). It is difficult to prove stability of the TVD nonlinear method (LeVeque, 1998; Toro, 2009). However, a number of techniques are available for analyzing the stability of the nonlinear systems, such as convergence, compactness, function space, and total-variable stability (LeVeque, 2002). Aldrighetti (2007) used the von Neumann method to analyze the stability of the non-linear system (shallow water), under the assumption that the differential equations are linear. According to Aldrighetti (2007), the stability of the semi-implicit method depends only on the choice of the operator used to discretize the convective and viscous terms. In this study, flux limiter functions are used to improve the stability. The superbee flux limiter ϕ_{SB} lies along the upper boundary of the TVD region. The total variation (TV) is a decreasing function of time $TV(\mathbf{U}_j^{n+1}) \leq TV(\mathbf{U}_j^n)$, where $TV(\mathbf{U}_j^n) = \sum_{i=-\infty}^{\infty} |\mathbf{U}_{j+1}^n - \mathbf{U}_j^n|$ (Toro, 2009). Total variation stable methods rely on mesh-dependency. In the numerical experiments, the ODE solver is the fourth order Runge-Kutta method. Gottlieb et al. (2001) showed that higher order time discretization methods preserve

the strong stability (SSP) properties of first-order Euler time stepping, in the TVD time discretization. The Godunov's type methods time step is restricted by the CFL condition. No difference in the solution was detected for numerical experiments that use smaller and larger values of CFL numbers up to the stability limit. The solution is assumed to be monotone with minimal numerical dissipation.

4.4 Accuracy of the numerical model

A high order TVD Runge-Kutta type time discretization method is presented here (Shu and Osher, 1988). The centered-TVD scheme used in the simulation is second-order accurate in space, as explained in Chapter 4.2.1. The FLIC scheme is a combination of the first-order accurate FORCE scheme and the second-order accurate Richtmyer version of the Lax-Wendroff scheme. The Lax-Friedrichs method is only first-order accurate. The superbee flux limiter maintains the second-order accuracy of the centered-TVD scheme. Equation (4.6) can expand with the higher order and lower order fluxes,

$$\mathbf{F}(\mathbf{U})^{m}_{j+\frac{1}{2}} = \frac{1}{2}\left[\left(\mathbf{1}+\phi_{j+\frac{1}{2}}\right)\mathbf{F}\left(\mathbf{U}^{n,RI}_{j+\frac{1}{2}}\right)+\left(\mathbf{1}-\phi_{j+\frac{1}{2}}\right)\mathbf{F}(\mathbf{U})^{n,LF}_{j+\frac{1}{2}}\right]. \tag{4.13}$$

The superbee flux limiter range is $0 \leq \phi_{SB} \leq 2$ for the energy based flow parameter function. According to the superbee flux limiter values, the interface fluxes are

$$\phi_{SB} = \begin{cases} 0, & \mathbf{F}(\mathbf{U})^{m}_{j+\frac{1}{2}} = \frac{1}{2}\left[\mathbf{F}\left(\mathbf{U}^{n,RI}_{j+\frac{1}{2}}\right)+\mathbf{F}(\mathbf{U})^{n,LF}_{j+\frac{1}{2}}\right], \\ 1, & \mathbf{F}(\mathbf{U})^{m}_{j+\frac{1}{2}} = \mathbf{F}\left(\mathbf{U}^{n,RI}_{j+\frac{1}{2}}\right), \\ 2, & \mathbf{F}(\mathbf{U})^{m}_{j+\frac{1}{2}} = \frac{1}{2}\left[3\mathbf{F}\left(\mathbf{U}^{n,RI}_{j+\frac{1}{2}}\right)-\mathbf{F}(\mathbf{U})^{n,LF}_{j+\frac{1}{2}}\right]. \end{cases} \tag{4.14}$$

The first order accurate Lax-Friedrichs flux contributes 50% of the total interface flux when the flux limiter function is zero. This is the minimum accuracy flux in the centered-TVD scheme used. The flux limiter function becomes zero in the no-flow-filled-tank condition (or a dry bed). This condition is unrealistic in real-world open channel flow.

The centered-TVD scheme using the superbee flux limiter function therefore always maintains second order accuracy during simulations.

5 Experiment procedure

The experimental setup is located at the University of South-Eastern Norway (USN). We refer to it here as the "Venturi rig." The Venturi rig was developed such that it is similar to a well flow circulation system. Equinor ASA funded the original Venturi rig set-up, and USN funded additional sensors, data logging system, etc. The Venturi channel was designed based on a standard geometry provided by Bamo (BAMO Mesures SAS, n.d.; Chhantyal, 2018). The experimental setup includes an open Venturi channel, a mud tank, ultrasonic level sensors, a Coriolis mass flow meter, a blender for the mixing tank, and other sensors, see Figure 5-1, Figure 5-2, and Figure 5-3.

(a) (b)

Figure 5-1. Experimental setup: (a) Open channel with level sensors, (b) Pump station.

Channel inclination can change $\pm 2°$ from the horizontal. The accuracy of the Rosemount-3107 ultrasonic level sensor is ± 2.5 mm for height < 1 m and the accuracy of the Coriolis flowmeter is ± 0.1 % for a flow rate < 1000 l/min. The level sensors are located at the center of the channel and can be moved along the central channel axis. We concentrated in this study primarily on the open channel flow rate, based on level sensor measurements.

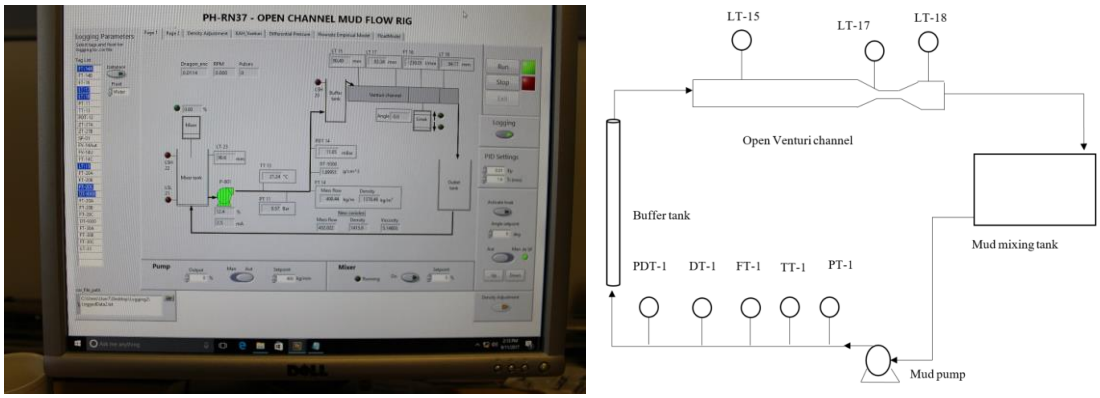

Figure 5-2. Flow loop of the experimental setup: LT - level transmitter, PT - pressure transmitter, TT - temperature transmitter, DT - density transmitter and PDT - differential pressure transmitter. The level transmitters can be moved along the central axis of the channel.

The experiments were carried out using two fluids: water and a non-Newtonian drilling fluid. The water-based drilling fluid contains potassium carbonate as a densifying agent and xanthan gum as viscosifier. Viscosity was measured using an Anton Paar MCR 101 rheometer, and density was measured using an Anton Paar DMA 4500 density meter.

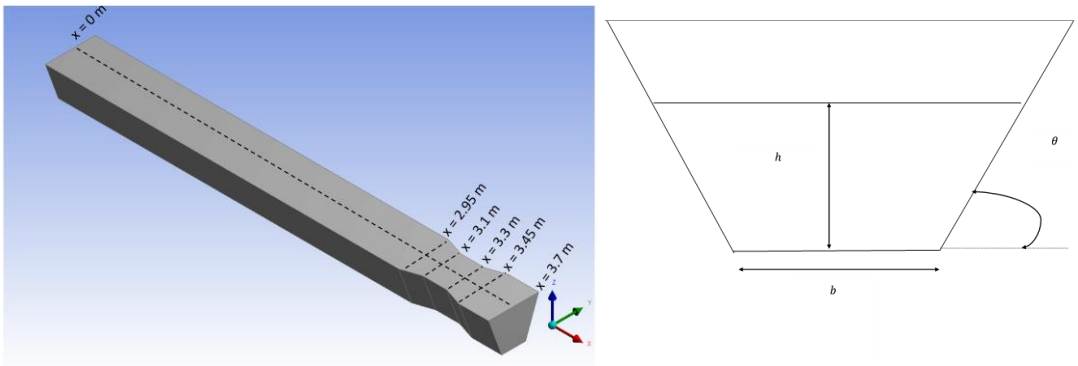

Figure 5-3. The dimension of the trapezoidal channel; x = 0 m at the inlet of the channel. The Venturi region is x = 2.95 m to x = 3.45 m. Bottom depth is 0.2 m for 0 m < x < 2.95 m and 3.45 m < x < 3.7 m. Bottom depth is 0.1 m for 3.1 m < x < 3.3 m. The trapezoidal angle is 70˚. In the channel cross sectional area, h, b and ϑ are flow depth, bottom width and trapezoidal angle respectively.

6 Summary of the articles and discussion

We strongly recommend reading the papers attached in full before reading this chapter.

6.1 Paper 1 – "Flow regime changes at hydraulic jumps in an open Venturi channel"

Paper 1 provides a comprehensive description of three types of jumps/expansion that can occur in non-prismatic (non constant continuous cross-section) open channels with Newtonian flow. The jumps are hydraulic jump, and oblique jump, and the expansion is subcritical flow to supercritical flow, see Figure 6-1. The experiments were carried out using the experiment setup described in Chapter 5. The experiment and simulation were carried out at channel inclination angles of 0˚, -0.7˚ and -1.5˚. The VOF method was used for the 3D CFD simulation.

(a) (b) (c)

Figure 6-1. The jumps and expansion occur in the open Venturi channel: (a) Expansion, (b) Hydraulic jump, (c) Oblique jump

- Flow state changed from supercritical to subcritical due to reflection from the contraction walls in the hydraulic jump. Two hydraulic jumps start from the contraction walls and meet at a triple point, so creating an oblique jump, when the flow state is supercritical and passes through a contraction section.
- Flow states can be recognized as being subcritical, critical or supercritical from the developed critical depth h_c equation, Equation (6.1). Flow depth above the critical depth is subcritical and lower is supercritical. A velocity profile is shown in Figure 6-2. This shows the magnitude of velocity variation in different flow

states. Supercritical flow has, in general, higher velocity and lower flow depth than subcritical flow.

$$g\left(b+\frac{h_c}{tan\theta}\right)^3 h_c^3 - Q^2\left(b+\frac{2h_c}{tan\theta}\right) = 0. \quad (6.1)$$

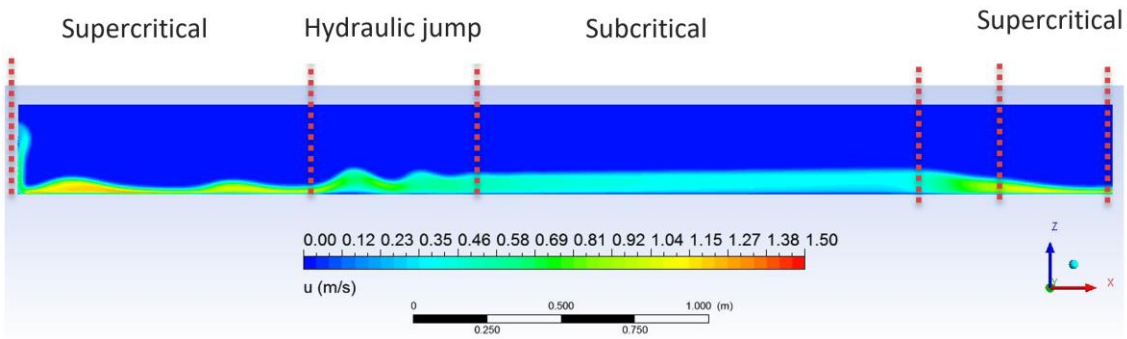

Figure 6-2. A steady state velocity profile of open Venturi channel. The channel inclination is – 0.7° and water flow rate is 400 kg/min.

- Turbulent intensity is high in the upstream supercritical flow due to high turbulence at the inlet, high turbulence in the hydraulic jump being due to large eddy formation.
- Hydraulic jumps that start from the contraction walls are stronger than the upstream flow, if the system entirely becomes subcritical, before the Venturi contraction. Upstream supercritical flow state converts fully subcritical when the channel has a horizontal or upward inclination. *Wall contraction reflection forces* become predominate due to gravity force not supporting the main flow direction.
- The h_2/h_1 ratio can reach 2-4 in a hydraulic jump. h_1 is flow depth before the hydraulic jump, and h_2 is flow depth after the hydraulic jump. The h_{max}/h_1 ratio can reach 3-4, even though an oblique jump has a lower energy loss than a hydraulic jump. h_{max} is at the top of the oblique jump.
- A hydraulic jump can travel into upstream if hydrostatic force is stronger than inertia force. The wall contraction and wall friction effects accelerate the hydrostatic force and decelerate the inertia force in open Venturi channels. A quasi-steady hydraulic jump occurs when the forces are balanced, the position of the hydraulic jump depending on the sizes of the forces. A quasi-steady

hydraulic jump oscillates backwards and forwards from the center of the hydraulic jump. The quasi-steady hydraulic jump oscillates at a distance of around $\pm 2h_{max}$.

- Level sensor readings can become noisy due to air enrichment from the hydraulic jump. The level sensors (ultrasonic level sensors) might give an inaccurate measurement of oblique jump formation at the Venturi throat. The level sensor might, due to shape of the free surface, average flow depth across the projected area. It is recommended more accurate level sensors are used for oblique jump measurements.
- There is no barrier in the expansion region and, therefore, no back wave propagation to the upstream flow.

6.2 Paper 2 – "Computational fluid dynamics study of flow depth in an open Venturi channel for Newtonian fluid"

Paper 2 focuses on the factors that relate to flow in an open Venturi channel. The CFD model and experimental setups described in Paper 1 were used in this work. This study may have the potential to provide support for open channel flow depth estimation. The main findings can be summarized as follows,

- The channel inclination can significantly influence on open Venturi channel flow regimes. Higher inclinations, $\alpha > 1°$, can keep a supercritical flow state from inlet to outlet than lower inclinations.
- Downstream flow depth changes with the inlet flow rate. However, there is no a linear relationship between the inlet flow rate and the downstream flow depth. Chapter 6.9.1 describes more about steady state flow depth and flow rate relationship.
- Wall roughness plays a significant role with the position of the hydraulic jump. Higher energy losses occur at higher wall roughness. If a quasi-steady hydraulic jump exists, then the hydraulic jump is closer to the inlet for a higher roughness wall than for a lower roughness wall.

- Large eddies are generated in a hydraulic jump. Air enrichment at the hydraulic jump gives high flow depth at the jump, this potentially creating errors in flow measurements. According to Chanson and Brattberg (2000), there can be two main regions in a hydraulic jump: a turbulent shear region and a recirculating flow region. The recirculating flow region, generally, is above the turbulent shear region. The recirculating region consists of large bubbles and strong unsteady recirculation. We have noticed in the simulations and experiments that a strong recirculation region formed above the turbulent shear region, see Figure 6-1-b and Figure 6-3.

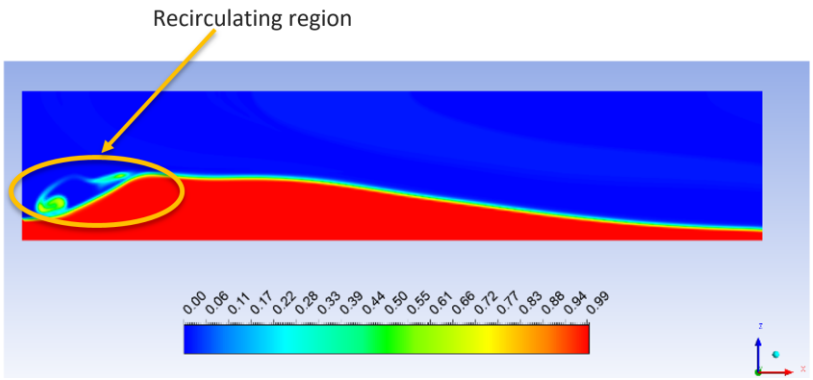

Figure 6-3. Water volume fraction of a hydraulic jump with recirculating region.

- The following turbulence models can be used for turbulence modeling in open channel flow. The final results of each model are equivalent. The models are standard $k-\varepsilon$ model, $k-\omega$ model, $k-\varepsilon$ RNG model, and $k-\varepsilon$ realizable model.
- A fine mesh in numerical simulations can capture a sharp interface between fluid and air. A mesh size of between 3 mm to 10 mm might be a good selection for accurate and economic numerical calculations. Irregular topography channels generate aspects such as the formation of a hydraulic jump, shocks, wave reflections, and other sudden changes in the flow. A fine mesh is required to numerically represent the effects of irregular topography on flow.

6.3 Paper 3 – "A solution method for one-dimensional shallow water equations using flux limiter centered scheme for open Venturi channels"

The conventional shallow water equations are modified to accurately capture the wall-reflection pressure-force effect in open Venturi channels. The conventional shallow water equations produce an artificial flux due to bottom width variation in the contraction and expansion regions. The artificial flux is due to the weak integration of total wall pressure acting on control volumes at contraction and expansion regions. The modified shallow water equations can be used to model both prismatic and non-prismatic channels. The total variation diminishing (TVD) scheme and the explicit Runge–Kutta fourth-order method were used to solve the modified shallow water equations. The simulated results were validated by experimental results and three-dimensional computational fluid dynamics results.

- The 1D shallow water equations need to be modified to include wall contraction and expansion effects. The pressure force from the sidewalls for a control volume might be challenging to add to the conventional shallow water method. The wall-reflection pressure-force acts in the opposite direction to the flow direction in the contraction region, so leading to a hydraulic jump in some cases. In the expansion region, the wall-reflection pressure-force acts in the flow direction, directing flow states such that they become supercritical. Compared to the conventional shallow water momentum-balance equation, Equation-(6.2), the expression $k_g h^2 g \frac{\partial b}{\partial x}$ is added to the new equation. Figure 6-4 shows a result comparison between the modified and conventional shallow water equations with experimental result.

$$\frac{\partial(Au)}{\partial t} = -\frac{\partial(Au^2)}{\partial x} - k_g \frac{\partial(Ah)}{\partial x} g + k_g h^2 g \frac{\partial b}{\partial x} + Ag\left(\sin\alpha - S_f\right). \quad (6.2)$$

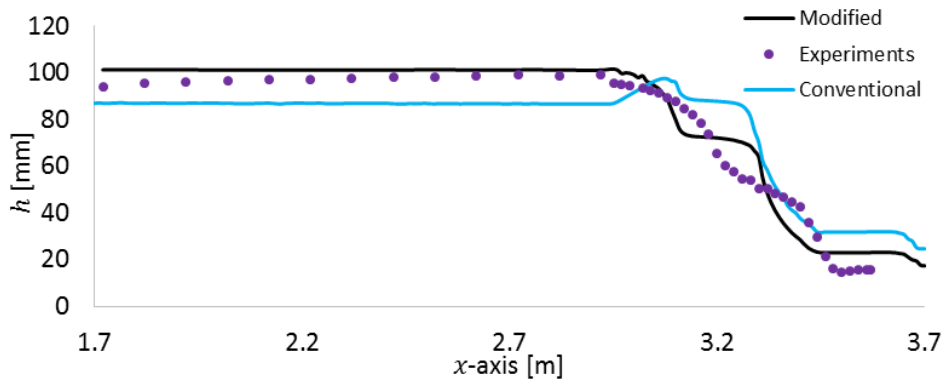

Figure 6-4. Quasi-steady state results, water flow rate at 400 kg/min, a comparison between the modified and conventional shallow water equations with experimental results.

- Poor treatment of the source term (due to irregular geometry, changes of width) produces significant oscillation in the flow depth. The conservativeness of the scheme can be severely damaged by this (Garcia-Navarro and Vazquez-Cendon, 2000). Studies propose pointwise and upwind approaches to the discretization of the source term (Garcia-Navarro and Vazquez-Cendon, 2000; Vázquez-Cendón, 1999). One main reason for this is poor capture of wall pressure. In this study, a higher order discretization method is suggested for the channel irregularity source term. The wall reflection pressure-force effect $\mathbf{S}_{\boldsymbol{R}}(\mathbf{U})_j^m$ is taken into consideration using the centered-TVD discretization method. The cell center value takes into account $\mathbf{S}_{\boldsymbol{R}}(\mathbf{U})_j^m$. The term has the first-order accuracy in space. Even though other researchers suggest wall-reflection pressure-force as a source term, we leave all pressure force in the advection term. This helps to remove artificial acceleration within the TVD scheme and to avoid this propagating into the ODE solver.
- Low flow depth initial conditions can reduce the stability of the numerical scheme at the high inclination angles. Due to high gravitational force in the flow direction, dry beds and discontinuities are generated downstream of the channel during start up when initial flow depth is low. This behavior is very common in long channels, where the channel length is greater than 2 m and inlet velocity is low. Flow depth furthermore becomes negative and the numerical scheme can

break down. As suggested in Paper 1, a threshold value of flow depth helps to maintain water depth non-negative.

- A dry bed condition is one of the main difficulties in shallow water flow modeling. Friction slopes can become very large, giving unphysical results when water depth approaches zero near the wet/dry interface (Tseng, 2004). A non-zero threshold flow depth can be used as a solution for this. In this study, the cell flux is forced to become zero where dry bed occurs, $h < 10^{-8}$m.
- Heat transfer from the liquid to the atmosphere is very small. This is because the fluid is at room temperature, and the temperature rise due friction is very small. The energy equation is, therefore, not solved as a conservation equation. The entropy of the system is a considerable factor in hyperbolic equation solving using TVD schemes in gas dynamics. Entropy is produced with the admissible shock, but would be reduced across an expansion shock (LeVeque, 2002). However, the entropy concept is not much popular in shallow water flow. The hyperbolic equation is an imperfect model for real open channel flow with friction due to the non-zero friction terms. Tseng (2004) used an entropy fix function for the approximate Riemann solvers method for the shallow water equations. Gassner et al. (2016) proved that the total energy based interface flux function precisely preserves entropy in the shallow water equations. The superbee flux limiter function is defined, in this study, in terms of the total energy of control volume.
- Abdo et al. (2018) noticed that shallow water equations cannot predict steady supercritical flow in a straight wall contraction. A possible reason for this may be the inaccurate estimation of the source term or the neglect of turbulence resistance (Hsu et al., 1998). The Manning's formula was used in this study as the turbulent friction model. A constant roughness value (k_m) was also used throughout all flow regimes. However, some researchers argue that Manning's friction might be a function of flow depth and Froude number (Hsu et al., 1998; Thomas and Hanif, 1995). Turbulent viscosity was set to zero in the 1D

simulation. According to the Thomas and Hanif (1995) study, varying the turbulent viscosity does not affect the converged solution.

- The 1D shallow water equations are well suited to open channel flow modeling using the high-resolution numerical schemes described in Chapter 4. The developed high-resolution scheme has strong stability at hydraulic jumps. The modified shallow water equations well matched with the experimental results in both unsteady and steady state.

6.4 Paper 4 – "Computational Fluid Dynamics Study of Shear Thinning Fluid (Drilling Fluid) Viscosity Models in an Open Venturi Channel"

Paper 4 is a computational fluid dynamic study of shear thinning fluid viscosity models in an open Venturi channel flow. The power-law model, the Herschel-Bulkley model, the Carreau viscosity model, and the Cross viscosity model were used to describe the rheology of the drilling fluids. The CFD model described in Chapter 0 was applied using ANSYS Fluent 16.2 commercial code. The viscosity and density of drilling fluids were measured using an Anton Paar MCR 101 rheometer and an Anton Paar DMA 4500 density meter. The experimental setup described in Chapter 0 was used to measure the flow depth of drilling fluid flow in the open channel.

- According to the rheometer results, at low shear rates the drilling fluid behaves as a pseudoplastic fluid, and at high shear rates the fluid shows Newtonian properties. The experimental drilling fluid can be modeled by the power-law (PL) model, the Herschel-Bulkley (HB) model, the Carreau viscosity model, and the Cross viscosity model. Figure 6-5 shows viscosity vs. shear rate for the non-Newtonian models.

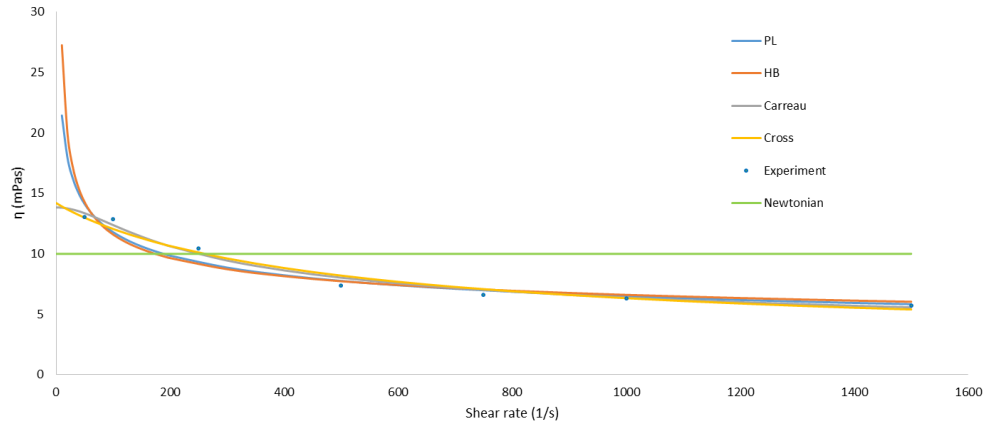

Figure 6-5. Shear stress vs. viscosity curves for non-Newtonian models. Experimental results are from the rheometer.

- Measuring and estimating the yield stress or viscosities at low shear rates are challenging both experimentally and numerically (Kelessidis et al., 2006; Møller et al., 2006). The Anton Paar MCR 101 viscosity meter allows the viscosity to be measured in this study when the shear rate is higher than 100 1/s (or 50 1/s). The power law and Herschel-Bulkley model shows a very high shear rate near to the zero shear rate, according to non-linear regression.
- The Fann 35A viscometer measures the rheological properties of drilling fluids in field operation. The viscometer is used because of its robustness and low cost (Fernandes et al., 2019). The Fann 35A viscometer can reach lower shear rates than the Anton Paar MCR 101 rheometer. However, the Anton Paar MCR 101 rheometer can produce shear stress continuously for each shear rate. The accuracy of the regression process is increased by the inclusion of a high number of shear rate values.
- The strain rate range was 0.02 to 2100 1/s for the complete open channel. The highest strain rate was on the walls of the channel, 2100 1/s, while the fluid near to the free surface had a strain rate range of 0.02 to 200 1/s.
- The shear stress τ_{zx} gradually falls from the bottom wall to the free surface in all the flow regimes, see Figure 6-6. The direction of the shear stress τ_{zx} can change, due to the secondary currents, in the subcritical and critical flow. This is called the dip-phenomena. The highest velocity propagates below the free surface due to the secondary currents of the lateral walls. The yield stress found

to be small, the drilling fluid used in this study, 0.1 Pas. The velocity dip is invisible in the supercritical flow.

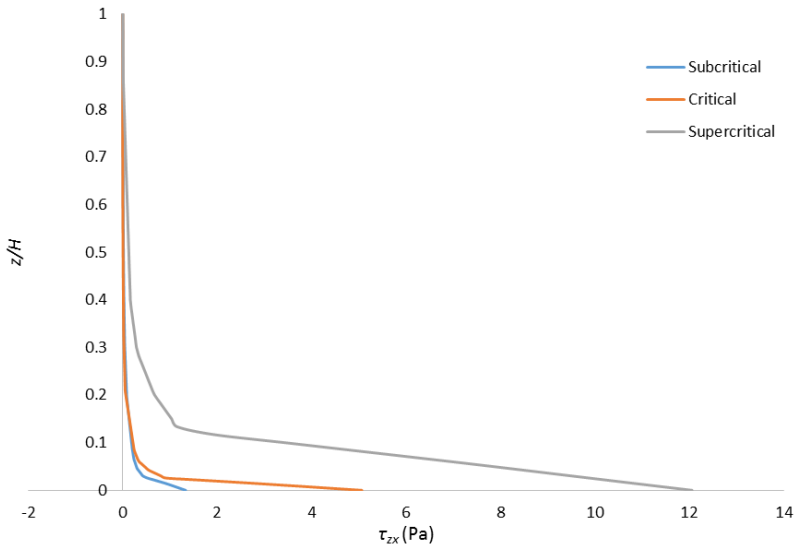

Figure 6-6. Shear stress in the x-direction perpendicular to the z-direction, τ_{zx}, for different flow regimes in the open Venturi channel at quasi steady state. The Carreau viscosity model was used for the viscosity calculation.

- The sidewall shear stress and bottom wall shear stress are very strong in supercritical flow compared to subcritical flow. The velocity gradient at the wall in general increases in the x – direction at the bottom of the wall. This is due to increasing velocity in the channel.
- Figure 6-7 shows viscosity variation with time for constant shear rates. Time-dependent shear thinning property, thixotropic, is very small in the drilling fluid used in this study. Thixotropic property of the drilling fluid disappears with high shear rates.

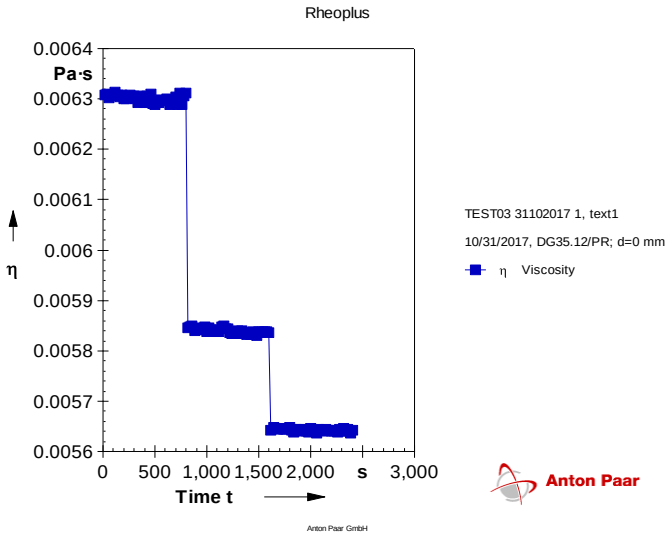

Figure 6-7. Viscosity variation with time for constant shear rates: For $0 < t < 800$ s, $\dot{\gamma} = 1300$ 1/s; 800 s $< t < 1600$ s, $\dot{\gamma} = 1700$ 1/s; 1600 s $< t < 2400$ s, $\dot{\gamma} = 2000$ 1/s.

6.5 Paper 5 – "1-Dimensional model of turbulent flow of Non-Newtonian drilling mud in non-prismatic channels"

In Paper 5, we model the 1D Saint-Venant system of shallow water equations for water-based drilling mud (non-Newtonian) in open Venturi channels for steady and transient conditions. Numerically, the friction force acting on the fluid in a control volume can be subdivided into two terms: external friction and internal friction. The external friction is due to the wall boundary effect and the internal friction is due to the non-Newtonian viscous effect. The higher order FLIC scheme and Runge-Kutta fourth order method were used to solve the new 1D non-Newtonian turbulence model, Equations (4.3) and (4.4).

- The momentum equation includes three source terms: gravity, external friction, and internal friction. The source term splitting method is solved based on strong stability preserving the fourth-order Runge-Kutta method. The external friction slope can become highly unstable at dry bed or near dry bed conditions, as explained in Paper 3, because flow depth h is at the denominator. The shear rate $\dot{\gamma} \approx 2V/R_h$ also has flow depth in the denominator. The internal friction slope can therefore become highly unstable at dry bed conditions.

- The modified shallow water equations for non-Newtonian fluid is well matched with experimental results. The average deviation from the experimental results is 5% in the PC model.
- The Reynolds number is higher than 5300 throughout the channel. Flow regimes therefore become subcritical-turbulent and supercritical-turbulent.
- The external friction term is highest for the lowest viscous fluid, and the internal friction term is lowest for the lowest viscous fluid (this being the rheology of the fluid used in this study, which relates to the Herschel-Bulkley model). The internal friction slope is predominant in the subcritical region. In the supercritical region, internal and external friction terms actively contribute to numerical calculations, see Figure 6-8.

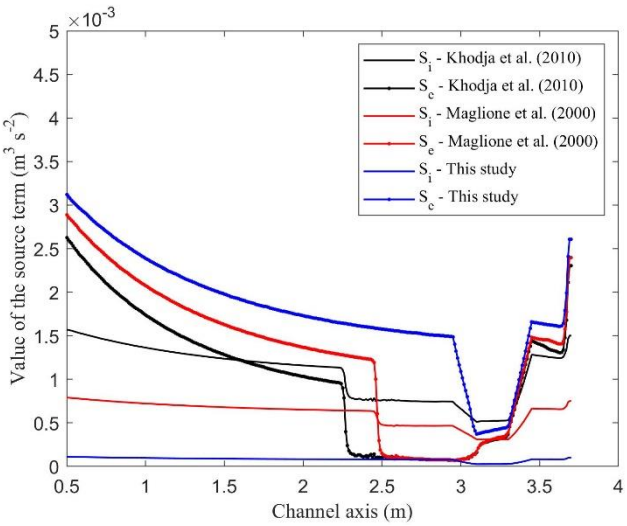

Figure 6-8. A comparison of internal friction and external friction for different drilling fluid, the rheology of drilling fluid based on the Herschel-Bulkley fluid. The results are at steady state flow in the open Venturi channel, the inlet flow rate is 0.0056 $m^3 s^{-1}$, and channel angle is -1.7°.

- Even though the flow meter shows sudden step changes, the level reading shows gradual changes, a complete step change taking more than 40 s. This is due to the time required for fluid to travel from the inlet of the open channel to the level sensor locations, and to unstable wave propagation.
- The flow-depth prediction error varies from 2 to 8 % in this study, depending on the model's assumptions and experimental results.

- The channel bed has a constant inclination in this study. The bed slope is therefore constant along the channel axis.
- The Reynolds number for open channel flow is, based on the apparent viscosity, $\mathrm{R}_e = 4\rho U R_h/\eta$. The gradual transition from laminar to fully developed turbulence is expected to begin at $\mathrm{R}_e > 500$ in open channel flow. Turbulent flow can easily propagate in a well return open channel flow, due to the variation of flow rate and fluid properties. There is a lack of a fundamental understanding of the turbulent flow of non-Newtonian fluids. One of the challenges is to include the turbulent fluctuation $\mathbf{u}'$, h' into the 1D model. This could be very complicated in the 1D model, where the non-Newtonian turbulent properties are included. However, the Reynolds stresses can be included in the 2D and 3D numerical schemes. The shallow channel laminar flow of a Bingham fluid, power-law fluid, and Herchel-Bulkley fluid for higher dimensions are available in the literature. We, in this study, use an alternative method to analyze the turbulent non-Newtonian properties in open channel 1D flow. We assumed that the non-Newtonian turbulence property is equal to the sum of Newtonian turbulence and non-Newtonian laminar properties. Newtonian turbulence is counted by the turbulent Manning's formula, and non-Newtonian laminar properties are counted by the pure non-Newtonian models such as the power-law, Heschel-Bulkley, and Carreau.
- In general, slurry' or mud' viscosities increase with concentration (Christian et al., 2014). The apparent viscosity of the drilling fluid used in this study was 0.005 Pa·s at a shear rate of 2000 s^{-1}. The flow regimes are mainly turbulent. In industry, drilling fluid viscosity varies from 0.001 to 0.02 Pas (Table 2-1). According to the Baas et al.(2009), open channel flow types can be turbulent flow, turbulence-enhanced transitional flow, lower and upper transitional plug flow, and quasi-laminar plug flow.

6.6 Paper 6 – "A Real-Time Flow-Measuring Algorithm for Open Venturi Channel Non-Newtonian Flow"

An algorithm for open Venturi channel flow estimation in real time for drilling fluid was developed in Paper 6. The higher order TVD Runge-Kutta method described in Paper 5 was used for numerical solving. A drilling-well return flow rate can be calculated in real time using a single level sensor reading. The algorithm has five main steps. Flow depth and mean velocity are the main function of the volume flow rate at a given time. The developed algorithm calculates the channel inlet flow rate, which is equal to the return line outlet flow rate.

- The average errors are 6.3 %, 4.1 % and 13.8 % respectively from LT-15, LT-17 and LT-18 level sensors based flow rate calculations, see Figure 6-9. Based on this result, we can conclude that the best location to place the level sensor is near to the Venturi contraction (just before the Venturi contraction begins). Near to the Venturi contraction, flow regimes are stable compared to the other region of the channel. Minimum disturbances occur near to the Venturi contraction due to strong subcritical flow.

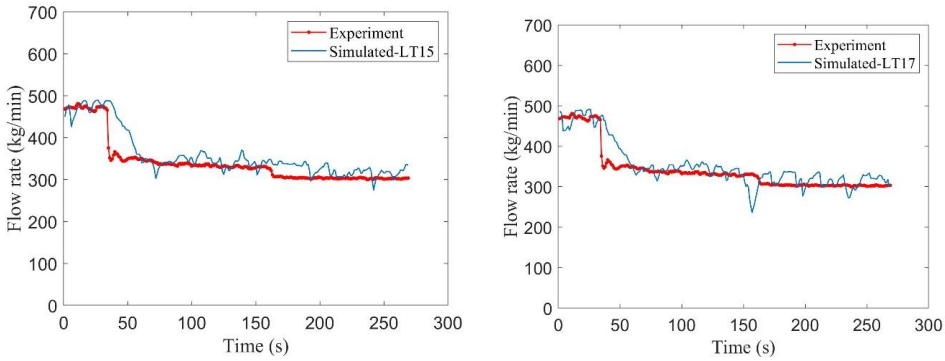

(a) (b)

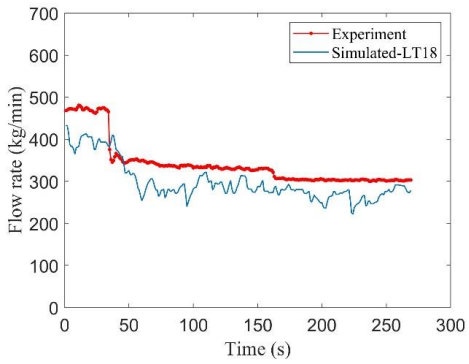

(c)

Figure 6-9. Mass flow rate experimental and simulated when the channel inclination at horizontal: (a) Flow rate calculation based on LT-15 level sensor reading, (b) Flow rate calculation based on LT-17 level sensor reading, (c) Flow rate calculation based on LT-18 level sensor reading.

- The algorithm calculates the inlet flow rate of the channel by using the level sensor readings at downstream of the channel. Here we make an important assumption that inlet flow depth is constant. The channel inlet is elevated above the channel bottom level using a buffer tank. Drilling fluid enters the channel from the buffer tank under gravity, flow states always being supercritical near the inlet due to the elevation of the inlet. The paper shows that the same volume flow rate under different inlet conditions can achieve the same downstream flow profile in an open Venturi channel, see Figure 6-10. The assumption about constant inlet flow depth is therefore valid for a range of flow rates. The inlet flow depth might need to be calibrated for a wide range of flow rates.

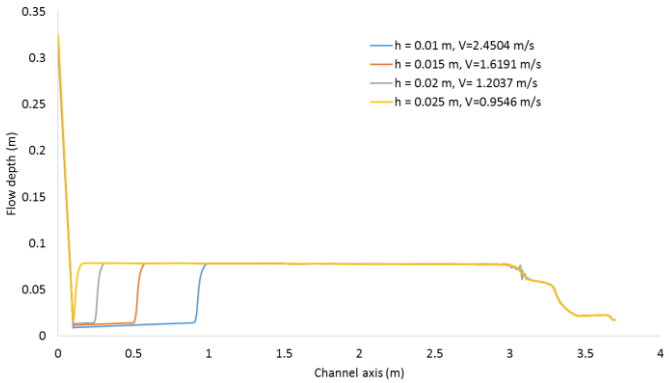

Figure 6-10. At steady state flow depth variation along the channel axis for different inlet condition for the same flow rate of 400 kg/min.

- We have not focused, in this study, on the advanced estimation methods. Jinasena and Sharma (2018) have, however, studied the advanced estimation method, in work conducted in parallel with this study. Recent studies (Agu et al., 2017; Jinasena and Sharma, 2018) of real time flow estimations in an open Venturi channel suggest a two non-intrusive level sensors measurement method. A single level sensor is required in this method. The level sensor is recommended located near the Venturi contraction, and the channel is recommended to have a horizontal inclination to minimize the disturbance.
- Online measurements are recommended started after a steady condition is reached, to improve the stability of the numerical algorithm.

6.7 Paper 7 – "Computational fluid dynamics study of the effects of drill cuttings on the open channel flow"

Well return flow includes drilling fluid, water, gas, formation fluid and drill cuttings. The return flow is, therefore, a multiphase flow when drilling. A computational fluid dynamics (CFD) study was carried out on the flow of drilling fluid and drill cuttings in open channel flow. Chapter 3.7 discusses the Eulerian multi-fluid VOF model used in this study. The primary objective of the study was to identify the effect of drill cuttings, and particle settlement on open channel flow depth.

- It is recommended to keep the drill cuttings volume fraction to less than 5% for trouble free annulus operations (Han et al., 2010; Pigott, 1941). The CFD result confirmed that the effect of drill cuttings on flow depth and mean velocity was found to be small for particle sizes less than 5 mm and solid volume fractions less than 10 % in a constant cross section and short open channels. See Figure 6-11.

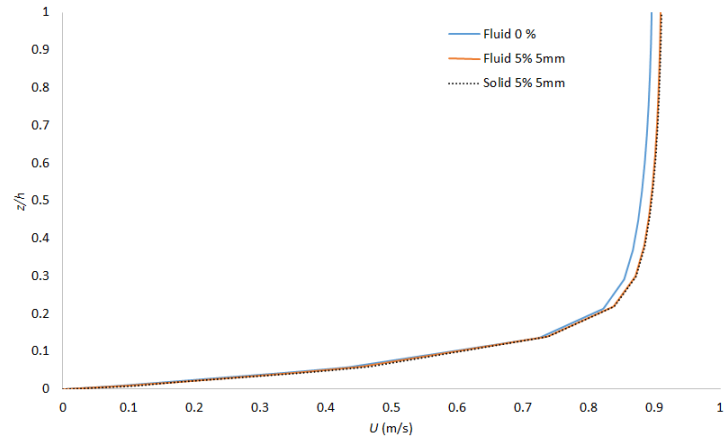

Figure 6-11. Steam wise velocity distribution with particle and without particle for the same inlet volume flow rate. The inlet velocity is 0.5665 m/s. The velocity is measured 0.7 m to the downstream from inlet of the channel.

- The conclusion might be different for long and non-prismatic channels. The increase in particle friction due to the rise of the total particle volume is also small, and energy loss is negligible.
- The liquid level decrease for a higher solids fraction. Higher concentration acts as a higher net density. Thus, the higher density and approximately the same friction will yield a lower flow depth.
- The highest particle setting is near the sidewall, and reaches 40 % solid volume fraction. Due to sidewall friction, particles have lower velocities near the sidewall. See Figure 6-12.

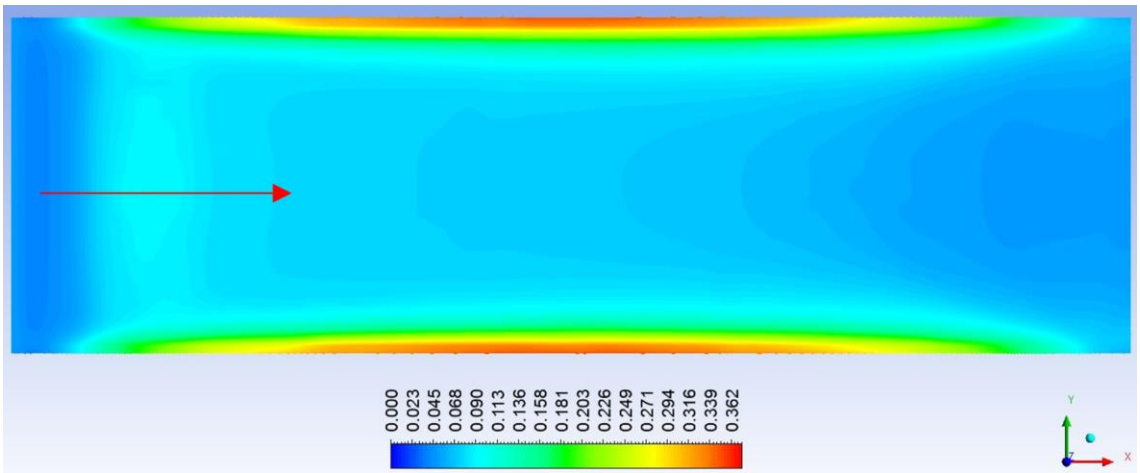

Figure 6-12. Particle settling bottom wall, the flow direction indicates by the arrow. Drill cutting size is 5 mm and inlet volume fraction is 0.05. The solid volume fraction of drill cuttings shows on the bottom at steady state, xy plane.

- A 3-D CFD simulation of two-phase or three-phase open channel flow takes many months of CPU time to run based on a 16-core 2.4 GHz Intel(R) CPU processor in a machine with 32 GB of RAM.

6.8 Paper 8 – "Study of fluidization regimes using OpenFOAM computational Fluid dynamics"

OpenFOAM CFD simulation was carried out for Geldart A, B C and D particles in a fluidization column. The simulations used the Euler-Euler method. Particle drag force was based on Ergun's formula, and Wen and Yu's model. This publication might be indirectly related to thesis work. However, multiphase flow friction models might be helpful in drill cuttings friction modeling.

6.9 Unpublished works

This section presents works/findings that are not published in the papers.

6.9.1 Relationship between flow rate and flow depth in the Venturi region at steady state

Flow rate can be formulated as a function of flow depth at steady state that results from the open venturi channel described in Paper 2. Figure 6-13 shows the Venturi region and symmetric contraction and expansion. Figure 6-14 shows the non-dimensional flow rate and non-dimensional flow depth relationships for different Venturi region locations. The different locations are marked using the non-dimensional length scale ξ. The relationship between flow rate and flow depth can be presented as a power-law function in the region $0.26 < \xi < 0.58$,

$$\frac{Q}{Q^*} = a\left(\frac{h}{h^*}\right)^b. \tag{6.3}$$

a and b are constants and depend on flow properties. There exist two solutions in the regions $\xi < 0.26$ and $\xi > 0.58$ for flow depth. The non-linearity between the flow rate and flow depth increases when moving away from the region $0.26 < \xi < 0.58$. It is

therefore wise to locate the level sensor and to measure the steady state flow rate in the region $0.26 < \xi < 0.58$. This region is, however, in the expansion of the Venturi and is, in general, supercritical. Unsteady flow measurement therefore becomes very noisy, as explained in Paper 6.

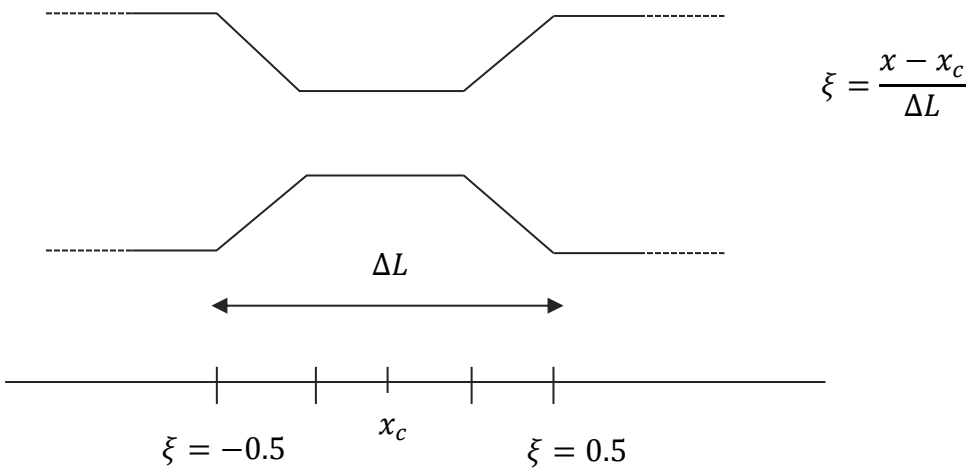

Figure 6-13. Top view of the Venturi region of the open channel. x_c is the center of the Venturi. ξ is the non-dimensional location of the Venturi region along the channel axis.

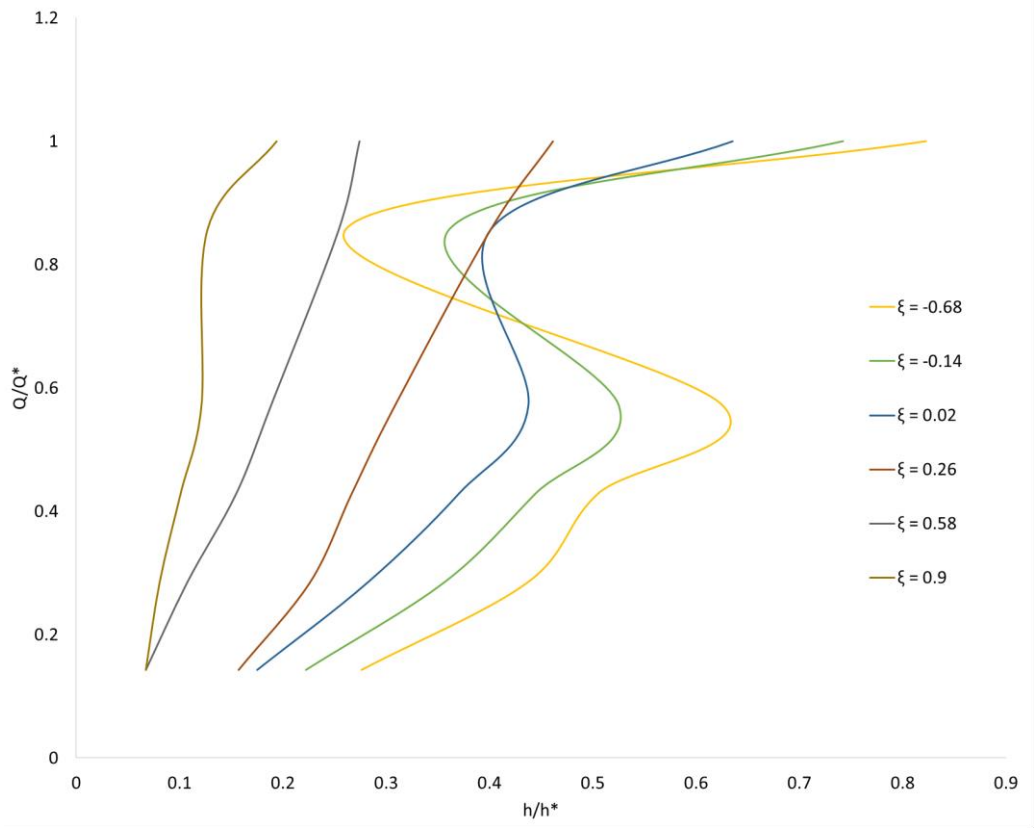

Figure 6-14. Relationship between non-dimensional flow rate and non-dimensional flow depth at different locations of the Venturi region at steady state. Q^* and h^* are maximum flow rate and maximum flow depth. ξ is the non-dimensional location of the Venturi region along the channel axis.

6.9.2 Non-Newtonian flow properties

The unpublished CFD results related to Paper 4 are discussed in this section.

6.9.2.1 Effect of Newtonian viscosity

There is a considerable difference in flow depth before and after the Venturi region where viscosity is increased, see Figure 6-15. Figure 6-16 shows the flow depth and average velocity profiles along the channel central axis for viscosities of 2 mPa·s and 20 mPa·s. The simulations were for constant fluid viscosities. The fluid has a higher velocity and lower flow depth at low viscosities than high viscosities. Internal losses increase when the fluid viscosity increases. This leads to a reduction in velocity, and flow regimes changing from supercritical to subcritical.

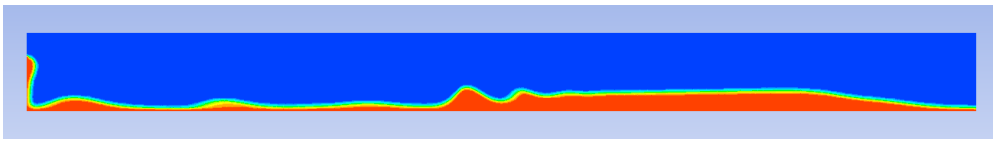

(a)

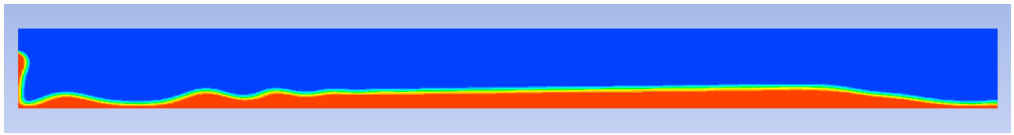

(b)

Figure 6-15. The volume fraction of fluid for different viscosities at steady state. The flow rate is 400 kg/min*. (a) 2* mPa·s*, (b) 20* mPa·s

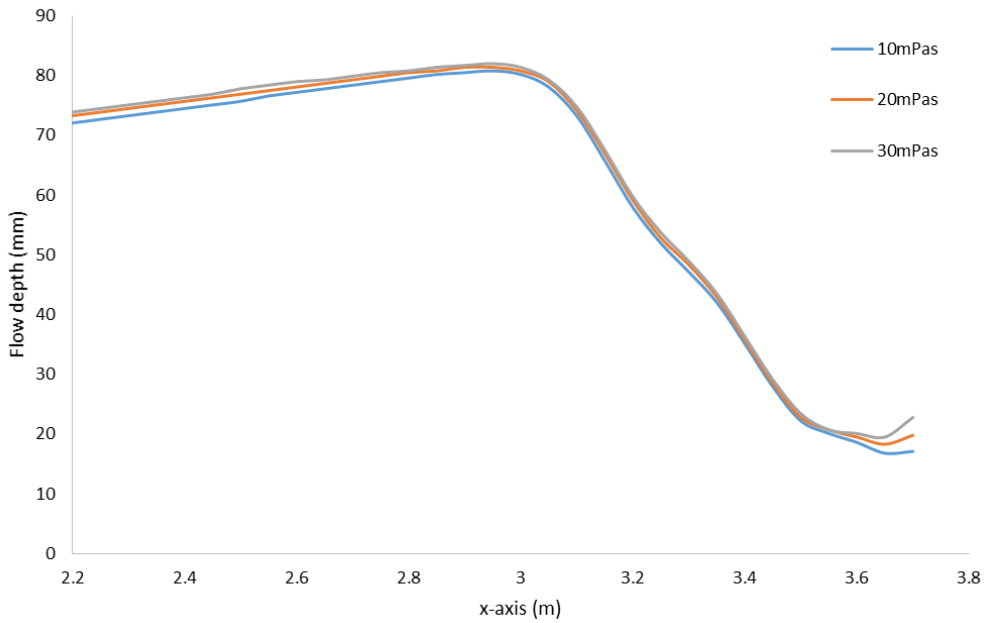

(a)

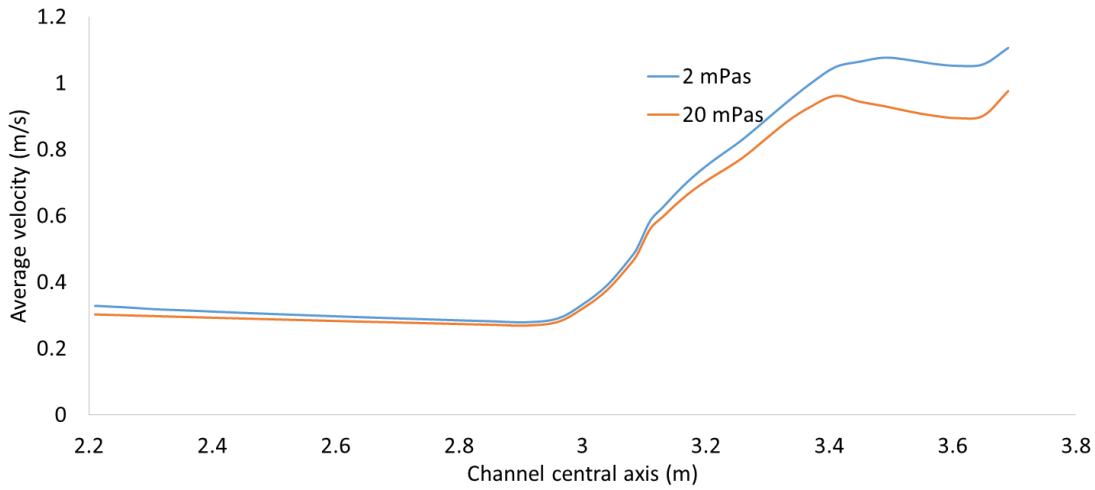

(b)

Figure 6-16. Comparison of flow depth and average velocity along the channel central axis for different viscosities of a fluid at steady state. The flow rate is 400 kg/min: (a) Flow depth, (b) Average velocity.

6.9.2.2 Velocity profiles

Figure 6-17 shows the velocity profiles before the Venturi, where flow is subcritical. Figure 6-18 shows the velocity profile after the Venturi, where flow is supercritical. The local shape of the channel is trapezoidal. The width of the channel increases from the bottom to the top due to the trapezoidal shape. This is why the velocity profiles widen from bottom to the free surface along the y-axis, as shown Figure 6-17 and Figure 6-18. The simulation parameters are equal to the Carreua fluid case in Paper 4. The velocity profiles in the subcritical region show a fully developed behavior from the bottom to the top. In the supercritical region, however, the fully developed velocity profiles are shown at the top. The velocity profile near to the wall becomes skewed in Figure 6-18, due to the expansion effect.

The other velocity profiles are discussed in Paper 4.

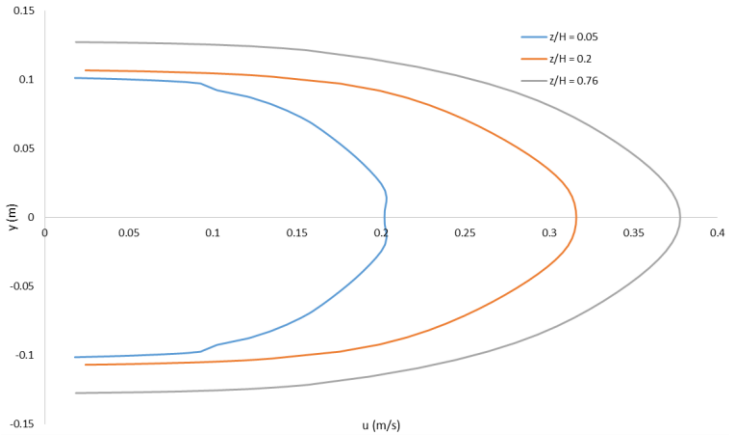

Figure 6-17 Velocity distribution along the y axis for different flow heights at x=2.81m. Velocity distribution profiles from bottom to free surface. The velocity distribution is from the Carreau model simulation.

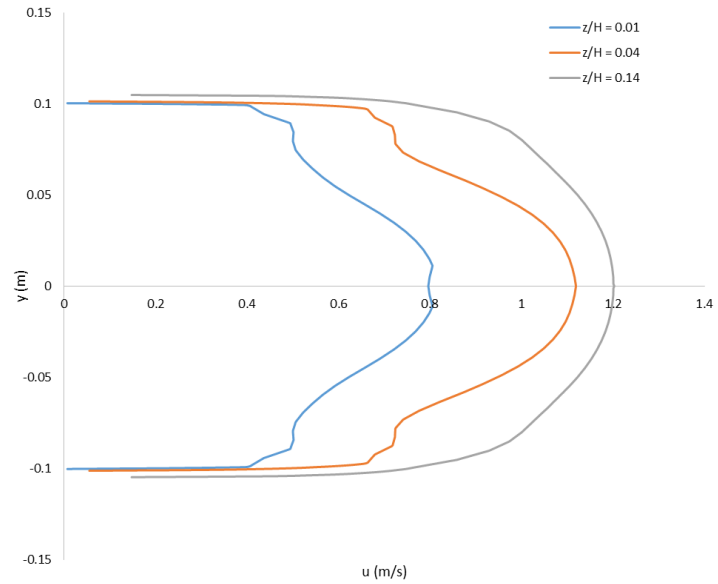

Figure 6-18. Velocity distribution along the y axis for different flow heights at x = 3.61m. Velocity distribution profiles from bottom to free surface. The velocity distribution is from the Carreau model simulation

6.9.3 An elevated inlet boundary for 1D model

A hydraulic jump can, in a non-prismatic (non-continuous cross-section shape) open channel, travel upstream and also downstream. The hydraulic jump travels upstream in open Venturi channels due to the wall reflection effect from the Venturi contraction. The inlet flow depth at the inlet boundary might be smaller than the hydraulic jump height in the 1D model. When a hydraulic jump reaches the inlet, it attempts to raise the inlet flow depth. However, due to the fixed and non-zero inlet boundary, a resultant

wave propagates downwards, where the subcritical region lies. An elevated inlet boundary was used in the 1-D model to keep the stability of the scheme at the inlet.

Figure 6-19 shows the flow direction, the hydraulic jump direction, and the resultant wave direction. The inlet is elevated above the channel bottom. The elevated inlet boundary handles the returned hydraulic jump smoothly.

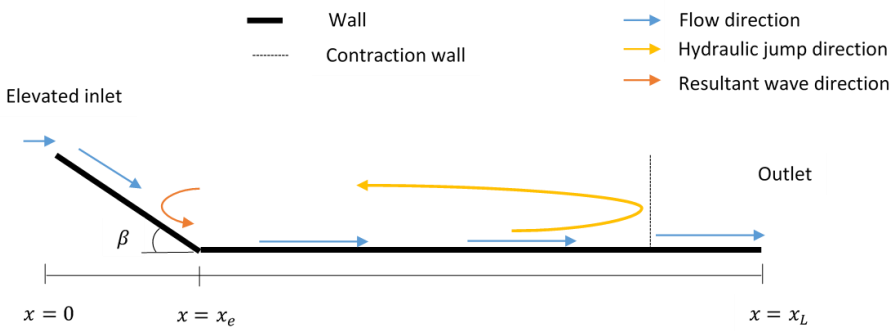

Figure 6-19. An elevated inlet showing the flow direction, the hydraulic jump direction, and the resultant wave direction

Gravity force and the flux limiter function are required to be modified in the region $0 < x < x_e$. Gravity force changes with β angle. The flux limiter function is based on total energy. The elevated height must therefore be taken into consideration in the flux limiter function.

6.9.4 Effect of pitch motion on open Venturi channel flow

Floating platforms have six degrees of freedom (DOF) such as translational surge, sway, and heave displacements and rotational roll, pitch, and yaw displacements (Jonkman, 2007), see Figure 6-20.

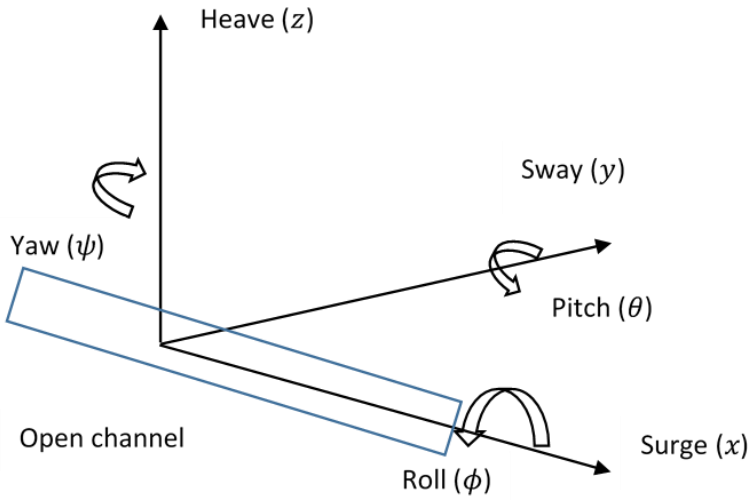

Figure 6-20. Six degrees of freedom

In this study, we consider the pitch motion in open channel 1D flow. We assume that the open Venturi channel is fixed to the platform. Therefore, platform moves directly affect the channel. The gravity slope is not a constant due to the pitch motion; it is a function of time and angular frequency of the platform. Figure 6-21 shows pitch motion of open channel flow on an offshore platform for harmonic motion.

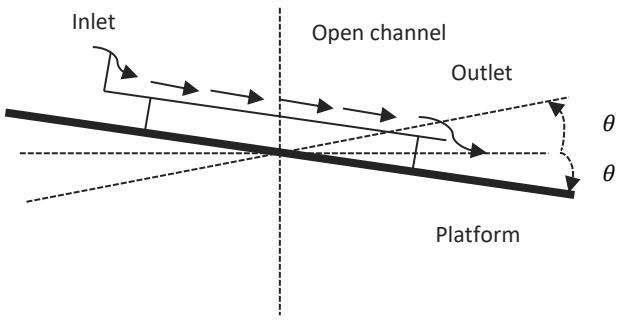

Figure 6-21. Pitch motion of open channel flow on offshore platform for harmonic wave.

The displacement of a platform due to pitch motion of a harmonic wave can be given as (Journée and Massie, 2000),

$\theta = \theta_a cos(\omega_p t + \varepsilon_\theta)$.

Here, θ, θ_a, ω_p, and ε_θ are respectively pitch angle, pitch amplitude, angular frequency, and phase shift. For small angles, the vertical motion of a platform can be presented as a combination of heave, pitch, and roll motions (Journée and Massie, 2000),

$H = z - x\theta + y\phi$.

Here, H is the vertical elevation of the platform, while x, y, and z are displacements due to surge, sway, and heave motions. ϕ is displacement due to the roll motion, and θ is displacement due to pitch motion. The vertical acceleration (Journée and Massie, 2000) is

$\ddot{H} = -\omega_p^2 H_a \cos(\omega_p t + \varepsilon_H)$.

The maximum vertical acceleration, $|\ddot{H}|_{\max} = \omega_p^2 H_a$, should be bound by, $|\ddot{H}|_{\max} \leq g$ $\Rightarrow H_a \leq \frac{g}{\omega_p^2}$, to avoid throwing away the fluid from the channel. The spar floating oil platforms are, typically, used in very deep water which has, generally, a 45-60 s pitch natural period (Koo et al., 2004). For an example, the amplitude of vertical motion should be $H_a \leq \frac{g}{\omega_p^2} = 503$ m for 45 s pitch wave period to avoid throwing away the drilling fluid from the channel. Therefore, we can assume that the vertical acceleration of the platform is insignificant for open channel flow.

The gravity slope is time varying due to the pitch motion. The gravity slope can be presented as

$S_g = \sin\left(\alpha + \theta_a cos(\omega_p t + \varepsilon_\theta)\right)$.

Here, α is the fixed channel inclination with respect to the platform. Equations (4.3) and (4.4) can be modified as,

$$\frac{\partial A}{\partial t} = -\frac{\partial (Au)}{\partial x}, \qquad (6.4)$$

$$\frac{\partial(Au)}{\partial t} = -\frac{\partial(Au^2)}{\partial x} - \frac{\partial\left(k_{g_1}Ah\right)}{\partial x}g + k_{g_2}h^2 g\frac{\partial b}{\partial x} + Ag\left(S_g - S_f - S_i\right). \qquad (6.5)$$

Simulations are conducted for three harmonic wave periods for the platform. The numerical scheme described in Chapter 4 is used for the simulations.

Table 6-1. Three cases of simulations for three harmonic pitch wave periods

Case No.	Wave period of platform (s)	Amplitude of pitch wave (degree)
1	0	0
2	1	4
3	12.5	4
4	45	4

Figure 6-22 shows the results of the three cases. The pitch waves start after 50 s for all three cases. There is a significant effect from the pitch wave on open channel flow for long wave periods (low frequency). For short wave periods, the impact of the pitch wave on the flow depth is insignificant. Long wave periods create sudden superficial to subcritical and subcritical to supercritical transitions, as well as dry bed conditions. This might be very challenging for flow estimation.

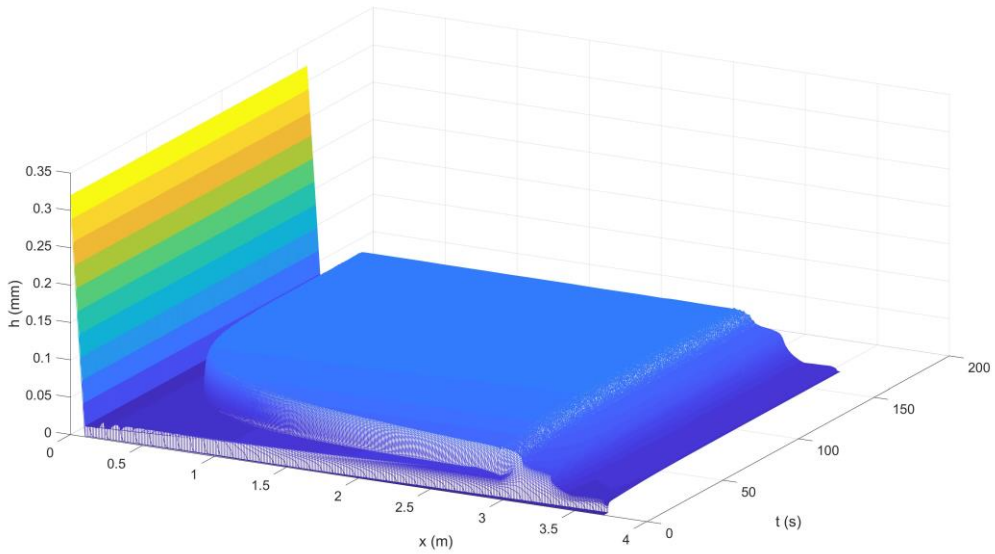

(a)

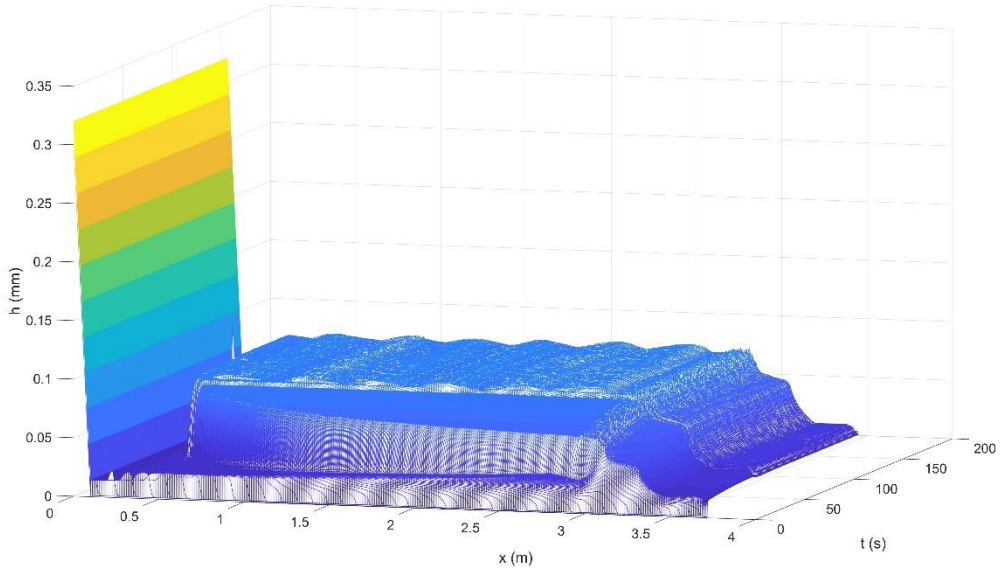
h (mm)
0.35
0.3
0.25
0.2
0.15
0.1
0.05
0
0
0.5
1
1.5
2
2.5
3
3.5
4
x (m)
0
50
100
150
200
t (s)

(b)

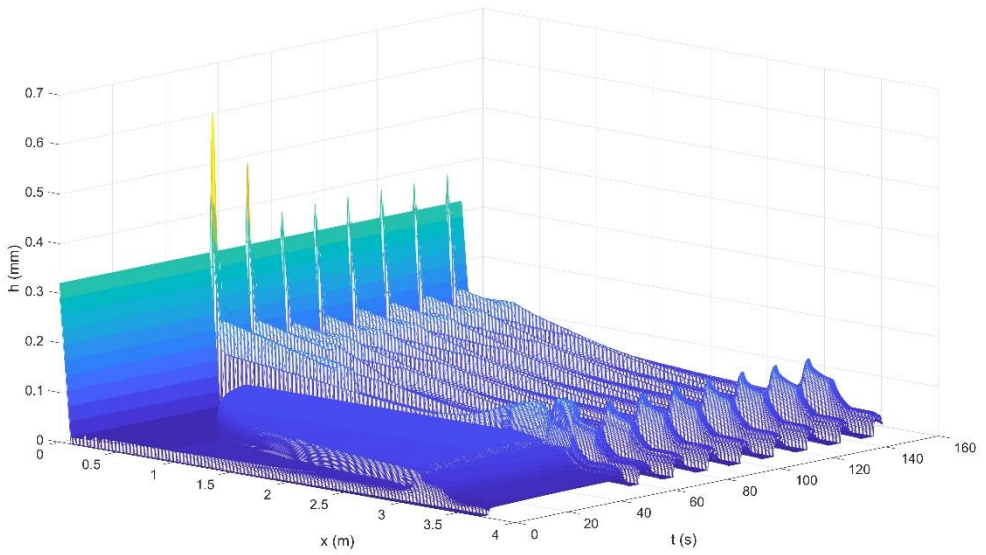
h (mm)
0.7
0.6
0.5
0.4
0.3
0.2
0.1
0
0
0.5
1
1.5
2
2.5
3
3.5
4
x (m)
0
20
40
60
80
100
120
140
160
t (s)

(c)

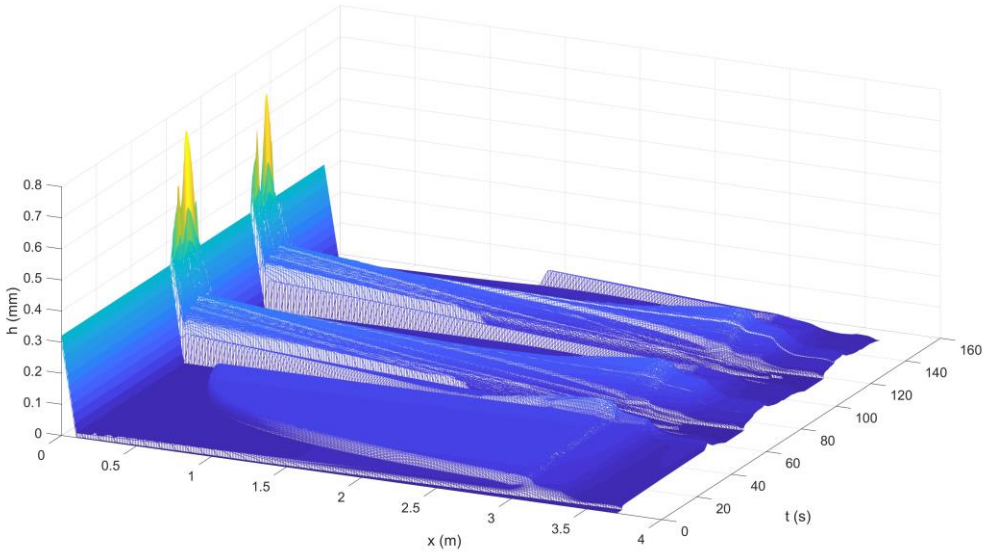

(d)

Figure 6-22. Flow depth variation with time along channel due to the pitch motion of the platform. The inlet drilling fluid flow rate is 400 kg/min. The pitch wave was activated after 50 s. The pitch amplitude is 4 degree:(a) Case-1, wave period 0 s (b) Case-1, wave period 1 s, (c) Case-2, wave period 12.5 s, (d) Case-3, wave period 45 s.

7 Conclusions and recommendations for future work

This Ph.D. thesis presents 3D computational fluid dynamics and 1D numerical modeling for open Venturi channel drilling fluid flow. The primary motivation behind the study was to develop a cost-effective and accurate flow sensor technology to measure the return flow of the drilling process, to address kick/loss detection. The CFD and numerical models results were validated using the experimental work carried out using a Venturi rig. Six journal papers and two conference papers document the main findings.

7.1 Main observations and conclusions

CFD and Experiments

- An open channel at a horizontal inclination gives a subcritical flow upstream from the Venturi contraction wall. After the Venturi contraction, flow transitions into a supercritical flow. A standing hydraulic jump or an oblique jump occurs for downward inclinations. Gravity effect is the main decider than viscous effect of flow regimes in an open channel drilling fluid flow. However, the viscous effect also can make a significant impact on flow regimes, especially in high viscous drilling fluids. Flow depth variation is 6 % when increase the viscosity from 10 mPa·s to 20 mPa·s (for a given shear rate), and flow depth variation is 80 % when channel inclination change in one degree. Flow depth variation is due to the changes of flow regimes.
- The VOF method can achieve high accuracy for 3D CFD free surface simulations. The difference between simulation and experiments can be as little as 2% in some cases. Non-Newtonian properties of the drilling fluid can be coupled with the VOF model and the turbulent models. It is recommended to have the mesh size less than 3 mm to accurately calculate the free surface. However, simulations are still accurate the mesh size up to 10 mm for average velocity less than 2 m/s.
- The value of shear stress τ_{zx} for drilling fluid flow in an open Venturi channel falls from the bottom wall to the free surface, for all flow regimes. The highest

wall shear stress occurs in supercritical flow, which is after the Venturi expansion. The drilling fluid used in these experiments gave shear rate range 0 to 2000 1/s in open Venturi channel flow. However, the average shear rate was 10 1/s throughout the flow domain. Secondary currents are stronger at subcritical flow than at supercritical flow.

- The Eulerian multi-fluid VOF method can be used to model drill cutting flow of drilling fluid in open channels. According to the simulation results, the effect of drill cutting on flow depth in a return flow for a short, prismatic channel, was found to be small. 3D CFD simulation for drilling fluid and drill cuttings in an open channel could be a challenging solution for industries, as computation time extends to several months. Progress in computers may make this feasible in the future.

1D model and Experiments

- After a number of modifications were made to the friction slopes in the shallow water equations, these equations became a good option for model based real time flow estimation in open Venturi channels. The developed 1-D model can achieve high accuracy and an excellent real-time calculation speed. The wall-reflection pressure-force effect from Venturi contraction and expansion is required as an additional term in the conventional shallow water equations, to neutralize artificial accelerations. For a non-Newtonian fluid flowing in an open channel, the friction slope is divided into external friction and internal friction. The external friction can be formulated using a Manning's based friction model, and internal friction can be formulated using a pure non-Newtonian model such as Herschel-Bulkley or Carreau models. According to the calculations of drilling fluids studied here, the external friction term is highest and internal friction term is lowest for lowest viscous fluid. The proposed method for solving the non-Newtonian shallow water equations is simple to program, straightforward and computationally economical.

- High-resolution TVD Runge-Kutta methods are recommended to solve non-linear shallow water equations with complex source terms. These kinds of high-resolution schemes are capable of handling discontinuities that are due to large hydraulic jumps and dry conditions. The second order accurate FLIC scheme using the source term splitting method is well-balanced, and preserves positivity, high accuracy, and good resolution for discontinuities.
- The inlet flow depth for a given flow rate is independent of downstream flow depth within a range and can achieve the same downstream condition for different inlet velocities in an open Venturi channel. This relationship is strong when the channel is horizontal. Using this technique, the flow rate can be calculated using a single level sensor reading. It is recommended that the level sensor is kept near to the Venturi contraction, this giving a minimum disturbance from surface waves. The developed algorithm can be used for real-time return flow estimation using a single level sensor.

7.2 Recommended future work

- The suggested CFD and 1D numerical methods should be verified with a real industrial offshore rig. The real-time density and viscosity variations must be included in the scheme. The temperature effect of the viscosity models might need to be considered.
- It is recommended that the effect of drill cuttings is analyzed using the experimental result. In this study, drill cuttings simulations were not validated using experimental results.
- The code should be improved using advanced computational tools for faster model running in real time.
- It is recommended that other shapes of channel contraction are to analyze. This might reduce the disturbance of level reading.
- Here, we have done a feasibility study of the effect of pitch motion on open channel platform. It is recommended to make a detail study about moving platform effect on open channel flow.

- The thixotropic effect of drilling fluids might need to be included in the drilling fluid model developed for open channels. Time-dependent structure and shear history might be significant for some drilling fluids. The simplification of neglecting the thixotropic or viscoelastic effects in the Herschel-Bulkley model is still widely accepted, because of the complexity of numerical models (Livescu, 2012).

References

Aarsnes, U.J.F., Busch, A., 2018. Transient modeling of one-dimensional solid-liquid flow in conduits. Int. J. Multiph. Flow 105, 102–111.

Abdo, K., Riahi-Nezhad, C.K., Imran, J., 2018. Steady supercritical flow in a straight-wall open-channel contraction. J. Hydraul. Res. 0, 1–15.

Absi, R., 2011. An ordinary differential equation for velocity distribution and dip-phenomenon in open channel flows. J. Hydraul. Res. 49, 82–89.

Agu, C.E., Hjulstad, Å., Elseth, G., Lie, B., 2017. Algorithm with improved accuracy for real-time measurement of flow rate in open channel systems. Flow Meas. Instrum.

Akan, A.O., 2006. Open channel hydraulics, 1st ed. Elsevier/Butterworth-Heinemann, Burlington.

Akers, B., Bokhove, O., 2008. Hydraulic flow through a channel contraction: Multiple steady states. Phys. Fluids 20, 56601.

Akhshik, S., Behzad, M., Rajabi, M., 2015. CFD–DEM approach to investigate the effect of drill pipe rotation on cuttings transport behavior. J. Pet. Sci. Eng. 127, 229–244.

Alderman, N., Ram Babu, D., L Hughes, T., Maitland, G., 1988. The rheological properties of water-based drilling fluids.

Alderman, N.J., Gavignet, A., Guillot, D., Maitland, G.C., 1988. High-Temperature, High-Pressure Rheology of Water-Based Muds. SPE Annu. Tech. Conf. Exhib.

Alderman, N.J., Haldenwang, R., 2007. A review of Newtonian and non-Newtonian flow in rectangular open channels. In: HYDROTRANSPORT 17. pp. 1–20.

Aldrighetti, E., 2007. Computational hydraulic techniques for the Saint Venant equations in arbitrarily shaped geometry. University of Trento.

Amanna, B., Khorsand Movaghar, M.R., 2016. Cuttings transport behavior in directional

drilling using computational fluid dynamics (CFD). J. Nat. Gas Sci. Eng. 34, 670–679.

ANSYS Fluent, 2009. 12.0 Theory Guide, Ansys Inc.

Baas, J.H., Best, J.L., Peakall, J., Wang, M., 2009. A Phase Diagram for Turbulent, Transitional, and Laminar Clay Suspension Flows. J. Sediment. Res. 79, 162–183.

BAMO Mesures SAS, n.d. Flow rate measurement in open channel : VENTURI CHANNEL [WWW Document]. URL https://www.bamo.eu/international/s4_page575.htm (accessed 1.23.19).

Berg, C., Malagalage, A., Agu, C.E., Kaasa, G.-O., Vaagsaether, K., Lie, B., 2015. Model-based drilling fluid flow rate estimation using Venturi flume. IFAC-PapersOnLine 48, 171–176.

Blanckaert, K., De Vriend, H.J., 2004. Secondary flow in sharp open-channel bends. J. Fluid Mech. 498, 353–380.

Bonakdari, H., Larrarte, F., Lassabatere, L., Joannis, C., 2008. Turbulent velocity profile in fully-developed open channel flows. Environ. Fluid Mech. 8, 1–17.

Brackbill, J.., Kothe, D.., Zemach, C., 1992. A continuum method for modeling surface tension. J. Comput. Phys. 100, 335–354.

Bradford, S.F., Sanders, B.F., 2002. Finite-Volume Model for Shallow-Water Flooding of Arbitrary Topography. J. Hydraul. Eng. 128, 289–298.

Burger, J., Haldenwang, R., Alderman, N., 2010a. Friction factor-Reynolds number relationship for laminar flow of non-Newtonian fluids in open channels of different cross-sectional shapes. Chem. Eng. Sci. 65, 3549–3556.

Burger, J., Haldenwang, R., Alderman, N., 2010b. Laminar non-Newtonian open channel flow: investigating velocity, wall shear stress and fluid depth. In: 18th International Conference on Hydrotransport. Rio De Janeiro, Brazil, pp. 193–206.

Burguete, J., García-Navarro, P., Murillo, J., García-Palacín, I., 2007. Analysis of the Friction Term in the One-Dimensional Shallow-Water Model. J. Hydraul. Eng. 133, 1048–1063.

Caenn, R., Darley, H.C.H., Gray, G.R., 2011. Composition and properties of drilling and completion fluids, 6th ed. Gulf Professional Pub.

Castro, M.J., Fernández-Nieto, E.D., Ferreiro, A.M., García-Rodríguez, J.A., Parés, C., 2009. High Order Extensions of Roe Schemes for Two-Dimensional Nonconservative Hyperbolic Systems. J. Sci. Comput. 39, 67–114.

Cayeux, E., Daireaux, B., 2013. Precise Gain and Loss Detection Using a Transient Hydraulic Model of the Return Flow to the Pit. SPE/IADC Middle East Drill. Technol. Conf. Exhib.

Cea, L., Puertas, J., Vázquez-Cendón, M.-E., 2007. Depth Averaged Modelling of Turbulent Shallow Water Flow with Wet-Dry Fronts. Arch. Comput. Methods Eng. 14, 303–341.

Chanson, H., Brattberg, T., 2000. Experimental study of the air–water shear flow in a hydraulic jump. Int. J. Multiph. Flow 26, 583–607.

Chhantyal, K., 2018. Sensor data fusion based modelling of drilling fluid return flow through open channels. University of South-Eastern Norway.

Chow, V. Te, 1959. Open-channel hydraulics. McGraw-Hill, New York.

Christian, A., Ismail, A., M., B.R., 2014. Turbulence Characteristics in Supercritical Open Channel Flows: Effects of Froude Number and Aspect Ratio. J. Hydraul. Eng. 140, 4014004.

Clark, R.K., Bickham, K.L., 1994. A Mechanistic Model for Cuttings Transport. SPE Annu. Tech. Conf. Exhib.

Crowe, C.T., Sommerfeld, M., Tsuji, Y., 1998. Multiphase Flows with Droplets and

Particles, CRC Press New York.

Datta, I., Debnath, K., 2014. Volume of Fluid Model of Open Channel Contraction. J. Inst. Eng. Ser. C 95, 251–259.

Dodge, D.W., Metzner, A.B., 1959. Turbulent flow of non-Newtonian systems. AIChE J. 5, 189–204.

Doron, P., Barnea, D., 1993. A three-layer model for solid-liquid flow in horizontal pipes. Int. J. Multiph. Flow 19, 1029–1043.

Fernandes, R.R., Turezo, G., Elias da Vinha Andrade, D., Franco, A.T., Ribeiro Negrão, C.O., 2019. Are the rheological properties of water-based and synthetic drilling fluids obtained by the fann 35a viscometer reliable? J. Pet. Sci. Eng.

Fernández-Nieto, E.D., Noble, P., Vila, J.-P., 2010. Shallow Water equations for Non-Newtonian fluids. J. Nonnewton. Fluid Mech. 165, 712–732.

Ferziger, J.H., Peric, M., 2002. Computational methods for fluid dynamics, 3rd ed. Springer Science & Business Media, Heidelberg New York.

Fraser, D., Lindley, R., Moore, D.D., Vander Staak, M., 2014. Early Kick Detection Methods and Technologies. SPE Annu. Tech. Conf. Exhib.

Garcia-Navarro, P., Vazquez-Cendon, M.E., 2000. On numerical treatment of the source terms in the shallow water equations. Comput. Fluids 29, 951–979.

Gassner, G.J., Winters, A.R., Kopriva, D.A., 2016. A well balanced and entropy conservative discontinuous Galerkin spectral element method for the shallow water equations. Appl. Math. Comput. 272, 291–308.

Gottlieb, S., Shu, C., Tadmor, E., 2001. High order time discretization methods with the strong stability property 43, 89–112.

Graham, B., Reilly, W.K., Beinecke, F., Boesch, D.F., Garcia, T.D., Murray, C.A., Ulmer, F.,

2011. The National Commission on the BP Deepwater Horizon Oil Spill and Offshore Drilling. Deep Water. Gulf Oil Disaster Futur. Offshore Drilling. Rep. to Pres.

Gucuyener, I.H., 1983. A Rheological Model for Drilling Fluids and Cement Slurries. Middle East Oil Tech. Conf. Exhib.

Guo, J., 2014. Modified log-wake-law for smooth rectangular open channel flow. J. Hydraul. Res. 52, 121–128.

Guo, J., Mohebbi, A., Zhai, Y., Clark, S.P., 2015. Turbulent velocity distribution with dip phenomenon in conic open channels. J. Hydraul. Res. 53, 73–82.

Haldenwang, R., 2003. Flow of non-newtonian fluids in open channels. Cape Technikon, Cape Town.

Haldenwang, R., Slatter, P., 2006. Experimental procedure and database for non-Newtonian open channel flow. J. Hydraul. Res. 44, 283–287.

Han, S.-M., Hwang, Y.-K., Woo, N.-S., Kim, Y.-J., 2010. Solid–liquid hydrodynamics in a slim hole drilling annulus. J. Pet. Sci. Eng. 70, 308–319.

Hauge, E., Aamo, O.M., Godhavn, J.-M., Nygaard, G., 2013. A novel model-based scheme for kick and loss mitigation during drilling. J. Process Control 23, 463–472.

Hemphill, T., Campos, W., Pilehvari, A., 1993. Yield-power law model more accurately predicts mud rheology. Oil Gas Journal;(United States) 91.

Hirt, C.W., Nichols, B.D., 1981. Volume of fluid (VOF) method for the dynamics of free boundaries. J. Comput. Phys. 39, 201–225.

Hotchkiss, R.H., Kern, E., 2012. Submerged hydraulic jumps [WWW Document]. Ira A. Fult. Coll. Eng. Technol. Brigham young Univ. URL http://krcproject.groups.et.byu.net/index.php (accessed 1.2.19).

Hsu, M.-H., Teng, W.-H., Lai, C., 1998. Numerical simulation of supercritical shock wave

in channel contraction. Comput. Fluids 27, 347–365.

Iehisa, N., Ryoukei, A., 2004. Turbulence Characteristics and Interaction between Particles and Fluid in Particle-Laden Open Channel Flows. J. Hydraul. Eng. 130, 988–1001.

International Standard-ISO 4359, 2013. Flow measurement structures-Rectangular, trapezoidal and U-shaped flumes.

Jha, S.K., 2017. Effect of particle inertia on the transport of particle-laden open channel flow. Eur. J. Mech. - B/Fluids 62, 32–41.

Jin, M., Fread, D.L., 1997. One-dimensional routing of mud/debris flows using NWS FLDWAV model. Debris-Flow Hazards Mitig. Mech. Predict. Assess. 687–696.

Jin, M., Fread, D.L., n.d. D MODELING OF MUD/DEBRIS UNSTEADY FLOWS.

Jinasena, A., Sharma, R., 2018. Model based Real–Time Flow Rate Estimation in Open Channels with Application to Conventional Drilling. In: 2018 18th International Conference on Control, Automation and Systems (ICCAS). pp. 546–551.

Jing, L., Kwok, C.Y., Leung, Y.F., Sobral, Y.D., 2016. Extended CFD--DEM for free-surface flow with multi-size granules. Int. J. Numer. Anal. Methods Geomech. 40, 62–79.

Jonkman, J.M., 2007. Dynamics modeling and loads analysis of an offshore floating wind turbine. National Renewable Energy Lab.(NREL), Golden, CO (United States).

Journée, J.M.J., Massie, W.W., 2000. Offshore hydromechanics. TU Delft.

Kelessidis, V.C., Maglione, R., Tsamantaki, C., Aspirtakis, Y., 2006. Optimal determination of rheological parameters for Herschel–Bulkley drilling fluids and impact on pressure drop, velocity profiles and penetration rates during drilling. J. Pet. Sci. Eng. 53, 203–224.

Kelly, D.M., 2017. A second-order accurate fluid-in-cell (FLIC) method for the 2D shallow

water equations with topography. Theor. Appl. Mech. Lett. 7, 35–40.

Keshavarz Moraveji, M., Naderi, M., 2016. Drilling rate of penetration prediction and optimization using response surface methodology and bat algorithm. J. Nat. Gas Sci. Eng. 31, 829–841.

Khandelwal, V., Dhiman, A., Baranyi, L., 2015. Laminar flow of non-Newtonian shear-thinning fluids in a T-channel. Comput. Fluids 108, 79–91.

Kidanemariam, A.G., Chan-Braun, C., Doychev, T., Uhlmann, M., 2013. Direct numerical simulation of horizontal open channel flow with finite-size, heavy particles at low solid volume fraction. New J. Phys. 15, 25031.

Kiger, K.T., Pan, C., 2002. Suspension and turbulence modification effects of solid particulates on a horizontal turbulent channel flow. J. Turbul. 3, N19.

Kocaman, S., Ozmen-Cagatay, H., 2012. The effect of lateral channel contraction on dam break flows: Laboratory experiment. J. Hydrol. 432–433, 145–153.

Koo, B.J., Kim, M.H., Randall, R.E., 2004. Mathieu instability of a spar platform with mooring and risers. Ocean Eng. 31, 2175–2208.

Kurganov, A., Levy, D., 2002. Central-Upwind Schemes for the Saint-Venant System. ESAIM Math. Model. Numer. Anal. 36, 397–425.

Kurganov, A., Noelle, S., Petrova, G., Sci, S.J.C., 2001. Semidiscrete central - upwind schemes for hyperbolic conservation laws and Hamilton – Jacobi equations. SIAM J. Sci. Comput. 23, 707–740.

Kurganov, A., Petrova, G., 2007. A second-order well-balanced positivity preserving central-upwind scheme for the Saint-Venant system. Commun. Math. Sci. 5, 133–160.

LeVeque, R.J., 1998. Balancing Source Terms and Flux Gradients in High-Resolution Godunov Methods: The Quasi-Steady Wave-Propagation Algorithm. J. Comput.

Phys. 146, 346–365.

LeVeque, R.J., 2002. Finite volume methods for hyperbolic problems, 1st ed. Cambridge University Press, Cambridge.

Li, S.Q., Wang, P., Lu, T., 2015. Numerical simulation of direct contact condensation of subsonic steam injected in a water pool using VOF method and LES turbulence model. Prog. Nucl. Energy 78, 201–215.

Liang, Q., Marche, F., 2009. Numerical resolution of well-balanced shallow water equations with complex source terms. Adv. Water Resour. 32, 873–884.

Lindsay, I., Stimpson, B., Corlett, A., 2001. Advanced Interpretation of Venturi Meter Measurements in Multiphase Flow. SPE Annu. Tech. Conf. Exhib.

Livescu, S., 2012. Mathematical modeling of thixotropic drilling mud and crude oil flow in wells and pipelines—A review. J. Pet. Sci. Eng. 98–99, 174–184.

Loisel, V., Abbas, M., Masbernat, O., Climent, E., 2013. The effect of neutrally buoyant finite-size particles on channel flows in the laminar-turbulent transition regime. Phys. Fluids 25, 123304.

Longo, S., Chiapponi, L., Di Federico, V., 2016. On the propagation of viscous gravity currents of non-Newtonian fluids in channels with varying cross section and inclination. J. Nonnewton. Fluid Mech. 235, 95–108.

M., G.A., Hanif, C.M., 1991. Numerical Simulation of Hydraulic Jump. J. Hydraul. Eng. 117, 1195–1211.

Manning, R., Griffith, J.P., Pigot, T.F., Vernon-Harcourt, L.F., 1890. On the flow of water in open channels and pipes.

Mitchell, R.F., Miska, S.Z., 2011. Fundamentals of drilling engineering. SPE textbook series ;

Møller, P.C.F., Mewis, J., Bonn, D., 2006. Yield stress and thixotropy: On the difficulty of measuring yield stresses in practice. Soft Matter.

Murthy, B.N., Ghadge, R.S., 2007. CFD simulations of gas–liquid–solid stirred reactor: Prediction of critical impeller speed for solid suspension. Chem. Eng. Sci. 62, 7184–7195.

Murty Bhallamudi, S., Hanif Chaudhry, M., 1992. Computation of flows in open-channel transitions. J. Hydraul. Res. 30, 77–93.

Nayeem, A.A., Venkatesan, R., Khan, F., 2016. Monitoring of down-hole parameters for early kick detection. J. Loss Prev. Process Ind. 40, 43–54.

Neff, J.M., 2010. Fate and effects of water based drilling muds and cuttings in cold water environments. Houst. Rep. to Shell Explor. Prod. Co.

Nezu, I., 2005. Open-channel flow turbulence and its research prospect in the 21st century. J. Hydraul. Eng. 131, 229–246.

Nezu, I., Nakagawa, H., Jirka, G.H., 1994. Turbulence in open-channel flows. J. Hydraul. Eng. 120, 1235–1237.

Nikuradse, J., 1950. LAWS OF FLOW IN ROUGH PIPES. Tech. Memo.

Norman, J., 2011. Coriolis sensors open lines to real-time data [WWW Document]. IADC Drill. Contract. URL http://www.drillingcontractor.org/coriolis-sensors-open-lines-to-real-time-data-10682 (accessed 12.28.18).

Openchannelflow, 2018. Flumes. Openchannelflow.

Orban, J.J., Zanner, K.J., Orban, A.E., 1987. New Flowmeters for Kick and Loss Detection During Drilling. SPE Annu. Tech. Conf. Exhib.

Paknejad, A., Schubert, J.J., Amani, M., 2009. Key Parameters in Foam Drilling Operations. IADC/SPE Manag. Press. Drill. Underbalanced Oper. Conf. Exhib.

Park, I.-R., Kim, K.-S., Kim, J., Van, S.-H., 2012. Numerical investigation of the effects of turbulence intensity on dam-break flows. Ocean Eng. 42, 176–187.

Patel, T., Gill, L., 2006. Volume Of Fluid Model Applied To Curved OpenChannel Flows. WIT Trans. Eng. Sci. 52.

Perthame, B., Simeoni, C., 2001. A kinetic scheme for the Saint-Venant system¶with a source term. CALCOLO 38, 201–231.

Picchi, D., Poesio, P., Ullmann, A., Brauner, N., 2017. Characteristics of stratified flows of Newtonian/non-Newtonian shear-thinning fluids. Int. J. Multiph. Flow 97, 109–133.

Pigott, R.J.S., 1941. Mud flow in drilling. In: Drilling and Production Practice.

Pu, J.H., 2015. Turbulence modelling of shallow water flows using Kolmogorov approach. Comput. Fluids 115, 66–74.

Qian, D., Lawal, A., 2006. Numerical study on gas and liquid slugs for Taylor flow in a T-junction microchannel. Chem. Eng. Sci. 61, 7609–7625.

Rahman, M., Chaudhry, M.H., 1997. Computation of flow in open-channel transitions. J. Hydraul. Res. 35, 243–256.

Ramadan, A., Skalle, P., Johansen, S.., 2003. A mechanistic model to determine the critical flow velocity required to initiate the movement of spherical bed particles in inclined channels. Chem. Eng. Sci. 58, 2153–2163.

Reitsma, D., 2010. A simplified and highly effective method to identify influx and losses during Managed Pressure Drilling without the use of a Coriolis flow meter. SPE/IADC Manag. Press. Drill. Underbalanced Oper. Conf. Exhib.

Rusche, H., 2003. Computational fluid dynamics of dispersed two-phase flows at high phase fractions. Imperial College London (University of London).

Sanders, B.F., Iahr, M., 2001. High-resolution and non-oscillatory solution of the St. Venant equations in non-rectangular and non- prismatic channels. J. Hydraul. Res. 39, 321–330.

Sarma, K.V.N., Lakshminarayana, P., Rao, N.S.L., 1983. Velocity distribution in smooth rectangular open channels. J. Hydraul. Eng. 109, 270–289.

Semi-kidd, 2016. Project description: Sensors and models for improved kick/loss detection in drilling (Semi-kidd). Porsgrunn.

Shu, C.-W., Osher, S., 1988. Efficient implementation of essentially non-oscillatory shock-capturing schemes. J. Comput. Phys. 77, 439–471.

Slatter, P.T., 1995. Transitional and turbulent flow of non-Newtonian slurries in pipes. University of Cape Town.

Song, L., Zhou, J., Guo, J., Zou, Q., Liu, Y., 2011. A robust well-balanced finite volume model for shallow water flows with wetting and drying over irregular terrain. Adv. Water Resour. 34, 915–932.

Stamnes, O.N., Zhou, J., Kaasa, G., Aamo, O.M., 2008. Adaptive observer design for the bottomhole pressure of a managed pressure drilling system. In: 2008 47th IEEE Conference on Decision and Control. pp. 2961–2966.

Stearns, F.P., 1883. A reason why the maximum velocity of water flowing in open channels is below the surface. Trans. Am. Soc. Civ. Eng 7, 331–338.

Steine, O.G., Rommetveit, R., Harris, T.W.R., 1995. Full Scale Kick Detection System Testing Relevant for Slim-Hole / HPHT Drilling. SPE Annu. Tech. Conf. Exhib.

Strang, G., 2016. Introduction to Linear Algebra, 4th ed, Wellesley-Cambridge Press.

Tachie, M.F., Bergstrom, D.J., Balachandar, R., 2003. Roughness effects in low- Re_θ open-channel turbulent boundary layers. Exp. Fluids 35, 338–346.

Thomas, M., Hanif, C.M., 1995. Depth-Averaged Open-Channel Flow Model. J. Hydraul. Eng. 121, 453–465.

Toro, E.F., 2009. Riemann solvers and numerical methods for fluid dynamics-A Practical Introduction, 3rd ed, Book. Springer Science & Business Media, Heidelberg.

Tseng, M.-H., 2004. Improved treatment of source terms in TVD scheme for shallow water equations. Adv. Water Resour. 27, 617–629.

Ubbink, O., 1997. Numerical prediction of two fluid systems with sharp interfaces. University of London PhD Thesis.

Ubbink, O., Issa, R.I., 1999. A Method for Capturing Sharp Fluid Interfaces on Arbitrary Meshes. J. Comput. Phys. 153, 26–50.

Ünalmis, Ö.H., Raul, V. V, 2016. World's First Optical Venturi Flowmeter. SPE Asia Pacific Oil Gas Conf. Exhib.

Vaagsaether, K., Knudsen, V., Bjerketvedt, D., 2007. Simulation of flame acceleration and DDT in H2-air mixture with a flux limiter centered method. Int. J. Hydrogen Energy 32, 2186–2191.

Vázquez-Cendón, M.E., 1999. Improved Treatment of Source Terms in Upwind Schemes for the Shallow Water Equations in Channels with Irregular Geometry. J. Comput. Phys. 148, 497–526.

Versteeg, H.K., Malalasekera, W., 2007. An introduction to computational fluid dynamics : the finite volume method, 2nd ed. Pearson Education Ltd.

Vukovic, S., Sopta, L., 2002. ENO and WENO Schemes with the Exact Conservation Property for One-Dimensional Shallow Water Equations. J. Comput. Phys. 179, 593–621.

Wan, T., Yao, J., Zishun, S., Li, W., Juan, W., 2011. Solution and drilling fluid properties of water soluble AM-AA-SSS copolymers by inverse microemulsion. J. Pet. Sci. Eng.

78, 334–337.

Wilson, A., 2014. Managed-Pressure Drilling - A Solution for Challenging Wells in Vietnam. J. Pet. Technol. 66, 86–88.

Xing, Y., Shu, C.-W., 2006. High order well-balanced finite volume WENO schemes and discontinuous Galerkin methods for a class of hyperbolic systems with source terms. J. Comput. Phys. 214, 567–598.

Xing, Y., Shu, C.-W., 2011. High-order finite volume WENO schemes for the shallow water equations with dry states. Adv. Water Resour. 34, 1026–1038.

Yang, S.-Q., Tan, S.-K., Lim, S.-Y., 2004. Velocity distribution and dip-phenomenon in smooth uniform open channel flows. J. Hydraul. Eng. 130, 1179–1186.

Zamora, M., Roy, S., 2000. The Top 10 Reasons to Rethink Hydraulics and Rheology. IADC/SPE Asia Pacific Drill. Technol.

Part II

Published papers

Paper 1

Flow regime changes at hydraulic jumps in an open Venturi channel for Newtonian fluid

This paper is published in The Journal of Computational Multiphase Flows
doi: 10.1177/1757482X17722890

Research Article

The Journal of
Computational Multiphase Flows

The Journal of Computational Multiphase Flows
0(0) 1–11
© The Author(s) 2017
Reprints and permissions:
sagepub.co.uk/journalsPermissions.nav
DOI: 10.1177/1757482X17722890
journals.sagepub.com/home/cmf

SAGE

Flow regime changes at hydraulic jumps in an open Venturi channel for Newtonian fluid

Prasanna Welahettige, Bernt Lie and Knut Vaagsaether

Abstract

The aim of this paper is to study flow regime changes of Newtonian fluid flow in an open Venturi channel. The simulations are based on the volume of fluid method with interface tracking. ANSYS Fluent 16.2 (commercial code) is used as the simulation tool. The simulation results are validated with experimental results. The experiments were conducted in an open Venturi channel with water at atmospheric condition. The inlet water flow rate was 400 kg/min. The flow depth was measured by using ultrasonic level sensors. Both experiment and simulation were done for the channel inclination angles 0°, -0.7°, and -1.5°. The agreement between computed and experimental results is satisfactory. At horizontal condition, flow in the channel is supercritical until contraction and subcritical after the contraction. There is a hydraulic jump separating the supercritical and subcritical flow. The position of the hydraulic jump oscillates within a region of about 100 mm. Hydraulic jumps coming from the contraction walls to the upstream flow are the main reasons for the conversion of supercritical flow into subcritical flow. An "oblique jump" can be seen where there is a supercritical flow in the contraction. There is a triple point in this oblique jump: the triple point consists of two hydraulic jumps coming from the contraction walls and the resultant wave. The highest flow depth and the lowest velocity in the triple point are found at the oblique jump.

Keywords

Venturi channel, flow depth, subcritical flow, supercritical flow, hydraulic jump, oblique jump

Date received: 1 March 2017; accepted: 5 July 2017

Introduction

Drill bit pressure control (Kick/Loss detection) is a critical task in oil well drilling. Drill mud flow control is one method to control the pressure at the drill bit. Coriolis flow meters are currently used for mud flow measurements. However, since these flow meters are expensive, open Venturi channel mud flow measurement could be a cost-effective alternative. It is thus of interest to understand the flow behavior in an open Venturi channel.

Molls and Hanif Chaudhry[1] have developed a model to solve unsteady depth-averaged equations and it was tested in a contraction channel in a computational study. Berg et al.[2] have done a feasibility study about the possibility of flow rate measurements in a Venturi flume. They recognized that the occurrence of a "level jump" depends on fluid properties, length of the flume, and computational time. Datta and Debnath[3] used the volume of fluid (VOF) model for an open channel with different contraction ratios. They observed that turbulence intensity increases as the contraction ratio decreases. Patel and Gill[4] used the VOF model for the curved open channel flow in computational fluid dynamics (CFD) simulation. Agu et al.[5] developed a numerical scheme to predict the transcritical flow in a Venturi channel using the Saint-Venant equations. When the supercritical flow regime passes through the critical flow regime into the subcritical flow regime, the

Department of Process, Energy and Environmental Technology, University College of Southeast Norway, Porsgrunn, Norway

Corresponding author:
Knut Vaagsaether, University Collage of Southeast Norway, Høgskolen i Sørøst-Norge, Kjølnes Ring 56, Porsgrunn, Telemark 3918, Norway.
Email: knut.vagsather@usn.no

Creative Commons Non Commercial CC-BY-NC: This article is distributed under the terms of the Creative Commons Attribution-NonCommercial 4.0 License (http://www.creativecommons.org/licenses/by-nc/4.0/) which permits non-commercial use, reproduction and distribution of the work without further permission provided the original work is attributed as specified on the SAGE and Open Access pages (https://us.sagepub.com/en-us/nam/open-access-at-sage).

hydraulic jump is propagated due to the energy losses.[6,7] Yen[8] studied open channel flow resistance. Benjamin and Onno[9] studied shallow water flow through a channel contraction. Wierschem and Aksel[10] studied hydraulic jumps and standing waves in a gravity-driven flow of viscous liquid in an open channel. Hänsch et al.[11] introduced a multifluid two-fluid concept combining a dispersed and a continuous gas phase in one computational domain that could be used to describe bubble behavior in a hydraulic jump. The VOF model can be used for the open channel flow.[12,13]

This study is the beginning of our future study for the development of a model for non-Newtonian fluid drill cutting flow control. The main objective of this study is to identify the flow regime changes of Newtonian fluid in an open Venturi channel. The simulation results are validated with experimental results.

CFD models

The fluid domain contains water and air. The interface is changing (water level changing) along the Venturi channel. The VOF method with surface tracking is applied to a fixed Eulerian mesh. The free surface between flowing fluid (water) and fluid above (air) is important for flow depth measurement. Water is considered as the secondary phase in these simulations (air might also be used as the secondary phase). Water volume fraction α_2 of the cells is contained by

$$0 < \alpha_2 < 1 \tag{1}$$

By assuming isothermal, incompressible, and immiscible conditions, the mass balance equation can be given as

$$\frac{\partial \alpha_2}{\partial t} = -div\left(\alpha_2 \vec{U}\right) \tag{2}$$

At the interface, an artificial compression term is activated. Therefore, equation (2) can be converted into[14–16]

$$\frac{\partial \alpha_2}{\partial t} = -div\left(\alpha_2 \vec{U}\right) - div\left(\alpha_2(1-\alpha_2)\vec{U}_r\right) \tag{3}$$

$\alpha_2(1-\alpha_2)$ is only active at the interface, since it will disappear when $\alpha_2 = 0$ or $\alpha_2 = 1$. Here, $\vec{U}$ is the three-dimensional velocity component, $\vec{U}_r$ is the velocity field suitable to compress the interface. The maximum velocity at the transition region is an approximation for $\vec{U}_r$. The compression is considered perpendicular to the interface.

Time discretization is based on the implicit Euler method. Pressure–velocity coupling is based on the Semi Implicit Method for Pressure Linked Equations scheme with a second-order upwind correction. The standard k−ε model is used for turbulence handling.

x momentum

$$\frac{\partial \rho u}{\partial t} + div\left(\rho u \vec{U}\right) = -\frac{\partial p}{\partial x} + div(\mu grad(u)) + F_{sx} \tag{4}$$

y momentum

$$\frac{\partial \rho v}{\partial t} + div\left(\rho v \vec{U}\right) = -\frac{\partial p}{\partial y} + div(\mu grad(v)) + F_{sy} \tag{5}$$

z momentum

$$\frac{\partial \rho w}{\partial t} + div\left(\rho w \vec{U}\right) = -\frac{\partial p}{\partial z} + div(\mu grad(w)) + F_{sz} + \rho g \tag{6}$$

Here u, v, and w are the velocity components in the x, y, and z directions, respectively. g is the acceleration of gravity. $\vec{F}_s$ is the surface tension force; it is active only at the free surface

$$\vec{F}_s = \sigma k \vec{n} \tag{7}$$

$$\vec{n} = \frac{grad(\alpha)}{|grad(\alpha)|} \tag{8}$$

$$k = div(\vec{n}) \tag{9}$$

Here σ is the surface tension coefficient,k is the curvature of the interface, and $\vec{n}$ is the normal vector to interface. The material properties, density ρ and viscosity μ, are considered as

$$\rho = \alpha_2\rho_2 + (1-\alpha_2)\rho_1 \tag{10}$$

$$\mu = \alpha_2\mu_2 + (1-\alpha_2)\mu_1 \tag{11}$$

ρ_1 and ρ_2 are the densities of air and water. μ_1 and μ_2 are the viscosities of air and water. Wall surface roughness is commonly characterized by the normalized roughness height K_s^+[6,12,17]

$$K_s^+ = \frac{\rho K_s u^*}{\mu} \tag{12}$$

Here K_s is the physical roughness height, while

$$u^* = C_\mu^{1/4}\kappa^{1/2} \tag{13}$$

Here $C_\mu = 0.09$ is a k−ε model constant and $\kappa = 0.4$ is the von Karman's constant. According to these conditions, there are three main flow regimes:

If $K_s^+ \leq 2.25$, the system is hydrodynamically smooth,

If $2.25 < K_s^+ \leq 90$, the system is transitional,

If $90 < K_s^+$ the system is fully rough.

The calculated K_s^+ value for this case is approximately 5.2. Therefore, transitional wall roughness is active. This calculation is based on the stainless steel physical roughness height.

Critical depth calculation

The dimensionless Froude number (Fr) is used for the characterization of the open-channel flows, which is defined as the ratio of the inertia force and hydrostatic force[6,12]

$$\mathrm{Fr} = \frac{\bar{U}}{\sqrt{gl}} \tag{14}$$

Here $\bar{U}$ is the velocity magnitude of the fluid and l is the characteristic length. There can be a wave propagation based on the velocity magnitude and the distance from bottom surface to the free surface level. The wave speed is given as

$$\bar{U}_{wave} = \bar{U} \pm \sqrt{gl} \tag{15}$$

Three types of waves can be categorized based on the Fr number value.

Case 1

If $\mathrm{Fr} < 1$, then $\bar{U} < \sqrt{gl}$, therefore $\bar{U}_{wave} < 0$ or $\bar{U}_{wave} > 0$. This is called subcritical flow. The wave disturbance can travel upstream as well as downstream. In this case, the downstream flow condition may affect the upstream flow. Here, $l > l_c$.

Case 2

If $\mathrm{Fr} = 1$, then $\bar{U} = \sqrt{gl_c}$, therefore $\bar{U}_{wave} = 0$. This is called critical flow. The propagated wave disturbance remains and it will not affect either upstream or downstream. Here, $l = l_c$.

Case 3

If $\mathrm{Fr} > 1$, then $\bar{U} > \sqrt{gl}$, therefore $\bar{U}_{wave} > 0$. This is called supercritical flow. The disturbances cannot travel upstream. Rapid flows are prominent for supercritical flow. Here, $l < l_c$.

Critical flow depth h_c is important in order to identify whether the flow condition is supercritical or subcritical. Figure 1 shows the sketch of a cross sectional view of the trapezoidal channel. Here b is the bottom depth, h_c is the critical flow depth, and θ is the trapezoidal angle.

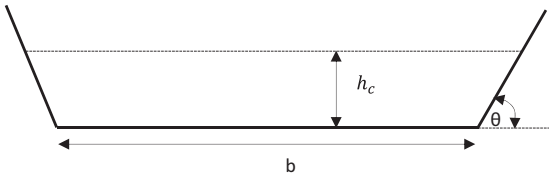

Figure 1. Cross sectional sketch of the trapezoidal open channel with critical flow depth.

At critical flow condition

$$\bar{U} = \sqrt{gl_c} \tag{16}$$

The flow rate (Q) can be defined as

$$\mathrm{d}Q = U\mathrm{d}A \tag{17}$$

The area (A) perpendicular to flow direction is given as

$$A = \left(b + \frac{h_c}{\tan\theta}\right)h_c \tag{18}$$

The ratio between area and free surface width gives the characteristic length for the trapezoidal. At critical flow

$$l_c = \frac{A}{b + \frac{2h_c}{\tan\theta}} \tag{19}$$

By substituting equations (17) to (19) for equation (16), a critical depth equation can be derived as

$$g\left(b + \frac{h_c}{\tan\theta}\right)^3 h_c^3 - Q^2\left(b + \frac{2h_c}{\tan\theta}\right) = 0 \tag{20}$$

In this study, the bottom width (b) is the only variable, with the critical depth and other parameters as constants along the x-axis. θ is equal to 70°. The total length of the channel is 3.7 m and the measurement start from the inlet of the channel (see Figure 2).

In this case, the bottom width can be defined as a function of x:

For $x = 0\,\mathrm{m}$ to $2.95\,\mathrm{m} : b = 0.2\,\mathrm{m}$

For $x = 2.95\,\mathrm{m}$ to $3.1\,\mathrm{m} : b = 0.2 - \frac{x-2.95}{1.5}$

For $x = 3.1\,\mathrm{m}$ to $3.3\,\mathrm{m} : b = 0.1\,\mathrm{m}$

For $x = 3.3\,\mathrm{m}$ to $3.45\,\mathrm{m} : b = 0.1 + \frac{x-3.3}{1.5}$

For $x = 3.45\,\mathrm{m}$ to $3.7\,\mathrm{m} : b = 0.2\,\mathrm{m}$

The calculated critical depth for the Venturi channel is shown in Figures 5, 7 and 10. Akan's[18] calculations are matching with these calculations.

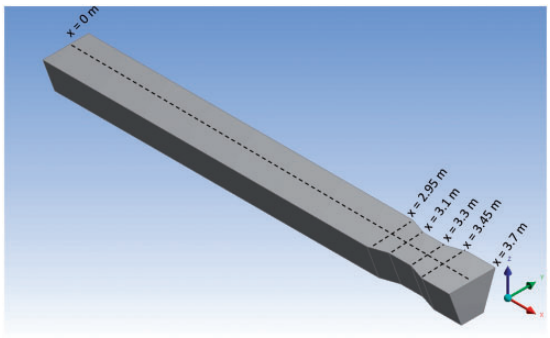

Figure 2. Three-dimensional geometry of a trapezoidal channel with a Venturi region; $x = 0$ m is the inlet of the channel. Contraction starts at $x = 2.95$ m and ends at 3.45 m. The bottom width is 0.2 m for $0\,\text{m} < x < 2.95\,\text{m}$ and $3.45\,\text{m} < x < 3.7\,\text{m}$. The bottom width is 0.1 m for $3.1\,\text{m} < x < 3.3\,\text{m}$. The trapezoidal angle is 70°. The bottom surface has a constant slope (flat).

Geometry, mesh, and boundary conditions

Geometry and mesh

A 3D geometry is shown in Figure 2, which is used in the simulations. The dimensions of the geometry match with the open channel experimental setup. ANSYS Fluent DesignModeler and ANSYS Meshing tools are used for drawing the geometry and generating the mesh, respectively. There is a large distance between the inlet and the start of the contraction. This is to achieve more stable flow conditions before the Venturi contraction in order to reduce upstream disturbances at the Venturi.

The mesh that is used in the simulation contains 0.74 million elements with a maximum cell size of 10 mm. Inflation layers are added near the wall boundaries for better prediction.

Boundary conditions

The upstream boundary condition was defined as "mass flow inlet" for each phase. The inlet water flow rate was 400 kg/min and air inlet flow rate is equal to zero. The outlet was considered a "pressure outlet." The top boundary, which was open to the atmosphere, was defined as a "pressure outlet" at "open channel" conditions. "Bottom level" was defined at $z = 0$ m. All solid walls were considered as "wall." These walls are stationary walls and no-slip condition applies. The wall roughness was matched with a stainless steel wall similar to experimental conditions. Roughness height is 15 μm for stainless steel. The roughness constant was set to 0.5.[3] The fluid domain initializes with only air at atmospheric condition. This means that water is added continuously to an empty channel (with air) at startup.

Experimental setup

The Venturi rig is located at University College of Southeast Norway (see Figure 3). The experimental results of this open Venturi channel are used for comparison with simulation results. The complete circuit of the rig contains a "mud" -mixing tank, a mud circulating pump, a Venturi channel, and a mud return tank. The sensing instruments in the setup are a Coriolis mass flow meter, pressure transmitters, temperature transmitters, and ultrasonic level transmitters. The level transmitters are located along the central axis of the channel and can be moved along the central axis. The accuracy of the Rosemount ultrasonic 3107 level transmitters is ±2.5 mm for a measured distance of less than 1 m.[19] The dimensions of the open channel are shown in Figure 2. All of the experimental values presented in this paper are average values of sensor readings taken over a period of 5 min in each location. The channel inclination can be changed; a negative channel inclination indicates a downward direction.

Results

Experiment and simulation were done with a water flow rate at 400 kg/min for different channel inclination angles: 0°, −0.7°, and −1.5°. The ensuing flow regime changes are observed in the evaluation of the results.

Subcritical flow to supercritical flow

In this case, water flow rate was set to 400 kg/min and the inclination angle was zero. This means that the channel was at horizontal condition. Figure 4 shows the experimental flow depth in the Venturi region and simulated water surface for the complete channel. The water surface is very stable before the contraction. Flow depth is reduced and flow velocity is increased after the Venturi contraction.

Figure 5 shows the flow depth along the centerline from $x = 1.7$ m to $x = 3.7$ m for both experiment and simulation. The calculated critical depth is important for identifying the flow regimes, whether they are subcritical or supercritical. The flow depth in range of $1.7\,\text{m} < x < 3.18\,\text{m}$ is subcritical because flow depth is higher than critical depth. Flow depth below critical depth ($3.18\,\text{m} < x < 3.7\,\text{m}$) shows supercritical flow behavior. Subcritical flow behavior is propagated due to the barriers of the contraction to the flow path. There is no barrier at the end of the channel and, therefore, no back wave propagation to the upstream flow.

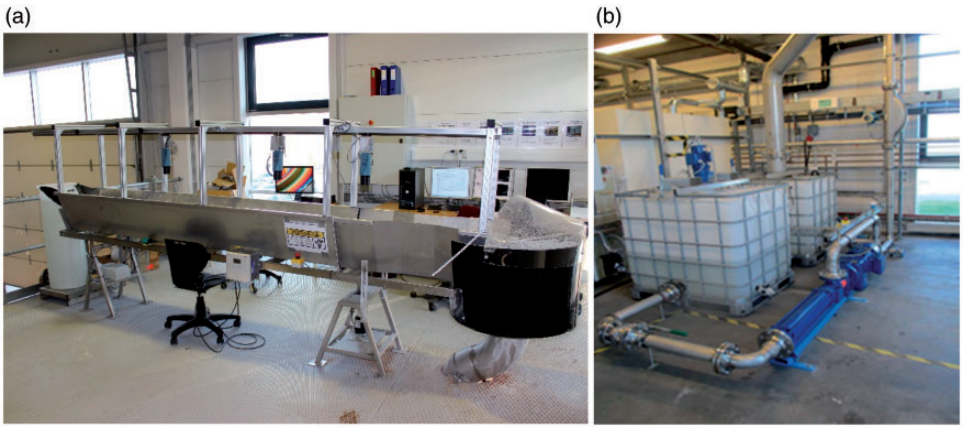

Figure 3. Experimental setup: (a) Open channel with level sensors and (b) pump station.

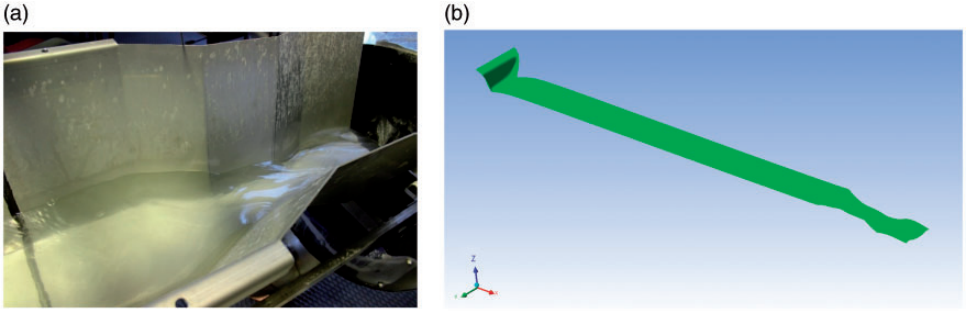

Figure 4. Water flow rate 400 kg/min and open channel at horizontal position: (a) Experimental flow depth at the Venturi region, (b) simulated flow surface for full channel (iso-surface of water volume fraction of 0.5). The flow direction is left to right.

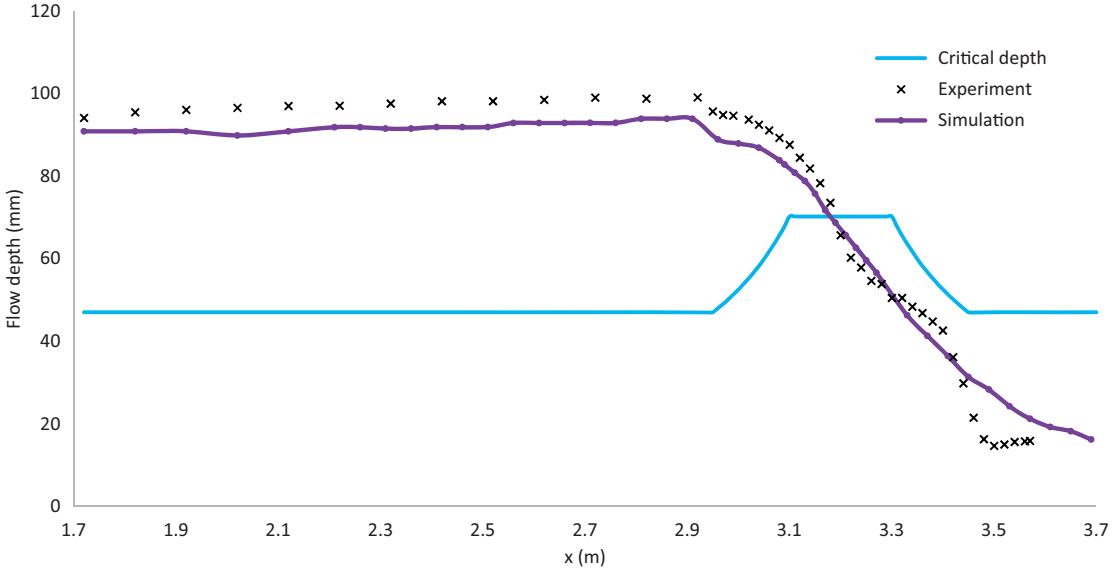

Figure 5. Critical depth, experimental flow depth, and simulated flow depth for water flow rate at 400 kg/min and inclination angle 0° along the channel's central axis (*x*-axis).

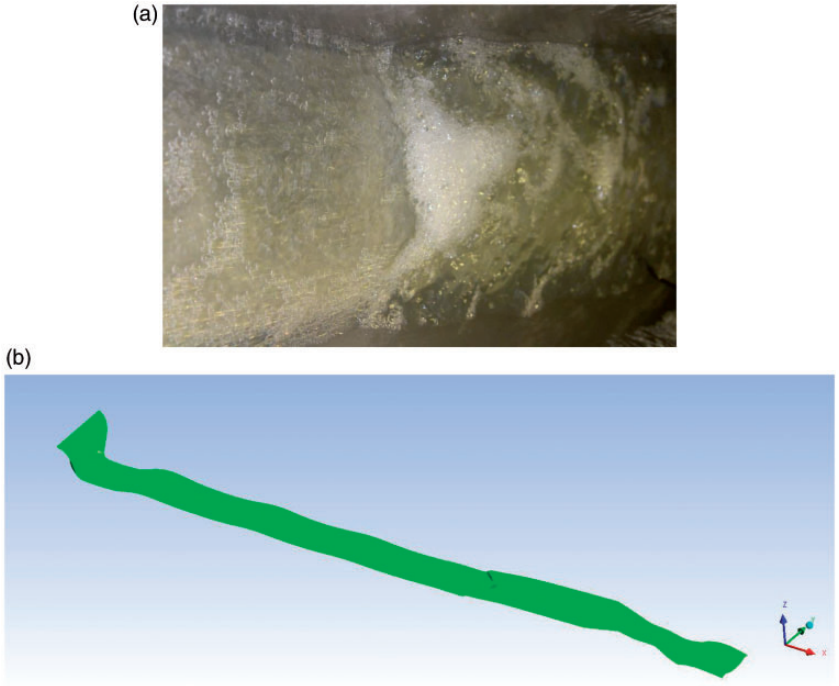

Figure 6. Water flow rate 400 kg/min and the channel inclination −0.7° in downward direction: (a) Experimental flow depth before the contraction and (b) simulated flow surface for full channel (iso-surface of water volume fraction of 0.5). The flow direction is left to right.

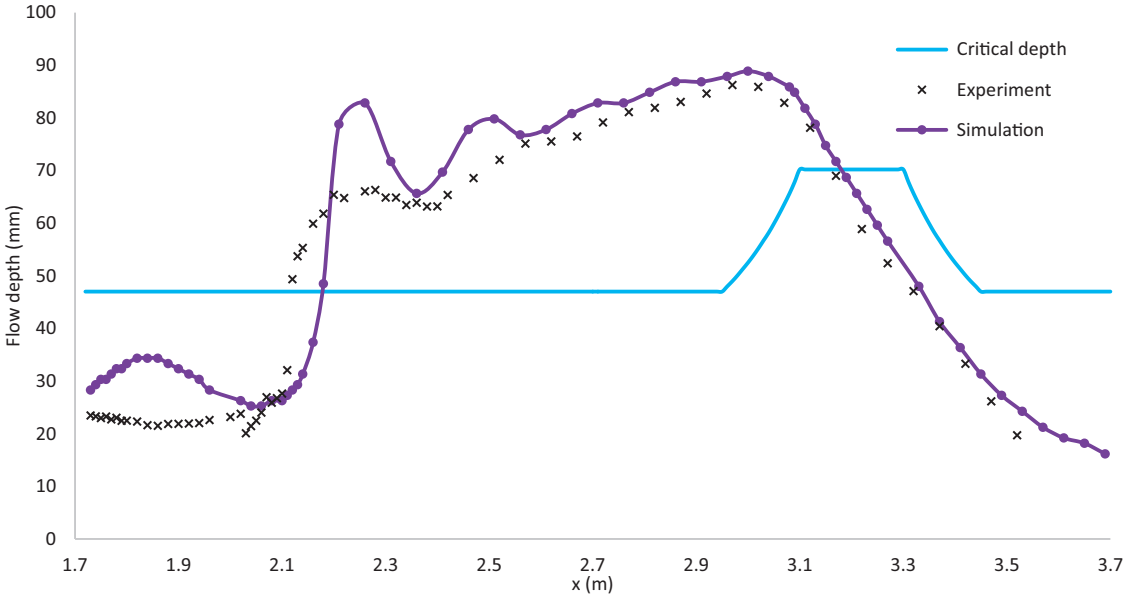

Figure 7. Critical depth, experimental flow depth, and simulated flow depth for water flow rate at 400 kg/min and inclination angle −0.7°.

Because of this, the flow becomes supercritical at the end of the channel.

Supercritical flow to subcritical flow (hydraulic jump)

To generate a hydraulic jump before the contraction region, the channel inclination angle was changed to −0.7° in the downward direction. Because of this, gravity flow support (gsin 0.7) came in the x direction. The water flow rate was 400 kg/min. Figure 6 shows the hydraulic jump results of experimental and simulated iso-surface. This hydraulic jump was propagated before the contraction region (at $x = 2.26$ m). Flow depth was lower before the hydraulic jump and higher after the

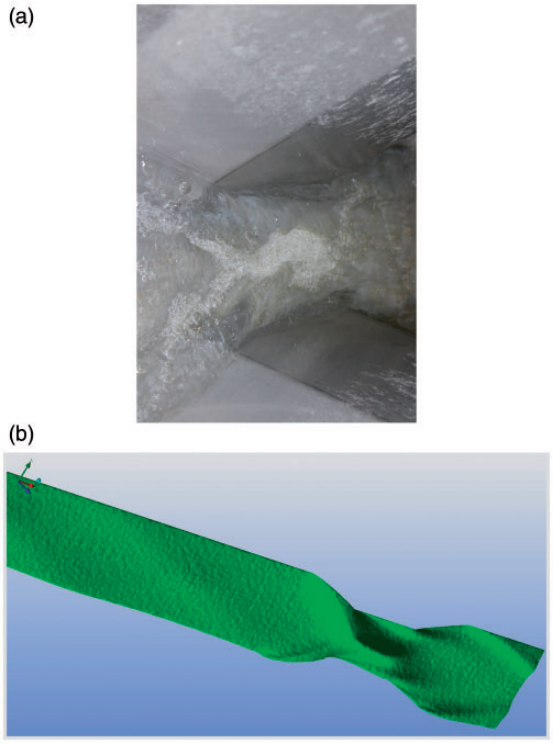

Figure 8. Water flow rate 400 kg/min and channel inclination −1.5° in downward direction: (a) Experimental flow depth before the contraction and (b) simulated flow surface for full channel (iso-surface of water volume fraction of 0.5). Flow direction is left to right.

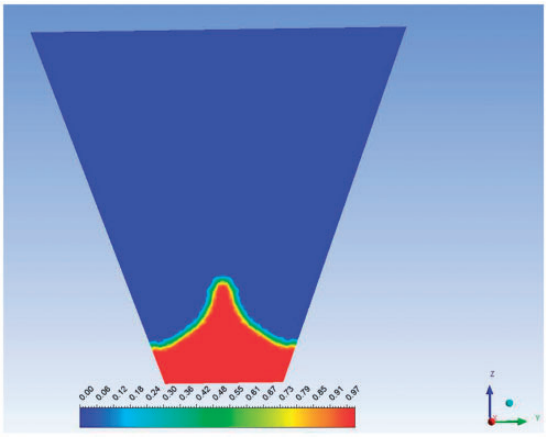

Figure 9. The cross sectional view of the oblique jump. Water volume fraction at x = 3.19 m.

hydraulic jump. In the quasi steady state, the toe of the hydraulic jump oscillated backward and forward within approximately 100 mm. Air entrainment generated more bubbles at the hydraulic jump toe as seen in Figure 6(a) and described by Xiang et al.[20]

As shown in Figure 7, at $x = 1.7$ m to $x = 2.17$ flow depth was lower than critical depth and flow was supercritical. At $x = 1.8$ m to $x = 3.17$ m, flow depth was higher than critical depth and flow was subcritical. The hydraulic jump was propagated due to the conversion of supercritical flow into subcritical flow. Because of the unsteady hydraulic front in the region $x = 1.7$ m to $x = 2.5$ m, experimental results and simulated results are only approximately matched: the hydraulic jump front was moving forward and backward due to the hydraulic jumps coming from the contraction walls. This hydraulic jump was strong enough to convert supercritical flow into subcritical flow. Because of this, flow depth gradually increased up to $x = 3.0$ m. Flow depth started to decrease from $x = 3.0$ m to the outlet. This was due to no hydraulic jump propagation into the upstream, as explained above. Also in this case, flow depth became supercritical after $x = 3.18$ m. The water surface was very stable after $x = 3.18$ m. Therefore, simulation results almost exactly match the experimental results.

Supercritical flow at the Venturi (oblique jump)

In this case, the channel inclination angle was further increased to −1.5° in the downward direction. The flow rate was 400 kg/min. Flow velocity was very fast compared to the other cases. The average flow depth along the channel was almost flat up to the contraction region. However, there was a large "oblique jump"

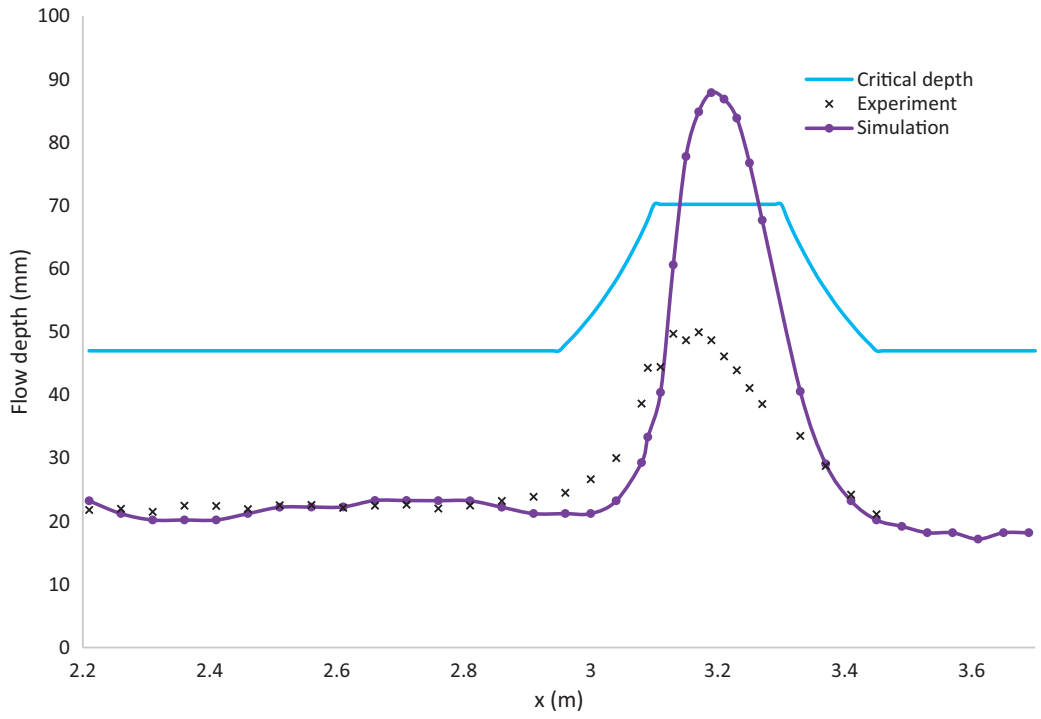

Figure 10. *Oblique jump:* Critical depth, experimental flow depth, and simulated flow depth for water flow rate at 400 kg/min and inclination angle -1.5°.

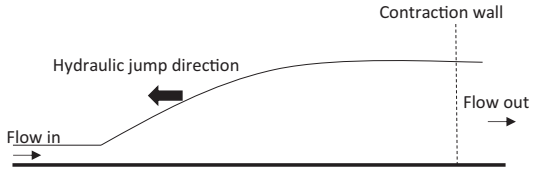

Figure 11. The direction of hydraulic jump propagation at transient condition.

after the Venturi contraction, as shown in Figure 8. The simulated results show a similar oblique jump. The water level near the contraction wall increased due to a hydraulic jump coming from the walls. The oblique jump disappeared at the end of the Venturi due to channel expansion. When the channel expands, there is no strong hydraulic jump coming from the walls compared to channel contraction.

The Rosemount Ultrasonic 3107 Level Transmitter used for measurement has a 6° beam half angle.[19] It measures the average flow depth in its projecting area. The width of the oblique jump is small, as shown in Figure 9. Therefore, the level sensors only measure average values of the flow depth and do not provide a separate measurement of the highest value of flow depth.

The "oblique jump" starts at the end of the contraction of Venturi and ends with the start of the expansion of the Venturi ($x = 3.1$ m to $x = 3.3$ m) as shown in Figure 10. The simulated flow depth reaches a maximum of up to 87 mm. The experimental values show smaller values compared to the simulation due to flow depth averaging as explained previously. The average flow depth is supercritical in the whole channel because it is smaller than critical depth. The oblique jumps are strongly visible at supercritical flow.

Discussion

Hydraulic jumps coming from the contraction walls are stronger than the upstream flow, when the system is completely subcritical before the Venturi contraction. Figure 11 shows the hydraulic jump coming from the contraction walls to the upstream flow in transient condition. We assume at the beginning that there is no water inside the channel. As water is added into the channel, it will hit the contraction walls and propagate a hydraulic jump. The strength of the hydraulic jump is determined by the channel inclination angle and flow rate. The downward angle gives a gravitational support to increase the flow velocity. For a hydraulic jump to occur in the middle of the channel, the upstream force (friction balancing force coming with upstream fluid) needs to be strong enough to neutralize the hydraulic jump coming to the upstream. The position of the hydraulic jump depends on the balancing of these two forces.

Figure 12 shows the velocity vectors of the central axial plane and the cross sectional velocity vectors

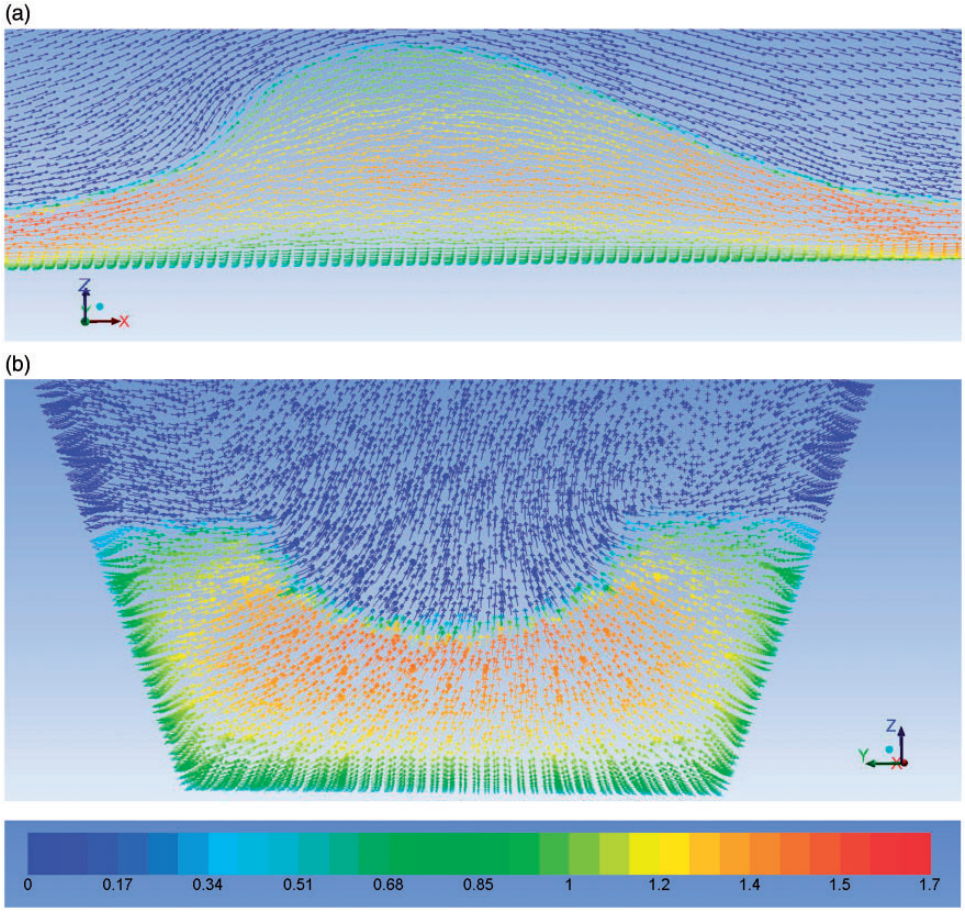

Figure 12. Velocity vectors: (a) Velocity vectors of the central axial plane at the oblique jump and (b) cross sectional view of the velocity vectors at x = 3.08 m (before the oblique jump in contraction region).

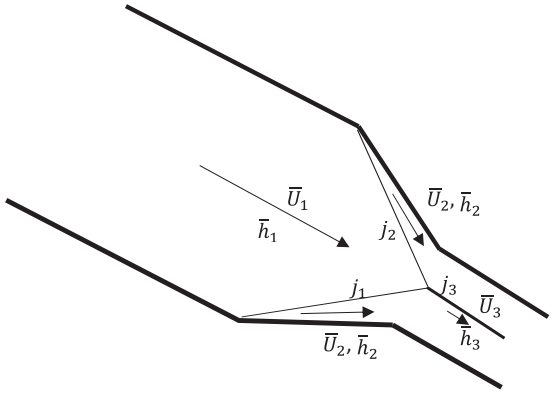

Figure 13. Hydraulic jump arrangement in an oblique jump: Average velocities and average flow depths are shown. $\bar{U}_1$ and $\bar{h}_1$ present before the hydraulic jump. $\bar{U}_2$ and $\bar{h}_2$ present between wall and hydraulic jump. $\bar{U}_3$ and $\bar{h}_3$ present at the oblique jump.

before the oblique jump at $x = 3.08$ m. The air velocity vectors, which are above the water velocity vectors, are negligible. The supercritical velocity has reduced at the oblique jump. Flow depth near to the wall has increased before the oblique jump and flow velocity has decreased in those locations. The fluid velocity direction has turned into the y direction near to the contraction wall. Flow depth also increases in this region.

The oblique jump can be demonstrated as shown in Figure 13. There are three jumps meeting in a triple point. j_1 and j_2 jumps are the hydraulic jumps propagated from the contraction walls. In theory, $j_1 = j_2$. The third jump (j_3) is a resultant jump (oblique jump) of these two hydraulic jumps. There are three main flow velocities ($\bar{U}_1, \bar{U}_2$, and $\bar{U}_3$) and three main flow depths ($\bar{h}_1, \bar{h}_2$, and $\bar{h}_3$) can be recognized: flow before the hydraulic jump, flow at the hydraulic jump, and flow at the oblique jump. The average flow velocities and average flow depths can be categorized as $\bar{U}_1 > \bar{U}_2 > \bar{U}_3$ and $\bar{h}_1 < \bar{h}_2 < \bar{h}_3$.

Conclusions

An open channel at a horizontal inclination angle gives a subcritical flow until the Venturi contraction wall. After the Venturi contraction, flow transitions into

a supercritical flow. For a hydraulic jump to occur in the middle of the channel, the upstream force (friction balancing force coming with upstream fluid) needs to be strong enough to neutralize the hydraulic jump coming to the upstream. The position of the hydraulic jump depends on the balancing of these two forces. As a supercritical flow regime transitions into a subcritical flow regime, a hydraulic jump is generated and flow depth increases. The average velocity in supercritical flow is higher than the average velocity in subcritical flow. When the whole channel flow is at supercritical condition, an oblique jump is generated after the Venturi contraction. The resulting jump of the triple point gives an oblique jump.

Acknowledgment

The authors also gratefully acknowledge the resources for experiments and simulations provided by the University College of Southeast Norway.

Declaration of conflicting interests

The author(s) declared no potential conflicts of interest with respect to the research, authorship, and/or publication of this article.

Funding

The author(s) disclosed receipt of the following financial support for the research, authorship, and/or publication of this article: Economic support from The Research Council of Norway and Statoil ASA through project no. 255348/E30 "Sensors and models for improved kick/loss detection in drilling (Semi-kidd)" is gratefully acknowledged.

References

1. Molls T and Hanif Chaudhry M. Depth-averaged open-channel flow model. *J Hydraul Eng* 1995; 121: 453–465.
2. Berg C, Malagalage A, Agu CE, et al. Model-based drilling fluid flow rate estimation using Venturi flume. In: *Paper presented at the IFAC Workshop on automatic control in offshore oil and gas production*, Florianópolis, Brazil, 27–29 May 2015.
3. Datta I and Debnath K. Volume of fluid model of open channel contraction. *J Inst Eng (India) Ser C* 2014; 95: 251–259.
4. Patel T and Gill L. Volume of fluid model applied to curved open channel flows. In: Rahman M (ed.) *Advances in fluid mechanics, WIT transactions on engineering sciences*. Canada and CA Brebbia, UK: Dalhousie University, and Wessex Institute of Technology, 2006, pp.361–369.
5. Agu CE, Elseth G and Lie B. *Simulation of transcritical flow in hydraulic structures*. Linköping: SIMS, 2015, pp.369–375.
6. Osman Akan A. *Open channel hydraulics*. Oxford: Butterworth-Heinemann, 2006.
7. Douglas JF, Gasiorek JM and Swaffield JA. *Fluid mechanics*, 4th ed. Essex: Pearson Education Limited, 1978.
8. Yen BC. Open channel flow resistance. *J Hydraul Eng* 2002; 128: 20–39.
9. Benjamin A and Onno B. Hydraulic flow through a channel contraction: multiple steady states. *Phys Fluids* 2008; 20: 1–15.
10. Wierschem A and Aksel N. Hydraulic jumps and standing waves in gravity-driven flows of viscous liquids in wavy open channels. *Phys Fluids* 2004; 16: 3868–3877.
11. Hänsch S, Lucas D, Krepper E, et al. A multi-field two-fluid concept for transitions between different scales of interfacial structures. *Int J Multiphase Flow* 2012; 47: 171–182.
12. ANSYS ®, Academic Research, Release 16.2 and Help System. *ANSYS fluent theory guide*. ANSYS, Inc., 2016.
13. OpenFoam Foundation Ltd. *OpenFoam, The open source CFD toolbox, user guide*. OpenFOAM Foundation, 2015.
14. Rusche H. *Computational fluid dynamics of dispersed two-phase flows at high phase fractions*. London: Imperial College of Science, Technology & Medicine Department of Mechanical Engineering, 2002.
15. Ubbink O. *Numerical prediction of two fluid systems with sharp interfaces*. Department of Mechanical Engineering, Imperial College of Science, Technology & Medicine, January 1997.
16. Weller HG, Tabor G, Jasak H, et al. A tensorial approach to computational continuum mechanics using object-oriented techniques. *Comput Phys* 1998; 12: 620–631.
17. Versteeg HK and Malalasekera W. *An introduction to computational fluid dynamics: the finite volume method*, 2nd ed. Harlow: Pearson Education, 2007.
18. Akan O. *Open channel hydraulics*. Oxford: Butterworth-Heinemann, 2006, pp.315–359.
19. Rosemount and Emerson process management. Rosemount Ultrasonic. *3107 Level and 3108 Flow Transmitters,* 2014, p.07.
20. Xiang M, Cheung SCP, Tu JY, et al. A multi-fluid modelling approach for the air entrainment and internal bubbly flow region in hydraulic jumps. *Ocean Eng* 2014; 91: 51–63.

Appendix

Notation

A	area (m^2)
C_μ	constant value
E_s	specific energy head (m)
$\vec{F}_s$	surface intention force (N/m^3)
Fr	Froude number
g	gravity (m/s^2)
h	hydraulic depth (m)
h_c	critical depth (m)
k	curvature of interface (m)
K_s	physical roughness height (m)

K_s^+ normalized roughness height
l characteristic length (m)
l_c critical characteristic length (m)
$\vec{n}$ normal vector to interface
t time (s)
u velocity component in x direction (m/s)
$\vec{\mathrm{U}}$ three-dimensional velocity components (m/s)
$\bar{U}$ average velocity magnitude of fluid (m/s)
$\bar{U}_{wave}$ average velocity magnitude of wave (m/s)
v velocity component in y direction (m/s)
w velocity component in z direction (m/s)

α volume fraction
κ von Karman's constant
σ surface tension coefficient (N/m)
ρ density (kg/m^3)
μ viscosity (Pa s)
ν dynamic viscosity (m^2/s)

Paper 2

Computational fluid dynamics study of flow depth in an open Venturi channel for Newtonian fluid.

This paper is presented at the 58th SIMS.
doi:10.3384/ecp1713829

Computational fluid dynamics study of flow depth in an open Venturi channel for Newtonian fluid

Prasanna Welahettige[1], Bernt Lie[1], Knut Vaagsaether[1]

[1]Department of Process, Energy and Environmental Technology
University College of Southeast Norway
Porsgrunn, Norway
knut.vagsather@usn.no

Abstract

Open Venturi channel flow measurement could be a cheap method to be used in drill bit pressure control. The main objective of this study is to identify the factors related with the flow depth in an open Venturi channel. A commercial computational fluid dynamics tool was used for the simulations. The simulation results were validated with the previous related experimental results. The agreement between simulation and experimental data was satisfactory. The open Venturi channel at a horizontal angle gave a higher flow depth before the contraction region compared to its negative angles (downward). When the channel inclination angle was reduced, flow velocity increased and flow depth reduced. Likewise, flow became supercritical and created a hydraulic jump. The wall roughness played a significant role with the starting position of the hydraulic jump. This was due to the energy loss between wall and fluid. There is an energy loss in a hydraulic jump, when the supercritical flow transition into the subcritical flow. Large eddies were generated in a hydraulic jump. Flow depths difference between supercritical and subcritical is a factor to generate the large eddies. Fine meshes gave sharp interfaces, which was similar to what is seen in reality. The difference turbulence models: standard k-ε model, k-ω model, k-ε RNG model and k-ε realizable model gave almost the same flow depths.

Keywords: Flow depth, velocity, open Venturi channel, hydraulic jump, energy loss

1 Introduction

Hydraulic jumps generate due to transition of the supercritical flow into the subcritical flow in an open Venturi channel (Welahettige *et al.*, 2017). In a hydraulic jump, a strong shear layer is formed at the toe of the wave (Hornung *et al.*, 1995). The resistance phenomena in an open channel can be explained by using the inner and outer layer theory (Ben, 2002). A constant value for the roughness coefficient is not recommended for an open channel flow (Konwar & Sarma, 2015). The Colebrook White explicit equation is comparatively suitable for friction handling about the unsteady varied flow and the tidal computations in an open channel (Ahmed, 2015). The level jump in a Venturi channel depends upon the fluid properties and the length of the flume (Berg *et al.*, 2015). There are few studies on flow depth parameters related to the open Venturi channel in literature. This study focused on the flow depth variation in an open Venturi channel for Newtonian fluid. Computational fluid dynamics (CFD) simulations were validated with experimental results (Welahettige *et al.*, 2017). ANSYS Fluent R16.2 commercial simulation tool was used for the simulations.

2 CFD models

The Volume of fluid (VOF) method was used for the simulations where phase interaction was based on the continuum surface force model and the phase localize compressive scheme (ANSYS, 2013). Equation. 1 gives the species mass balance. Here, α_2 is the water volume fraction, U is the three-dimensional velocity component, and U_r is the maximum velocity at the transition region. $\alpha_2\ (1-\alpha_2)$ is non zero only at the interface (Rusche, 2002), (Weller *et al.*, 1998) and (Ubbink, 1997).

$$\frac{\partial \alpha_2}{\partial t} + div\ (\alpha_2\ U) = -\ div\ (\alpha_2\ (1-\ \alpha_2)\ U_r). \quad (1)$$

The normalized wall roughness (K_s^+) is given as, (ANSYS, 2013), (Akan, 2006) and (Versteeg & Malalasekera, 2007):

$$K_s^+ = \rho\ K_s\ u^*/\ \mu. \quad (2)$$

$$u^* = C_\mu^{1/4} \kappa^{1/2}$$

Here, K_s is the physical roughness. $u^*$is a constant equal to 0.346. Here $C_\mu = 0.09$ is a k-ε model constant and $\kappa = 0.4$ is the von Karman's constant. Density (ρ) and viscosity (μ) are considered as,

$$\rho = \alpha_2\ \rho_2 + (1 - \alpha_2)\rho_1 \quad (3)$$

$$\mu = \alpha_2\ \mu_2 + (1 - \alpha_2)\ \mu_1. \quad (4)$$

Here, ρ_1 and ρ_2 are the densities of air and water. μ_1 and μ_2 are the viscosities of air and water.

Time discretization was based on the implicit Euler method for transient simulations. The semi implicit method for pressure linked equations (SIMPLE) scheme was used to calculate the pressure-velocity coupling. The hyperbolic partial differential equations were solved by using the second order upwind scheme (Versteeg & Malalasekera, 2007) and (ANSYS, 2013).

3 Geometry

Figure 1 shows a 3-D geometry that was used for the simulations. Boundaries were inlet, outlet, wall, and atmosphere. X-direction was the main flow direction, from the inlet to the outlet. The channel width was in Y-direction. The flow depth was measured in Z-direction. The main mesh contained 0.74 million computational cells. The elements near to the wall boundaries were modified by adding inflation layers.

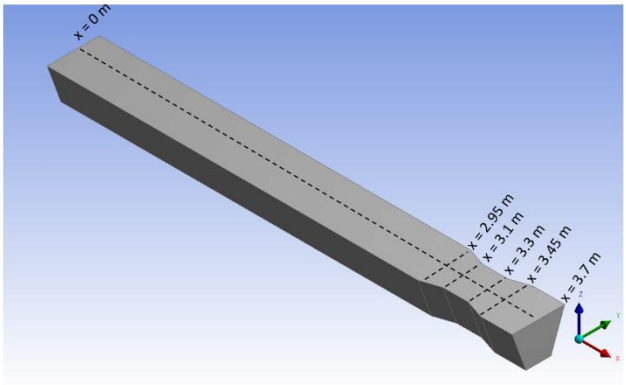

Figure 1. 3-D geometry of the trapezoidal channel; $x = 0$ m was defined as the inlet of the channel. The Venturi region was $x = 2.95$ m to $x = 3.45$ m. The bottom depth was 0.2 m for 0 m $< x <$ 2.95 m and 3.45 m $< x <$ 3.7 m. The bottom depth was 0.1 m for 3.1 m $< x <$ 3.3 m. The trapezoidal angle was 70˚.

4 Results and discussion

4.1 Flowrate and flow depth

Figure 2 shows flow depths along the channel central axis for different flow rates. The channel inclination angle was zero degrees (horizontal) for all the cases in Figure 2. Simulations were done for water the flow rates: 100 kg/min, 200 kg/min, 300 kg/min, 400 kg/min and 700 kg/min. The experimental water flow rate result, which was equal to 400 kg/min, was used for the validation (Welahettige *et al.*, 2017). The contraction region started at $x = 2.95$ m (see Figure 1). The flow depth increased with increased of the flow rate. The flow depth increment with the flow rates was not a linear relationship due to the geometry of the channel. Flow depth near to the contraction walls slightly increased in high flow rates (e.g. 700 kg/min). Low flow rates showed almost horizontal flow depths until the Venturi contraction walls (e.g. 200 kg/min). The flow depth was reduced from the end of the Venturi contraction to the outlet of the channel for all the cases. There were no barriers at the end of the channel and the channel expanded after the contraction. Therefore, flow condition was changed from subcritical to supercritical, when flow depth reduced at the end of the channel (Welahettige *et al.*, 2017). In generally, the channel at horizontal angle gives subcritical flow before the contraction and supercritical flow after the contraction for all flow rates. The flow transition from subcritical to supercritical occurs at the Venturi region for all flow rates (when the channel at horizontal angle).

Figure 3 shows the average velocities along the x-axis for different flow rates. The average water velocity was calculated by considering the average of all cell's velocities in the considered cross section (except air velocities in the cross section). Velocities before the contraction region were averagely constant in each cases. This was due to the constant flow depths in this region (see Figure 2). Velocity gradually increased after the Venturi region due to the flow depth reduction. According to Bernoulli's law, the potential energy converts into the kinetic energy in this region. Mass flow rate ($\dot{m}$) is given as

$$\dot{m} = \rho\, h \left(b + \frac{h}{\tan\theta}\right) \overline{U}. \qquad (5)$$

Here, b is the bottom width, θ is the trapezoidal angle, ρ is the density of water. Flow depth (h) and the average velocity perpendicular to the area ($\overline{U}$) are variables with the mass flow rate for a considered position. When the mass flow rate increases, both flow depth and flow velocity increase in the channel. Because of this, the high mass rates give higher flow depths and higher flow velocities compared to the low mass flow rates.

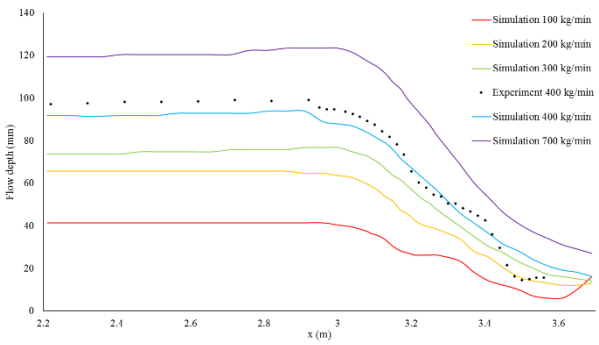

Figure 2. Flow depth changes along the channel centerline axis in the Venturi region for different flow rates. The channel inclination angle was zero degrees. The

experimental result was from (Welahettige et al., 2017) for 400 kg/min water flow rate.

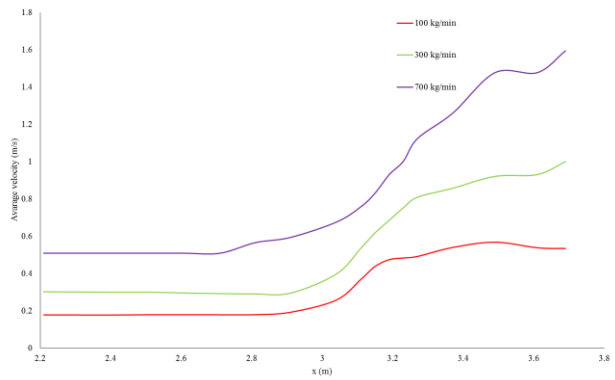

Figure 3. The average velocity along the x-axis for different water flow rates. The channel inclination angle was zero degrees for all cases. The average velocity was calculated as the average cross sectional velocity perpendicular to x-axis.

4.2 Different channel inclination angles and flow depths

Figure 4 shows the flow depth variation with the channel inclination angles. In this case, flow rate was 400 kg/min for all the cases. When the channel inclination angle was a negative value, a gravitational support added to the flow direction (x-direction). When the channel inclination angle was a positive value, a gravitational support added opposite to the flow direction. The highest flow depth was given before the Venturi contraction, when the channel inclination angle was +1.5 degree. In this region, flow became subcritical due to the barriers such that the contraction walls and the gravitation opposite force (only in the positive channel inclination cases). The channel at the horizontal angle, the flow depth was almost a flat surface. Because only the contraction walls hydraulic jumps were affected opposite to the flow direction, except the friction force. When the channel inclination angle was a negative value, the flow depth before the Venturi contraction reduced due to flow convert into the supercritical flow (Welahettige *et al.*, 2017). At -1.0 degree angle, the flow depth increased in the Venturi region due to the oblique jump propagation (Welahettige *et al.*, 2017). There was a level fluctuation in -0.7 degree angle case at $x = 2.2$ m. This was due to the hydraulic jump propagation. The flow depths after the Venturi showed almost equal values for all the angles because of all the cases reached to the supercritical flow condition at the end of the channel.

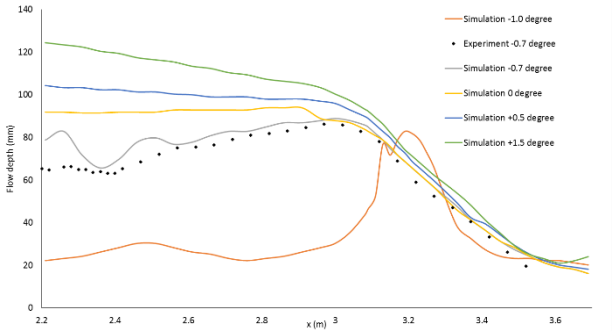

Figure 4. Flow depth change along the x-axis due to variation of channel inclination angles. The water flow rate was 400 kg/min. Flow depth was measured along the channel central axis. The experimental result was taken from (Welahettige *et al.*, 2017).

Figure 5 gives the average flow velocity for different inclination angles, the water flow rate at 400 kg/min. the high velocities for the negative inclination showed due to the supercritical flow behavior. There was a large difference of velocities between -1 degree case and horizontal case before the Venturi contraction. Even before the contraction walls; the flow reached to the supercritical condition in the negative inclination cases. However, there was no significant velocity difference after the contraction region in these cases. This was due to the fluid convert into the supercritical and the flow depths were averagely equal in all the cases.

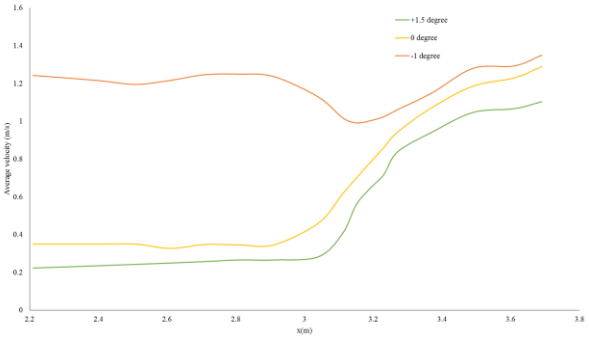

Figure 5. The average velocity along the x-axis for different channel inclination angles. The water flow rate was 400 kg/min.

4.3 Wall roughness height effect on flow depth

The wall roughness height related with wall friction and heat losses (ANSYS, 2013). Figure 6 shows the steady state water volume fraction for different the wall roughness values. The water flow rate was 400 kg/min and the channel at horizontal angle for all the cases. When the wall roughness height was increased, a hydraulic jump was generated before the Venturi region. In other words, toe of the hydraulic jump was moved to the upstream direction. This was due to increase of energy loss from the walls, when increased the wall roughness height. When energy loss increased, it could

not continue as a supercritical flow. Therefore, hydraulic jump moved to the upstream. Wall roughness height 0.000015 m was given a good matching with the experiment results.

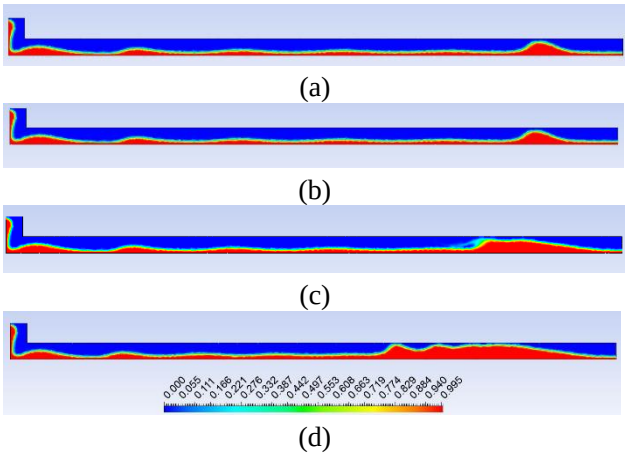

Figure 6. Steady state water volume fraction comparison for different wall roughness height. Water flow rate was 400 kg/min and the channel inclination angle was zero degrees; (a) Wall roughness height = 0 m, (b) Wall roughness height = 0.000015 m, (c) Wall roughness height = 0.0001 m, (d) Wall roughness height = 0.001 m.

4.4 Velocity distribution

The case with the flow rate 300 kg/min and the inclination angle zero degrees was used for the velocity distribution analysis. The average Reynolds number was approximately 46 000 and the flow was averagely turbulent. Air velocity was approximately zero above the water surface except at the interface. The VOF model solves a single momentum equation. Therefore, the interface has a same velocity for air and water. The water velocity at the wall was zero due to the no-slip boundary condition. Figure 7 shows water velocity magnitudes along the z-axis: before the Venturi contraction ($x = 2.51$ m), at the middle of Venturi ($x = 3.19$ m) and after the expansion of the Venturi ($x = 3.61$ m). The velocity distribution before the contraction walls were lower value compared to the other two locations because subcritical flow gave high flow depths and low velocities. The velocity increased from the bottom to the top in all the cases. This was due to the gradually reduction of friction from the bottom to the top.

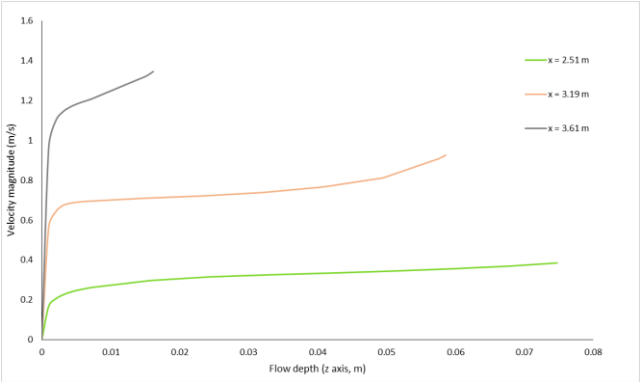

Figure 7. Water velocity magnitude along the vertical central lines in different location of the Venturi region; at x = 2.51 m (before the Venturi contraction), x = 3.19 m (at the middle of the Venturi), x = 3.61 m (after the Venturi expantion); The water flow rate was 300 kg/min and the channel inclination angle was zero degrees.

4.5 Mesh dependency evaluation

The mesh dependency evaluation was done with following meshes shown in Table 1. Total number of elements in a mesh was increased by reducing the maximum face size of cells.

Table 1. Mesh details for mesh dependency analysis: total number of elements and maximum face size

	Total number of elements	Maximum face size (mm)
01.	16 815	20
02.	23 217	15
03.	61 464	10
04.	104 910	8
05.	378 635	5
06.	159 8267	3

Figure 9 shows water volume fraction along the z-axis at $x = 3.19$ m for the different meshes. The coarse meshes (20 mm and 15 mm) gave wide range of interface variations. However, the fine meshes give sharp interfaces. In reality, there is very sharp interface between water and air. Therefore, the finer meshes gave more accurate results than the coarser meshes. This implies that mesh size is a critical factor for VOF simulations. It is recommended to have a fine mesh for small flow depths.

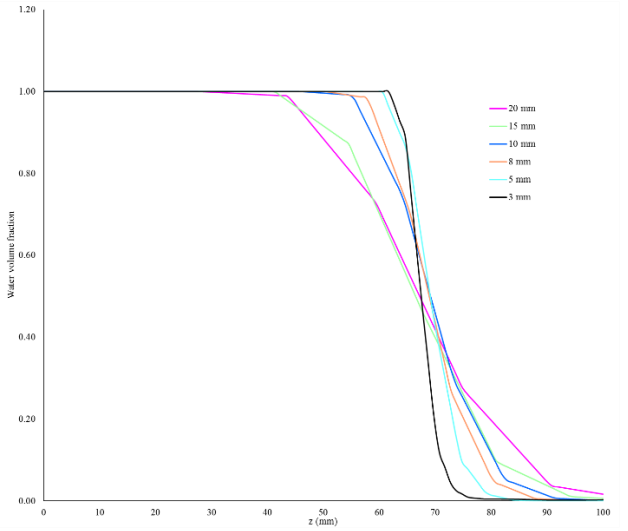

Figure 8. Mesh dependency analysis: The maximum cell face sizes in the meshes 20 mm, 15 mm, 10 mm, 8 mm, 5 mm and 3 mm: Water volume fraction along z-axis at $\boldsymbol{x = 3.19}$ m.

4.6 Effect of turbulence models on flow depth

Figure 7 shows water volume fraction along the y-axis for different turbulence models at $x = 3.19$ m. There was no significant effect for the flow depth from different turbulence models: standard k-ε model, k-ω model, k-ε RNG model and k-ε realizable model. At the steady state, all the turbulence models gave similar results. However, the standard k-ε model took higher computational time compared to the other turbulence models.

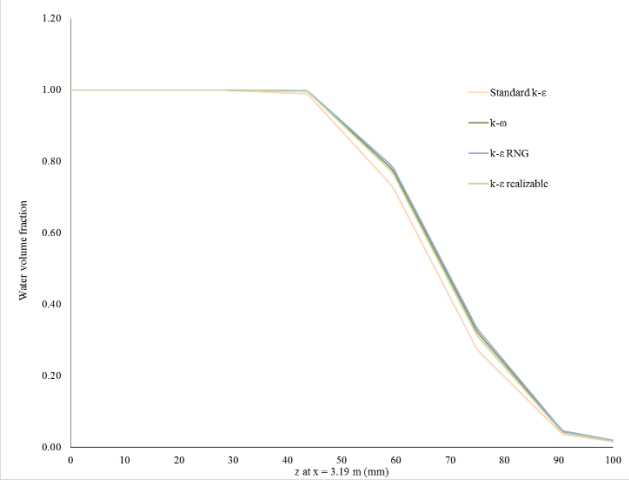

Figure 9. Water volume fraction along the z-axis at $\boldsymbol{x = 3.19}$ m for different turbulence model: Standard k-ε model, k-ω model, k-ε RNG model and k-ε realizable model.

4.7 Energy loss in a hydraulic jump

Figure 10 shows a hydraulic jump. There were large eddies propagation in a hydraulic jump. Hydraulic jump was very unstable due to the higher turbulence (Xiang *et al.*, 2014). A short and fine domain mesh (3 mm mesh in mesh dependency test) was used for the energy calculation. The flow rate was 400 kg/min and the channel inclination angle was -1.5 degree.

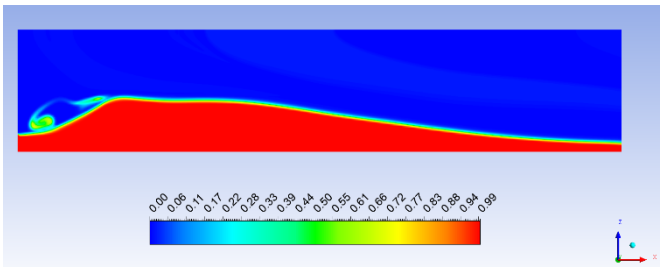

(a)

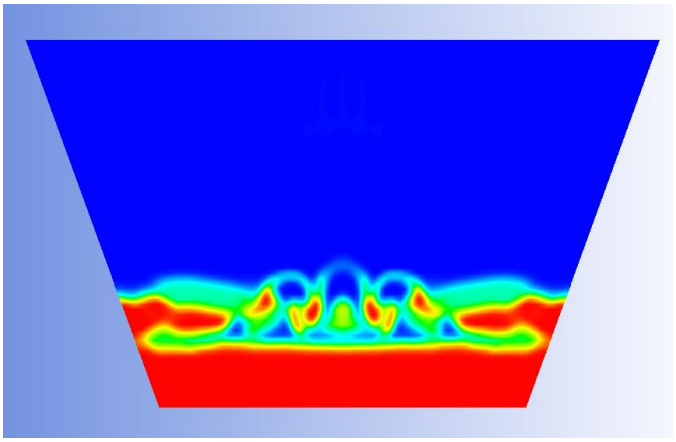

(b)

Figure 10. Water volume fraction of a hydraulic jump, (a) Central axis plane, (b) Channel cross sectional view at a hydraulic jump

The specific energy head (E_s) at a point can be given as the sum of the potential energy and the kinetic energy for 1-D system.

$$E_{s,1-D} = h + h_{hs} + \frac{\overline{U}^2}{2g} \quad (7)$$

Here, h is the flow depth, h_{hs} is the hydrostatic head, and $\overline{U}$ is the average flow velocity. The potential energy head was a sum of the flow depth and the hydrostatic head. The gravity point of the flow depth was assumed at the half of the flow depth. The specific energy difference before and after the hydraulic jump was due to the energy loss. The hydraulic jump approximately was in $x = 2.7$ m to $x = 2.85$ m. Specific energy head, kinetic energy head and potential energy head is shown in Figure 11. When the flow depth increased, the kinetic energy reduced in the hydraulic jump. The kinetic energy was predominant before started the hydraulic jump. Then it was drastically reduced in the hydraulic jump. This was due to the main flow kinetic energy participated to increase the turbulence kinetic energy. There was a head loss in the hydraulic jump, which was approximately 0.47 m in this case. The head

loss was due to the turbulence eddies finally converted into the internal energy.

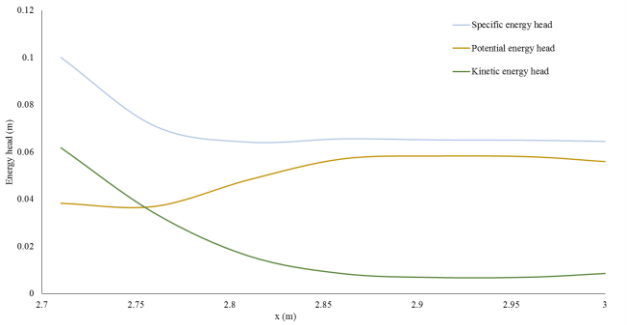

Figure 11. Energy loss in a hydraulic jump: specific energy head, potential energy head, and kinetic energy head.

This research study will be further extended into oil well drill mudflow analysis in an open Venturi channel.

5 Conclusions

The open Venturi channel at the horizontal angle gives a high flow depth before the contraction region. When the channel inclination angle is downward, the flow velocity increases and flow depth reduces. Because of this, flow becomes supercritical. The wall roughness height plays a significant role with the starting point of a hydraulic jump, due to the energy loss between wall and fluid. There is an energy loss in a hydraulic jump, when the supercritical flow transition into the subcritical flow. Fine mesh gives a sharp interface, which is similar with the reality. Turbulence models: Standard k-ε model, k-ω model, k-ε RNG model and k-ε realizable model give almost similar flow depths. However, standard k-ε model was taken higher computational time compared to the other models.

Acknowledgment

The economic support from The Research Council of Norway and Statoil ASA through project no. 255348/E30 “Sensors and models for improved kick/loss detection in drilling (Semi-kidd)” is gratefully acknowledged. As well as authors acknowledge to University College of Southeast Norway for giving resources for simulations.

References

Ahmed Z. (2015). *Review of friction formulae in open channel flow* Paper presented at the Eighteenth International Water Technology Conference, IWTC18

Akan O. (2006). *Open Channel Hydraulics*. Oxford: Butterworth-Heinemann.

ANSYS I. (2013). ANSYS Fluent Theory Guide.

Ben C. (2002). Open Channel Flow Resistance. *Journal of Hydraulic Engineering, 128*(1), 20-39. doi:doi:10.1061/(ASCE)0733-9429(2002)128:1(20)

Berg C., Malagalage A., Agu C., Kaasa G., Vaagsaether K. and Lie B. (2015). Model-based drilling fluid flow rate estimation using Venturi flume. *IFAC Workshop on Automatic Control in Offshore Oil and Gas Production, 2*, 177-182.

Hornung H., Willert C. and Turner S. (1995). The flow field downstream of a hydraulic jump. *Journal of Fluid Mechanics, 287*, 299-316. doi:10.1017/S0022112095000966

Konwar L. and Sarma B. (2015). Analysis and Verification of Resistance Co-Efficient with Different Flow Parameters Having Different Bed Conditions to Open Channel Flow. *International Advanced Research Journal in Science, Engineering and Technology, 2*(8), 106-110.

Rusche H. (2002). *Computational Fluid Dynamics of Dispersed Two-Phase Flows at High Phase Fractions.* (Doctor of Philosophy), University of London Exhibition Road, London.

Ubbink O. (1997). *Numerical prediction of two fluid systems with sharp interfaces.* (Degree of Doctor of Philosophy), Imperial College of Science, Technology & Medicine.

Versteeg H. and Malalasekera W. (2007). *An introduction to computational fluid dynamics: The finite volume method* (2 ed.). Harlow, England: Pearson Education.

Welahettige P., Lie B. and Vaagsaether K. (2017). Flow regime changes at hydraulic jumps in an open Venturi channel for Newtonian fluid. *The journal of computational multiphase flow, Accepted.*

Weller H., Tabor G., Jasak H. and Fureby C. (1998). A tensorial approach to computational continuum mechanics using object-oriented techniques. *Computers in Physics, 12*(6), 620-631. doi:http://dx.doi.org/10.1063/1.168744

Xiang M., Cheung S. C. P., Tu J. Y. and Zhang W. H. (2014). A multi-fluid modelling approach for the air entrainment and internal bubbly flow region in hydraulic jumps. *Ocean Engineering, 91*, 51-63. doi:https://doi.org/10.1016/j.oceaneng.2014.08.016

Paper 3

A solution method for 1D shallow water equations using FLIC scheme for open Venturi channels

This paper is published in The Journal of Computational Multiphase Flows.
Doi: 10.1177/1757482X18791895

Check for updates

Research article

The Journal of Computational Multiphase Flows

The Journal of Computational Multiphase Flows
0(0) 1–11
© The Author(s) 2018
Reprints and permissions:
sagepub.co.uk/journalsPermissions.nav
DOI: 10.1177/1757482X18791895
journals.sagepub.com/home/cmf
SAGE

A solution method for one-dimensional shallow water equations using flux limiter centered scheme for open Venturi channels

Prasanna Welahettige, Knut Vaagsaether and Bernt Lie

Abstract

The one-dimensional shallow water equations were modified for a Venturi contraction and expansion in a rectangular open channel to achieve more accurate results than with the conventional one-dimensional shallow water equations. The wall-reflection pressure–force coming from the contraction and the expansion walls was added as a new term into the conventional shallow water equations. In the contraction region, the wall-reflection pressure–force acts opposite to the flow direction; in the expansion region, it acts with the flow direction. The total variation diminishing scheme and the explicit Runge–Kutta fourth-order method were used for solving the modified shallow water equations. The wall-reflection pressure–force effect was counted in the pure advection term, and it was considered for the calculations in each discretized cell face. The conventional shallow water equations produced an artificial flux due to the bottom width variation in the contraction and expansion regions. The modified shallow water equations can be used for both prismatic and nonprismatic channels. When applied to a prismatic channel, the equations become the conventional shallow water equations. The other advantage of the modified shallow water equations is their simplicity. The simulated results were validated with experimental results and three-dimensional computational fluid dynamics result. The modified shallow water equations well matched the experimental results in both unsteady and steady state.

Keywords

Shallow water equations, wall-reflection pressure–force, total variation diminishing scheme, open Venturi channel, contraction and expansion walls, hydraulic jump, flow depth

Received 19 January 2018; accepted 3 May 2018

Introduction

The shallow water equations (SWEs) are used in various applications, such as river flow, dam break, open channel flow, etc. Compared to the 3D SWEs, 1D SWEs have a much lower cost in time-dependent simulations.[1] Kurganov et al.[2] introduced a semidiscrete central-upwind numerical scheme for solving the Saint-Venant equations, which is suitable for use with discontinuous bottom topographies.[3] This scheme avoids the breakdown of numerical computation when the channel is at dry or near dry states. Another computational difficulty is that small flow depth leads to enormous velocity values near the dry states.[3] By accurately calculating the wall-reflection pressure–force it is possible to prevent artificial acceleration of the flow.[4] Spurious numerical waves propagate when the time discretization step is too large.[5,6] The total variation diminishing (TVD) method does not allow to increase total variation in time.[7] According to Toro,[7] the centered TVD scheme consists of a flux limiter blending of the FORCE scheme and the Richtmyer scheme. High-resolution schemes and flux limiters are suitable for avoiding

Department of Process, Energy, and Environmental Technology, University College of Southeast Norway, Porsgrunn, Norway

Corresponding author:
Prasanna Welahettige, University College of Southeast Norway, Høgskolen i Sørøst-Norge, Kjølnes Ring 56, Porsgrunn, Telemark 3918, Norway.
Email: prasanna.welahettige@usn.no

Creative Commons Non Commercial CC BY-NC: This article is distributed under the terms of the Creative Commons Attribution-NonCommercial 4.0 License (http://www.creativecommons.org/licenses/by-nc/4.0/) which permits non-commercial use, reproduction and distribution of the work without further permission provided the original work is attributed as specified on the SAGE and Open Access pages (https://us.sagepub.com/en-us/nam/open-access-at-sage).

phase error for monotone solutions.[8] Partial differential equations can be solved by splitting them into a hyperbolic problem and a source problem.[7] In the operator-splitting approach, the eigenvector projection and improved approaches are used for source term treatments.[9] An open Venturi channel on the horizontal plane gives a subcritical flow regime before the Venturi contraction walls, and the flow regime changes from critical to supercritical after the Venturi expansion walls.[10] As far as we know, a possibility of use of the flux limiter centered (FLIC) scheme for solving the 1D SWE at unsteady and steady states for nonprismatic channels is not available in the literature. The paper addresses this area with some modifications of SWE.

The underlying assumptions of 1D SWE are summarized as follows: velocity is uniform in the cross-section, water level in the cross-section is presented as a horizontal line, vertical acceleration is negligible, and streamline curvature is small. Therefore, pressure can be considered to be hydrostatic pressure.[11] Based on the conservation of mass and momentum, the Saint-Venant system of the conventional SWE can be written as[12,13]

$$\frac{\partial A}{\partial t} = -\frac{\partial (Au)}{\partial x} \tag{1}$$

$$\frac{\partial (Au)}{\partial t} = -\frac{\partial \left(Au^2\right)}{\partial x} - \frac{\partial (Ah)}{\partial x} g + Ag\sin\alpha - AgS_f \tag{2}$$

Here, A is the cross-sectional area perpendicular to the x-direction, u is the velocity, h is the flow depth, g is the acceleration due to gravity, α is the channel inclination angle, and S_f is the friction slope.

Here, modified SWEs are developed for the Venturi contraction and expansion for a rectangular channel. The centered TVD scheme is used for solving the modified SWE. MATLAB R2017a was used for the 1D simulations. The experiments were carried out in a trapezoidal open Venturi channel. The developed model is validated through experimental results without using analytical results. The paper proceeds from conventional SWE ("Modified 1-D SWEs for open Venturi channel" section) to the model development of modified SWE ("Centered TVD method for the modified 1D SWEs") and the implementation of the TVD scheme for the modified SWE. The modified equations are then compared to the conventional SWE and validated with experimental results.

Modified 1D SWEs for open Venturi channel

A rectangular open Venturi channel is used for model development. The principle sketch is shown in Figure 1. The channel has a continuous bottom topography. In the Venturi section, the bottom width of the channel varies in the x-direction. The walls are perpendicular to the bottom surface. The inlet of the channel is defined at $x = 0$ m. The walls are stationary. A control volume is shown in the Venturi contraction region.

Model development

Figure 2 shows a spatial and time discretized grid for one time step, which is based on the finite volume method.[14] n is the time index, $n \in \{1, 2, \ldots, N\}$. At time $t = n$, x coordinates are discretized. j is the node index in the spatial grid, $j \in \{1, 2, \ldots, l\}$. We assume that Δx is a constant for all cells. The aim of an iteration step is to find the conserved variables at time $t = n + 1$ and $x = j$ from $t = n$ variable values. Time step is variable and is defined as $\Delta t = t^{n+1} - t^n$.

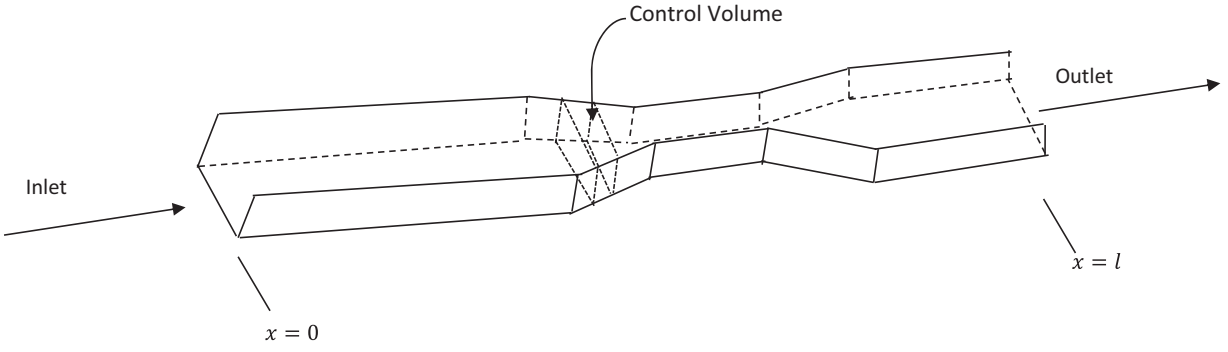

Figure 1. Principle sketch of the open Venturi channel with a rectangular cross-section. The selected control volume is in the Venturi contraction region. The top surface is open to the atmosphere.

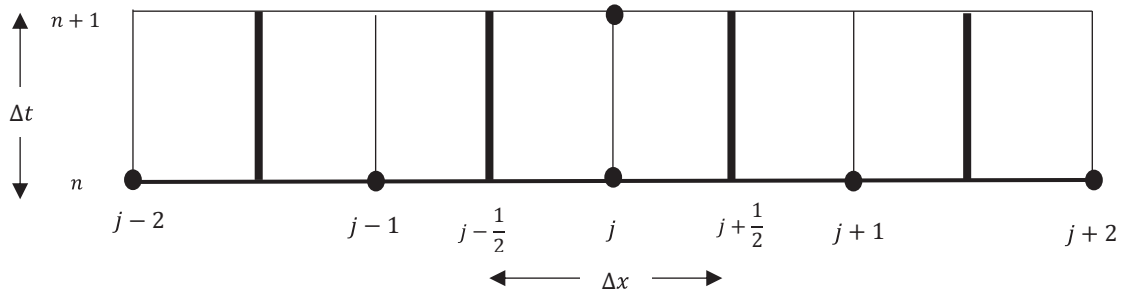

Figure 2. Semidiscretized grid, spatial discretization presented with *j*-notations, and time discretization presented with *n* notations.

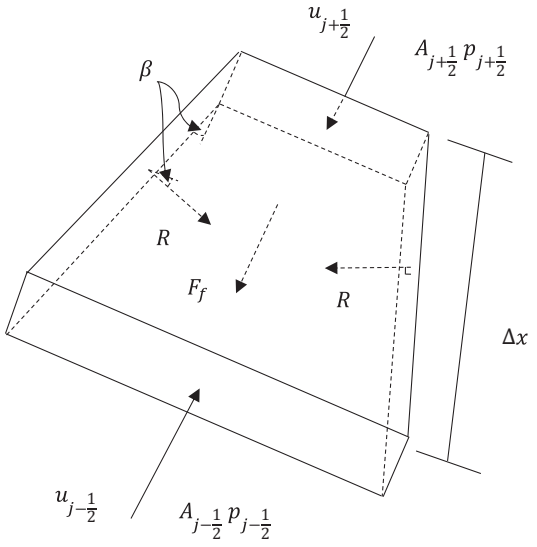

Figure 3. Forces on the control volume in the *x*-direction, gravitational force is not shown.

The model emphasizes the impact of contraction and expansion walls. The control volume is in the Venturi contraction region to consider a maximum number of boundaries. Figure 3 shows the forces acting on the control volume in the *x*-direction. The gravitational and the bottom wall-reflection forces act in the *z*-direction and are not shown. If there is a channel downward inclination, a portion of the gravitational support is added in the *x*-direction. The height of the control volume is equal to the flow depth, which varies from the inlet to the outlet of the control volume. Therefore, the inlet area (A_j) and the outlet area (A_{j+1}) are not equal. Changes in flow depth from the inlet to the outlet are assumed to be linear at any given time. *R* is the reflection pressure–force coming from the side boundaries. This component is not included in the conventional 1D SWE (see equation (2)). Sanders and Iahr[4] noticed that the hydrostatic force coming from the channel walls in nonprismatic channels needs to be treated with precision, in order to avoid an artificial acceleration of the flow in the calculation. *R* acts in the *y*-direction only if there are no contraction or expansion regions. Therefore, the 1D conventional SWE can be applied to prismatic channels without any issue. Here, we assumed that the 1D conventional SWE does not consider the pressure–force coming from the sidewalls in $\frac{\partial(Ah)}{\partial x}g$. Easy numerical calculation and accurate pressure–force calculation are the advantages of having a separate term for the reflection pressure–force coming from the sidewalls. The wall-reflection pressure–force is equal to the hydrostatic pressure acting on the wall. *R* is acting perpendicular to the sidewalls. According to the assumption that the changes in flow depth from the inlet to the outlet of the control volume are linear, we can assume that the wall-reflection pressure–forces coming from each of the two sidewalls of the control volume are equal. Here, F_f is the resultant friction force from both sidewalls and the bottom surface. β is the contraction angle of the control volume

$$\tan\beta = \frac{\Delta b}{2\Delta x}$$

$$\Delta b = \; b_{i-\frac{1}{2}} - b_{i+\frac{1}{2}}$$

b is the bottom width of the channel. For a contraction and an expansion region, the sign of the Δb value becomes negative and positive, respectively. The sign of the Δb determines the sign of *R*. *R* acts opposite to the flow direction in a contraction region and in support of the flow direction in an expansion region.

Fundamental conservation laws are used for model development; the temperature is assumed to be constant at room temperature, and density is also assumed to be constant. Two conservation equations are produced by applying mass and momentum balances to the control volume. There is no difference in the mass balance equation compared to the conventional SWE, which is equal to equation (1). Applying the momentum balance to the control volume

$$\frac{\partial(mu)_j}{\partial t} = (\dot{m}u)_{j-\frac{1}{2}} - (\dot{m}u)_{j+\frac{1}{2}} + \sum_i F_i \tag{3}$$

Here, m is the mass, u is the velocity, and F is the force. The x-directional forces acting on the control volume are pressure–force F_p, gravitational force F_g, friction force F_f, sidewall-reflection pressure–force F_R, and other external forces F_e. Assuming there are no other external forces working on the control volume, $F_e = 0$.

The pressure applied to the cross-section is a sum of atmospheric pressure and hydrostatic pressure. Atmospheric pressure is balanced from both sides of the cell faces as well as the top and bottom surfaces. The resultant hydrostatic pressure–force coming from the adjacent control volumes is

$$F_p = k_g\left((Ah)_{j-\frac{1}{2}} - (Ah)_{j+\frac{1}{2}}\right)\rho g$$

k_g is the ratio between the gravity height of the cross-sectional area to the flow depth. In this study, it is assumed that the gravity of the flow depth is half of its total height for a rectangular cross-sectional area. F_p is not included as all pressure–forces apply on the control volume in the x-direction. If the channel is a prismatic channel, F_p includes all pressure–forces that act on the control volume in the x-direction. Therefore, as explained above, the wall-reflection pressure–force coming from the sidewalls needs to be considered for nonprismatic channels

$$F_R = -2R\sin\beta = -2\sin\beta\int_0^{A_{sw,j}} p_{sw}\mathrm{d}A \tag{4}$$

Here, A_{sw} is the sidewall area of the control volume (one side). p_{sw} is equal to the hydrostatic pressure acting on the sidewall. According to the assumptions, flow depth variation is linear from the inlet to the outlet of the control volume; therefore, average values can be used for the wall-reflection pressure–force and the area of the sidewalls, respectively

$$F_R \approx -2\overline{p}_{sw,j}\overline{A}_{sw,j}\sin\beta \tag{5}$$

The central differencing approach for the flow depth of a channel with a rectangular cross-section, $h_j = \frac{h_{j+\frac{1}{2}}+h_{j-\frac{1}{2}}}{2}$, leads to

$$\overline{A}_{sw,j} = h_j\frac{\Delta x}{\cos\beta}$$

$$\overline{p}_{sw,j} = k_g h_j \rho g$$

F_R becomes

$$F_R = -2k_g\Delta x h_j^2\rho g\tan\beta \tag{6}$$

When the channel has an inclined plane, a gravitational force acts with or against the flow direction. α is the channel inclination angle. When the channel inclines downward, α has a negative sign and the gravitational force acts with the direction of the flow. When the channel inclines upward, α has a positive sign and the gravitational force acts against the direction of the flow. The sign of F_g is decided by α. V is the volume of the control volume and is a function of b, h, and x at any given time. The accurate volume calculation of the control volume is a very important step in identifying the different flow regimes in open nonprismatic channels.[10] The friction slope S_f gives the boundary friction force per unit weight of liquid present in the open channel.[12] According to Manning's formula, the friction slope of the open channel can be presented as[12]

$$S_f = \frac{k_M^2}{k_n^2 r_{h,j}^{4/3}}u_j^2$$

Here, k_M is the Manning roughness factor, r_h is the hydraulic radius, and $k_n = 1.0\ \mathrm{m}^{1/3}\ \mathrm{s}^{-1}$ is the unit corrector. For a rectangular channel, the hydraulic radius is $\frac{bh}{b+2h}$. By substituting momentum and force terms into equation (3), the modified momentum balance equation can be stated as

$$\begin{aligned}\frac{\partial(Au)}{\partial t} = &-\frac{\partial\left(Au^2\right)}{\partial x} - k_g\frac{\partial(Ah)}{\partial x}g \\ &+ k_g h^2 g\frac{\partial b}{\partial x} + Ag\left(\sin\alpha - S_f\right)\end{aligned} \tag{7}$$

Compared to the conventional shallow water momentum balance equation, equation (2), the expression $2k_g h^2 g\frac{\partial b}{\partial x}$ is added to the new equation. The new term is related to the wall-reflection pressure–force in that it becomes zero when there is no contraction or expansion in the channel (when $\frac{\partial b}{\partial x} = 0$). In general, this term is only active in contraction or expansion regions.

Free falling at the end of the channel

In the experimental setup, the channel end was open, and the water was unhindered in flowing out of the channel. Accordingly, in the simulation, the physics of the last cells at the channel end needed to be modified with free falling properties. There is no friction effect when water does not touch the walls. Therefore, $S_f = 0$, and a high gravitational force was

added to the flow direction at the end of the channel. This effect is described by angle α, and it reaches to 70°–90°.

Centered TVD method for the modified 1D SWEs

The conservation equations are based on a rectangular open Venturi channel. The bottom width $b(x)$ is only a function of x. The velocity, $u(x,b,t)$ and the flow depth $h(x,b,t)$ are functions of x, $b(x)$, and time t. The modified SWE (equations (1) and (3)) can be stated for a rectangular channel

$$\frac{\partial\, h}{\partial t} = -\frac{1}{b}\frac{\partial(hub)}{\partial x} \tag{8}$$

$$\frac{\partial(hu)}{\partial t} = -\frac{1}{b}\frac{\partial\left(b\dfrac{(hu)^2}{h}\right)}{\partial x} - \frac{1}{2b}\frac{\partial\left(bh^2\right)}{\partial x}g + \frac{1}{2b}h^2 g\frac{\partial b}{\partial x} + hg\left(\sin\alpha - \frac{k_M^2}{k_n^2}\left(\frac{b+2h}{bh}\right)^{\frac{4}{3}}\left(\frac{hu}{h}\right)^2\right) \tag{9}$$

In equation (9), $\frac{\partial b}{\partial x}$ is approximately equal to $2\tan\beta$, when Δx is not very small. It reduces the complexity of hyperbolic equation solving and allows for easy comparison with the conventional SWE. The compact form of the transport equations is

$$\mathbf{U}_t + \frac{1}{b}\mathbf{F}(\mathbf{U})_x = \frac{1}{b\Delta x}\mathbf{S}_1(\mathbf{U}) + \mathbf{S}(\mathbf{U}) \tag{10}$$

Here

$$\mathbf{U} = \begin{pmatrix} h \\ hu \end{pmatrix} = \begin{pmatrix} u_1 \\ u_2 \end{pmatrix},$$

$$\mathbf{F}(\mathbf{U}) = \begin{pmatrix} hub \\ b\dfrac{(hu)^2}{h} + \dfrac{gbh^2}{2} \end{pmatrix} = \begin{pmatrix} bu_2 \\ \dfrac{bu_2{}^2}{u_1} + \dfrac{gbu_1{}^2}{2} \end{pmatrix},$$

$$\mathbf{S}_1(\mathbf{U}) = \begin{pmatrix} 0 \\ h^2 g\dfrac{\Delta b}{2} \end{pmatrix} = \begin{pmatrix} 0 \\ \dfrac{\Delta b}{2}gu_1^2 \end{pmatrix},$$

$$\mathbf{S}(\mathbf{U}) = \begin{pmatrix} 0 \\ hg\left(\sin\alpha - \dfrac{k_M^2}{k_n^2}\left(\dfrac{b+2h}{bh}\right)^{4/3}\left(\dfrac{hu}{h}\right)^2\right) \end{pmatrix} = \begin{pmatrix} 0 \\ u_1 g\left(\sin\alpha - \dfrac{k_M^2}{k_n^2}\left(\dfrac{b+2u_1}{bu_1}\right)^{4/3}\left(\dfrac{u_2}{u_1}\right)^2\right) \end{pmatrix} \tag{11}$$

Here, $\mathbf{U}$ is the column vector of the conserved variables: u_1 and u_2. $\mathbf{F}(\mathbf{U})$ is the x-directional column vector of the fluxes. $\mathbf{S}(\mathbf{U})$ is the column vector of the source terms. The new term, which is the wall-reflection pressure–force, is presented as an extra source term, $\mathbf{S}_1$. The sidewall-reflection pressure–force effect is part of the pure advection term. However, it is written as a source term for the sake of easy numerical calculation. The pure advection term (advection flux and wall-reflection effect) is solved first with the centered TVD method. The source term is then solved with an ordinary differential equations (ODE) solver, the explicit Runge–Kutta fourth-order method. The initial condition for the ODE solver is the solution coming from the centered TVD scheme. Here, we emphasize the solving of the TVD scheme (not the ODE solving), because it is included in the wall-reflection pressure–force term. The variation of the bottom width (b) presents the channel contraction and expansion effects numerically. The bottom-width variation effect is highlighted in the TVD solving method used here, compared to the conventional TVD solving method. The pure advection term is solved as

$$\mathbf{U}_j^{n+1} = \mathbf{U}_j^n - \frac{\Delta t}{b_j\Delta x}\left[\mathbf{F}(\mathbf{U})_{j+\frac{1}{2}}^n - \mathbf{F}(\mathbf{U})_{j-\frac{1}{2}}^n - \mathbf{S}_1(\mathbf{U})_j^n\right] \tag{12}$$

The source term is solved as

$$\mathbf{U}_j^{n+1} = \mathbf{U}_{j,TVD}^{n+1} + \Delta t\mathbf{S}\left(\mathbf{U}_{j,TVD}^{n+1}\right) \tag{13}$$

Here, $\mathbf{U}_{j,TVD}^{n+1}$ is the solution coming from the TVD method. The FLIC scheme is used to calculate the flux of the cell face[7]

$$\mathbf{F}(\mathbf{U})_{j+\frac{1}{2}}^n = \mathbf{F}(\mathbf{U})_{j+\frac{1}{2}}^{n,LO} + \varnothing_{j+\frac{1}{2}}\left[\mathbf{F}(\mathbf{U})_{j+\frac{1}{2}}^{n,HO} - \mathbf{F}(\mathbf{U})_{j+\frac{1}{2}}^{n,LO}\right] \tag{14}$$

Here, *HO* is the high-order flux, and *LO* is the low-order monotone flux. The Richtmyer scheme (*RI*) is used

to calculate the high-order flux, and the FORCE scheme is used to calculate the low-order flux. $\varnothing$ is the flux limiter function. The high-order flux can be calculated as[8]

$$\mathbf{F}(\mathbf{U})_{j+\frac{1}{2}}^{n,HO} = \mathbf{F}\left(\mathbf{U}_{j+\frac{1}{2}}^{n,RI}\right) \tag{15}$$

$$\mathbf{U}_{j+\frac{1}{2}}^{n,RI} = \frac{1}{2}[\mathbf{U}_j^n + \mathbf{U}_{j+1}^n] + \frac{\Delta t}{2b_{j+\frac{1}{2}}\Delta x}\left[\mathbf{F}\left(\mathbf{U}_j^n\right) - \mathbf{F}\left(\mathbf{U}_{j+1}^n\right)\right] \tag{16}$$

The low-order flux is based on the FORCE scheme[7]

$$\mathbf{F}(\mathbf{U})_{j+\frac{1}{2}}^{n,LO} = \mathbf{F}(\mathbf{U})_{j+\frac{1}{2}}^{n,FORCE} = \frac{1}{2}\left[\mathbf{F}(\mathbf{U})_{j+\frac{1}{2}}^{n,LF} + \mathbf{F}\left(\mathbf{U}_{j+\frac{1}{2}}^{n,RI}\right)\right] \tag{17}$$

The Lax–Friedrichs (LF) scheme can be presented as[7]

$$\mathbf{F}(\mathbf{U})_{j+\frac{1}{2}}^{n,LF} = \frac{1}{2}\left[\mathbf{F}\left(\mathbf{U}_j^n\right) + \mathbf{F}\left(\mathbf{U}_{j+1}^n\right)\right] + \frac{b_{j+\frac{1}{2}}\Delta x}{2\Delta t}[\mathbf{U}_j^n - \mathbf{U}_{j+1}^n] \tag{18}$$

The SUPER-BEE flux limiter ($\varnothing$) is used as the flux limiter.[7,15] The cell face flux depends on the value of flow parameter r, which is the flux limiter function. The general idea of r is that it is the ratio of upwind change to local change. Here, a total energy-based method is used to calculate these changes. q is defined as the total energy per unit mass which is the sum of potential and kinetic energies per unit mass

$$q = \frac{1}{2}hg + \frac{1}{2}u^2 = \frac{1}{2}u_1 g + \frac{1}{2}\left(\frac{u_2}{u_1}\right)^2 \tag{19}$$

Time step is related to wave propagation speed. S_{max} is the maximum wave propagation speed. The wave propagation speed is calculated from the Froude number. The time step can be calculated as

$$S^n{}_{max} = max\left(abs\left(u_j + \sqrt{h_j g}\right)\right), \quad \forall \text{ j} \tag{20}$$

$$\Delta t = \frac{c_{max}\ \Delta x}{S^n{}_{max}} \tag{21}$$

According to the observations, Courant numbers higher than 0.7 led to high numerical diffusions at $\Delta x = 0.01$ m. A constant time step gave very diffusive and inaccurate results; therefore, a variable time step was used instead.

Modified versus conventional SWEs for open Venturi channels

To compare the advantages of the modified SWE over conventional SWE, measurements and data from the experimental setup are used to supply the necessary variables. The results validate the modification. In the next section, the calculated results will further be compared to the measured results of the experiment as well as to the modeled results of 3D computational fluid dynamics (CFD). A more detailed description of the experimental setup will be given in section 6; here we only consider the values necessary for the calculations.

The total length of the channel is 3.7 m. The Venturi contraction region is $2.95\,\text{m} < \text{x} < 3.1$ m, and the expansion region is $3.3\ \text{m} < \text{x} < 3.45$ m. The width of the channel along the x-axis is given as

$$0\ \text{m} \le x \le 2.95\ \text{m}: \quad b = 0.2\ \text{m},$$

$$2.95\ \text{m} < x < 3.1\ \text{m}: \quad b = 0.2 - \frac{x - 2.95}{1.5},$$

$$3.1\ \text{m} \le x \le 3.3\ \text{m}: \quad b = 0.1\ \text{m},$$

$$3.3\ \text{m} < x < 3.45\ \text{m}: \quad b = 0.1 + \frac{x - 3.3}{1.5},$$

$$3.45\ \text{m} \le x \le 3.7\ \text{m}: \quad b = 0.2\ \text{m}$$

At initial conditions, the whole channel was filled with water, and all the node points were measuring the same flow depth and zero velocity. According to this condition, there was no flux propagation. However, in the contraction and expansion regions, the conventional SWE produced a flux difference, because of $\frac{\partial(Ah)}{\partial x}g = h^2 g\frac{\partial b}{\partial x}$ for constant h. At constant flow depth and zero velocity, the expression $\frac{\partial b}{\partial x}$ can erroneously produce a flux gradient in a contraction or an expansion region. This is because the conventional SWE do not account for the wall-reflection pressure–force effect. In the modified SWE, this error is avoided by considering the wall-reflection pressure–force effect in the pure advection term.

Figure 4 shows a comparison between conventional SWE and modified SWE results after 0.01 s. The initial flow depth was 100 mm in the whole channel with zero velocity. At the contraction and expansion regions, flow depths and velocities change considerably in the conventional SWE. Moreover, these variations expand with time and extend into the whole channel. This error produces inaccurate results.

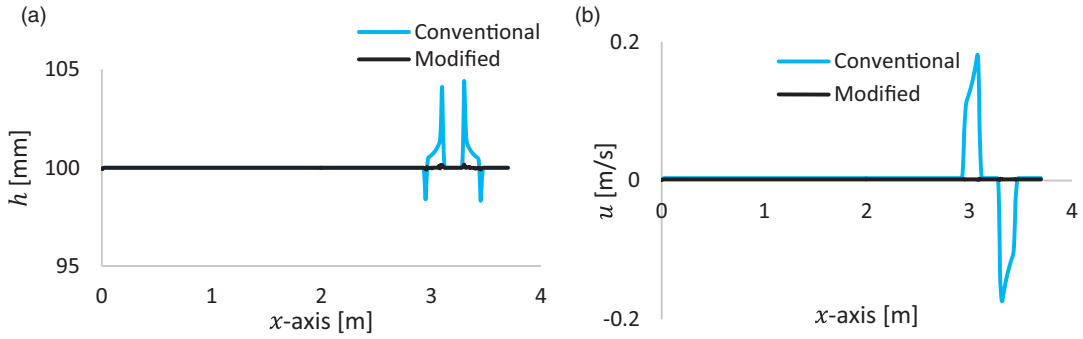

Figure 4. Comparison between conventional and modified SWE with zero velocity and constant flow depth in the whole channel at initial conditions. Results after 0.01 s: (a) flow depth along the *x*- axis and (b) velocity along the *x*- axis.

Model validation

The calculated results for the modified SWE are further validated by experimental and 3D CFD results.

Model validation with experimental results

The open Venturi channel used for the experimental model validation was located at University College of Southeast Norway. Level transmitters were located along the central axis of the channel. The transmitters were movable along the axis. The accuracy of the Rosemount ultrasonic 3107 level transmitters was ±2.5 mm for a measured distance of less than 1 m.[10] The channel had a trapezoidal shape with a trapezoidal angle of 70°. In modeling and simulations, a rectangular channel was used with all the other dimensions equal to the experimental setup. All of the experimental values presented in this paper are average values of sensor readings taken over a period of 5 min at each measuring point. It is possible to change the channel inclination angle (α); negative values for α indicate a downward inclination.

From the inlet, water was added to the channel at the horizontal plane ($\alpha = 0^{\circ}$) until the flow reached quasi-steady state while the outlet was kept open. Figures 5 and 6 show the comparison of simulated and experimental results. The constant flow rate at the inlet was 6.67 kg/s. Flow depth and velocity at the inlet were constant values of, respectively, 100 mm and 0.33 m/s, which were approximately equal to the inlet conditions of the experimental setup. The last five computation cells had free falling properties to account for the free falling water at the end of the channel of the experimental setup. The wall-reflection pressure–force coming from the Venturi contraction walls could be clearly observed while the channel was at the horizontal plane. In this condition, the gravitational force is zero. When water collapsed onto the Venturi contraction walls, a hydraulic jump was propagated. The hydraulic jump travelled upstream until it reached the inlet. With the channel at the horizontal plane, this hydraulic jump propagation was caused only by the wall-reflection pressure–force and friction–force effects.[10,16] According to the critical depth calculation in Welahettige et al.,[10] the average critical flow depth before the contraction region is 48.4 mm. Figure 5 shows a dynamic situation of the flow profile. The contraction wall-reflection pressure–force acts opposite to the flow direction. This is the reason for the hydraulic jump travelling upstream. The wall-reflection pressure–force causes the flow regime to change from supercritical flow to subcritical flow in the hydraulic jump.[16] The wall-reflection pressure–force coming from the contraction walls reduces the speed of the upstream flow, which causes the change in the flow regime.

Figure 6 shows the quasi-steady state results, following Figure 5. The flow depth comparison between the simulated and the experimental results in Figure 6(a) indicates the accuracy of the modified SWE. The modified SWE result is well matched with the experimental results compared to the conventional SWE. The channel at the horizontal plane, the Venturi contraction can cause a significant change in the flow regime. According to the flux calculation in the contraction and the expansion regions, the results from the conventional SWE deviated from the experimental results at quasi-steady state. The wall-reflection pressure–force coming from the contraction walls changed the flow regime from supercritical to subcritical, whole channel section before the contraction region. The velocity profile in Figure 6(b) can be used to explain the wall-reflection pressure–force effect in the Venturi expansion region. At the expansion region ($3.3 < x < 3.45$ m), the velocity drastically increased due to the wall-reflection pressure–force effect. At the channel expansion, the wall-reflection pressure–force effect comes in support of the flow

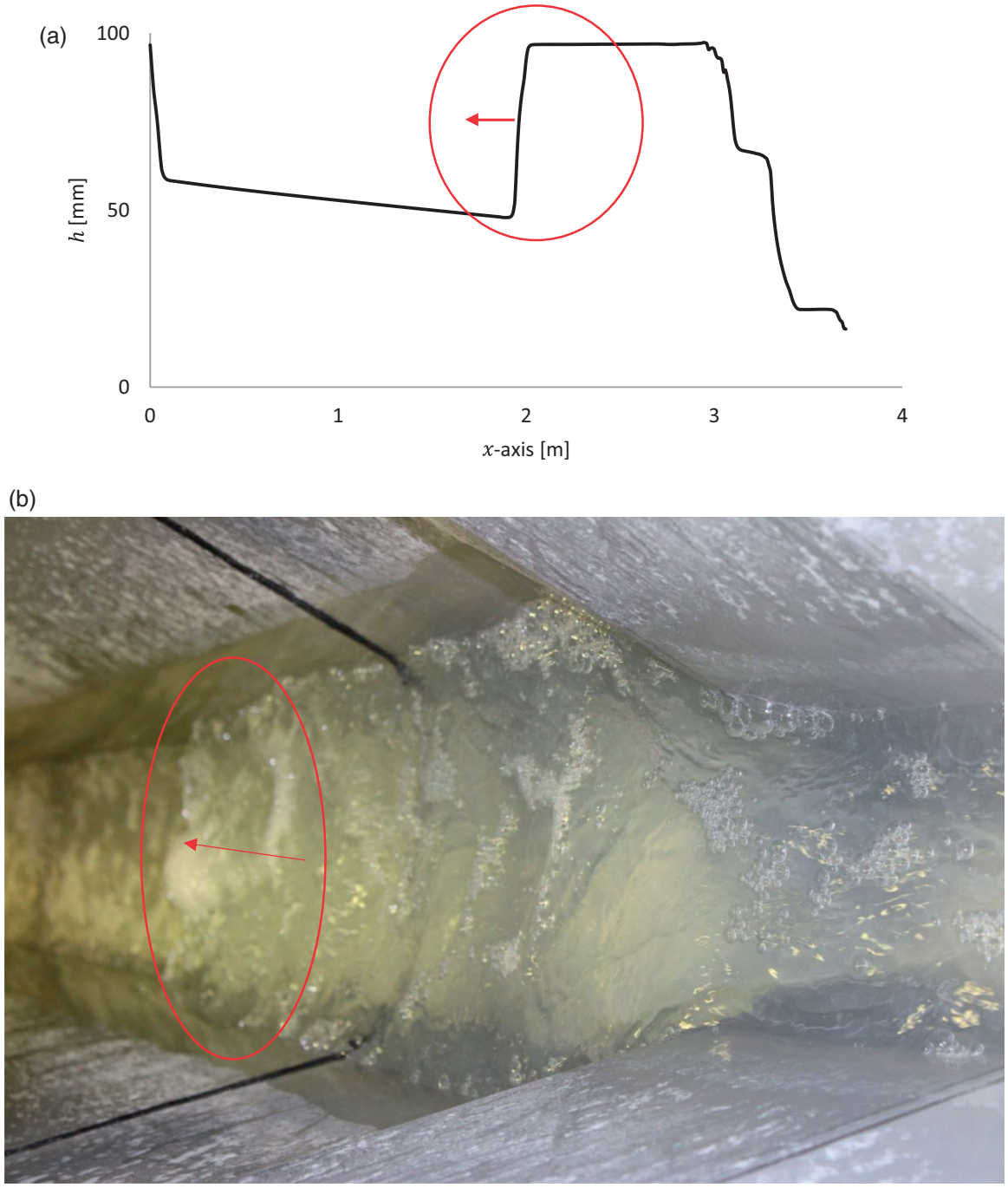

Figure 5. The hydraulic jump is moving upstream due to the wall-reflection pressure–force effect coming from the Venturi contraction walls, a dynamic result after 8.9 s. The arrows show the traveling direction of the hydraulic jump. The flow direction is opposite to the direction of the arrow. (a) The simulated flow depth result along the central axis and (b) the experimental results.

direction, which results in increased velocity. Before the contraction region ($x < 2.95$ m), the velocity reduced compared to the expansion region. This indicates the sign of the wall-reflection pressure–force: at the Venturi contraction region the sign is negative, and at the Venturi expansion region it is positive.

Model validation with 3D CFD result

Further, the result of the modified SWE result was compared to a CFD result.[16] Three-dimensional CFD simulations are based on the volume of fluid method. Water and air are the materials in the fluid domain. An artificial compression term is activated at the

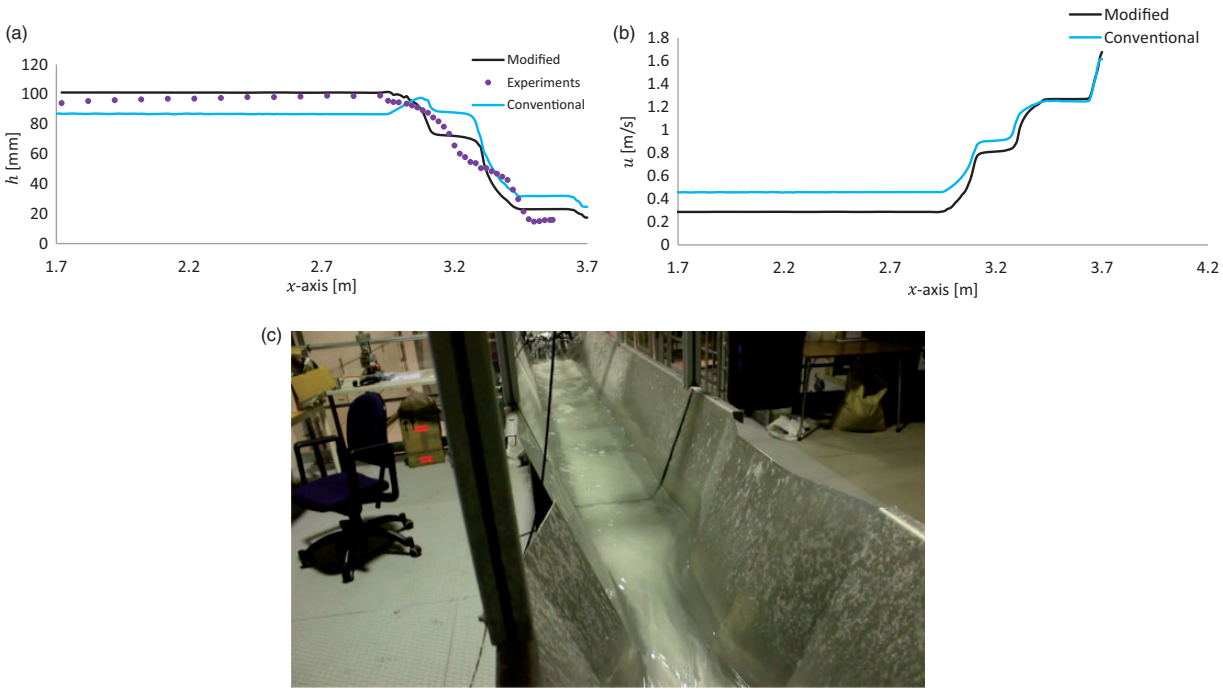

Figure 6. Quasi-steady state results, flow rate at 400 kg/min; (a) The simulated flow depth results along the central axis, (b) the simulated velocity results along the central axis, and (c) the experimental result.

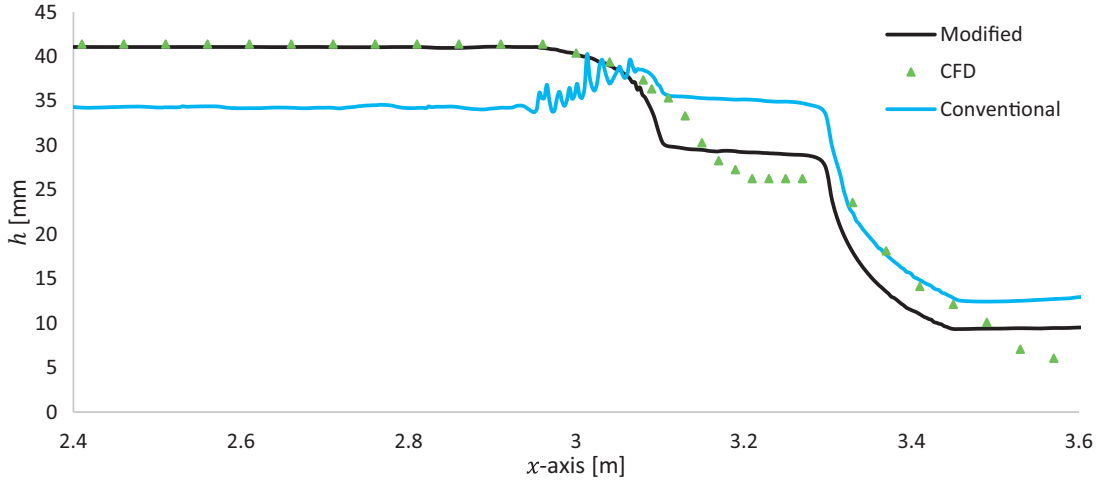

Figure 7. A comparison with 3D CFD result with the modified and the conventional shallow water results, quasi-steady state, the flow rate at 100 kg/min. The CFD result is from Welahettige et al.[16] CFD: computational fluid dynamics.

interface.[17–19] Time discretization is based on the implicit Euler method for a transient calculation. Pressure–velocity coupling is based on the SIMPLE scheme with a second-order upwind correction. The standard k–ε model is used for the turbulence handling. Wall surface roughness is used to calculate the wall friction, which is 15 μm. The mesh contains 0.74 million elements with a maximum cell size of 10 mm. ANSYS Fluent 16.2 (commercial code) was used as the simulation tool.[10,16] The 3D CFD study was done with the same experimental setup for 100 kg/min flow rate. The quasi-steady state results are shown in Figure 7. The modified SWE result was well matched with the CFD result compared to the conventional SWE. A similar flow profile was achieved by Berg et al.[20] from CFD simulation for an open Venturi

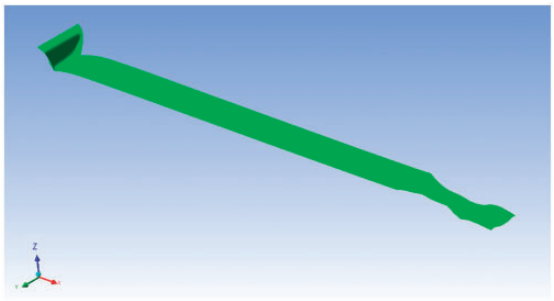

Figure 8. Water flow rate 400 kg/min and open channel at horizontal position: Simulated flow surface for the full channel (iso-surface of water volume fraction of 0.5). The flow direction is left to right.[10]

channel. The error propagated in the contraction and expansion regions caused the high deviation when using the conventional SWE.

Figure 8 shows a flow surface for the full channel (iso-surface of water volume fraction of 0.5) from the 3D CFD simulations,[10] which is related to Figure 6(a). The flow rate is 400 kg/min, and the channel is at a horizontal angle. One-dimensional simulation surface profile is well matched with the 3D CFD surface profile.

Conclusion and future work

The 1D conventional SWEs cannot be applied to a channel with a contraction and an expansion region (Venturi channel). Because conventional SWE neglect the wall-reflection pressure–force effect, they are suitable for prismatic channels only. The modified 1D SWEs are developed by considering the wall-reflection pressure–force effect. The modified SWEs can be applied to both prismatic and nonprismatic channels, especially those with contraction and the expansion regions.

This study will further extend into drilling fluid flow measurement in an open Venturi channel. The non-Newtonian properties of drilling fluid will be considered. Further, the scenario of a reflection hydraulic jump hitting the inlet will be considered in the future study.

Acknowledgment

The authors gratefully acknowledge the resources for experiments and simulations provided by the University College of Southeast Norway.

Declaration of conflicting interests

The author(s) declared no potential conflicts of interest with respect to the research, authorship, and/or publication of this article.

Funding

The author(s) disclosed receipt of the following financial support for the research, authorship, and/or publication of this article: Economic support from The Research Council of Norway and Statoil ASA through project no. 255348/E30 "Sensors and models for improved kick/loss detection in drilling (Semi-kidd)" is gratefully acknowledged.

ORCID iD

Prasanna Welahettige http://orcid.org/0000-0001-7913-2724

References

1. Vreugdenhil CB. *Numerical methods for shallow-water flow*. Dordrecht: Springer Netherlands, 1994.
2. Kurganov A, Noelle S, Petrova G, et al. Semidiscrete central-upwind schemes for hyperbolic conservation laws and Hamilton–Jacobi equations. *SIAM J Sci Comput* 2001; 23: 707–740.
3. Kurganov A and Petrova G. A second-order well-balanced positivity preserving central-upwind scheme for the Saint-Venant system. *Commun Math Sci* 2007; 5: 133–160.
4. Sanders BF and Iahr M. High-resolution and non-oscillatory solution of the St. Venant equations in non-rectangular and non-prismatic channels. *J Hydraul Res* 2001; 39: 321–330.
5. Bermudez A and Vazquez ME. Upwind methods for hyperbolic conservation laws with source terms. *Comput Fluids* 1994; 23: 1049–1071.
6. Vázquez-Cendón ME. Improved treatment of source terms in upwind schemes for the shallow water equations in channels with irregular geometry. *J Comput Phys* 1999; 148: 497–526.
7. Toro EF. *Riemann solvers and numerical methods for fluid dynamics – a practical introduction*. 3rd ed. Heidelberg: Springer Science & Business Media, 2009.
8. LeVeque RJ. *Finite volume methods for hyperbolic problems*. 1st ed. Cambridge: Cambridge University Press, 2002.
9. Tseng M-H. Improved treatment of source terms in TVD scheme for shallow water equations. *Adv Water Resour* 2004; 27: 617–624.
10. Welahettige P, Lie B and Vaagsaether K. Flow regime changes at hydraulic jumps in an open Venturi channel for Newtonian fluid. *J Comput Multiphase Flows* 2017; 9 (4): 169–179.
11. Aldrighetti E. *Computational hydraulic techniques for the Saint Venant equations in arbitrarily shaped geometry*. University of Trento, 2007. http://eprints.biblio.unitn.it/1395/1/PhDTS_n.52_.pdf
12. Akan AO. *Open channel hydraulics*. 1st ed. Burlington: Elsevier/BH, 2006.
13. Szymkiewicz R. *Numerical modeling in open channel hydraulics*. New York: Springer, 2010.
14. Versteeg HK and Malalasekera W. *An introduction to computational fluid dynamics: the finite volume method*. 2nd ed. Gosport, Hants: Pearson Education Ltd, 2007.

15. Roe PL. Characteristic-based schemes for the Euler equations. *Annu Rev Fluid Mech* 1986; 18: 337–365.
16. Welahettige P, Lie B and Vaagsaether K. Computational fluid dynamics study of flow depth in an open Venturi channel for Newtonian fluid. In: *Proceedings of the 58th SIMS*, pp.29–34. Reykjavik: Linköping University Electronic Press.
17. Ubbink O. *Numerical prediction of two fluid systems with sharp interfaces*. PhD Thesis, University of London, UK, 1997.
18. Rusche H. *Computational fluid dynamics of dispersed two-phase flows at high phase fractions*. Exhibition Road, London: Imperial College London (University of London), 2003.
19. Weller HG, Tabor G, Jasak H, et al. A tensorial approach to computational continuum mechanics using object-oriented techniques. *Comput Phys* 1998; 12: 620–631.
20. Berg C, Malagalage A, Agu CE, et al. Model-based drilling fluid flow rate estimation using Venturi flume. *IFAC-PapersOnLine* 2015; 48: 171–176.

Paper 4

Computational Fluid Dynamics Study of Shear Thinning Fluid (Drilling Fluid) Viscosity Models in an Open Venturi Channel.

This paper is published in the International Journal of Petroleum Science and Technology

International Journal of Petroleum Science and Technology
ISSN 0973-6328 Volume 13, Number 1 (2019), pp. 9-20
© Research India Publications
http://www.ripublication.com

Computational Fluid Dynamics Study of Shear Thinning Fluid (Drilling Fluid) Viscosity Models in an Open Venturi Channel

Prasanna Welahettige, Bernt Lie, Knut Vaagsaether

Faculty of Technology, University College of Southeast Norway, Porsgrunn, Norway.

Abstract

We aim to develop an improved kick/loss detection technology by developing smart flow-sensor technology for returned flow from the oil well in open Venturi channels. This is a detailed study about a capacity of use of non-Newtonian fluid models in open Venturi channels. A water-based drilling fluid was used for the experiments. According to the rheometer results, at low shear rates, the fluid behaves as a pseudoplastic fluid, and at high shear rates, the fluid shows Newtonian properties. The experimental drilling fluid can be modelled with the power-law (PL) model, the Herschel-Bulkley (HB) model, the Carreau viscosity model, and the Cross viscosity model. Experimental flow depth measurements in an open Venturi channel were used to validate the simulation results. For the complete open channel, the strain rate range was 0.02 to 2100 1/s. The highest strain rate was on the walls of the channel, with 2100 1/s, while the fluid near to the free surface had a strain rate range of 0.02 to 200 1/s. All non-Newtonian models mentioned above can be used for the drilling fluid at a shear rate range of 0 to 2100 1/s in open Venturi channel flows. Even though different non-Newtonian models predict different wall shear stresses, these differences do not significantly affect the open channel flow depth and velocity values.

Keywords: Drilling fluid, shear thinning, non-Newtonian, viscosity, models, CFD

1 INTRODUCTION

Operating conditions for drill operation may cause various problems: if the downhole pressure is too high, the drilling mud may force drill cuttings and oil into the reservoir formation (“loss”), thus reducing the permeability at later production. On the other hand, if the downhole pressure is too low, it may allow for the premature flow of oil

from the reservoir into the drill string. For safe drill operation, it is critical to detect the occurrence of "kick" and "loss". In principle, "kick" and "loss" may be detected if there is a difference in drill oil returned from the drill string compared to what is pumped down.

We intend to improve kick/loss detection by developing smart flow-sensor technology for returned fluid flow from the drilling well in open Venturi channels. On-line model development needs to have a good understanding of the behavior of the drilling fluids. This is a detailed study of non-Newtonian fluid models, and the effect of their parameters on flow depth and velocity. Even though computational fluid dynamics (CFD) simulation of drilling fluid flow in pipes is available in the literature, there are few cases of 3-D CFD drilling flow analysis in open Venturi channels: this research gap is attempted to be addressed with this study. One of the advantages of using a Venturi region is that it can generate both subcritical and supercritical flows, respectively, before and after the Venturi region for the same flow rate.

2 NON-NEWTONIAN FRICTION MODELS

Viscous force can be considered a surface force, and it is a function of the local deformation rate or strain rate. Local deformation consists of linear elongation deformation and linear shearing deformation. The power-law (PL) model, $n < 1$, can be considered as a shear-thinning model [1].

$$\eta = k\dot{\gamma}^{n-1}. \tag{1}$$

The Herschel-Bulkley model combines the properties of Bingham and power-law fluids. When, $n < 1$, the Herschel-Bulkley model can be considered as a shear-thinning fluid model [2–4]. The yield stress τ_y is the shear stress at zero shear rate.

$$\eta = \frac{\tau_y}{\dot{\gamma}} + k\dot{\gamma}^{n-1} \tag{2}$$

The Carreau viscosity model gives a solution for the significant deviations of the power-law model at very high and very low shear rates. At low shear rates, $\dot{\gamma} \ll 1/\lambda$, the Carreau model acts like the Newtonian law model, and at high shear rates, $\dot{\gamma} \gg 1/\lambda$, it acts like the power-law model [4–6]. For the shear-thinning fluid, the viscosity reduces from η_0 to η_∞ when the shear rate is increased.

$$\eta = \eta_\infty + (\eta_0 - \eta_\infty)(1 + (\lambda\dot{\gamma})^2)^{\frac{n-1}{2}} \tag{3}$$

In the Cross model [7], the relaxation time λ is the controlling parameter.

$$\eta = \eta_\infty + \frac{(\eta_0 - \eta_\infty)}{(1 + (\lambda\dot{\gamma})^{1-n})} \tag{4}$$

3 CFD MODEL

The ANSYS Fluent 16.2 commercial tool is used for the simulations. The primary and secondary phases are air and non-Newtonian fluid, respectively, in the multiphase volume of fluid (VOF) model. The standard k-ε model[8] was used as the turbulence model, and the semi-implicit method for the pressure linked equations (SIMPLE) scheme was used for the pressure-velocity decoupling. The non-Newtonian properties were fed by changing the viscosity model parameters of the fluid. Equations (1)-(4) are used for viscosity calculation for each non-Newtonian model. Non-Newtonian viscosity is considered to be a function of the shear rate in ANSYS Fluent [9]. The interface is considered a shape interface. Grid fineness gives a sharp interface between air and liquid [10]. A constant flow rate was given at the inlet, which was 400 kg/min for drilling fluid and zero for the air in x-direction. The bottom and the sidewalls were considered stationary walls at no-slip shear conditions. The wall roughness height was 15 µm [10]. In a previous study [10], mesh dependence was analyzed, and the same mesh was used in this study as well . The mesh used in the simulation contains 0.37 million elements with a maximum cell face size 10 mm and minimum cell face size 0.54 mm, see Figure 1.

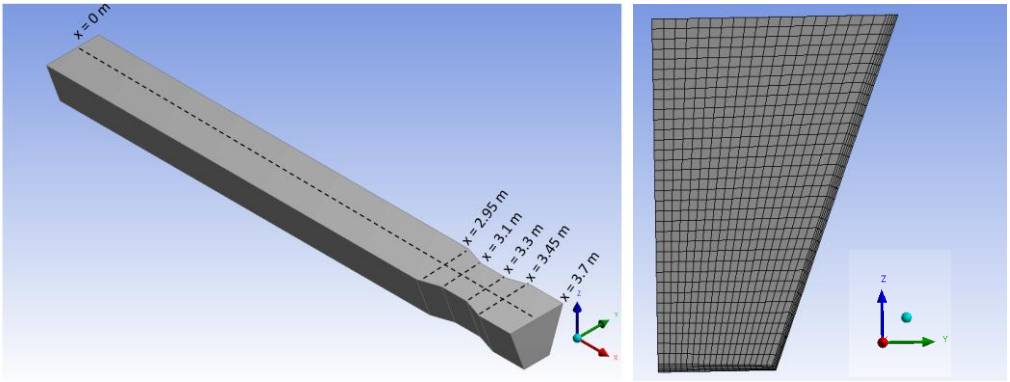

Figure 1. The channel used in the simulation is drawn similar with the channel used in experiment. The shape of the channel is trapezoidal and contains a Venturi section. The left side shows half of the cross-section of the mesh.

4 VISCOSITY AND DENSITY MEASUREMENTS FIT NON-NEWTONIAN MODELS

A water-based drilling fluid was used for the experiments; it contained Potassium carbonate, Xanthan gum, and water. An Anton Paar MCR 101 viscosity meter was used for viscosity measurements. The minimum shear rate, it is able to give, is 100 1/s, less than this value produce large error in viscosity measuring. The effect of shear rates below 100 1/s is studied with simulation results. At lower shear rates, the fluid behaves as a pseudoplastic fluid. As the shear rate increases, the fluid gradually shows Newtonian properties. The rheology of the xanthan gum solution is matched with Rodd et al. [11] and Zhong et al.[12] studies. The density of the fluid is 1340 kg/m^3 at room temperature and assumed to be constant at room temperature. The density of drilling fluid was measured using Anton Paar DMA 4500: The density of the fluid is 1340 kg/m^3

at room temperature and assumed to be constant at room temperature.

The viscosity of shear-thinning fluids decreases from η_0 to η_∞, when the shear rate is increased [4]. For shear-thinning fluids $n < 1$: the curve fitting was done by fitting model parameters to the experimental viscosity values against the shear rate. The curve-fitted parameters for Equations (1)-(4) are shown in Table 1. Figure 2 shows viscosity vs. shear rate for the non-Newtonian models. The models' parameters are based on the curve-fitted values from Table 1.

Table 1. The curve-fitted parameters for non-Newtonian fluid models based on the rheometer experimental results.

	k	n	τ_y	λ	η_0	η_∞
PL	0.0390	0.7402	-	-	-	-
HB	0.0281	0.7882	0.1	-	-	-
Carreau	-	0.6443	-	0.0095	0.01384	0.00032
Cross	-	0.04	-	0.0021	0.0142	0.00247
Newtonian	0.01	1	-	-	-	-

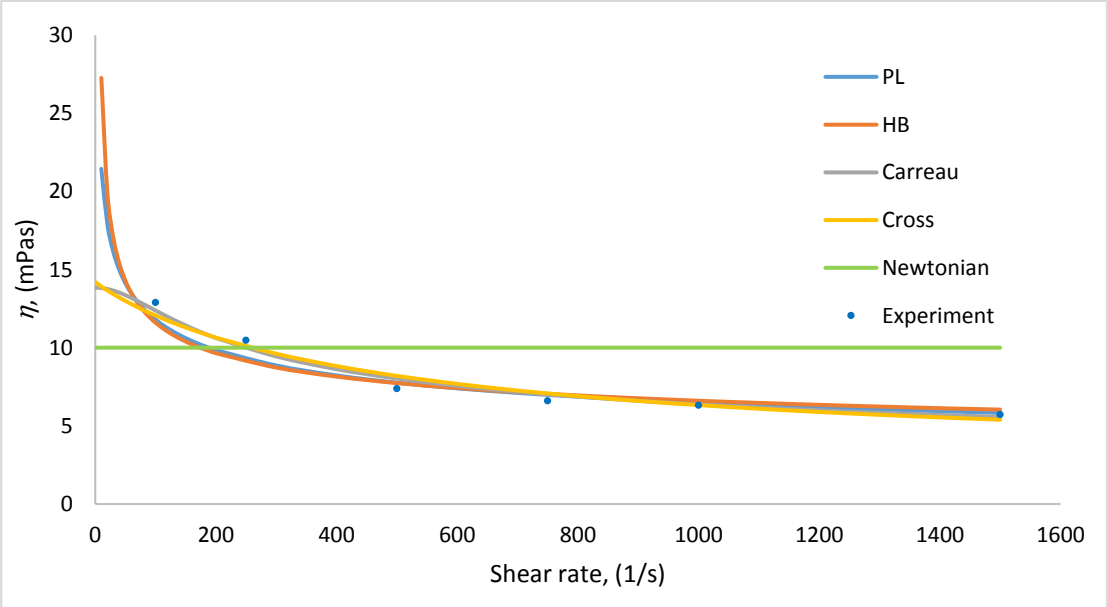

Figure 2. Shear stress vs. viscosity curves for non-Newtonian models. The model parameters are from Table 1. Experimental results are from the rheometer.

5 EXPERIMENTAL SETUP

The open Venturi channel used in the experiment contains level sensors, those can movable along the channel central axis (see Figure 3). Flow loop of the rig contains: an open Venturi channel, a mud return tank, a mud pump, and a buffer tank. The ultrasonic level transmitters' readings and the Coriolis mass flow meter's reading are used in this study to evaluate the model results. The channel can be tilted, and two tilted angles are used in this study.

Figure 3. The Venturi rig located at University of South-Eastern Norway.

6 RESULTS

In this section, simulation results are validated by comparing them with experimental results. The effects of the non-Newtonian model parameters are discussed in section 7.

6.1 Comparison of non-Newtonian viscosity models with experimental results

The simulated models' results are compared with the experimental results as shown in Figure 4 and Figure 5. Flow-depth variations along the central channel axis are compared for the channel at a horizontal angle and for the channel at -0.7 ° downward. Both results are steady state, although the channel with a gravity angle has a hydraulic jump at quasi-steady state. A similar hydraulic jump was observed for water in our previous study [13].

With the channel at a horizontal angle, simulation and experimental results are well matched. All the non-Newtonian fluid models give almost equal results. With the channel at a -0.7° angle downward, the simulations show considerable variation before the Venturi contraction. This variation is due to the very unstable hydraulic jump in the channel; the hydraulic jump can oscillate 100 mm to the backward and upward [13]. In the simulated results, the hydraulic jump is symmetric along the channel width (along with the y-axis). However, it is non-symmetric in reality. This is also a reason for having a difference in flow depth. All the models give the same results after the Venturi expansion. Assumedly, all the models show similar results, because the fluid does not have strong non-Newtonian properties. The results might show more variation, if the drilling fluid had high viscous properties. Due to the unstable motion of the quasi-

steady hydraulic jump, the flow depth is varying rapidly before the Venturi contraction. However, after the Venturi expansion, flow becomes supercritical-laminar. Due to this laminar flow behavior, experimental results and simulated results are well matched after the Venturi expansion. The critical depth value is 47 mm before and after the Venturi region, because of the same bottom width [13]. At the critical depth, the Froude number is equal to one [14]. We consider two points for the analysis of the results before and after the Venturi region, respectively, $x = 2.81$ m and $x = 3.61$ m. According to the critical depth value, the flow is subcritical at $x = 2.81$ m and supercritical at $x = 3.61$ m.

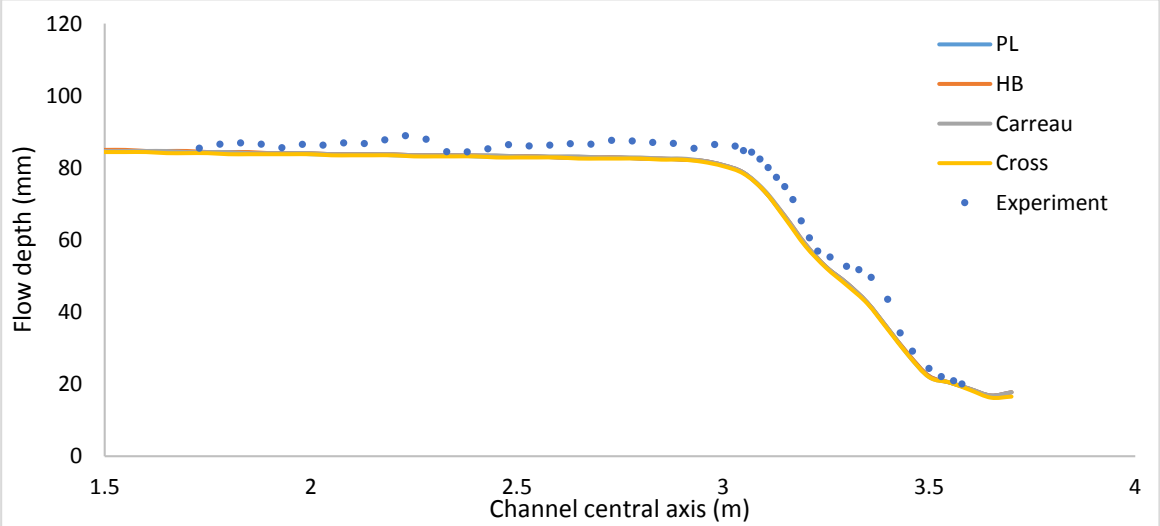

Figure 4. Flow depth along the channel axis – comparison of the viscosity models' simulated results and experimental results: The channel at a horizontal angle at steady state.

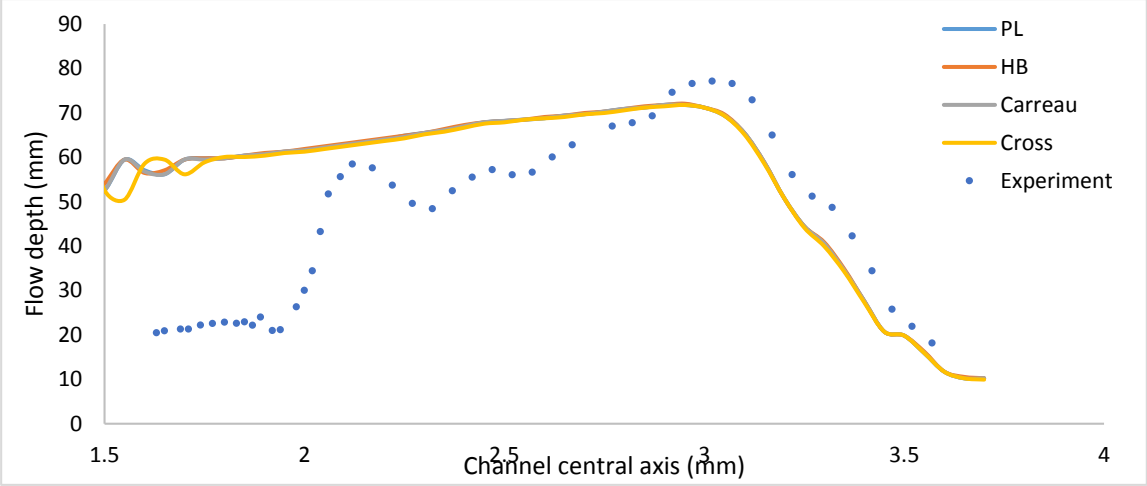

Figure 5. Flow depth along the channel axis – comparison of the viscosity models' simulated results and experimental results: (a) The channel at a horizontal angle at steady state, (b) The channel at a -0.7 ° angle downward with a hydraulic jump at steady state.

7 DISCUSSION

7.1 Velocity distributions

The simulated velocity magnitudes along the z-axis are shown for the non-Newtonian models before and after the Venturi region, in Figure 6 and Figure 7, respectively: Figure 6 shows the velocity profile of subcritical flow, which is before the Venturi contraction, and Figure 7 shows the velocity profile of supercritical flow, which is after the Venturi region. At supercritical flow, the inner region disappears for a flow depth above 7 mm. After a height of 7 mm, the turbulent core becomes strong in the supercritical region. However, near to the side wall, there is a level up in supercritical flow compared to subcritical flow, see Figure 8. This might be due to the channel expansion effect, as well as a y-directional velocity reduction from the wall, which leads to the conversion of kinetic energy into potential energy. According to Longo et al. [15], another minor effect might originate from yield stress. The yield stress of this particular fluid, however, has a small value (0.1 Pa), which indicates that this effect does not play a role here. All of the non-Newtonian models give similar velocity profiles for subcritical and supercritical flows.

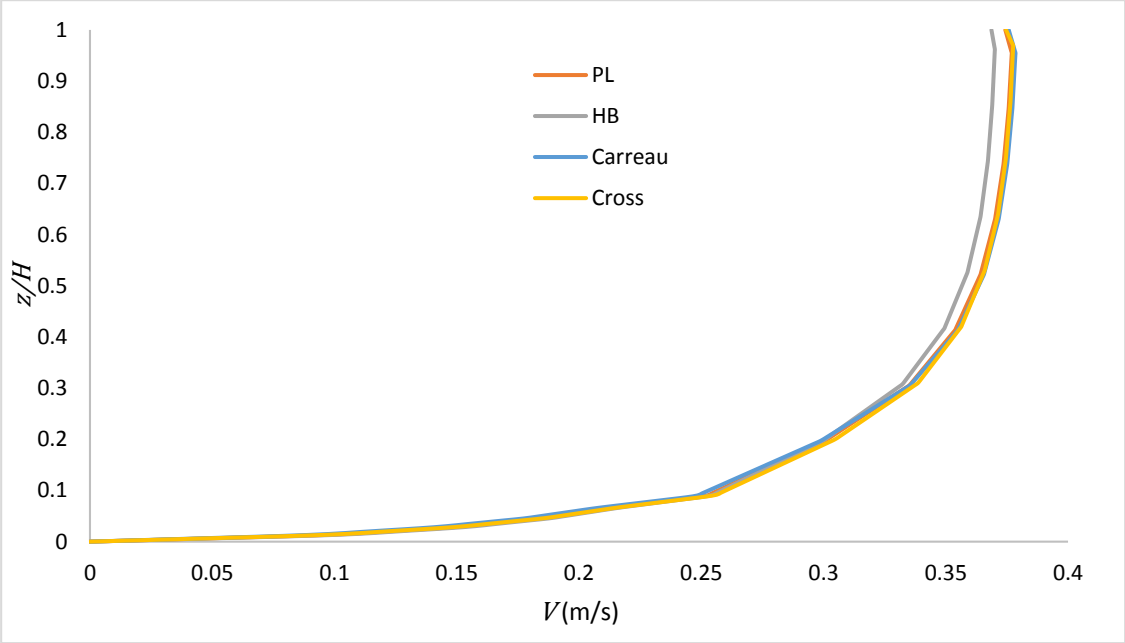

Figure 6. Vertical direction velocity profiles – comparison for non-Newtonian viscosity models at x=2.81 m, before the Venturi region.

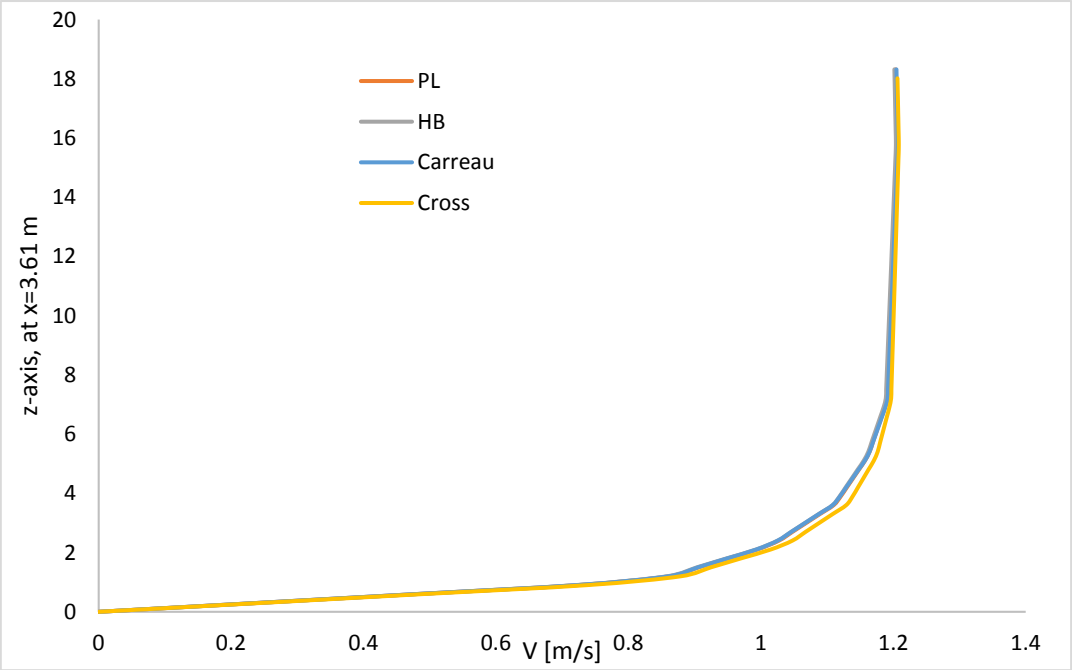

Figure 7. Vertical direction velocity profiles – comparison for non-Newtonian viscosity models at x=3.61 m, after the Venturi region.

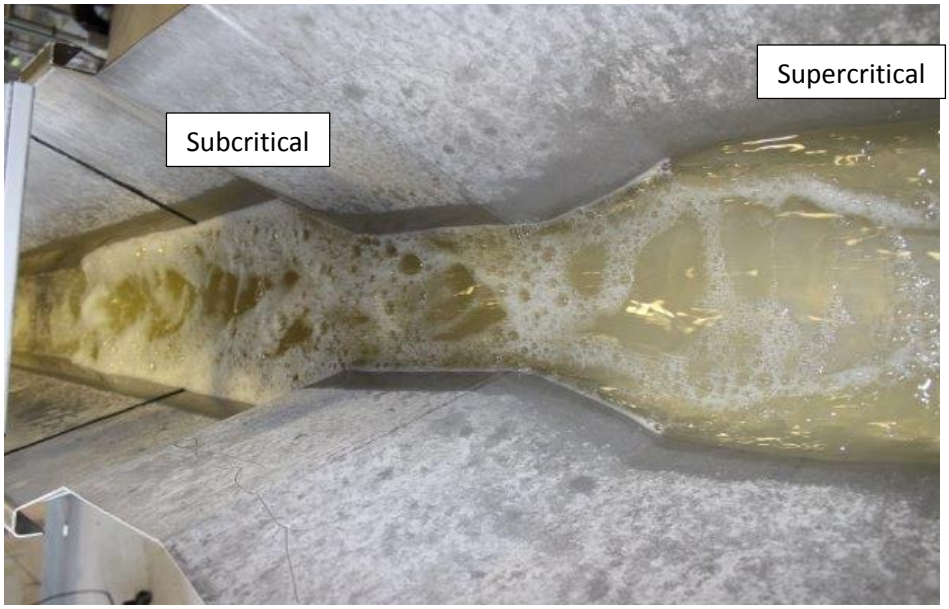

Figure 8. Experimental flow profiles before and after the Venturi region.

7.2 Simulated shear stress before and after the Venturi region

The shear stress, τ_{zx} is a function of the velocity gradient along the z-direction $\partial u/\partial z$

and the viscosity of the fluid at a given time. Figure 9 shows the shear stress τ_{zx} for subcritical, critical and supercritical flow regimes at steady state. The value of the shear stress τ_{zx}, lessens from the bottom wall to the free surface for all flow regimes: the highest wall shear stress is given by supercritical flow, which is after the Venturi region. According to the shear stress curves, the inner region margins are at $z/H = 0.133$ and $z/H = 0.0429$ for supercritical and subcritical flow, respectively. According to Longo et al. [15], the inner shear region height for the open channel can be calculated, $z/H = 1 - \tau_0/(\rho g \sin\beta)$. By substituting, $\tau_0 \approx \tau_{zx,wall}$, we can approximate the inner region height mentioned above. The shear stress near to the free surface gives negative values with respect to the bottom shear stress direction for subcritical and critical flow. This is due to the secondary currents coming from the side walls [16,17] and is called the dip-phenomenon. Here we have noticed that the dip-phenomenon is not visible in supercritical flow.

Figure 10 shows shear stress in the x-direction perpendicular to the y-direction, τ_{yx}. Here, $y = 0$ is the center of the channel and shear stress profiles are at $z = 0.01$m above the bottom wall. The sidewall shear stress is very strong in supercritical flow compared to subcritical flow. It is also larger than the bottom wall shear stress difference of supercritical and subcritical flow. At the center of the subcritical flow, the shear stress direction is converted to the negative direction, which is due to the secondary currents as explained above. However, due to the smooth sidewalls, these secondary currents in subcritical flow are not very strong. The wall shear stress coming from the bottom wall is stronger than that coming from the sidewalls, with 12 Pa and 8 Pa, respectively.

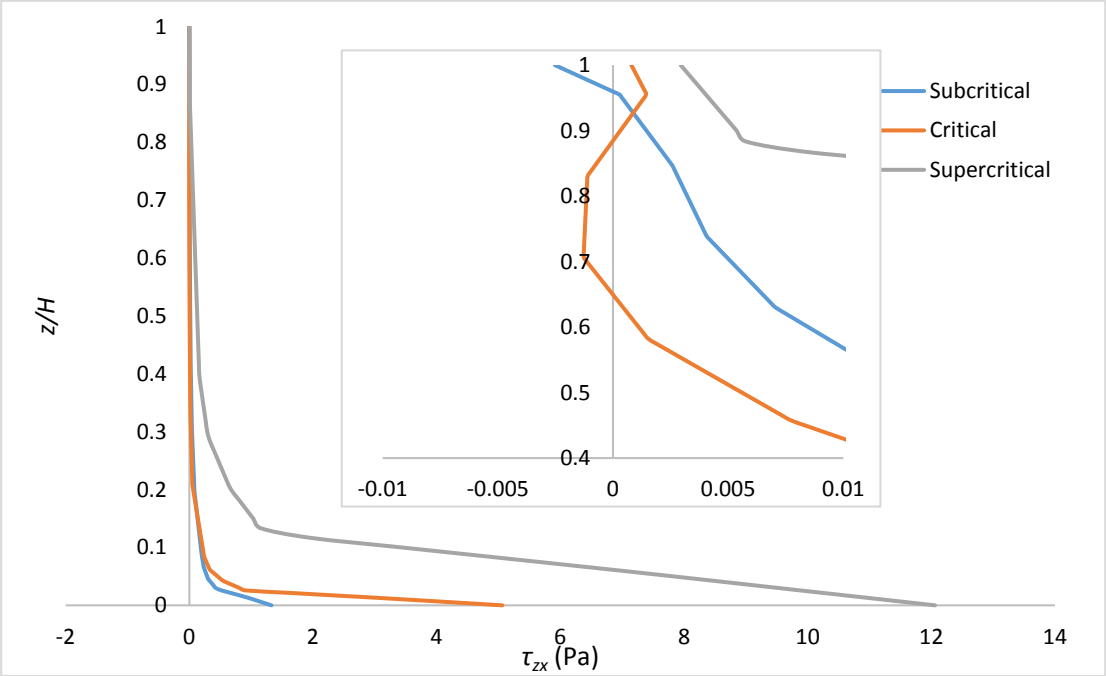

Figure 9. Shear stress in the $\boldsymbol{x}$*-direction perpendicular to the* $\boldsymbol{z}$*-direction,* $\boldsymbol{\tau_{zx}}$*, for different flow regimes in the open Venturi channel at quasi steady state. The Carreau viscosity model was used for the viscosity calculation.*

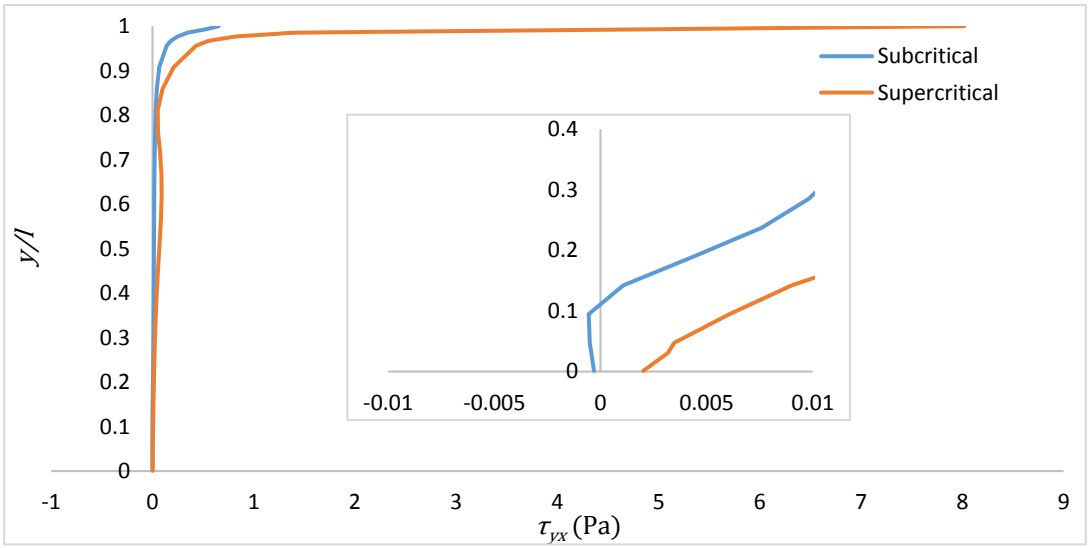

Figure 10. Shear stress in the x-direction perpendicular to the y-direction, τ_{yx}, for different flow regimes in open Venturi channel at the quasi steady state. The Carreau viscosity model was used for the viscosity calculation. Here, $z = 0.01$ m is the height from the bottom, and $l = 0.104$ m.

7.3 Shear rate at the wall

The velocity gradient at the bottom wall can have an impact on wall shear stress. Figure 11 shows the $(\partial u/\partial z)_{z=0}$ variation along the x-axis. Here, the channel is at a horizontal angle. All models give similar results except for a minor difference of the Cross model at the end of the channel. In general, the velocity gradient at the wall increases in x-direction at the bottom of the wall. This is due to the increasing velocity in the channel. The wall shear rates are also given the same values by the all the models. Therefore, these all the models can be used to simulate the model drilling fluid.

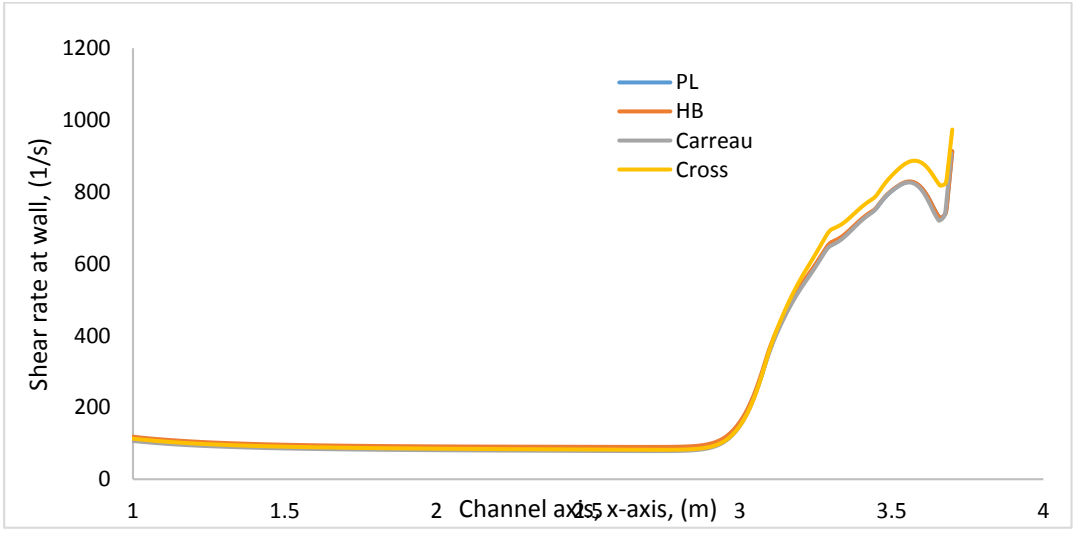

*Figure 11. Shear rate at the wall along the **x**-axis – comparison of different non-Newtonian models*

8 CONCLUSION

The 3-D CFD simulations were done for the experimental drilling fluid flow in an open Venturi channel. The model drilling fluid shows shear-thinning properties at lower shear rates and Newtonian properties at higher shear rates. The non-Newtonian models' results for shear-thinning fluid were validated with the experimental results. The results of all models matched well with the flow depth after the Venturi region with a quasi-steady hydraulic jump in the channel. There is a larger inner layer in subcritical flow than in supercritical flow. The velocity profiles are more fully developed after the Venturi region than before the Venturi region. The viscosity of the fluid has a greater effect on the flow depth after the Venturi contraction than before the Venturi contraction. The Xanthan gum water-based model drilling fluid in an open Venturi channel can be simulated with all of the non-Newtonian models examined in this study: the power-law model, the Herschel-Bulkley model, the Carreau viscosity model and the Cross viscosity model.

Nomenclature

H Flow depth (m)

k Fluid consistency index of the power-law model

n Flow behavior index of the power-law model

U Average velocity (m/s)

τ Shear stress (Pa)

τ_y Yield shear stress (Pa)

β Channel slope angle (degree)

$\dot{\gamma}$ Shear rate (1/s)

η Viscosity (Pa·s)

η_0 Viscosity at low rate of shear or viscosity at yield stress (Pa·s)

η_∞ Viscosity at high rate of shear (Pa·s)

λ Relaxation time (s)

Acknowledgments

We gratefully acknowledge the economic support from The Research Council of Norway and Statoil ASA through project no. 255348/E30 "Sensors and models for improved kick/loss detection in drilling (Semi-kidd)". Sumudhu Karunarathna, Khim Chhantyal, Asanthi Jinasena, Morten Jondahl and Håkon Viumdal are acknowledged for their kind support with the experiments.

REFERENCES

1. Khandelwal V, Dhiman A, Baranyi L. Laminar flow of non-Newtonian shear-thinning fluids in a T-channel. *Comput Fluids* 2015; 108: 79–91.
2. Herschel WH, Bulkley R. Measurement of consistency as applied to rubber-benzene solutions. *Proc ASTM Part II* 1926; 26: 621–629.
3. Saramito P. A new elastoviscoplastic model based on the Herschel–Bulkley viscoplastic model. *J Non-Newtonian Fluid Mech* 2009; 158: 154–161.
4. Chhabra RP, Richardson JF. *Non-Newtonian Flow and Applied Rheology : Engineering Applications.* 2nd ed. Butterworth-Heinemann, 2011.
5. Carreau PJ. Rheological Equations from Molecular Network Theories. *Trans Soc Rheol* 1972; 16: 99–127.
6. Picchi D, Poesio P, Ullmann A, et al. Characteristics of stratified flows of Newtonian/non-Newtonian shear-thinning fluids. *Int J Multiph Flow* 2017; 97: 109–133.
7. Cross MM. Relation between viscoelasticity and shear-thinning behaviour in liquids. *Rheol Acta* 1979; 18: 609–614.
8. Launder BE, Spalding DB. The numerical computation of turbulent flows. In: *Numerical Prediction of Flow, Heat Transfer, Turbulence and Combustion*. Elsevier, 1983, pp. 96–116.
9. ANSYS Fluent. *12.0 Theory Guide*. 2009.
10. Welahettige P, Lie B, Vaagsaether K. Computational fluid dynamics study of flow depth in an open Venturi channel for Newtonian fluid. In: *Proceedings of the 58th SIMS*. Reykjavik: Linköping University Electronic Press, pp. 29–34.
11. Rodd AB, Dunstan DE, Boger DV. Characterisation of xanthan gum solutions using dynamic light scattering and rheology. *Carbohydr Polym* 2000; 42: 159–174.
12. Zhong L, Oostrom M, Truex MJ, et al. Rheological behavior of xanthan gum solution related to shear thinning fluid delivery for subsurface remediation. *J Hazard Mater* 2013; 244–245: 160–170.
13. Welahettige P, Lie B, Vaagsaether K. Flow regime changes at hydraulic jumps in an open Venturi channel for Newtonian fluid. *J Comput Multiph Flows* 2017; 9(4): 169–179.
14. Akan AO. *Open channel hydraulics*. 1st ed. Elsevier/BH, 2006.
15. Longo S, Chiapponi L, Di Federico V. On the propagation of viscous gravity currents of non-Newtonian fluids in channels with varying cross section and inclination. *J Nonnewton Fluid Mech* 2016; 235: 95–108.
16. Nezu I. Open-channel flow turbulence and its research prospect in the 21st century. *J Hydraul Eng* 2005; 131: 229–246.
17. Yang S-Q, Tan S-K, Lim S-Y. Velocity distribution and dip-phenomenon in smooth uniform open channel flows. *J Hydraul Eng* 2004; 130: 1179–1186.

Paper 5

1-Dimensional Non-Newtonian (drilling mud) turbulent modelling for non-prismatic channels.

This paper is submitted to the Journal of Petroleum Exploration and Production Technology.

Journal of Petroleum Exploration and Production Technology
https://doi.org/10.1007/s13202-019-00772-9

ORIGINAL PAPER - EXPLORATION ENGINEERING

One-dimensional model of turbulent flow of non-Newtonian drilling mud in non-prismatic channels

Prasanna Welahettige[1] · Joachim Lundberg[1] · Dag Bjerketvedt[1] · Bernt Lie[1] · Knut Vaagsaether[1]

Received: 1 April 2019 / Accepted: 23 August 2019
© The Author(s) 2019

Abstract

One-dimensional model of non-Newtonian turbulent flow in a non-prismatic channel is challenging due to the difficulty of accurately accounting for flow properties in the 1-D model. In this study, we model the 1-D Saint–Venant system of shallow water equations for water-based drilling mud (non-Newtonian) in open Venturi channels for steady and transient conditions. Numerically, the friction force acting on a fluid in a control volume can be subdivided, in the 1-D drilling mud modelling and shallow water equations, into two terms: external friction and internal friction. External friction is due to the wall boundary effect. Internal friction is due to the non-Newtonian viscous effect. The internal friction term can be modelled using pure non-Newtonian viscosity models, and the external friction term using Newtonian wall friction models. Experiments were carried out using a water-based drilling fluid in an open Venturi channel. Density, viscosity, flow depth, and flow rate were experimentally measured. The developed approach used to solve the 1-D non-Newtonian turbulence model in this study can be used for flow estimation in oil well return flow.

Keywords One-dimensional model · Non-Newtonian · Drilling mud · Open channel · Shallow water equations · Flux-limiter-centred scheme

List of symbols

A	Cross-sectional area (m^2)
b	Bottom width (m)
k_s	Roughness height (m)
f	Friction factor (−)
F_f	Friction force (N)
$\mathbf{F}(\mathbf{U})$	x-directional column vector of flux
g	Acceleration of gravity (m s^{-2})
h	Flow depth (m)
k	Flow consistency index (Pa s^n)
k_1	A constant (-)
k_2	A constant (-)
k_M	Manning roughness factor (−)
k_n	Unit corrector, ($m^{1/3}$ s^{-1})
l	Free surface width (m)
n	Flow behaviour index (−)
R_e	Reynold number (−)
R_h	Hydraulic radius (m)
S	Friction slope (m^3 s^{-2})
$\mathbf{S}_R(\mathbf{U})$	x-directional column vector of wall reflection term
$\mathbf{S}(\mathbf{U})$	x-directional column vector of source term
u	x-directional velocity component (m s^{-1})
u_1, u_2	Conserved variables
$\mathbf{U}$	Column vector of conserved variable
V	Average velocity (m s^{-1})
ρ	Density of the fluid (kg m^{-3})
τ	Shear stress (Pa)
τ_Y	Yield stress (Pa)
α	Channel angle from the horizontal plane (°)
$\dot{\gamma}$	Shear rate (s^{-1})
θ	Trapezoidal angle (°)
η_0	Viscosity at low rate of shear/ viscosity at yield stress (Pa s)
η_{500}	Viscosity at shear rate 500 s^{-1} (Pa s)
η_∞	Viscosity at high rate of shear (Pa s)
λ	Relaxation time (s)

✉ Knut Vaagsaether
knut.vagsather@usn.no

Prasanna Welahettige
prasanna.welahettige@usn.no

Joachim Lundberg
Joachim.Lundberg@usn.no

Dag Bjerketvedt
Dag.Bjerketvedt@usn.no

Bernt Lie
Bernt.Lie@usn.no

[1] Faculty of Technology, University of South-Eastern Norway, Porsgrunn, Norway

Published online: 31 August 2019

Abbreviation

e	External friction
i	Internal friction
DF	D Fread
FLIC	Flux limiter centred
HB	Herschel–Bulkley
PC	Pierre Carreau
PL	Power law
RH	Rainer Haldenwang
TVD	Total variation diminishing

Introduction

One-dimensional prediction of non-Newtonian turbulent effect is more challenging than 2-D and 3-D shallow water flow prediction. One-dimensional models are, however, considerably more economical. There can be two types of friction assumptions in non-Newtonian fluids: internal friction due to viscous effect and external friction due to channel boundaries (Jin and Fread 1997, Fread 1988, 1993). External friction from channel walls can, in 1-D modelling, be calculated from the Darcy–Weisbach equation, the Chezy equation, and the Manning formula (Manning 1891; Chow 1959; Akan 2006; Abdo et al. 2018). This is similar to the Newtonian flow friction force from the walls. The Manning formula is the most widely used (Rahman and Chaudhry 1997; Sanders and Iahr 2001; Agu et al. 2017; Welahettige et al. 2018). The open-channel flow friction factor can be expressed as being equivalent to the pipe flow friction factor, pipe diameter being replaced by four times the open-channel hydraulic radius for Newtonian flow (Chow 1959; Akan 2006; Alderman and Haldenwang 2007). $f = 16/Re^*$ is widely used for the rectangular-channel friction factor for a fully developed non-Newtonian laminar flow. R_e^* is here a generalization of the Reynolds number (Kozicki and Tiu 1967; Burger et al. 2010). There are in general two types of laminar flow regimes in open-channel flow when $Re < 500$, and there are small flow depth and small flow velocities: subcritical laminar and supercritical laminar (Chow 1959). Laminar flows are, however, not significant in large-scale flow applications such as oil well return open-channel flow. Turbulent flow is, however, easily propagated due to high flow rates, wall friction, shape of the channel, and viscous forces.

Internal friction from the non-Newtonian fluid flow in open channels can be modelled using pure non-Newtonian flow models such as the power law (Kozicki and Tiu 1967) and the Herschel–Bulkley model (Jin and Fread 1999; Haldenwang 2003). A number of non-Newtonian turbulent open-channel friction factors have been reviewed by Alderman and Haldenwang (2007). According to the dip phenomenon (Stearns 1883), maximum velocity in open channels takes place below the free surface in narrow channels with an aspect ratio of $l/h < 5$ (Sarma et al. 1983; Yang et al. 2004; Bonakdari et al. 2008; Absi 2011). Where the bed is rough, the curvature of the velocity distribution increases due to the weak secondary motion from the lateral solid walls, transporting low momentum fluid to the central section (Nezu et al. 1994). The dip phenomenon is not widely used in 1-D modelling due to the difficulty of the formulation. Rectangular channels are very common in 1-D shallow water equation modelling. Trapezoidal open channels are less widely modelled because the trapezoidal shape of the cross section increases the complexity of the equations. Mozaffari et al. (2015) and Liu et al. (2017) have studied time-dependent properties of non-Newtonian fluid.

Supercritical and subcritical flow regimes can, where the channel is horizontal, be observed occurring simultaneously before and after the Venturi region (Welahettige et al. 2017a, b). Higher-order Godunov-type numerical schemes are recommended for solving the open-channel conservation equations due to the following issues: unsteady hydraulic jump propagation, to avoid negative flow depth (reduce numerical viscosity) and maintain stability at dry or near-dry conditions (Sanders and Iahr 2001; Kurganov and Petrova 2007). The flux-limiter-centred (FLIC) scheme using the source term splitting method is well suited to solving 1-D shallow water equations (Welahettige et al. 2018). The FLIC scheme is used to calculate the interface fluxes, the lower-order flux and higher-order flux being combined using a flux limiter function. The higher-order flux comes from the Richtmyer scheme, and the lower-order flux from the first-order-centred (FORCE) scheme, which is a combination of the Lax–Friedrichs and the Richtmyer schemes (Toro 2009).

A large number of studies have been conducted into drilling mud pipe flow (Alderman et al. 1988; Bailey and Peden 2000; Maglione et al. 2000; Piroozian et al. 2012; Livescu 2012; Aslannezhad et al. 2016). There are, in contrast, fewer published studies on drilling mud flow in open channels. The primary objective of this research paper is therefore to validate the 1-D numerical model for drilling mud in open non-prismatic channels flow using experimental results. The developed models will be used in the future for well return flow estimation. Model accuracy depends on the validity of the assumptions. Pure non-Newtonian models are combined with the turbulence models to provide a source term for the centred total variation diminishing (TVD) scheme. Viscosity, density, flow depth, and flow rates are measured experimentally at the laboratory scale for a water-based drilling mud.

Numerical schemes

The shear rate variation from the bottom wall to the free surface can be formulated in 3-D and 2-D models by the velocity gradient $\dot{\gamma}_{zx} = \partial u/\partial z$ where $z \leq h$. Here, $\dot{\gamma}_{zx}$ is the

shear rate in the x-direction perpendicular to the z-direction. It is, however, challenging to include the shear rate into a 1-D model. Three main shear stresses apply in 3-D fluid flow in the x-direction: a linear elongation deformation (τ_{xx}) and two shear linear deformations (τ_{zx} and τ_{yx}). Linear elongation deformation can, assuming incompressible liquid properties, be neglected (Versteeg and Malalasekera 2007). Bottom surface velocity becomes zero under the no-slip condition, and shear stress from the air is negligible at the free surface. There are two strong velocity gradients for Newtonian fully developed turbulent open-channel flow: the inner region, which is approximately 20% of the flow depth, and the outer region (Bonakdari et al. 2008). The dip correction factor can be neglected if the aspect ratio is > 5 and the velocity profile is similar to the log law for smooth walls (Yang et al. 2004; Absi 2011). The shear stress effect from the side wall from wide, open channels is smaller than the shear stress from the bottom walls, $\tau_{yx} \ll \tau_{zx}$. Therefore, τ_{yx} can be neglected for 1-D (Longo et al. 2016). The average shear stress and shear rate for 1-D models, based on the assumptions made, can be considered to be $\tau \approx \tau_{zx}$, and $\dot{\gamma} \approx \dot{\gamma}_{zx}$, respectively. The shear stress correlated to the power law (PL), the Herschel–Bulkley (HB), and the Pierre Carreau (PC) model can be given as

$$\tau_{\mathrm{PL}} = k\dot{\gamma}^{n} \tag{1}$$

$$\tau_{\mathrm{HB}} = \tau_{Y} + k\dot{\gamma}^{n} \tag{2}$$

$$\tau_{\mathrm{PC}} = \dot{\gamma}\left(\eta_{\infty} + \left(\eta_{0} - \eta_{\infty}\right)\left(1 + (\lambda\dot{\gamma})^{2}\right)^{\frac{n-1}{2}}\right). \tag{3}$$

The 1-D shallow water equations need to include a modification for the contraction and expansion region of open Venturi channels, to avoid artificial accelerations (Fread 1993; Sanders and Iahr 2001; Welahettige et al. 2018). An additional term has been suggested for the general shallow water equations in our previous study to accurately take into account the non-prismatic effect of the channel walls (Welahettige et al. 2018). The new term is a function of the flow depth and the variation of channel bottom width, $k_{g_2} h^2 g \partial b/\partial x$. For prismatic channels ($\partial b/\partial x = 0$), the shallow water equations are converted to the general shallow water equations. In this study, we, however, attempt to formulate the non-Newtonian friction slope as a separate term for 1-D shallow water equations, S_i. One-dimensional shallow water equations in Saint–Venant's form for locally trapezoidal channels and for non-Newtonian fluid can therefore be presented as:

$$\frac{\partial A}{\partial t} = -\frac{\partial (Au)}{\partial x}, \tag{4}$$

$$\frac{\partial (Au)}{\partial t} = -\frac{\partial \left(Au^2\right)}{\partial x} - \frac{\partial \left(k_{g_1} Ah\right)}{\partial x} g + k_{g_2} h^2 g \frac{\partial b}{\partial x} + Ag\sin\alpha - S_f - S_i. \tag{5}$$

Unlike rectangular channels, the cross-sectional area (A) is not a linear function of flow depth (h) (Fig. 1). The relation between the flow depth and the cross-sectional area can be expressed as (Welahettige et al. 2018)

$$h = \frac{-b + \sqrt{b^2 + 4k_1 A}}{2k_1}, k_1 = \frac{1}{\tan\theta}. \tag{6}$$

k_{g_1} is the ratio between the gravity height of the cross-sectional area and the flow depth in the trapezoidal shape. This helps calculate an accurate hydrostatic pressure (Welahettige et al. 2018). k_{g_2} is the ratio between the gravity height of the sidewall cross-sectional area and the flow depth. The affected sidewall area is approximately of rectangular shape. Therefore, $k_{g_2} \approx 0.5$. However, k_{g_1} is a function of b and h. Therefore, using a constant value for k_{g_1} is not valid. It is always higher than 0.5 (Welahettige et al. 2018):

$$k_{g_1} = \frac{1}{2} + \frac{h^2 k_1}{6A}. \tag{7}$$

According to the turbulent pipe flow of a non-Newtonian fluid, shear stress can be formulated as a combination of the effect of dynamic viscosity (μ) and eddy momentum kinematic viscosity (μ_t), $\tau_{zx} = \left(\mu/\rho + \mu_t/\rho\right)\mathrm{d}\left(\rho V_x\right)/\mathrm{d}z$ (Douglas et al. 2001; Chhabra and Richardson 2011). This approach can be used for open-channel non-Newtonian turbulent flow. In turbulent flow, wall shear stress is predominant in the laminar region and turbulent eddies are predominant in the turbulent core. Laminar sublayer thickness is, in general, very small in turbulent flow (Versteeg and Malalasekera 2007). The laminar sublayer effect can therefore essentially be described by a pure laminar rheological model, and the turbulent core effect can essentially be described by the Newtonian turbulence model. The Manning formula adds wall friction by considering the hydraulic radius of the channel for the numerical model of the 1-D shallow water equations (Chow 1959). According to our previous study, Manning's turbulence friction model produces good results for open-channel turbulent water flow (Welahettige et al. 2018). The friction slope for the turbulent

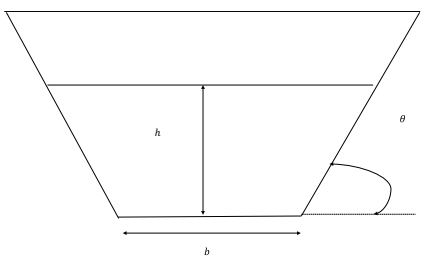

Fig. 1 Channel cross section area: Here, h, b, and θ are flow depth, bottom width, and trapezoidal angle

open-channel flow is, according to Manning's formula (Akan 2006; Welahettige et al. 2018),

$$S_{e\mathrm{M}} = \frac{k_{\mathrm{M}}^2 A g}{k_n^2 R_h^{4/3}} |u|\mathrm{u}. \tag{8}$$

The hydraulic radius for trapezoidal channels is

$$R_h = \frac{A}{b + \frac{k_2}{k_1}\left(-b + \sqrt{b^2 + 4k_1 A}\right)}, k_2 = \frac{1}{\sin\theta}. \tag{9}$$

The Reynolds number for pipe flow $Re = \rho VD/\eta$ can be converted into an open-channel Reynolds number by replacing D with $4R_h$. D is here the pipe diameter, and η is the effective viscosity of a non-Newtonian fluid. According to the Hagen–Poiseuille equation, $8V/D$ is the shear rate at the wall for Newtonian or non-Newtonian pipe flow (Chhabra and Richardson 2011). For the open channel, the shear rate for non-Newtonian flow is $\dot{\gamma} \approx 2V/R_h$ (Haldenwang 2003). We use this shear rate to describe the shear stress. The shear rate $\dot{\gamma} \approx 2V/R_h$ is valid only for laminar flow. The turbulent effect is, however, included in Manning's formula. Here, we assume that the laminar region is dominated by internal friction and that the turbulent region is dominated by external friction. This assumption is valid in the open channel due to the higher shear rates at the wall boundary and lower shear rates at the free surface. Kozicki and Tiu's (1967) power-law-based Reynolds number, Zhan and Ren's, Albulanga's and Naik's (Alderman and Haldenwang 2007) Bingham plastic-based Reynolds numbers, and Slatter's (1995) and Haldenwang's (2003) Herschel–Bulkley-based Reynolds numbers are widely used for open-channel non-Newtonian flow. Using the same approach, Reynolds numbers for open-channel flow can be derived from the power law, the Herschel–Bulkley, and the Carreau viscosity models. Effective viscosity $\eta = \tau/\dot{\gamma}$ is taken from Eqs. (1)–(3),

$$R_e = \frac{4\rho V R_h}{\eta}. \tag{10}$$

If we assume $\eta_t/\rho d\left(\rho V_x\right)/\mathrm{d}z \ll \mu/\rho d\left(\rho V_x\right)/\mathrm{d}z$ for laminar region channel flow, then the friction force due to the non-Newtonian viscous effect is $F_i = \tau\left(b + 2k_2 k_{g_1} h\right)\Delta x$. This is based on the assumption that average shear stress applies to the gravity height of the flow depth in a control volume. The internal friction slope can be introduced as a function of the internal friction factor,$S_i = A\rho g f_i$. The dimensionless non-Newtonian friction factor can be introduced as

$$f_i = \frac{\tau\left(b + 2k_2 k_{g_1} h\right)}{\rho\left(b + k_1 h\right) hg}. \tag{11}$$

For a rectangular channel, the non-Newtonian friction factor then becomes $f_i = \tau/(\rho g h)$ where $k_1 = 0$ and $k_2 = 0$. Jin and Fread (1997) derived a similar non-Newtonian friction factor for mud fluid in a rectangular open-channel flow. Non-Newtonian friction factors for the power law, Herschel–Bulkley, and Carreau fluids can be derived as follows:

$$f_{i\mathrm{PL}} = \frac{\left(b + 2k_2 k_{g_1} h\right)}{\rho\left(b + k_1 h\right) hg} k\left(\frac{2V}{R_h}\right)^n. \tag{12}$$

$$f_{i\mathrm{HB}} = \frac{\left(b + 2k_2 k_{g_1} h\right)}{\rho\left(b + k_1 h\right) hg}\left(\tau_Y + k\left(\frac{2V}{R_h}\right)^n\right). \tag{13}$$

$$f_{i\mathrm{PC}} = \frac{\left(b + 2k_2 k_{g_1} h\right)}{\rho\left(b + k_1 h\right) hg}\left(\frac{2V}{R_h}\left(\eta_\infty + \left(\eta_0 - \eta_\infty\right)\left(1 + \left(\lambda\frac{2V}{R_h}\right)^2\right)^{\frac{n-1}{2}}\right)\right). \tag{14}$$

Equations (4)–(5) are solved using the FLIC scheme and Runge–Kutta fourth-order explicit scheme, for rectangular channels of water (without internal friction slope) by Welahettige et al. (2018). The FLIC scheme and Runge–Kutta fourth-order explicit scheme are used for solving the advection term and the source terms, respectively. This method also extends to the 1-D turbulent non-Newtonian fluid. In this study, we implement the FLIC scheme and Runge–Kutta fourth-order scheme for the turbulent non-Newtonian fluid in a trapezoidal shaped channel. Flow rate Q can be given as $Q = AV$, where the average velocity across the cross section is considered to be $u \approx V$. The area perpendicular to the flow direction is a function of time, flow depth, and spatial domain $A = A(t, h, x)$, and the average velocity is a function of time and spatial domain $V = V(t, x)$. The pure advection Eq. (15) is solved with conserved variables $u_1 = A$ and $u_2 = AV$. For continuous bottom topography channels, the bottom-width variation effect is highlighted in the TVD solving method used here. This can be compared with the conventional centred TVD solving method, $1/\Delta x \mathbf{S}_{\boldsymbol{R}}(\mathbf{U})$ (Welahettige et al. 2018). The pure advection term (advection flux and wall reflection effect) is solved first using the centred TVD method.

$$\mathbf{U}_j^{m+1} = \mathbf{U}_j^m - \frac{\Delta t}{\Delta x}\left[\mathbf{F}(\mathbf{U})_{j+\frac{1}{2}}^m - \mathbf{F}(\mathbf{U})_{j-\frac{1}{2}}^m - \mathbf{S}_{\boldsymbol{R}}(\mathbf{U})_j^m\right]. \tag{15}$$

Here,

$$\mathbf{U} = \begin{pmatrix} A \\ AV \end{pmatrix} = \begin{pmatrix} u_1 \\ u_2 \end{pmatrix},$$

$$\mathbf{F}(\mathbf{U}) = \begin{pmatrix} AV \\ AV^2 + k_{g_1} Ahg \end{pmatrix} = \begin{pmatrix} u_2 \\ \frac{u_2^2}{u_1} + k_{g_1} u_1 hg \end{pmatrix},$$

$$\mathbf{S_R}(\mathbf{U}) = \begin{pmatrix} 0 \\ k_{g_2} h^2 g \Delta b \end{pmatrix},$$

$$\mathbf{S}(\mathbf{U}) = \begin{pmatrix} 0 \\ u_1 g \sin\alpha - \mathrm{S}_e - \mathrm{S}_i \end{pmatrix}.$$

For PL, HB, and PC models, the source terms are $\mathbf{S}(\mathbf{U}) = \begin{pmatrix} 0 \\ u_1 g \sin\alpha - \mathrm{S}_e - S_{i\mathrm{PL}} \end{pmatrix}$, $\mathbf{S}(\mathbf{U}) = \begin{pmatrix} 0 \\ u_1 g \sin\alpha - \mathrm{S}_e - S_{i\mathrm{HB}} \end{pmatrix}$, and $\mathbf{S}(\mathbf{U}) = \begin{pmatrix} 0 \\ u_1 g \sin\alpha - \mathrm{S}_e - S_{i\mathrm{PC}} \end{pmatrix}$, respectively, with their friction slopes, the internal friction slopes being $S_{i\mathrm{PL}} = A\rho g f_{i\mathrm{PL}}$, $S_{i\mathrm{HB}} = A\rho g f_{i\mathrm{HB}}$, and $S_{i\mathrm{PC}} = A\rho g f_{i\mathrm{PC}}$.

The wall reflection effect $\mathbf{S_R}(\mathbf{U})_j^m$ is solved here as an advection term, due to the simple numerical calculation of the $\partial b/\partial x$ term, and to minimize numerical diffusion (Welahettige et al. 2018). One advantage of using the centred TVD scheme is to avoid the strictly hyperbolic requirement of the partial differential equations. m is here the time index, $m \in \{1, 2, \ldots, N\}$. j is the node index in the spatial grid, $j \in \{1, 2, \ldots, l\}$. The source terms (gravity effect, external friction, and internal friction) are then solved using an ordinary differential equation (ODE) solver, the explicit Runge–Kutta fourth-order method (Toro 2009). The initial condition for the ODE solver is the solution from the centred TVD scheme.$k_{g_1}(u_1)$, $h(u_1)$, $R_h(u_1)$, $\mathrm{S}_e(u_1, u_2)$, $S_{i\mathrm{PL}}(u_1, u_2)$, $S_{i\mathrm{HB}}(u_1, u_2)$, and $S_{i\mathrm{PC}}(u_1, u_2)$ can be derived in terms of conserved variables by substituting u_1 and u_2 with A and AV.

$$\mathbf{U}_j^{n+1} = \mathbf{U}_{j,TVD}^{n+1} + \frac{1}{6}\left(\mathrm{K}_1 + 2\mathrm{K}_2 + 2\mathrm{K}_3 + \mathrm{K}_4\right). \tag{16}$$

The explicit Runge–Kutta fourth-order method parameters are $\mathrm{K}_1 = \Delta t \mathbf{S}\left(t^n, \mathbf{U}_{j,\mathrm{TVD}}^{n+1}\right)$, $\mathrm{K}_2 = \Delta t \mathbf{S}\left(t^n + \Delta t/2, \mathbf{U}_{j,\mathrm{TVD}}^{n+1} + \mathrm{K}_1/2\right)$, $\mathrm{K}_3 = \Delta t \mathbf{S}\left(t^n + \Delta t/2, \mathbf{U}_{j,\mathrm{TVD}}^{n+1} + \mathrm{K}_2/2\right)$, and $\mathrm{K}_4 = \Delta t \mathbf{S}\left(t^n + \Delta t, \mathbf{U}_{j,\mathrm{TVD}}^{n+1} + \mathrm{K}_3\right)$.

Non-Newtonian turbulent friction factors available in the literature for open channels are used for comparison purposes. Haldenwang (2003) derived a turbulent flow friction factor for Herschel–Bulkley fluid flow in open channels based on (Slatter 1995) model. Internal and external frictions are combined in Haldenwang's friction factor $S_{ei\mathrm{RH}}$. Haldenwang's friction slope for trapezoidal open channels can be given as

$$S_{ei\mathrm{RH}} = \frac{0.165AV^2}{R_h\left(2.5\ln\frac{2R_h}{k_s} - 76.86\eta_{500} - 9.45\right)^2}. \tag{17}$$

The source for the Haldenwang model is

$$\mathbf{S}(\mathbf{U}) = \begin{pmatrix} 0 \\ u_1 g \sin\alpha - S_{ei\mathrm{RH}} \end{pmatrix}.$$

The apparent viscosity of the shear rate is 500 1 s^{-1}, η_{500}, which is a constant. Here, k_s is the roughness height and is 15 μm in this study, which is similar to the value for steel walls. Fread (1988; Jin and Fread 1997) has derived a friction slope due to internal viscous dissipation with the rheological properties of the power law equation and a yield stress (similar to the Herschel–Bulkley model). This includes a semi-empirical velocity profile. According to Fread's model, the internal friction factor for trapezoidal channels can be presented as

$$S_{i\mathrm{DF}} = \left[\frac{\tau_y A}{\rho l}\left[1 + \left(\frac{\left(\frac{1}{n}+1\right)\left(\frac{1}{n}+2\right)AVl}{\left(0.74 + \frac{0.656}{n}\right)\left(\frac{\tau_y}{k}\right)^{\frac{1}{n}}A^2}\right)^{\frac{1}{\frac{1}{n}+0.15}}\right]\right]. \tag{18}$$

The source for the Fread model is

$$\mathbf{S}(\mathbf{U}) = \begin{pmatrix} 0 \\ u_1 g \sin\alpha - \mathrm{S}_e - S_{i\mathrm{DF}} \end{pmatrix}.$$

Here, l is the free surface width. For trapezoidal channels, l becomes $b + 2k_1 h$.

In the sequel, PL, HB, PC, Haldenwang, and Fread models are solved by using the FLIC scheme and Runge–Kutta fourth-order method. The only differences are the source terms. We call the models as PL, HB, PC, and Fread where they are combined with Manning's friction.

Experimental setup

Venturi rig

The complete flow loop of the rig contains a mud-mixing tank, a mud-circulating pump, an open Venturi channel, and a mud return tank. See Figs. 2 and 3. The sensing instruments in the setup are a Coriolis mass flow meter, pressure transmitters, temperature transmitters, and ultrasonic level transmitters. Chhantyal et al. (2017) and Agu et al. (2017) also conducted experiments using the same experimental setup. Level transmitters are located along the central axis of the channel and can be moved along the central axis. The accuracy of the Rosemount ultrasonic 3107 level transmitters is ± 2.5 mm for a measured distance of less than 1 m (Welahettige et al. 2017b). The accuracy of temperature transmitter is ± 0.19 °C at 20 °C. The accuracy of Coriolis mass flow meter is ± 0.1%. All the experimental values presented in this paper are averaged values of level sensor readings taken throughout a period of 5 min at each location. The channel inclination can be changed. A negative channel inclination (α angle) indicates a downward direction. The

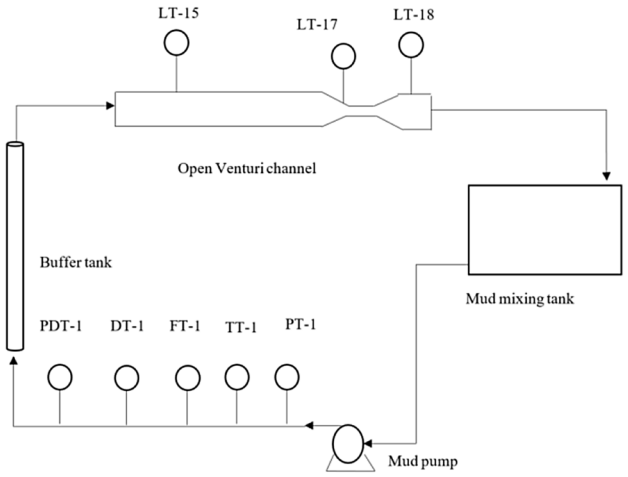

Fig. 2 Flow loop of the experimental setup: *LT* level transmitter, *PT* pressure transmitter, *TT* temperature transmitter, *DT* density transmitter, and *PDT* differential pressure transmitter. The level transmitters are possible to move along the central axis of the channel

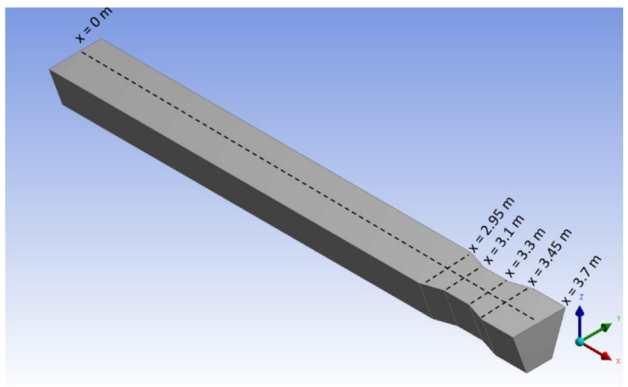

Fig. 3 Dimension of the trapezoidal channel; $x=0$ m is at the inlet of the channel. The Venturi region is $x=2.95$ m to $x=3.45$ m. The bottom depth is 0.2 m for 0 m $<x<$ 2.95 m and 3.45 m $<x<$ 3.7 m. The bottom depth is 0.1 m for 3.1 m $<x<$ 3.3 m. The trapezoidal angle is 70° (Welahettige et al. 2017b)

dimensions of the trapezoidal channel are shown in Fig. 3; the main flow direction is in the x-direction.

Viscosity and density measurements

The water-based drilling mud used for the experiments contained potassium carbonate as a densifying agent and xanthan gum as viscosifier (Chhantyal 2018). The drilling mud viscosity and density were measured using an Anton Paar MCR 101 rheometer and an Anton Paar DMA 4500 density meter. At the beginning of the experiments, the viscosity meter reached a constant room temperature, 25 °C, within 20 min. The constant temperature was maintained throughout the experimental period. For a fixed shear rate value, 40 measuring points were taken within 800 s. The averages of 40 measuring points were considered in this study. The standard deviation of viscosity is small, 1×10^{-5}, within the 40 measuring points. This indicates that the rheometer reaches a steady state. The combined uncertainty of viscosity is 0.015 mPa s, which is calculated based on the quantifying uncertainty in analytical measurement (QUAM) method (Ellison et al. 2000). An external Anton Paar Viscotherm VT 2 cooling system has a standard temperature uncertainty of 0.02 K (Idris et al. 2017). For DMA 4500, the temperature accuracy is ±0.03 K. The uncertainty of density is determined as 0.34 kg/m^3 (Han et al. 2012).

The experimentally measured viscosity data were fitted to Eqs. (1)–(3) based on nonlinear regression techniques: the power law model, the Herschel–Bulkley model, and the Carreau model as shown in Fig. 4. The curve-fitted parameters from Table 1 are used: Herschel–Bulkley model for Haldenwang, Fread, PL, HB, and PC models. The density of the drilling mud is 1336 kg m^{-3}. Experimental viscosity measurements are in the range of the rheometer accuracy limit where the shear rate is 100–1500 s^{-1}. A shear rate of less than 100 s^{-1} shows a significant variation in all the models. The accuracy may not be significant in the open Venturi channel flow where the shear rate is less than 100 s^{-1} for the fluid we used in the experiment. This is because flow regimes are turbulent and the average shear rate is higher than 100 1 s^{-1}. This will be further analysed by comparing PL, HB, and PC model results. The average errors between

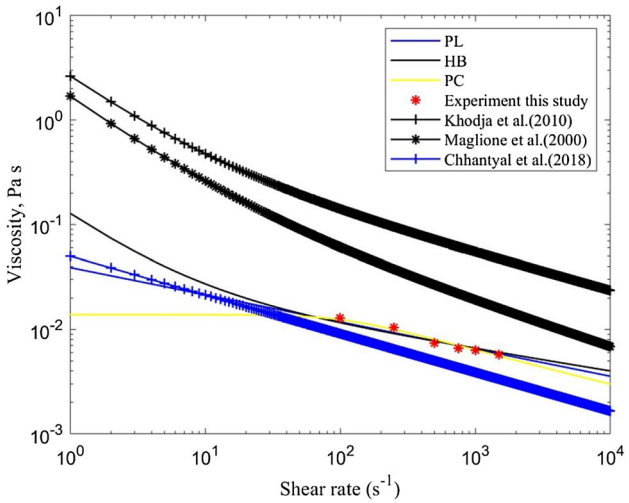

Fig. 4 Shear stress versus viscosity curves for the drilling mud used in this study. The model parameters are from Table 1. Experimental results are from the Anton Paar MCR 101 rheometer. PL, HB, and PC are model-fitted results from the experimental results. Khodja et al.'s (2010), Maglione et al.'s (2000), and Chhantyal's (2018) drilling fluid data are also taken from the literature and used for the comparison

the calculated and the experimental values are 6.14%, 7.7%, and 4.4%, respectively, for the power law model, the Herschel–Bulkley model, and the Carreau model with $100\ s^{-1} < \dot{\gamma} < 1500\ s^{-1}$. According to the nonlinear least squares approach in MATLAB R2018a, coefficients are calculated with 95% confidence bounds. The R-squared values are above 0.95 for all the fitted models. The calculated yield stress is 0.1451 Pa based on the Herschel–Bulkley model. The yield stress is a small value for the fluid used in this study. The open-channel flow is highly turbulent and has a high Reynolds number; the small yield stress will not significantly influence the flow regimes in the open-channel flow at high turbulence level.

The drilling fluid used in this study shows shear thinning properties in the range of shear rate $100\ s^{-1} < \dot{\gamma} < 1500\ s^{-1}$ (Fig. 4).

Real and experimental drilling fluids from the literature are used for further comparison in the open-channel flow modelling. Khodja et al.'s (2010) and Maglione et al.'s (2000) real drilling fluids rheology based on the Herschel–Bulkley model is shown in Fig. 4 and Table 1. Chhantyal (2018) used a model drilling mud and the experimental setup used in this study. The model drilling mud rheology was given in terms of the power law model.

Results and discussion

The rheological parameter and flow parameters used in the simulations are shown in Tables 1, 2, and 3.

Steady results

Haldenwang, Fread, PL, HB, and PC model results are compared with experimental flow depth along the channel at a steady state (Fig. 5). The results are steady state, reached from an unsteady condition. At the beginning, the drilling fluid enters the empty channel at a constant inlet flow rate. Steady results are achieved after 310 s. The critical flow depth (h_c) is 40 mm at $0 \le x \le 2.95$ and $3.45 \le x \le 3.7$, and bottom width and flow depth are the same in the two ranges (Welahettige et al. 2018). According to the Froude number, the flow regime is subcritical ($h > h_c$) before the Venturi region and supercritical ($h < h_c$) after the Venturi region (Fig. 5). All the models derived in this study (PL, HB, and PC) give similar results, which indirectly imply that the curve-fitted rheological parameters for each model act in the same way as for the drilling fluid used in this study. The fluid accumulates before the Venturi contraction when the channel is horizontal. Then, due to the channel contraction effect, a hydraulic jump moves upstream before the steady state is reached. The flow depth increases and the velocity decreases due to high energy loss, the friction models giving

Table 1 Rheological parameters of the drilling muds used in this study. Figure 4 shows the related rheology curves

	k (Pa s^n)	n	τ_y (Pa)	λ (s)	η_0 (Pa s)	η_∞ (Pa s)
PL	0.0390	0.7402	–	–	–	–
HB	0.0281	0.7882	0.1451	–	–	–
PC	–	0.6443	–	0.0095	0.01384	0.00032
Khodja et al. (2010)	0.626	0.643	2.013	–	–	–
Maglione et al. (2000)	0.334	0.576	1.360	–	–	–
Chhantyal (2018)	0.05	0.63	–	–	–	–

Table 2 Flow parameters used in the simulations: model drilling fluids

	Flow rate (kg min^{-1})	Inlet velocity (m s^{-1})	Density (kg m^{-3})
Steady simulations	433	1.3030	1336
Unsteady simulations	480–300	1.444–0.9028	1336
Chhantyal (2018)	350	1.2172	1156

Table 3 Drilling fluid: Herschel–Bulkley fluid rheological parameters and flow parameter

Source	k (Pa s^n)	n	τ_y (Pa s^n)	Density (kg m^{-3})	Inlet flow rate (m^3 s^{-1})
Khodja et al. (2010)	0.626	0.643	2.013	1225	0.0056
Maglione et al. (2000)	0.334	0.576	1.360	1190	0.0056
This study	0.0281	0.7882	0.1	1336	0.0056

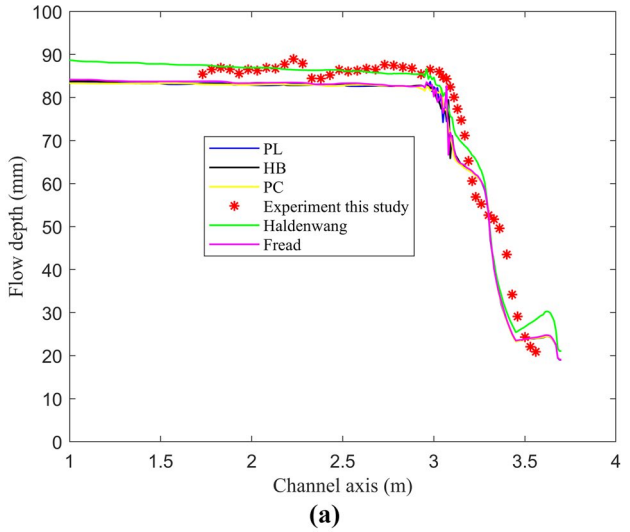

(a)

(b)

Fig. 5 A comparison of different friction models for the flow depth variation along the channel axis: The channel inclination is $\alpha = 0°$. The inlet flow rate is 433 kg min^{-1}. **a** Experimental and simulated flow depth comparison, **b** steady-state image of the free surface

higher friction. The Haldenwang model shows higher friction in this case than the PL, HB, and PC models. According to Eq. (17), wall roughness height for the channel is assumed to be 15 μm, the value for steel walls. This wall roughness value was tested in our previous study (Welahettige et al. 2017b). The PL, HB, and PC models, however, used the Manning roughness factor for steel-smooth walls, which is 0.012. The average deviation from experimental results is 5% in PL, HB, and PC models at a steady state.

The PL model results are further compared with the Chhantyal's (2018) experimental results (Fig. 6). The rheology of the drilling fluid is given in terms of the power law model. They used a mechanical filter to remove foam, flow depth, therefore being less influenced by foam than in our experimental results. The flow depth difference between experiment and simulation is reduced in the subcritical region when the foam is removed. The PL model gives a good prediction of the Chhantyal's (2018) experimental results. The average deviation from the experimental result is 8%. The yield stress of the fluid is comparatively small. The viscosity of the fluid used in Chhantyal's work is

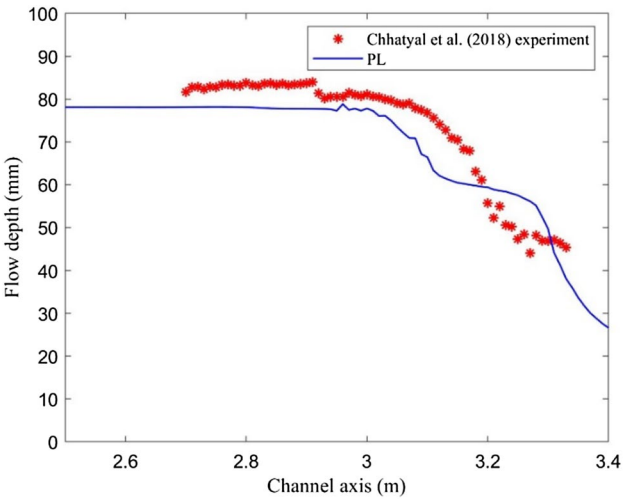

Fig. 6 A flow depth comparison with Chhantyal's (2018) experimental result at a steady state with PL model results. The flow rate is 350 kg/min and the channel angle is horizontal. The power law rheological parameters are $k = 0.05$ Pa s^n and $n = 0.63$

0.04 Pa s at 1 s^{-1} shear rate, as shown in Fig. 4. The average viscosity value calculated in the simulation is 0.005 Pa s at a steady state, at an average shear rate of 450 s^{-1}. This implies that, in this case, the open-channel flow regimes do not reach the small shear rate ranges. The effect of low shear rates might therefore be insignificant.

Unsteady results

Figure 7 shows flow depth variation with time for step changes in the channel inlet flow rate. The pump outlet flow mass rate varies between 10 and 40 kg min^{-1} from the set point. At the beginning of the experiment, the channel flow rate is 470 kg min^{-1} at a steady state. Step changes are carried out for the set point of the pump flow rate at time $t = 64$ s and $t = 188$ s. We show here two-level sensors readings, LT-18 and LT-15. They are fixed at $x = 2.12$ m and $x = 3.2$ m from the inlet of the channel, above the free surface along the channel central axis. The PC model and the Haldenwang model results are compared with the experimental readings at the dynamic condition. LT-18 is located after the Venturi region. LT-15 is located before the Venturi region. Even though sudden step changes in the flow rate occur at time $t = 64$ s and $t = 188$ s, the experimental level reading gradually changes flow depth, a complete step change taking more than 40 s. This is despite the pump having a small time constant of 1.6 s. This is due to the time required for fluid to travel from the inlet of the open channel to the level sensor locations, and to unstable wave propagation. Higher flow depth is shown in LT-15 than in LT-18 due to the hydraulic jump formation travelling upstream before the Venturi contraction. The PC model results give a higher accuracy

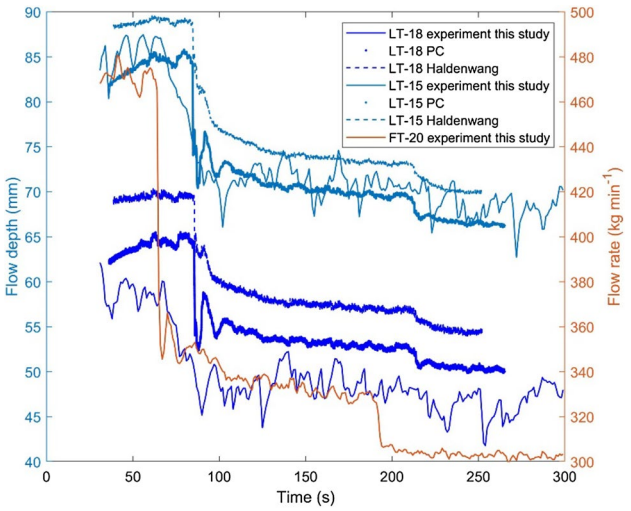

Fig. 7 Flow depth variation with steps change of inlet flow rate: the ultrasonic level sensor is positioned LT-18 and LT-15 at $x = 3.20$ m and $x = 2.12$ m. The channel is at the horizontal angle. The left vertical axis demonstrates the flow depth in mm, and the right vertical axis demonstrates the flow rate in kg min^{-1}

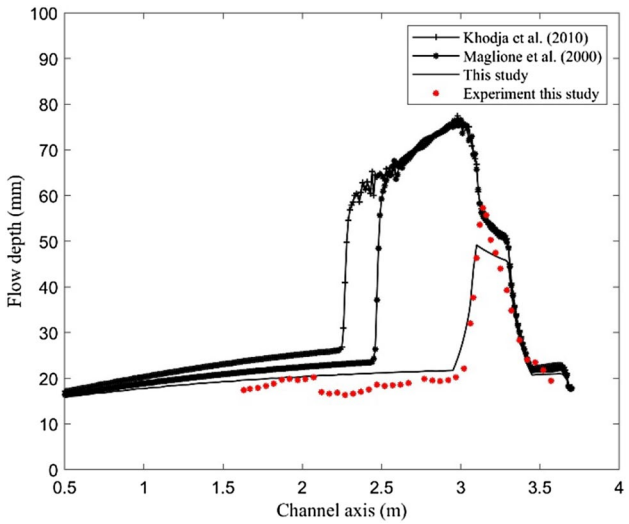

Fig. 8 Flow depth variation for drilling fluids, the rheology based on the Herschel–Bulkley model. The constant inlet flow rate is 0.0056 m^3 s^{-1}, and the channel angle is − 1.7°

than the Haldenwang model. The average deviation from the experimental results is 5% in the PC model.

The accuracy of the models depends on the assumptions used in model development, the curve-fitted rheological parameter, and boundary conditions. An assumption for the 1-D models is that velocity is only considered in the x-direction, V_x. However, the velocity component V_z is comparatively small due to free surface movement in the z-direction, which is restricted by the surface tension of the fluid and gravitational force, $V_x \gg V_z$. Channel sidewalls are balanced with the velocity component in the y-direction, $V_x \gg V_y$. However, contraction and expansion of side walls influence and change the direction of the flow path (Welahettige et al. 2017b). The average aspect ratio was 4 in this study. The effect of the dip phenomena was therefore assumed to be small. In this study, the average error of flow depth is 0–6%.

One of the main advantages of using a 1-D model compared to a 3-D model is less execution time. According to our 3-D CFD simulation of the same case (related to Fig. 5 for water), the 1-D model took 1 min to execute and the 3-D CFD model took more than 5 h (Welahettige et al. 2017b).

Effect of source terms

There are no direct experimental results for the derived friction slopes in this study. The internal and external friction slopes are therefore calculated for different drilling fluids. The three drilling fluids all have different densities and viscosities, the rheology of the fluids being given in the Herschel–Bulkley model. Figure 8 shows a drilling fluid flow depth comparison. The Herschel–Bulkley parameters that specify the drilling fluid rheology are shown in Table 3. According to the viscosity and shear rate curves, for a given shear rate (> 40 s^{-1}), fluid viscosity ranked from the highest to lowest is the Khodja et al.'s (2010) fluid, the Maglione et al.'s (2000) fluid, and the fluid of this study. The inlet flow rate was kept constant at 0.0056 m^3 s^{-1} for all the fluids. The different densities, however, imply that the inlet mass flow rate is different for each fluid. As explained above, a flow depth that is larger than the critical flow depth is subcritical and contrast supercritical. The Reynolds number is higher than 5300 throughout the channel. Flow regimes therefore become subcritical turbulent and supercritical turbulent. The Reynolds number is calculated from Eq. (10) by substituting effective viscosity for Eq. (3). The channel inclination angle is − 1.7°. Experimental flow depth and the PC model results are well matched for the entire region of the channel. The model drilling fluid used in this study creates an oblique jump at the Venturi throat (Welahettige et al. 2017b). The two other drilling fluids show a hydraulic jump formation at the quasi-steady state. The fluid used in this study, however, has a lower viscosity than the two other drilling fluids and the highest density. This causes lower energy loss and high mass flow rates. The fluid used in this study gives supercritical flow regimes throughout the channel. However, the inlet supercritical flow regimes cannot be maintained for the high viscous fluids (Khodja's and Maglione's drilling fluids), because they generate a hydraulic jump and the level rises to keep the same flow rate at the steady state. Khodja's drilling fluid has a higher density than Maglione's drilling fluid. Khodja's drilling fluid does, however, show greater movement of the hydraulic jump front in the upstream direction due to the higher viscosity of the fluid. The friction

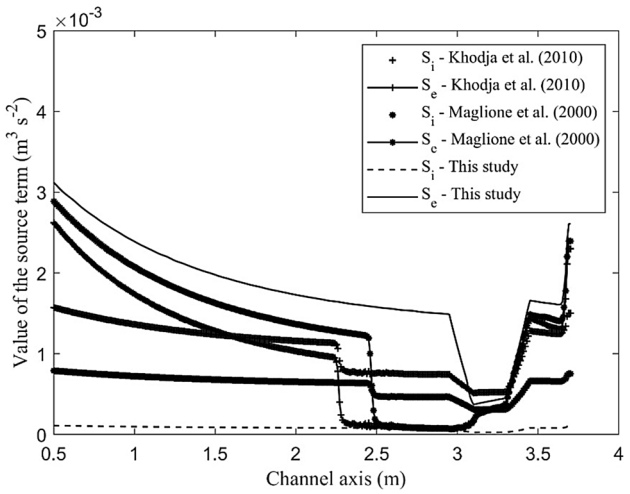

Fig. 9 A comparison of internal friction and external friction for different drilling fluid, the rheology of drilling fluid based on the Herschel–Bulkley fluid. The results are at a steady-state flow in the open Venturi channel, the inlet flow rate is 0.0056 m^3 s^{-1}, and the channel angle is − 1.7°

slopes used to calculate the flow depth in the drilling fluid are studied further in Fig. 9.

The calculated friction slope terms, internal friction slope (S_i) and external friction slope (S_e), are shown in Fig. 9. The external friction term is the highest for the lowest viscous fluid, and the internal friction is the lowest for the lowest viscous fluid (the fluid used in this study, which relates to the HB model). Flow depths are supercritical and subcritical before and after the hydraulic jumps. In the subcritical region, the internal friction slope is predominant. In the supercritical region, internal and external friction terms actively contribute to numerical calculations.

Conclusion

In this study, a 1-D non-Newtonian turbulent model for non-prismatic open-channel flow was developed based on non-Newtonian rheological models and Newtonian turbulence models. The fluid friction term can be divided into two terms: internal friction and external friction. Internal friction is due to non-Newtonian viscosity and external friction is due to wall friction. The higher-order FLIC scheme and Runge–Kutta fourth-order method were used to solve the new 1-D non-Newtonian turbulence models. The approach used to solve the 1-D non-Newtonian turbulence model in this study can be used for flow estimation in oil well return flow. The flow depth prediction error varies from 2 to 8% in this study, depending on the model's assumptions and experimental results. The internal friction term is predominant in subcritical flow because laminar flow regimes participate in improving the viscous forces, at a steady state. The external friction and internal friction terms contribute to supercritical flow regimes.

Acknowledgements Economic support from the Research Council of Norway and Equinor ASA through Project No. 255348/E30 "Sensors and models for improved kick/loss detection in drilling (Semi-kidd)" is gratefully acknowledged. The authors also gratefully acknowledge Åsmund Hjulstad, Christian Berg, and Sumudhu Karunarathna for sharing knowledge about non-Newtonian rheology.

Funding This work is partially supported by the Research Council of Norway and Equinor ASA through Project No. 255348/E30.

Open Access This article is distributed under the terms of the Creative Commons Attribution 4.0 International License (http://creativecommons.org/licenses/by/4.0/), which permits unrestricted use, distribution, and reproduction in any medium, provided you give appropriate credit to the original author(s) and the source, provide a link to the Creative Commons license, and indicate if changes were made.

References

Abdo K, Riahi-Nezhad CK, Imran J (2018) Steady supercritical flow in a straight-wall open-channel contraction. J Hydraul Res. https://doi.org/10.1080/00221686.2018.1504126

Absi R (2011) An ordinary differential equation for velocity distribution and dip-phenomenon in open channel flows. J Hydraul Res 49:82–89

Agu CE, Hjulstad Å, Elseth G, Lie B (2017) Algorithm with improved accuracy for real-time measurement of flow rate in open channel systems. Flow Meas Instrum. https://doi.org/10.1016/j.flowmeasinst.2017.08.008

Akan O (2006) Open channel hydraulics. Elsevier, Amsterdam

Alderman NJ, Haldenwang R (2007) A review of Newtonian and non-Newtonian flow in rectangular open channels. Hydrotransport 17:1–20

Alderman N, Ram Babu D, Hughes TL, Maitland G (1988) The rheological properties of water-based drilling fluids. Proc Xth Int Congr Rheol 1:140–142

Aslannezhad M, Khaksar manshad A, Jalalifar H (2016) Determination of a safe mud window and analysis of wellbore stability to minimize drilling challenges and non-productive time. J Pet Explor Prod Technol 6:493–503. https://doi.org/10.1007/s13202-015-0198-2

Bailey WJ, Peden JM (2000) A generalized and consistent pressure drop and flow regime transition model for drilling hydraulics. SPE Drill Complet 15:44–56. https://doi.org/10.2118/62167-PA

Bonakdari H, Larrarte F, Lassabatere L, Joannis C (2008) Turbulent velocity profile in fully-developed open channel flows. Environ Fluid Mech 8:1–17. https://doi.org/10.1007/s10652-007-9051-6

Burger J, Haldenwang R, Alderman N (2010) Friction factor-Reynolds number relationship for laminar flow of non-Newtonian fluids in open channels of different cross-sectional shapes. Chem Eng Sci 65:3549–3556. https://doi.org/10.1016/j.ces.2010.02.040

Chhabra RP, Richardson JF (2011) Non-Newtonian flow and applied rheology : engineering applications, 2nd edn. Butterworth-Heinemann, Oxford

Chhantyal K (2018) Sensor data fusion based modelling of drilling fluid return flow through open channels. University of South-Eastern Norway, Notodden

Chhantyal K, Viumdal H, Mylvaganam S (2017) Soft sensing of non-Newtonian fluid flow in open Venturi channel using an array of ultrasonic level sensors—AI models and their validations. Sensors (Switzerland). https://doi.org/10.3390/s17112458

Chow VT (1959) Open-channel hydraulics. McGraw-Hill, New York

Douglas JF, Gasiorek JM, Swaffield JA (2001) Fluid mechanics, 4th edn. Prentice Hall, Harlow

Ellison SLR, Rosslein M, Williams A (2000) EURACHEM/CITAC Guide CG 4, Quantifying uncertainty in analytical measurement. In: Quantifying uncertainty in analytical measurement, 2 edn. Eurachem

Fread DL (1988) The NWS DAMBRK model: Theoretical background/user documentation. Hydrol Res Lab, National Weather Service, NOAA

Fread DL (1993) Flow routing. In: Maidment DR (ed) Handbook of hydrology, Chapter 10. McGrawHill, New York, USA, pp 10.6–10.7

Haldenwang R (2003) Flow of non-newtonian fluids in open channels. Cape Technikon, Cape Town

Han J, Jin J, Eimer DA, Melaaen MC (2012) Density of water (1)+ monoethanolamine (2)+ CO2 (3) from (298.15 to 413.15) K and surface tension of water (1) + monoethanolamine (2) from (303.15 to 333.15) K. J Chem Eng Data 57:1095–1103. https://doi.org/10.1021/je2010038

Idris Z, Kummamuru NB, Eimer DA (2017) Viscosity measurement of unloaded and CO2-loaded aqueous monoethanolamine at higher concentrations. J Mol Liq 243:638–645. https://doi.org/10.1016/J.MOLLIQ.2017.08.089

Jin M, Fread DL (1997) One-dimensional routing of mud/debris flows using NWS FLDWAV model. Debris-Flow Hazards Mitigation: Mechanics, Prediction, and Assessment 687–696

Jin M, Fread DL (1999) 1D modeling of mud/debris unsteady flows. J Hydraul Eng 125:827–834

Khodja M, Canselier JP, Bergaya F et al (2010) Shale problems and water-based drilling fluid optimisation in the Hassi Messaoud Algerian oil field. Appl Clay Sci 49:383–393. https://doi.org/10.1016/J.CLAY.2010.06.008

Kozicki W, Tiu C (1967) Non-newtonian flow through open channels. Can J Chem Eng 45:127–134. https://doi.org/10.1002/cjce.5450450302

Kurganov A, Petrova G (2007) A second-order well-balanced positivity preserving central-upwind scheme for the Saint-Venant system. Commun Math Sci 5:133–160

Liu F, Darjani S, Akhmetkhanova N et al (2017) Mixture effect on the dilatation rheology of asphaltenes-laden interfaces. Langmuir 33:1927–1942. https://doi.org/10.1021/acs.langmuir.6b03958

Livescu S (2012) Mathematical modeling of thixotropic drilling mud and crude oil flow in wells and pipelines—A review. J Petrol Sci Eng 98–99:174–184. https://doi.org/10.1016/J.PETROL.2012.04.026

Longo S, Chiapponi L, Di Federico V (2016) On the propagation of viscous gravity currents of non-Newtonian fluids in channels with varying cross section and inclination. J Nonnewton Fluid Mech 235:95–108. https://doi.org/10.1016/J.JNNFM.2016.07.007

Maglione R, Robotti G, Romagnoli R (2000) In-situ rheological characterization of drilling mud. SPE J 5:377–386. https://doi.org/10.2118/66285-PA

Manning R (1891) On the flow of water in open channels and pipes. Inst Civil Eng Ireland Trans 20:161–207

Mozaffari S, Tchoukov P, Atias J et al (2015) Effect of asphaltene aggregation on rheological properties of diluted athabasca bitumen. Energy Fuels 29:5595–5599. https://doi.org/10.1021/acs.energyfuels.5b00918

Nezu I, Nakagawa H, Jirka GH (1994) Turbulence in open-channel flows. J Hydraul Eng 120:1235–1237

Piroozian A, Ismail I, Yaacob Z et al (2012) Impact of drilling fluid viscosity, velocity and hole inclination on cuttings transport in horizontal and highly deviated wells. J Pet Explor Prod Technol 2:149–156. https://doi.org/10.1007/s13202-012-0031-0

Rahman M, Chaudhry MH (1997) Computation of flow in open-channel transitions. J Hydraul Res 35:243–256. https://doi.org/10.1080/00221689709498429

Sanders BF, Iahr M (2001) High-resolution and non-oscillatory solution of the St. Venant equations in non-rectangular and non- prismatic channels. J Hydraul Res 39:321–330. https://doi.org/10.1080/00221680109499835

Sarma KVN, Lakshminarayana P, Rao NSL (1983) Velocity distribution in smooth rectangular open channels. J Hydraul Eng 109:270–289

Slatter PT (1995) Transitional and turbulent flow of non-Newtonian slurries in pipes. University of Cape Town, Cape Town

Stearns FP (1883) A reason why the maximum velocity of water flowing in open channels is below the surface. Trans Am Soc Civ Eng 7:331–338

Toro EF (2009) Riemann solvers and numerical methods for fluid dynamics-a practical introduction, 3rd edn. Springer, Heidelberg

Versteeg HK, Malalasekera W (2007) An introduction to computational fluid dynamics : the finite method, vol 2. Pearson Education Ltd, Bengaluru

Welahettige P, Lie B, Vaagsaether K (2017a) Computational fluid dynamics study of flow depth in an open Venturi channel for Newtonian fluid. In: Proceedings of the 58th SIMS. Linköping University Electronic Press, Reykjavik, pp 29–34

Welahettige P, Lie B, Vaagsaether K (2017b) Flow regime changes at hydraulic jumps in an open Venturi channel for Newtonian fluid. J Comput Multiph Flows. https://doi.org/10.1177/1757482x17722890

Welahettige P, Vaagsaether K, Lie B (2018) A solution method for 1-D shallow water equations using FLIC scheme for open Venturi channels. J Comput Multiph Flows 10(4):228–238. https://doi.org/10.1177/1757482X18791895

Yang S-Q, Tan S-K, Lim S-Y (2004) Velocity distribution and dip-phenomenon in smooth uniform open channel flows. J Hydraul Eng 130:1179–1186

Publisher's Note Springer Nature remains neutral with regard to jurisdictional claims in published maps and institutional affiliations.

Paper 6

A Real-Time Flow-Measuring Algorithm for Open Venturi Channel Non-Newtonian Flow

This paper is published in the International Journal of Petroleum Science and Technology.

International Journal of Petroleum Science and Technology
ISSN 0973-6328 Volume 13, Number 1 (2019), pp. 1-7
© Research India Publications
http://www.ripublication.com

A Real-Time Flow-Measuring Algorithm for Open Venturi Channel Non-Newtonian Flow

Prasanna Welahettige, Bernt Lie, Knut Vaagsaether

Department of Process, Energy and Environmental Technology
University College of Southeast Norway, Porsgrunn, Norway.

Abstract

A real-time flow measuring algorithm is developed for the open Venturi channel non-Newtonian flow measurement. Using a single level sensor reading at downstream of the open Venturi channel, a drilling-well return flow rate can be calculated in real time. The experiments are conducted with different flow rates with step changes in pump outlet flow rate. The Coriolis flowmeter readings used to validate the calculated flow rates based on the level sensors. Three levels sensors record the reading when channel at a horizontal inclination. The level sensors are located at upstream of the Venturi contraction, near to the Venturi contraction and after the Venturi contraction. The minimum error occurs from the level sensor located near to the Venturi contraction. The strong subcritical flow regimes give a less disturbance for real-time flow measurements. The 1-dimensional flow model well employed subcritical flow than the supercritical flow. We recommend locating the level sensor near to the Venturi contraction, where the maximum subcritical flow occurs.

1 INTRODUCTION

Open Venturi channel Newtonian and Non-Newtonian flow models were developed in our previous studies (Welahettige et al., 2018, 2019). In this study, we develop a real-time flow-measuring algorithm to measure the mud return in well drilling in open Venturi channels. The motivation behind the study is to develop a new flow sensor technology for the kick and loss detection in well drilling. Agu et al. (2017) introduced a flow measuring algorithm for open channels, using two sensor readings. Jinasena et al. (2018) proposed a model based real-time flow rate estimation method for open channel.

2 EXPERIMENTAL SETUP

The objective of the flow measurement is to find the channel inlet flow rate, which is equal to the pump outlet flow rate. In the real field, the wellbore outlet flow rate is equal to the channel inlet flow rate. Figure 1 shows the flow loop of the experimental setup.

Three level sensors are used to measure the flow depth of the open Venturi channel, and a Coriolis flowmeter is located between the buffer tank and the mud pump. The Coriolis flow meter readings are used to validate the numerical result. The ultrasonic level sensors accuracy is ±0.25 %, and the Coriolis mass flow meter accuracy is ±0.1 %.

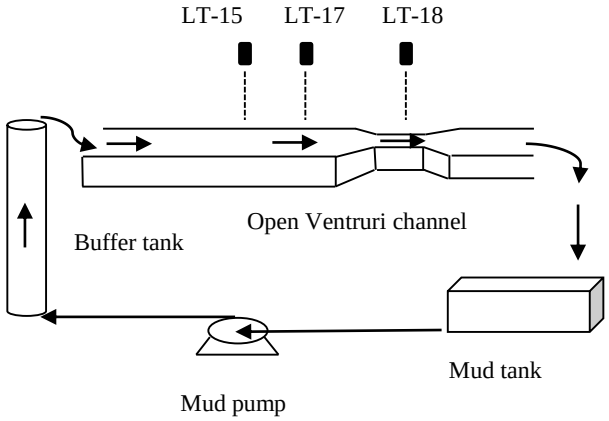

Figure 1. Flow loop of the experimental setup: The Coriolis flow meter is located between pump outlet and buffer tank. Three level sensors LT-15, LT-17 and LT-18 are located along the channel central axis.

3 ALGORITHM FOR FLOW RATE CALCULATION

The Saint-Venant equations for the non-Newtonian turbulent flow can be present as follow (Welahettige et al., 2019),

$$\frac{\partial A}{\partial t} = -\frac{\partial (Au)}{\partial x}, \tag{1}$$

$$\frac{\partial (AV)}{\partial t} = -\frac{\partial (AV^2)}{\partial x} - \frac{\partial (k_{g_1} Ah)}{\partial x} g + k_{g_2} h^2 g \frac{\partial b}{\partial x} + Ag \sin\alpha - S_e - S_i. \tag{2}$$

Here, A is the cross-sectional area of the channel, which is a function of flow depth h. V is the average velocity, k_{g_1} and k_{g_1} are model parameters, α is the channel inclination angle, S_e is the external friction slope, S_i is the internal friction slope, b is the bottom width. The internal friction slope is calculated from based on the Herschell-Bulkley model, and the external friction is calculated from the Manning's friction model (Welahettige et al., 2019). The FLIC scheme and Runge-Kutta 4th order explicit scheme are used to solve the Equation-1 and 2. The finite volume method is used to discretize the fluid domain.

The algorithm is developed to calculate the inlet flow rate of the channel by using the level sensor readings at downstream, see figure 2. Here, we used only one level sensor reading to measure the flow rate in the open Venturi channel. The buffer tank outlet flow enters to the channel in gravity. The buffer tank inlet is elevated from the channel bottom level, which can be elevated up to 2-3 times of flow depth. Therefore, the flow regimes are always supercritical at the inlet. The inlet flow depth can keep as a constant by varying the inlet velocity to calculate the flow rate. We have noticed that same flow

depth can achieve in the downstream for different inlet flow depth but same flow rate. The contraction section of the open channel makes a significant variation of the flow regimes. The upstream hydraulic jump neutral the inlet variation between the A and V for the same flow rate.

Previous time step conserved variables are used as the initial condition for the spatial domain. When the iteration starts the first time, the initial conditions are fixed to low flow depth and low velocities. This method might help to avoid unnecessary large the overshoot and undershoot in the numerical result.

Step-1: Calculate the h and V for the whole fluid domain from the interface fluxes. The FLIC scheme and the source term splitting method can be used (Toro, 2009; Welahettige et al., 2018). Here, $i = 1, 2, \ldots L$. L is the last control volume of the 1-D fluid domain.

Step-2 and Step-3: Calculate for the time iteration for the all the control volume. Calculate until $t = T$, where T is the step length of the level sensor reading.

Step-4: Check the difference between calculated flow depth (h_c) and the measured flow depth (h_m) at the same location of the channel. If the difference is an acceptable level, the flow rate is $Q = A_0 V_0$. If not, set the inlet condition into new values. Here h_c is the calculated flow depth of a control volume where it is the same location of the level sensor.

Set: $h_m > h_c$means, the guessed inlet flow rate is lower than the actual flow rate. Therefore increase the inlet flow velocity by $V_0 = V_0 + \Delta V$. $h_m < h_c$ means, the guessed flow rate higher than the actual flow rate. Therefore reduce the inlet flow velocity by $V_0 = V_0 - \Delta V$. Then return to the step-1.

4 RESULTS

The real-time experiment results used to validate the numerical model result. The open Venturi channel is at the horizontal inclination. The level sensors LT-15, LT-17 and LT-18 are located at the centerline of the channel, and the distances from the inlet of the channel are 2.12 m, 2.42 m and 3.2 m respectively. The level sensors readings (experimental results) are shown in Figure 3. The step changes occur at $t = 35$ s and $t = 158$ s. Due to the turbulent wave motion, a noisy result came out from the level sensors. LT-15 level height is comparatively small all the time, which is due to the level sensor located at transitional region of supercritical to subcritical flow. Generally, the supercritical flow has a lower flow depth than the subcritical flow. The level sensors LT-17 and LT-18 show similar flow height even though they are placed before and after the Venturi contraction.

Based on the level sensor online measurements, the flow rates are calculated using the developed algorithm. Figure 4 shows a comparison of the calculated flow depth and the Coriolis flowmeter reading in the real time. We want to emphasize the flow measuring ability, at the real-time in this study. Therefore, the experimental results are raw data, without smooth by the filtering. Figure 4 shows the calculated flow rate and the Coriolis flowmeter reading in real time based on the level sensor readings. Compared to the LT-18, the LT-15 and LT-17 readings give a good match with the pump outlet flow rates.

5 DISCUSSION

The calculation speed can improve by increasing the Δh and ΔV values. However, the values affect the accuracy of the results. Here we selected 0.0001 for both Δh and ΔV. The level sensors recorde on every second. The number of iteration required to achieve 1 s of flow time is $N \approx 350$ in this study. However, we recommend achieving a steady state numerical result before starting the on-line measurement. A steady-state result can achieve by setting $N \approx 30000$ for first level sensor reading. After that, it can set to $N \approx 350$. This method increases the accuracy and reduces numerical viscosity. Depending on the channel geometry, fluid properties, and flow rate, those N values can vary.

The flow rate calculates $Q = AV$, and here have two unknown parameters A and V. To solve the Saint-Venant equations, the inlet boundary condition needs to know. In this study, we noticed that by keeping constant the Inlet A, and allowing for varying the parameter V for the same flow rate freely, can achieve the same condition downstream of the channel. Figure 5 shows a steady state flow depth variation along the channel central axis for different inlet conditions by maintaining the same inlet flow rate of 400 kg/min. The inlet flow depth varies 0.01 m to 0.025 m. However, all the cases give same flow depth near to the Venturi region and after the Venturi region. Varying only the velocity at the inlet of the open Venturi channel, same flow condition can achieve near to the Venturi contraction region. This method is quite essential for easy numerical calculations. We selected channel inlet flow depth as 0.02 m for the all the simulations flow rate 100 kg/min to 700 kg/min. The maximum flow depth achieves in all the simulations less than 0.1 m. We recommend selecting inlet flow depth minimum five times lower than maximum flow depth. Otherwise very high inlet flow velocities increase the numerical viscosities.

The average error between the numerical and experimental results are calculated from, $\frac{1}{N_{total}} \sum_{j=1}^{T_{end}} \left| \dot{m}_{m,j} - \dot{m}_{c,j} \right| / \dot{m}_{m,j}$. Here, $\dot{m}$ is the mass flow rate, T_{end} is the end time, N_{total} is the total number of level sensor readings. The average errors are 6.3 %, 4.1 % and 13.8 % respectively from LT-15, LT-17 and LT-18 level sensors based flow rate calculations. Based on this result, we can conclude that the best location to place the level sensor is near to the Venturi contraction (just before the Venturi contraction begins). Near to the Venturi contraction, flow regimes are stable compared to the other region of the channel. Minimum disturbances occur near to the Venturi contraction due to strong subcritical flow.

Even though the sudden step changes occur in the pump outlet flow rate, the simulated results gradually vary the flow rate. The time required to reach the level sensors location of the fluid flow might be the reason to make a difference between the experiment and the simulation at the step changes. The algorithm is suitable for online flow rate measurement in given viscosities and densities. Further, it needs to develop for online varying viscosity and density parameters of the return fluid.

6 RECOMMENDATIONS

- Place the level sensor near to the Venturi contraction (just before the Venturi contraction begins) for accurate flow measurement, when channel inclination at horizontal.
- After reach to the steady-state numerical condition, start the online measurement: This increases the stability of the algorithm.
- If the channel length very long after the Venturi region; the fluid domain after the Venturi region might be insignificant.

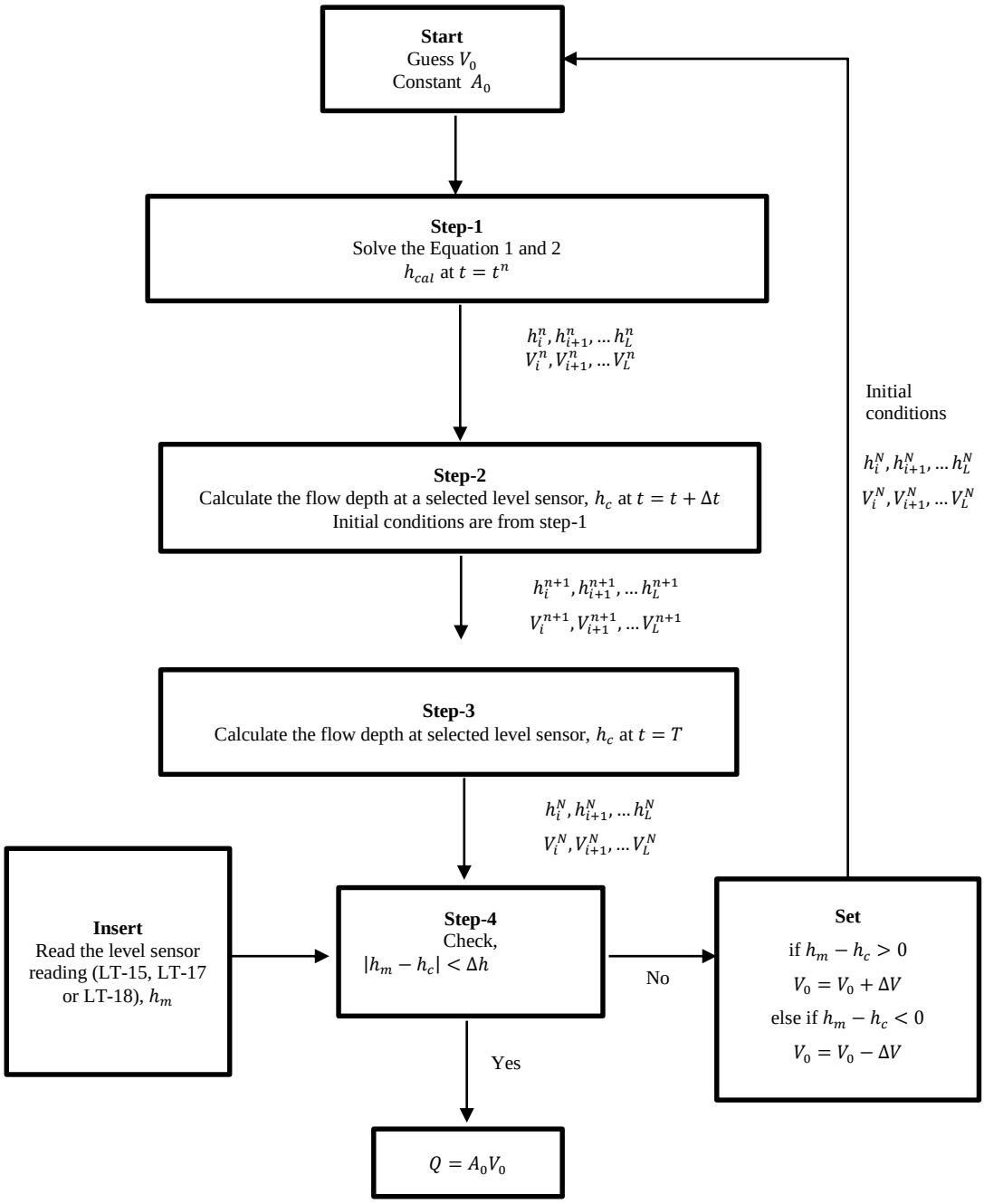

Figure 2. Algorithm for calculating the open Venturi channel flow rate in real time.

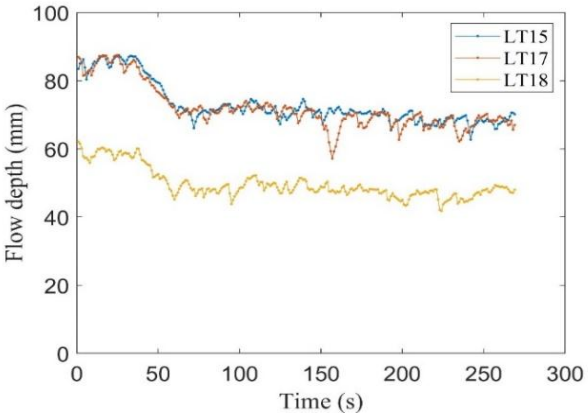

Figure 3. The real-time experimental results of level sensors readings. The channel angle is at horizontal.

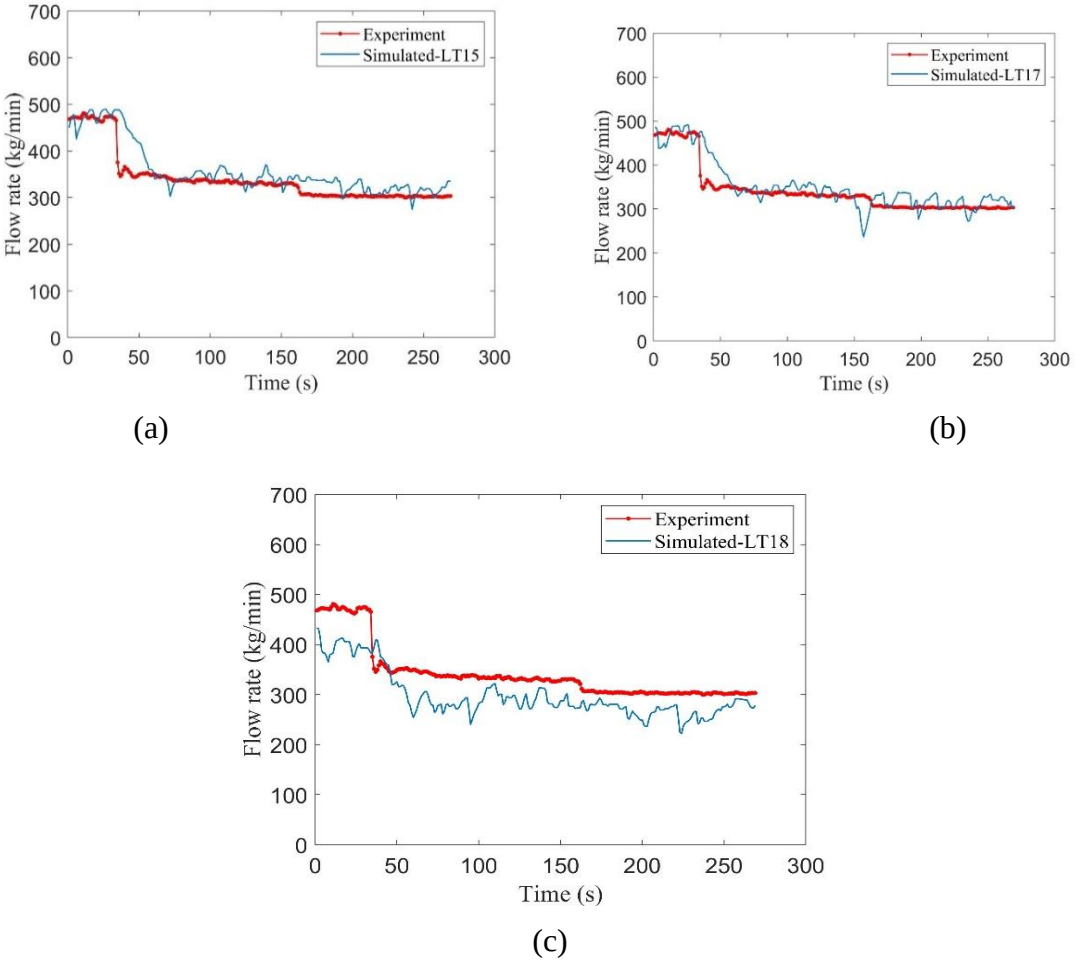

Figure 4. Mass flow rate experimental and simulated when the channel inclination at horizontal: (a) Flow rate calculation based on LT-15 level sensor reading

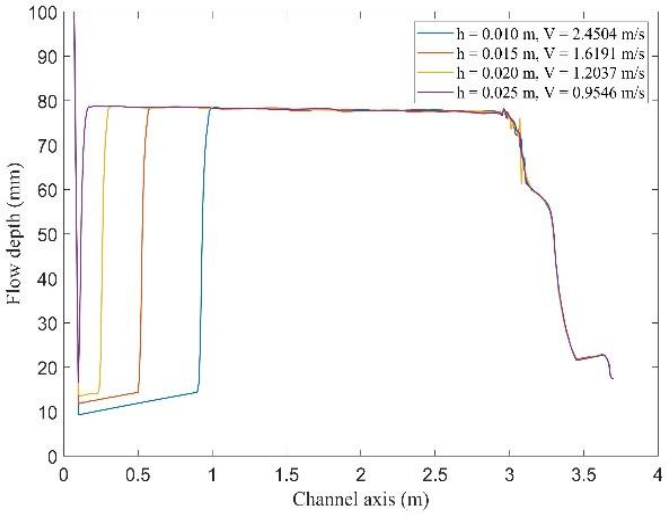

Figure 5. At steady state flow depth variation along the channel axis for different inlet condition for the same flow rate of 400 kg/min.

ACKNOWLEDGMENT

Economic support from The Research Council of Norway and Statoil ASA through project no. 255348/E30 "Sensors and models for improved kick/loss detection in drilling (Semi-kidd)" is gratefully acknowledged.

REFERENCES

[1] Agu, C.E., Hjulstad, Å., Elseth, G., Lie, B., 2017. Algorithm with improved accuracy for real-time measurement of flow rate in open channel systems. Flow Meas. Instrum. 57, 20–27.

[2] Jinasena, A., Ghaderi, A., Sharma, R., 2018. Modeling and Analysis of Fluid Flow through A Non-Prismatic Open Channel with Application to Drilling.

[3] Toro, E.F., 2009. Riemann solvers and numerical methods for fluid dynamics-A Practical Introduction, 3rd ed, Book. Springer Science & Business Media, Heidelberg.

[4] Welahettige, P., Lundberg, J., Bjerketvedt, D., Lie, B., Vaagseather, K., 2019. 1-Dimensional Non-Newtonian (drilling mud) turbulent modelling for non-prismatic channels. J. Nonnewton. Fluid Mech. Submited.

[5] Welahettige, P., Vaagsaether, K., Lie, B., 2018. A solution method for 1-D shallow water equations using FLIC scheme for open Venturi channels. J. Comput. Multiph. Flows 10(4), 228–238.

Paper 7

Computational fluid dynamics study of the effects of drill cuttings on the open channel flow

This paper is submitted to the International Journal of Chemical Engineering.
doi.org/10.1155/2019/6309261

Hindawi
International Journal of Chemical Engineering
Volume 2019, Article ID 6309261, 9 pages
https://doi.org/10.1155/2019/6309261

Research Article

Computational Fluid Dynamics Study of the Effects of Drill Cuttings on the Open Channel Flow

Prasanna Welahettige,[1] **Christian Berg**,[1,2] **Joachim Lundberg**,[1] **Bernt Lie**,[1] **and Knut Vaagsaether**[1]

[1]*Department of Process, Energy and Environmental Technology, University of South-Eastern Norway, Porsgrunn 3918, Norway*
[2]*Kelda Drilling Controls, Porsgrunn 3933, Norway*

Correspondence should be addressed to Knut Vaagsaether; knut.vagsather@usn.no

Received 23 April 2019; Revised 18 July 2019; Accepted 31 July 2019; Published 22 August 2019

Academic Editor: Sébastien Déon

Copyright © 2019 Prasanna Welahettige et al. This is an open access article distributed under the Creative Commons Attribution License, which permits unrestricted use, distribution, and reproduction in any medium, provided the original work is properly cited.

A three-dimensional computational fluid dynamics (CFD) study was carried out for drilling fluid flow with drill cuttings in open channels. The flow is similar to the return flow when drilling, stream containing drilling fluid, and drill cuttings. The computational model is under the framework of the Eulerian multifluid volume of the fluid model. The Herschel–Bulkley rheological model was used to describe the non-Newtonian rheology of the drilling fluid, and the computational model was validated with experimental results for two-phase flow in the literature. The effect of flow depth and flow velocity in an open channel was studied for drill cutting size of up to 5 mm and for a solid volume fraction of up to 10%. For constant cross section and short open channels, the effect of drill cuttings on flow depth and mean velocity was found to be small for particle sizes less than 5 mm and solid volume fractions less than 10%. High momentum force in the downward direction can carry the solid-liquid mixture at higher velocities than a lower density mixture. Higher inclination angles mean that the gravity effect upon the flow direction is more significant than the particle friction for short channels.

1. Introduction

Open Venturi channel flow measurement might be an alternative to expensive Coriolis flow meters in measuring well return flows while drilling [1]. It can also be an alternative in conventional drilling when there is no choke and where flow is "always" open channel, Coriolis therefore not being an option. The open channel is located at the well return line in the topside of the rig (see Figure 1). Identifying the effect of drill cuttings on open channel flow is, however, a challenge.

Several studies have been carried out on sediment flow in an open channel. The particle sizes in these studies were, however, in the 1 μm to 500 μm range [2–5]. Studies of pipe flow drill cutting transport have also been carried out for various particle sizes and volume fractions [6, 7]. Ofei et al. [8] used the Eulerian-Eulerian model for drill cutting simulation of the horizontal wellbore. The annular pressure losses increase with increase in annular fluid velocity. Drill mud has higher pressure losses compared to water, and the mud has better carrying capacity, especially at smaller diameter ratios of the annulus. According to Epelle and Gerogiorgis [9], the higher pressure losses are due to higher drag by the fluid on particles and frictional effects. Whirling motion increases the particle-particle and particle-wall collisions; this is also responsible for increase in pressure drop in the annulus. Heydari et al. [10] studied CFD simulation on cuttings transport phenomena in various annuluses. They used the Herschel–Bulkley model as the rheological model, the Reynolds stress model as the turbulence model, and the Wen and Yu drag model as the drag model. Near the wall of horizontal annulus flow, cuttings do not flow easily, and velocity becomes almost zero. Pang et al. [11] studied three regions of cuttings in a horizontal annulus flow: a fixed bed region, a moving bed region, and a suspension region. The cuttings suspension region contributes as a major cuttings transport method in a horizontal

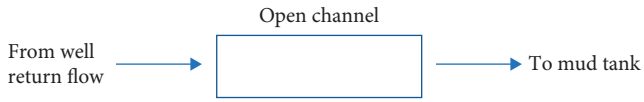

Figure 1: The open channel is located between the choke valve and the mud tank.

annulus. The height of the cuttings bed decreases with increase in effective viscosity of the drilling fluid in annulus flow [12]. Increase in effective viscosity can reduce the cuttings bed area [13].

According to the Muste et al.'s [4] experimental study on water-particle flow in open channel flow, bulk velocity of flow is reduced as particle concentration increases and suspended particles affect turbulence mechanisms over the inner region of the flow. Jha and Bombardelli [2] developed a two-phase model for the transport of nonuniform suspended sediment in an open channel (water and sediment). The influence of particle size is significant for the mean velocity. Increase in the particle concentration in the bed only affects the turbulent kinetic energy [14]. A laminar flow occurs in open channel slurry flows if the yield stress is significantly high. Coarse particle settling might affect the height of vertical flow depth [5]. The Sanders et al. [15] and Spelay's [5] experimental studies involve coarse sand slurries in an open channel flow. Treinen [16] and Talmon et al. [17] studied shear settling in laminar open channel flow numerically.

Drill cuttings have a size range from clay-sized particles to coarse gravel, 2 μm to more than 30 mm [18], the highest concentration of particle size in well drilling being 4 mm. According to the literature, the volumetric fraction of cuttings is normally less than 5% for trouble-free annulus operations [19, 20]. There has, however, to the best of our knowledge, not been published much on drill cuttings flow in open channel flow. This study therefore aims to contribute to the lack of knowledge on the cuttings effect upon open channel flow depth and velocity profile. Non-Newtonian drilling fluid flow with drill cuttings was studied in this paper using CFD simulations, the CFD model being validated using the experiment results from the literature. The primary objective of the study was to identify the effect of drill cuttings and particle settling on open channel flow depth.

2. CFD Model

An Eulerian multifluid volume of the fluid model (multifluid VOF) was used for the simulation of the granular particles. Each phase is a continuous phase. Three phases are considered in this study. The governing continuity equation for the q^{th} phase (g, l, and s phases, respectively, air, drilling fluid, and drill cuttings) is

$$\frac{\partial \alpha_q \rho_q}{\partial t} + \nabla \cdot \left(\alpha_q \rho_q \vec{u}_q\right) = 0. \quad (1)$$

There are three equations similar to equation (1) for each phase. There is no net mass transfer between phases. The total volume fraction is equal to unity, $\alpha_g + \alpha_l + \alpha_s = 1$. The momentum conservation equation for the q^{th} phase [7, 21, 22] is

$$\frac{\partial \alpha_q \rho_q \vec{u}_q}{\partial t} + \nabla \cdot \left(\alpha_q \rho_q \vec{u}_q \vec{u}_q\right) = -\alpha_q \nabla P + \nabla \cdot \bar{\bar{\tau}}_q + \alpha_p \rho_q \vec{g} + \sum_{i=1}^{2} \beta_{qi}\left(\vec{u}_i - u_q\right) + \left(\vec{F}_{\text{lift},q} + \vec{F}_{\text{Vm},q}\right). \quad (2)$$

There are, one for each phase, three momentum equations from equation (2). Densities are constant. The effective viscosity of the drilling fluid was calculated using the Herschel–Bulkley model. Drill cuttings are considered to be spherical, monotonous (same size and shape), granular, and solid particles. Several interactions can occur in open channel flow: air-drilling fluid, drilling fluid-drill cuttings, drill cuttings-drill cuttings, wall-drill cuttings, wall-drilling fluid, drilling fluid-drilling fluid, and air-drill cuttings. Here, air-drill cuttings interaction can be neglected by assuming that the particles are submerged in the drilling fluid. The gas-liquid interface drag was calculated using the Schiller and Naumann drag model [23, 24]. Solid-liquid interface drag was calculated using the Wen and Yu drag model [25]. Lift force and virtual mass forces were neglected for the gas phase due to the secondary phase densities being more significant than the gas density [26]. The ANSYS Fluent 18.2 commercial CFD tool was used for the simulations.

Figure 2 shows the multifluid VOF method computing cycle in transient condition for two-phase flow. Here, the discretized momentum equation is solved using a guessed pressure field in the initial step (the previous iteration result being used after this), to yield the velocity field. The pressure correction terms can be found from the calculated velocity field and the continuity equation. The corrected pressure and velocity fields can be calculated from the calculated pressure correction and velocity correction terms. An assumption in the SIMPLE algorithm is that the velocity corrections for the neighboring cells are omitted in each iteration cycle. However, the omission terms do not affect the final solution because the correction factors become zero in a converged result [27].

3. Simulation Parameters

A rectangular channel was used for the 3D CFD simulations. The channel length was 1 m, width 0.3 m, and height 0.2 m. The mesh had 0.7 million structured hexahedral elements including inflation near the walls (see Figure 3).

The inflation layers were added for accurately capturing the flow effects near the walls. The average mesh size was 25 mm, which is 5 times larger than the largest particle size used in the study. This avoids particles spanning the many fluid cells. Edge sizing was implemented to improve the resolution of the mesh. The mesh had low skewness (<0.8) and high orthogonality (>0.9). To optimize the grid sizes until the results become independent of grid size, a grid independence study was conducted. The inlet drill cutting mass flow rate was 1.12599 kg/s. The outlet drill cutting mass flow rate was monitored for different mesh sizes in the test. The results were taken after reaching the steady state. Table 1 shows the mesh specification for different meshes. Figure 4 shows a solid mass flow rate comparison for the different

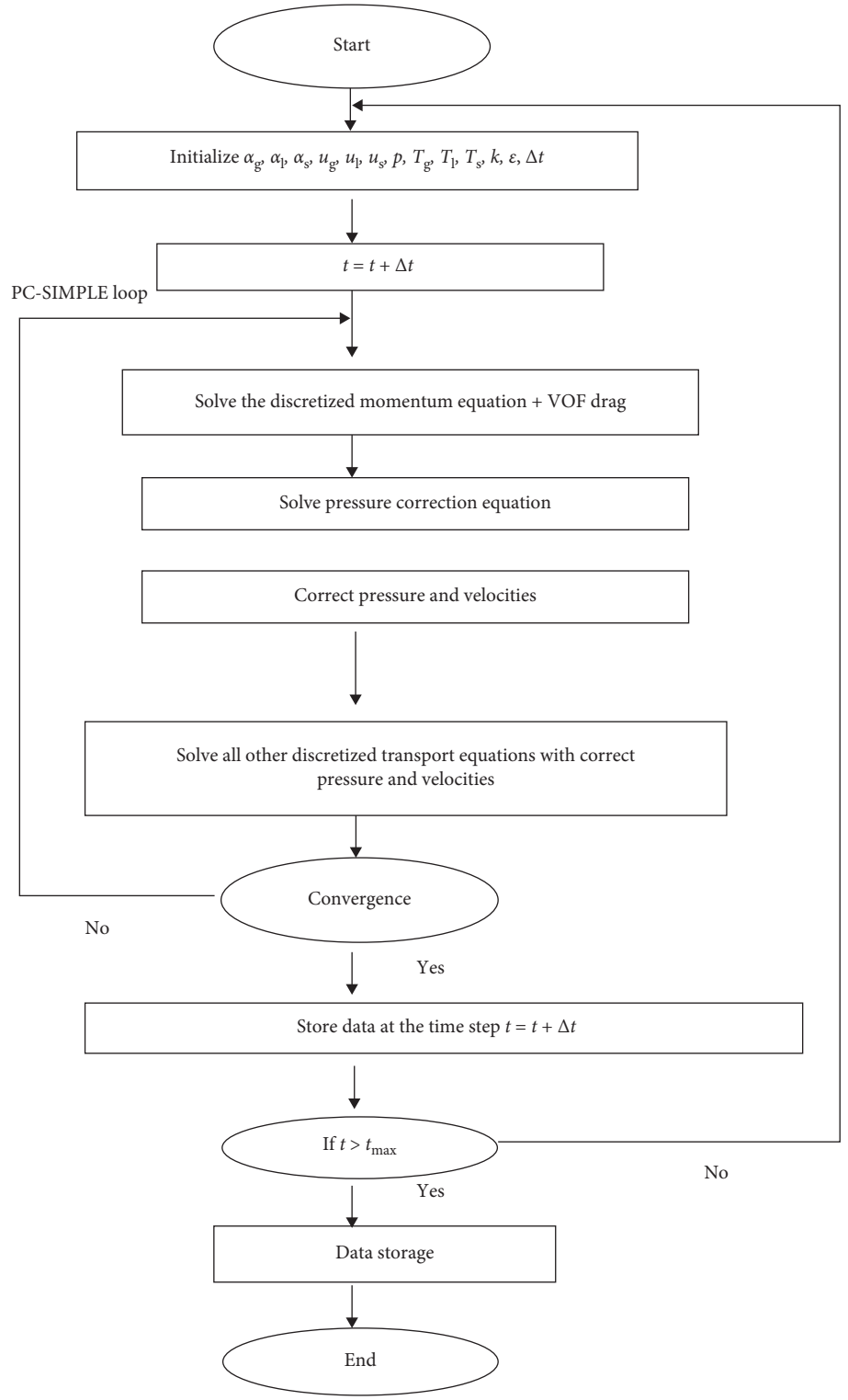

Figure 2: Computing cycle of transient multifluid VOF model for three-phase flow.

meshes. Mesh 3 and Mesh 4 give good mass balance at steady-state condition. Mesh 3 was used for further studies because it has comparatively fewer numbers of elements than Mesh 4.

The drilling fluid used in this study was taken from Kelessidis et al.' study [28]. The fluid has a high yield stress, and the other properties are given in Table 2. Drill cutting and drilling fluid enter the channel as a mixture at the same inlet velocity.

Based on the maximum Courant number, the time step is refined near the free surface in VOF calculations. The maximum allowed Courant number is 0.25 in this study. The

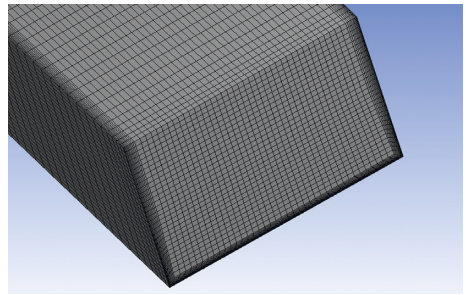

Figure 3: 3D section of meshed open channel geometry. The rectangular channel height, width, and length are, respectively, 0.2 m, 0.3 m, and 1 m.

Table 1: Different mesh for mesh independency check.

	Mesh 1	Mesh 2	Mesh 3	Mesh 4	Mesh 5	Mesh 6
Hexahedral cells	0.342	0.487	0.7	1.02	1.35	1.93

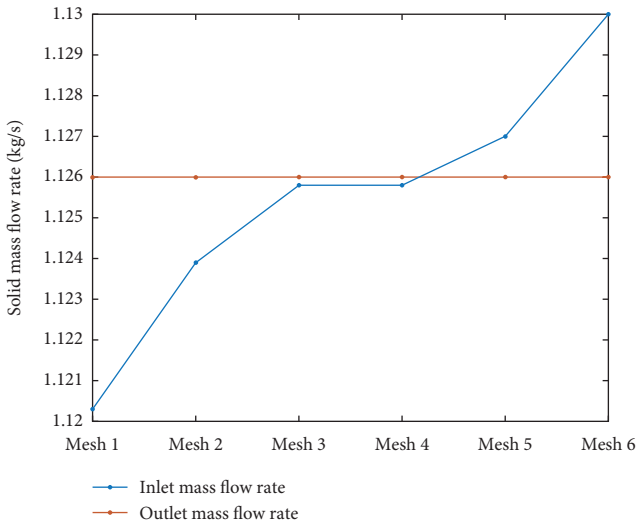

Figure 4: Solid mass flow rate comparison for different meshes. The number of elements in each mesh is given in Table 1.

global Courant number depends on the mesh size, velocity field, and time step size used for the transport equations. Volume fraction values are computed at the previous time step in the explicit approach of the multifluid VOF model, and the standard finite-difference interpolation scheme is used in ANSYS Fluent [26]. The simulation carried out in the transient condition and the time step was maintained at less than 0.001 s for two-phase flow and 0.0001 s for three-phase flow, to achieve converged results. These time steps allow keeping the global Courant number less than two. The flow time is 20 s in each simulation; in this condition, the fluid domain reached the steady state. The steady-state condition was monitored after a constant solid-phase flow rate was reached at the outlet. The no-slip condition applies to the wall-fluid and wall-particle. The pressure field is assumed to be shared by all three phases, this being in proportion to their volume fraction [22]. The solid particle maximum packing fraction is 0.63 for the spherical shape. Particle-particle and wall-particle restitution coefficients were, respectively, 0.9 and 0.09 [6]. The inlet was considered as a velocity inlet. The inlet velocities are constants for all three phases. Air volume flow rate at the inlet became zero for the cases. The outlet and top boundaries are considered as pressure outlets. The pressure outlets are at atmospheric pressure. Air is the primary phase, and drilling fluid and drill cuttings are considered to be the secondary phases. The gas-liquid surface tension coefficient was set to 0.072 N/m due to the water-based drilling fluid and slurries considered in this study. The spatial discretization schemes for gradient, momentum, volume fraction, turbulent kinetic energy, and turbulent dissipation rates are, respectively, least square cell-based, first-order upwind, compressive, second-order upwind, and second-order upwind. The Eulerian multifluid VOF model and the sharp-disperse interface modeling method were used to describe the flow of each phase. The standard $k - \varepsilon$ model is used to model turbulence using the second-order upwind scheme. The phase-coupled semi-implicit method for pressure-linked equations (SIMPLE) algorithm solves the pressure-velocity coupling. Transient formulation is based on the first-order implicit scheme.

The computational method is due to the lack of experimental results for heavy particle non-Newtonian open channel flow and high computation cost, validated for an experimental case of two-phase non-Newtonian flow in open channel. Haldenwang's [29] experiments with the flow of Kaolin slurry in an open channel were used to validate the two-phase model. The two phases in these experiments were slurry and air above the free surface. The slurry contained small solid Kaolin particles. The experiments were conducted in a rectangular 10 m long and 0.3 m wide channel. The rheology of the Kaolin slurry was described using the Herschel–Bulkley model.

Table 2: Simulation flow parameters. Case 1 is used in this study. Case 2 is used for model validation.

	Case 1	Case 2
Fluid and solid	Water-bentonite suspension [28]	10% v/v Kaolin slurry [29]
Fluid density (kg/m^3)	1165	1303
Particle density (kg/m^3)	2650	—
Mean particle diameter (mm)	5, 1	—
Inlet solid volume fraction (%)	5, 10	—
Inlet velocity (m/s)	1	0.567
Shape of the channel	Rectangular	Rectangular
Channel inclination	3	2
Yield stress τ_y (Pa)	11.3025	21.311
Flow consistency index k (Pa·s^n)	5.9115	0.524
Flow behavior index n	0.2645	0.468

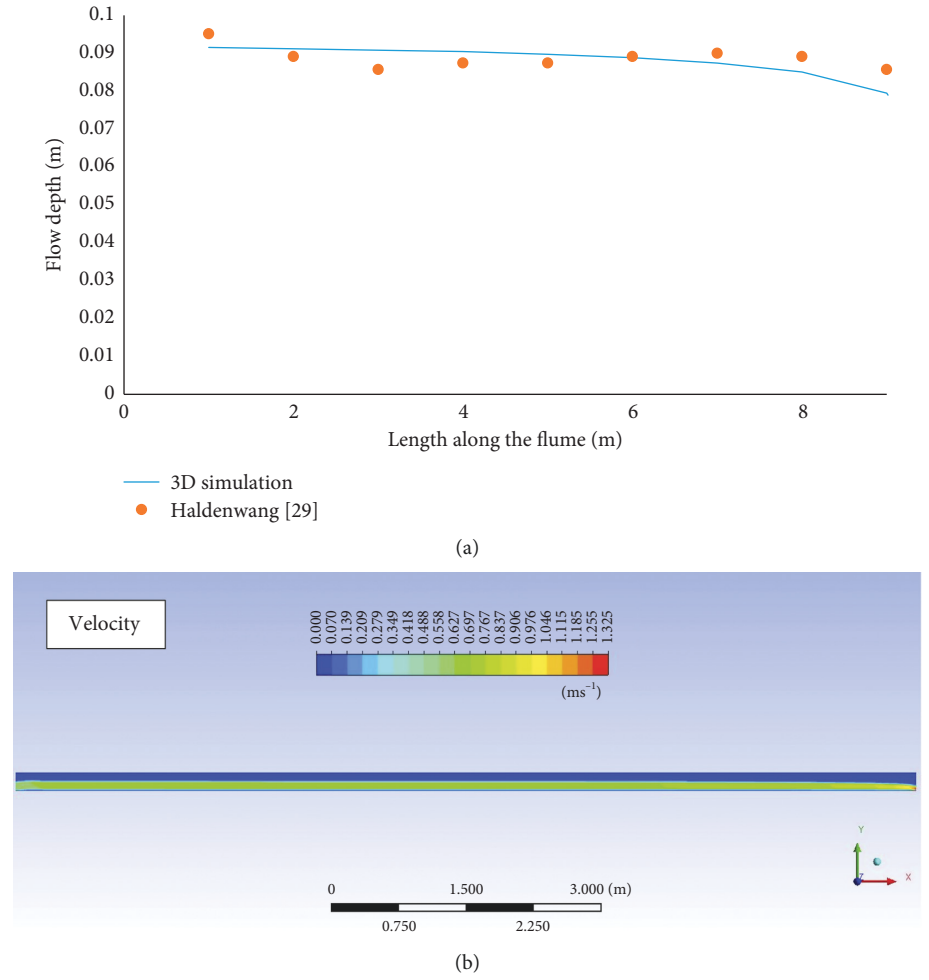

Figure 5: Case 2: (a) a comparison between the 3D CFD result and the Haldenwang [29] experimental results for flow depth along the channel axis at steady state. The channel length is 10 m, and the width is 0.3 m. The fluid properties of Case 2 are given in Table 2. (b) Velocity profile, the flow direction is left to right.

4. Results and Discussion

4.1. 3D CFD Results Validation Using Literature Experimental Results. The two-phase CFD model was validated using the experimental results published by Haldenwang [29]. A comparison between the 3D CFD simulation and the Haldenwang [29] experiment results is shown in Figure 5. Flow depth was measured after the steady state, at flow time 249 s in the simulation. The free surface was captured from the VOF model. The fluid used in the experiments contained 10% Kaolin particles, ranging from 0.001 mm to 0.01 mm. The 3D simulation, however, considered the average fluid density that is based on the volume fraction of Kaolin and water. In the experiment, fluid enters the channel from a

buffer tank. A rectangular inlet geometry was used in the simulation. There, therefore, may be a discrepancy between the inlet conditions. The accuracy of the experimental result is 5%, and the simulated result accuracy is 6% for the experimental results. The 3D CFD result is therefore within the accuracy limit.

Open channel length should be considerably longer if a fully developed flow profile is to be achieved [5, 29]. A 3D CFD simulation of two-phase or three-phase open channel flow takes many months of CPU time to run based on a 16-core 2.4 GHz Intel (R) CPU processor in a machine with 32 GB of RAM [6]. A short channel (length 1 m) was therefore used in this study.

4.2. Effect of Drill Cutting on the Open Channel Flow Depth. Figure 6 shows flow depths along the channel for different particle sizes and different volume fractions. The two 5% solid volume fraction cases have two different particle sizes, 5 mm and 1 mm. Flow depth variation for these two cases is, however, negligible. This is furthermore proved by the 10% volume fraction cases. The effect of drill cutting size on flow depth is not significant. The CFD results of Amanna and Khorsand Movaghar [7] for cuttings transport around a drill pipe also proved that cutting size affects cuttings transport less than the other parameters. The cases of 5 mm particle sizes with 5% and 10% volume fractions show flow depth differing between the two cases. Particle volume fraction can have a considerable impact on flow depth. Flow depth changes by 2.5% when the solid volume fraction in a dilute phase is doubled. The difference in total particle volume between the 1 mm and 5 mm cases is small due to the fewer number of particles in the dilute phase. The increase in particle friction due to the rise of the total particle volume is also small, and energy loss is negligible. Higher volume fraction gives a lower level because higher concentration acts as a higher net density. Thus, the higher density and approximately the same friction will yield a lower level.

In all cases, the flow depth reduces along the channel length, which is due to the increase in velocity in the gravity flow. The highest cutting concentration gives the lowest flow depth due to the largest momentum.

4.3. Mean Streamwise Velocity Distribution. Streamwise velocity with particles and without particles is shown in Figure 7 for the same volume flow rate. Fluids with particle flow have a higher velocity than the no-solid case due to the higher momentum of the total mass flow rate. The average velocity difference between with particle and without particle is 2-3%. The slip velocity is very small, with the average value being 0.001 m/s. This result indicates that the impact of the mean flow velocity of the drill cuttings is very small. The local slip velocity can be large in the outer region of the flow for a fully developed flow [3].

4.4. Particle Settling. Very high wall friction applies to particle flow because of higher particle concentrations ($\approx 40\%$) on the bottom. Particle settling on the bottom of the

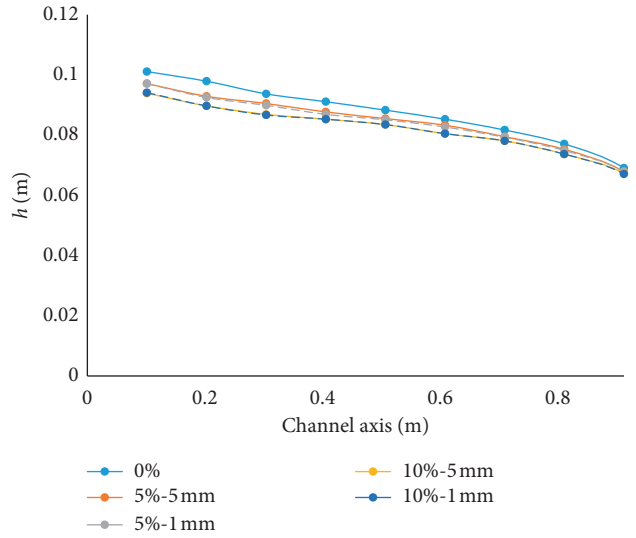

Figure 6: 3D CFD results of flow depth along the channel for different drill cuttings sizes and volume fraction at steady state. The inlet velocity is 0.5665 m/s for all cases, and the total inlet volume flow rate value is equal for each case.

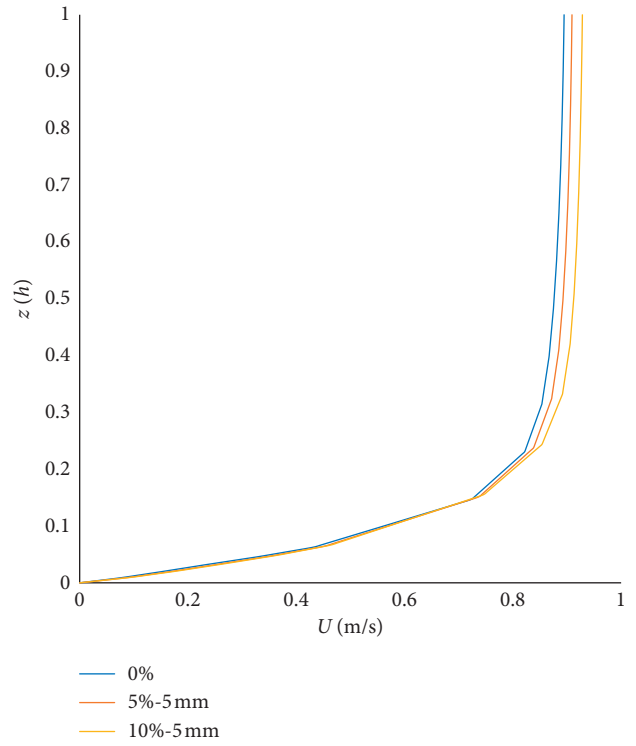

Figure 7: Steamwise velocity distribution with particle and without particle for the same inlet volume flow rate. The inlet velocity is 0.5665 m/s. The velocity is measured 0.7 m to the downstream from inlet of the channel.

open channels might lead to the simulations diverging due to the increase in turbulence. This is the main difficulty of modeling long open channel three-phase flow. This difficulty can be minimized with properly tuned under-relaxation factors and correctly chosen spatial discretization schemes. A converged result can be achieved when the time step

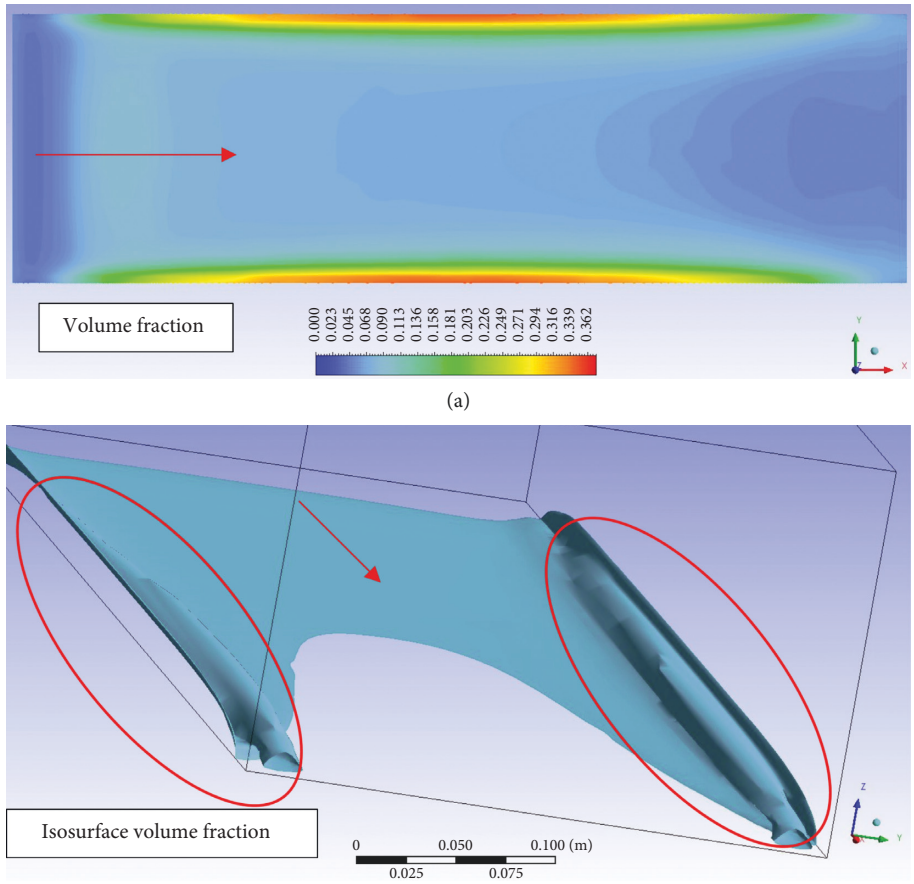

FIGURE 8: Particle settling bottom wall, the flow direction indicates by the arrow. Drill cutting size is 5 mm and inlet volume fraction is 0.05. (a) The solid volume fraction of drill cuttings on the bottom of the open channel at steady state, xy plane. (b) Isosurface of solid volume fraction at 0.08.

reaches a minimum ($<10^{-6}$ s). This, however, requires a computational time that is unrealistic. The channel used in this study is 1 m long with a low solid concentration. The short channel helped to reduce the computational time by reducing the number of computational cells. The settling distance is greater than the channel length. Particle settling is therefore considerably smaller in the channel used in this study than a long channel. Therefore, the results from this study mainly apply on to not fully developed flow. Figure 8 shows the particle volume fraction on the bottom wall at the steady state. The highest particle settling is near the sidewall and reaches 40% solid volume fraction. Due to sidewall friction, particles have lower velocities near the sidewall. Particle settling is, however, conceded to be small at the inlet and outlet of the channel due to the higher flow velocity carrying particles without these settling. At the bottom wall, particle settling is lower in the middle compared to near the sidewalls. This is due to high velocity at the middle compared to at the edges. Channel flow does not reach a fully developed condition. According to Kiger and Pan [3], the vertical direction flux of a particle is not equal to zero in the channel used. There is, therefore, no permanent settling of particles in the middle of the channel, particles in other words being suspended in the middle region of the channel. According to the experimental results of Jha [14], a maximum concentration of particles on the bed does not significantly affect the mean velocities and the distribution of particle concentration. It does, however, affect turbulent kinetic energy. We can therefore still argue that cuttings on the bed may not have a significant effect on open channel flow depth and velocities.

5. Conclusion

Drilling well return flow is a multiphase non-Newtonian flow of mainly drilling mud and drill cuttings. The effect of drill cuttings on open channel flow was studied, with the results being presented in this paper. This can be used for well return flow estimation. The multifluid VOF model 3D CFD simulations were carried out for drilling fluid flow with drill cuttings in open channels. The CFD model was validated using experiment results published in the literature. The effect of drill cutting size on flow depth was found to be small compared to the effect of the cuttings fraction. The drill cuttings volume fraction doubled from 5% to 10% in open channel flow, with the average variation of the flow depth

being 2.5%. The effect of cuttings on flow depth in well return flow modeling for a short, prismatic (constant cross section) open channel was found to be small. The conclusion might be different for long and nonprismatic channels. The increase in particle friction due to the rise of the total particle volume is also small, and energy loss is negligible. The liquid level decreases for a higher solid fraction. Higher concentration acts as a higher net density. Thus, the higher density and approximately the same friction will yield a lower flow depth.

Nomenclature

$\vec{F}_{\text{lift},q}$: Lift force of q phase (N)
$\vec{F}_{\text{Vm},q}$: Virtual mass force of q phase (N)
g: Gravity vector (m/s^2), gas phase
h: Flow depth (m)
k: Turbulence kinetic energy (m^2/s^2)
l: Liquid phase
P: Pressure shared by all phases (Pa)
s: Solid phase
T_g: Temperature of gas phase (K)
T_l: Temperature of liquid phase (K)
T_s: Temperature of solid phase (K)
$\vec{u}_q$: Three-dimensional velocity components of q phase (m/s)
U: Average velocity (m/s)
α_q: Volume fraction of q phase
α_l: Volume fraction of liquid phase
α_g: Volume fraction of gas phase
α_s: Volume fraction of solid phase
β_{qi}: Interphase momentum exchange coefficient
ε: Turbulence dissipation rate (m^2/s^3)
ρ_q: Density of q phase (kg/m^3)
$\bar{\bar{\tau}}_q$: Stress-strain tensor of q phase (Pa).

Data Availability

The CFD and experiment data used to support the findings of this study are included within the article.

Conflicts of Interest

The authors declare that they have no conflicts of interest.

Acknowledgments

The economic support provided by the Research Council of Norway and Equinor ASA through project no. 255348/E30 "Sensors and models for improved kick/loss detection in drilling (Semi-kidd)" is gratefully acknowledged. The authors thank Per Morten Hansen and Andre Vagner Gaathaug for their assistance.

References

[1] P. Welahettige, K. Vaagsaether, and B. Lie, "A solution method for one-dimensional shallow water equations using flux limiter centered scheme for open Venturi channels," *The Journal of Computational Multiphase Flows*, vol. 10, no. 4, pp. 228–238, 2018.

[2] S. K. Jha and F. A. Bombardelli, "Theoretical/numerical model for the transport of non-uniform suspended sediment in open channels," *Advances in Water Resources*, vol. 34, no. 5, pp. 577–591, 2011.

[3] K. T. Kiger and C. Pan, "Suspension and turbulence modification effects of solid particulates on a horizontal turbulent channel flow," *Journal of Turbulence*, vol. 3, p. N19, 2002.

[4] M. Muste, K. Yu, I. Fujita, and R. Ettema, "Two-phase flow insights into open-channel flows with suspended particles of different densities," *Environmental Fluid Mechanics*, vol. 9, no. 2, pp. 161–186, 2009.

[5] R. B. Spelay, "Solids transport in laminar, open channel flow of non-Newtonian slurries," Doctoral dissertation, The University of Saskatchewan, Saskatoon, Canada, 2007.

[6] S. Akhshik, M. Behzad, and M. Rajabi, "CFD-DEM simulation of the hole cleaning process in a deviated well drilling: the effects of particle shape," *Particuology*, vol. 25, pp. 72–82, 2016.

[7] B. Amanna and M. R. Khorsand Movaghar, "Cuttings transport behavior in directional drilling using computational fluid dynamics (CFD)," *Journal of Natural Gas Science and Engineering*, vol. 34, pp. 670–679, 2016.

[8] T. N. Ofei, S. Irawan, and W. Pao, "CFD method for predicting annular pressure losses and cuttings concentration in eccentric horizontal wells," *Journal of Petroleum Engineering*, vol. 2014, Article ID 486423, 16 pages, 2014.

[9] E. I. Epelle and D. I. Gerogiorgis, "A multiparametric CFD analysis of multiphase annular flows for oil and gas drilling applications," *Computers & Chemical Engineering*, vol. 106, pp. 645–661, 2017.

[10] O. Heydari, E. Sahraei, and P. Skalle, "Investigating the impact of drillpipe's rotation and eccentricity on cuttings transport phenomenon in various horizontal annuluses using computational fluid dynamics (CFD)," *Journal of Petroleum Science and Engineering*, vol. 156, pp. 801–813, 2017.

[11] B. Pang, S. Wang, Q. Wang et al., "Numerical prediction of cuttings transport behavior in well drilling using kinetic theory of granular flow," *Journal of Petroleum Science and Engineering*, vol. 161, pp. 190–203, 2018.

[12] B. Pang, S. Wang, G. Liu, X. Jiang, H. Lu, and Z. Li, "Numerical prediction of flow behavior of cuttings carried by Herschel-Bulkley fluids in horizontal well using kinetic theory of granular flow," *Powder Technology*, vol. 329, pp. 386–398, 2018.

[13] Y. Ignatenko, O. Bocharov, A. Gavrilov, and R. May, "Steady-state cuttings transport simulation in horizontal borehole annulus," in *Proceedings of the ASME 2018 37th International Conference on Ocean, Offshore and Arctic Engineering*, Madrid, Spain, June 2018.

[14] S. K. Jha, "Effect of particle inertia on the transport of particle-laden open channel flow," *European Journal of Mechanics—B/Fluids*, vol. 62, pp. 32–41, 2017.

[15] R. S. Sanders, J. Schaan, R. G. Gillies et al., "Solids transport in laminar open-channel flow of non-Newtonian slurries," in *Proceedings of the Hydrotransport, 15th International Conference, Incorporating the 11th International Symposium of Freight Pipelines*, pp. 597–611, BHR Group, Cranfield, UK, June 2002.

[16] J. M. Treinen, "Modelling transport and deposition of coarse particles in viscoplastic tailings beach flows," Doctoral dissertation, University of Colorado, Boulder, CO, USA, 2017.

[17] A. M. Talmon, L. Sittoni, E. Meshkati Shahmirzadi, and J. L. J. Hanssen, "Shear settling in laminar open channel flow: analytical solution, measurements and numerical simulation,"

in *Proceedings of the 21st International Seminar on Paste and Thickened Tailings*, R. J. Jewell and A. B. Fourie, Eds., pp. 181–194, Australian Centre for Geomechanics, Perth, Australia, July 2018.

[18] J. M. Neff, "Fate and effects of water based drilling muds and cuttings in cold water environments," Report to Shell Exploration and Production Company, Neff & Associates LLC, Houston, TX, USA, 2010.

[19] R. J. S. Pigott, "Mud flow in drilling," in *Drilling and Production Practice*, American Petroleum Institute, Washington, DC, USA, 1941.

[20] S.-M. Han, Y.-K. Hwang, N.-S. Woo, and Y.-J. Kim, "Solid-liquid hydrodynamics in a slim hole drilling annulus," *Journal of Petroleum Science and Engineering*, vol. 70, no. 3-4, pp. 308–319, 2010.

[21] W. K. H. Ariyarathna, P. Welahettige, and M. C. Melaaen, "A parametric study for Euler-granular model in dilute phase vertical pneumatic conveying," *International Journal of Computational Methods and Experimental Measurements*, vol. 6, no. 1, pp. 46–58, 2018.

[22] B. N. Murthy, R. S. Ghadge, and J. B. Joshi, "CFD simulations of gas-liquid-solid stirred reactor: prediction of critical impeller speed for solid suspension," *Chemical Engineering Science*, vol. 62, no. 24, pp. 7184–7195, 2007.

[23] S. Akhshik, M. Behzad, and M. Rajabi, "CFD-DEM approach to investigate the effect of drill pipe rotation on cuttings transport behavior," *Journal of Petroleum Science and Engineering*, vol. 127, pp. 229–244, 2015.

[24] Z. Naumann and L. Schiller, "A drag coefficient correlation," *Zeitschrift des Vereins Deutscher Ingenieure*, vol. 77, pp. 318–323, 1935.

[25] D. Gidaspow, *Multiphase Flow and Fluidization: Continuum and Kinetic Theory Descriptions,* Academic Press, San Diego, CA, USA, 1994.

[26] ANSYS Fluent, *12.0 Theory Guide*, ANSYS, Inc., Canonsburg, PA, USA, 2009.

[27] H. K. Versteeg and W. Malalasekera, *An Introduction to Computational Fluid Dynamics : The Finite Volume Method*, Pearson Education Ltd., Harlow, UK, 2nd edition, 2007.

[28] V. C. Kelessidis, R. Maglione, C. Tsamantaki, and Y. Aspirtakis, "Optimal determination of rheological parameters for Herschel-Bulkley drilling fluids and impact on pressure drop, velocity profiles and penetration rates during drilling," *Journal of Petroleum Science and Engineering*, vol. 53, no. 3-4, pp. 203–224, 2006.

[29] R. Haldenwang, *Flow of Non-Newtonian Fluids in Open Channels*, Cape Technikon, Cape Town, South Africa, 2003.

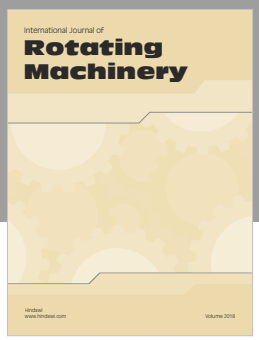

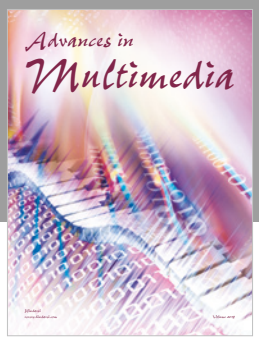

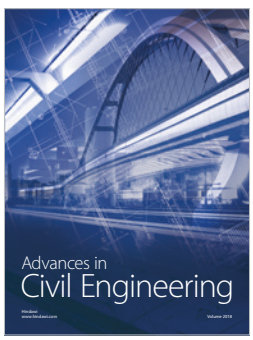

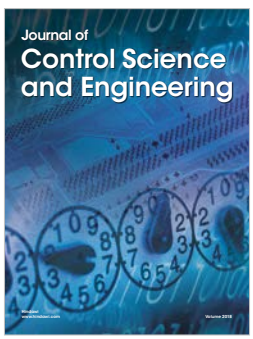

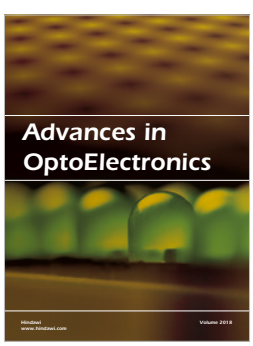

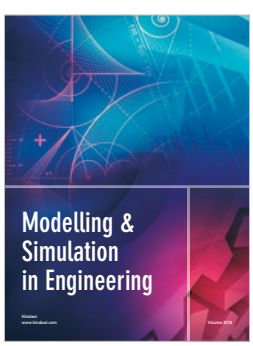

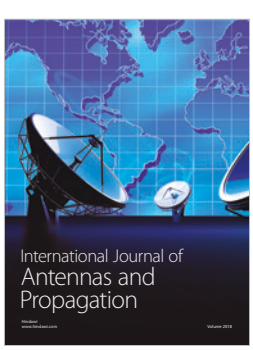

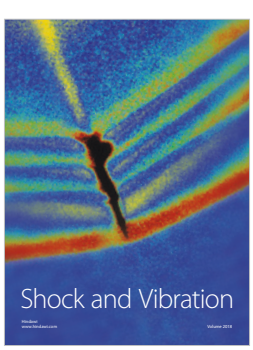

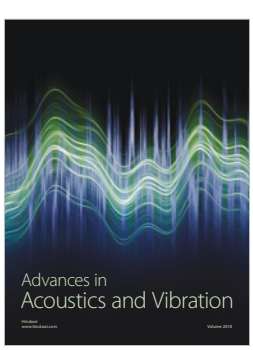

Hindawi

Submit your manuscripts at
www.hindawi.com

Paper 8

Study of Fluidization Regimes using OpenFOAM Computational Fluid Dynamics

This paper is presented at the 58th SIMS.
doi:10.3384/ecp17138128

Study of Fluidization Regimes using OpenFOAM Computational Fluid Dynamics

Prasanna Welahettige[1], Bernt Lie[1], Knut Vaagsaether[1], Britt M.E Moldestad[1]

[1]Department of Process, Energy and Environmental Technology
University College of Southeast Norway
Porsgrunn, Norway
knut.vagsather@usn.no

Abstract

The objective of this study was using computational fluid dynamics simulation with OpenFOAM to study the fluidization properties for four types of particles classified as Geldart A, B, C and D. Fluidization regimes were studied for particles with the same density but different diameters. The particle diameters were selected based on Geldart's classification of particles. The simulation results were validated against experimental data. Pressure gradient, flow regime change, bubble rise, bubble splitting and bed expansion were studied for all four types of particles for different superficial velocities. Group-B and D particles easily produced bubbles. However, Group-C and A particles gave very high bed expansion, and no clear bubbles were observed. Bed with the Group-D particles, the bubbles was large and some of the bubbles reached the diameter of the bed. Group-B particles gave smaller and on average more stable bubbles than Group-D particles. There was no bubble formation from Group-C and Group-A until the inlet superficial velocity was 25 times and 5 times larger, respectively, than their minimum fluidization velocities.

Keywords: Fluidization, bubble, Geldart's classification, pressure gradient, flow regimes, OpenFOAM

1 Introduction

The gas-solid fluidization process can be divided into two basic steps: the packed bed and the fluidization regime. The packed bed pressure drop can be explained using the Ergun equation up to a minimum fluidization. The pressure drop across the fluidization flow regime can be explained using the mixture momentum balance equation. At the minimum fluidization condition, the buoyant force and the drag force are equal and balance each other in opposite directions (Gidaspow, 1994). According to Geldart's classifications of powder, uniformly sized powders can be classified into four basic types: aeratable (Group-A), bubbling (Group-B), cohesive (Group-C) and spoutable (Group-D), (Geldart, 1972). Group-A particles show considerable bed expansion before the bubbles appear. Group-B particles give bubbles as soon as the gas velocity exceeds the minimum fluidization condition (Kunii & Levenspiel, 1991). The agglomerate diameter of Group-A particles depends upon a force balance between cohesive, drag, gravity, and collision forces (Motlagh *et al.*, 2014). Group-C particles have difficulties in rising due to the inter particle forces that are stronger than the fluid forces exerted on particles (Gidaspow, 1994). Group-D particles give a slower bubble rise velocity than the gas velocity (Kunii & Levenspiel, 1991). (Wang X. *et al.*, 2007) showed that Nano-sized particles possess both Group-A and Group-B behavior. Group-B bubbles, which are at the interface between dense phase and freeboard, affect bed collapse time (Pei *et al.*, 2009). (Pandit *et al.*, 2005) found that high bed expansion happens at the particle size boundary between Group-A and B. (Alavi & Caussat, 2005) found that the fluidization behavior improved for the highest vibration strengths. (Zhang *et al.*, 2008) simulated Group-A and B particles using a commercial computational fluid dynamics (CFD) tool. There are a number of CFD studies on the gas-solid fluidization. However, few open source CFD studies about all four types of Geldart's groups of particles are published. In this work, all four types of particles were simulated using OpenFOAM 4.0, 2-D simulations. The standard "twoPhaseEulerFoam" model was used for the simulations. All the four particle types were studied with respect to of pressure gradients, flow regime changes, bed expansion, bubble formations and bubble rises.

2 Numerical models

The Euler-Euler model was used to simulate both phases. In this approach, the sum of phase volume fractions equals unity and the phase volume fraction is a continuous function of space and time (Rusche, 2002).

$$\alpha_g + \alpha_s = 1 \quad (1)$$

Here, α is the volume fraction and subscripts g and s indicate gas and solid phases. Continuous phase velocity varies significantly over the volume when the flow becomes turbulent. Therefore, average velocities are introduced in the continuity equation (Crowe *et al.*, 2011),

$$\frac{\partial \rho_g \alpha_g}{\partial t} + \nabla . \left(\rho_g \bar{U}_g \alpha_g\right) = 0. \quad (2)$$

The x momentum equation for continuous phase can be given as (Rusche, 2002) and (Crowe *et al.*, 2011).

$$\frac{\partial \rho_g \alpha_g \bar{u}_g}{\partial t} + \nabla \cdot (\alpha_g \rho_g \bar{u}_g \bar{U}_g) = -\alpha_g \frac{\partial \bar{\mathrm{p}}}{\partial \mathrm{x}} + \nabla \cdot \bar{\tau}_{g,x} + \alpha_g \rho_g g_x + \bar{\mathrm{M}}_{g,x} \quad (3)$$

Here, $\bar{u}_g$ is the x directional velocity of the continuous phase, ρ_g is the density of the continuous phase, $\vec{U}_g$ is three dimensional velocity components of the continuous phase, $\bar{\mathrm{p}}$ is the pressure, $\bar{\tau}_{g,x}$ is the x component Reynold average stresses, g_x is the acceleration of gravity in the x direction, $\bar{\mathrm{M}}_{g,x}$ is the average interface momentum transfer term per unit volume,

$$\bar{\mathrm{M}}_{g,x} = F_d + F_l + F_{vm} + F_o \quad (4)$$

Here, F_d is the drag force, F_l is the lift force, F_{vm} is the virtual force and F_o is the other force. Lift force, virtual force and other forces were neglected. The drag force for unit volume is,

$$\mathrm{F}_d = \beta'(v_s - v_g) \quad (5)$$

The friction coefficient between fluid and solid (β') (Gidaspow, 1994) depends on α_g:

if $\alpha_g < 0.8$, Ergun's formula applies,

$$\beta' = 150 \frac{{\alpha_s}^2 \mu_g}{\alpha_g (d_p \emptyset_s)^2} + 1.75 \frac{\rho_g |v_g - v_s| \alpha_s}{\emptyset_s d_p}, \quad (6)$$

while if $\alpha_g > 0.8$, Wen and Yu's formula applies,

$$\beta' = \frac{3}{4} C_D \frac{\alpha_g |v_g - v_s| \rho_g \alpha_s}{d_p} {\alpha_g}^{-2.65}. \quad (7)$$

Here, μ_g is the gas viscosity and the drag coefficient(C_D) depends on Reynold's number:

if $Re_s < 1000$,

$$C_D = \frac{24}{Re_s}(1 + 0.15(Re_s)^{0.687}), \quad (8)$$

if $Re_s \geq 1000$,

$$C_D = 0.44. \quad (9)$$

Here,

$$Re_s = \frac{\alpha_g \rho_g |v_g - v_s| d_p}{\mu_g}. \quad (10)$$

The restitution coefficient, which evaluates the particle-particle collision, was 0.8. The Johnson-Jackson model calculates friction stress between wall and particles. The minimum fluidization velocity ($u_{g,mf}$) is

$$u_{g,mf} = \frac{d_p^2 (\rho_p - \rho_g) g}{150 \mu_g} \frac{\alpha_{g,mf}^3 \emptyset_p^2}{\alpha_{s,mf}}. \quad (11)$$

Here, d_p is the particle diameter, ρ_p is the density of the particle, $\emptyset_p$ is the sphericity of the particle. Maximum bubble size ($d_{b,max}$) according to Mori and Wen (Kunii & Levenspiel, 1991) is

$$d_{b,max} = 0.65 \left(\frac{\pi}{4} d_t^2 (u_0 - u_{mf})\right)^{0.4}. \quad (12)$$

Here, d_t is the channel width. According to the Grace correlation (Gidaspow, 1994), a single bubble velocity (u_{br}),

$$u_{br} = 0.711 \sqrt{g d_b}. \quad (13)$$

The velocity of bubbles in a bubbling bed is

$$u_b = u_0 - u_{mf} + u_{br}. \quad (14)$$

Here, d_B is the average bubble diameter and u_0 is the inlet gas velocity.

2-D simulations were done using the open source CFD code OpenFOAM 4.0. The forward Euler method was used for the time discretization. Pressure-velocity coupling was solved by the pressure implicit with splitting of operators (PISO) algorithm with second order upwind correction.

Grid size (mesh resolution) is a critical factor for the gas-solid two fluid method (TFM). Grid size needs to have sufficient scale resolution to accurately predict the bed expansion (Wang J. *et al.*, 2011). When the grid size is smaller than 10 times the particle diameter, a homogenous drag model reached its asymptotic results (Lu *et al.*, 2009). The simulations failed to predict Geldart's A particle when using a fine mesh (Lu *et al.*, 2011) and (Wang J. *et al.*, 2009). Therefore, 7 mm minimum cell size mesh was used for 1.5 mm maximum size particle diameter.

3 Physical properties of gas-solid system

Table 1 shows physical properties of the particle groups. Particle density and fluid density were constants for the groups. Corresponding particle diameters were selected

based on Geldart's powder classification diagram (Geldart, 1972).

Table 1. Physical properties of gas-solid system

Parameters	Group-A	Group-B	Group-C	Group-D
Particle diameter, d_p, (µm)	60	350	15	1500
Particle density, ρ_s, (kg/m^3)	2500	2500	2500	2500
Fluid density, ρ_g, (kg/m^3)	1.225	1.225	1.225	1.225
Calculated minimum fluidization velocity, $u_{g,mf}$, (m/s)	0.0035	0.15	0.00024	2.4

4 Results and discussion

Results were categorized for each group as a comparison. Pressure gradient across a bed was calculated as an average pressure difference between two points in the bed, which were 30 mm and 235 mm vertical height from the bed bottom. The average pressure was calculated as an area average pressure. The channel with was 0.084 m and channel height was different depending on the expansion of the groups.

4.1 Group-A

4.1.1 Pressure gradient

The pressure gradient increased proportionally with the inlet superficial velocity until the minimum fluidization velocity was reached. At minimum fluidization, the packed bed gave a maximum pressure gradient as shown in Figure 1. The minimum fluidization velocity was 0.006 m/s. (Ye *et al.*, 2005)) also observed a similar pressure drop pattern with the inlet superficial velocities for Group-A particles.

4.1.2 Fluidization regimes

Figure 3 shows bed expansions with different inlet superficial velocities. There was no considerable bed expansion before the minimum fluidization velocity was reached. However, after the minimum fluidization, the bed expanded considerably. Here, the dense phase was gradually transitioned into the dilute phase. There was no bubble formation until the inlet superficial velocity was five times higher than the minimum fluidization velocity. This bubble less bed expansion behavior was also observed by (Wang X. *et al.*, 2007). However, when the inlet velocity was further increased, the airflow tried to create flow channels in the expanded bed. (Karimipour & Pugsley, 2010) also observed a similar behavior, when the bed expanded, it gradually compromised into a normal bubbling bed.

4.2 Group-B

4.2.1 Pressure gradient

Figure 4 shows pressure gradient variation with the inlet superficial velocity. The pressure gradient gradually increased until minimum fluidization occurred, and then it became (on average) constant. The minimum fluidization velocity was 0.16 m/s in the experiment and 0.18 m/s in the simulation. The average particle diameter was 350 µm in the experiment (Thapa & Halvorsen, 2013). However, in the simulation only 350 µm diameter particles was used. This could be the reason for having a little difference between the simulation result and the experimental result.

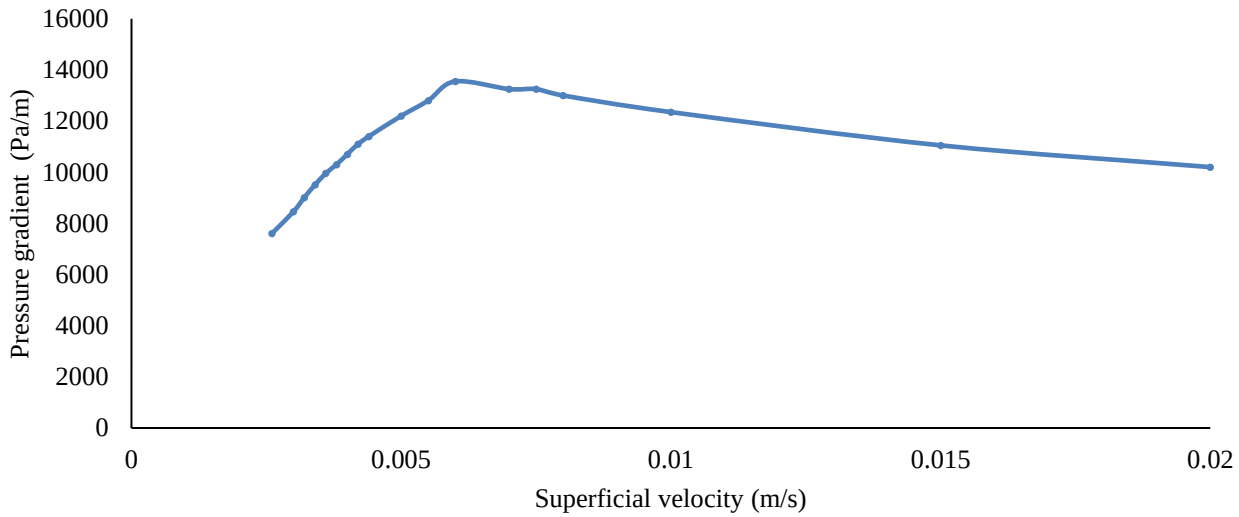

Figure 1. Group-A particles pressure-gradient variation with the inlet superficial velocity

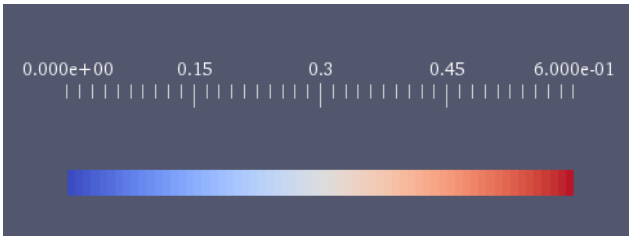

Figure 2. Color map for Figure 3, 5, 6, 7, 9, 11 and 12. Value zero (dark blue) represents the gas and value one (dark red) represents the solid.

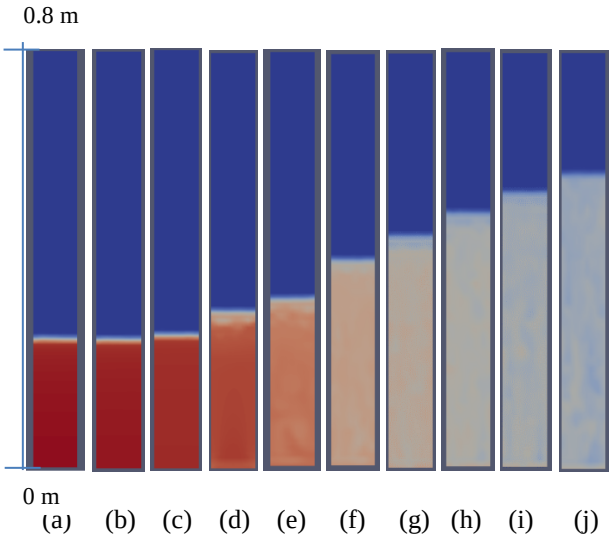

Figure 3. Solid volume fraction with different inlet superficial velocities, Geldart's classification Group-A, $\rho_s = 2500\ \mathrm{kg/m^3}$, $d_p = 60\ \mu\mathrm{m}$, the maximum column height is 0.8 m ; (a) 0.0026 m/s, (b) 0.0042 m/s, (c) 0.006 m/s, (d) 0.008 m/s, (e) 0.015 m/s, (f) 0.03 m/s, (g) 0.04 m/s, (h) 0.05 m/s, (i) 0.06 m/s, (j) 0.07 m/s

4.2.2 Fluidization regimes

Figure 5 shows a flow regime change with increase of the inlet superficial velocity. The packed bed can be considered as a normal packing (neither a dense packing nor a loose packing), because the minimum void fraction was 0.3564 and the sphericity was equal to one (Kunii & Levenspiel, 1991). There is no bubble formation in Figure 5.a. This was due to the gas velocity lower than the minimum fluidization velocity. Approximate minimum fluidization is shown in Figure 5.b. There was no bubble formation at this stage. The size of bubbles is expanded from Figure 5.c to Figure 5.f. The minimum bubbling occurred at the inlet surficial velocity in in range 0.2 m/s to 0.25 m/s. Figure 5.f shows a slug formation. A spouted bed behavior is shown in Figure 5.g. The spouted bed behavior was occurred, when the inlet superficial velocity was five times larger than the minimum fluidization velocity.

4.2.3 Bubble formation and rise

Figure 6 shows a bubble formation from the bottom of the bed and travel until the top of the bed. The bubble size increased gradually with time. The circular shape of the bubble changed into an elliptical shape at the end. This was due to the lower hydrostatic pressure applied to the bubble at the top of the bed. The average bubble-rise velocity from the formation to the end was 0.426 m/s (for the inlet superficial velocity 0.35 m/s), which was higher than the gas inlet velocity and higher than the minimum fluidization velocity. The diameter of the bubble varied from 0 mm to 42 mm. Here, the average bubble size was 50% of the bed diameter. According to Equation-14, the calculated average bubble-rise velocity was 0.482 m/s, which was approximately equal to the simulation result. Most of the bubbles rise faster than the inlet superficial gas velocity (Geldart, 1972). The high bubble velocity is due to the low void fraction in the bed. These low voidages support to rise the bubbles faster than the inlet superficial velocity. Increase or decrease of bubble diameter depends on the balance of coalescence and splitting frequencies (Horio M & Nonaka A, 1987). Group-B particle showed higher mixing than Group-A particles due to the more bubbles in the bed.

4.2.4 Bubble splitting

Figure 7 shows the bubble-splitting behavior. Here, dense phase particles collapsed onto the bubble and because of this, the bubble splits into two. Other bubbles and wall effects were also reasons to the bubble splitting.

4.3 Group-C

4.3.1 Pressure gradient

There are very few simulations related to Group-C particle fluidization found in literature. There is a real practical difficulty of the simulations, which takes higher simulation time due to very small velocities at minimum fluidization. In this study, a time step of 10^{-4} s was used for the simulations. Figure 8 shows pressure gradient variation with the inlet superficial velocity for Group-C particles. The minimum fluidization velocity was 3.75×10^{-4} m/s.

4.3.2 Flow regimes

Group-C particles behaved as a fluid as shown in Figure 9 and it gave the higher flow behavior compared to the other groups. Even though the inlet superficial velocity was 25 times larger than the minimum fluidization velocity, there was no bubble formation. This was due to the high cohesive properties of Group-C particles. Due to strong extra inter-particle forces, bubble formation does not occur in beds with Group-C particles

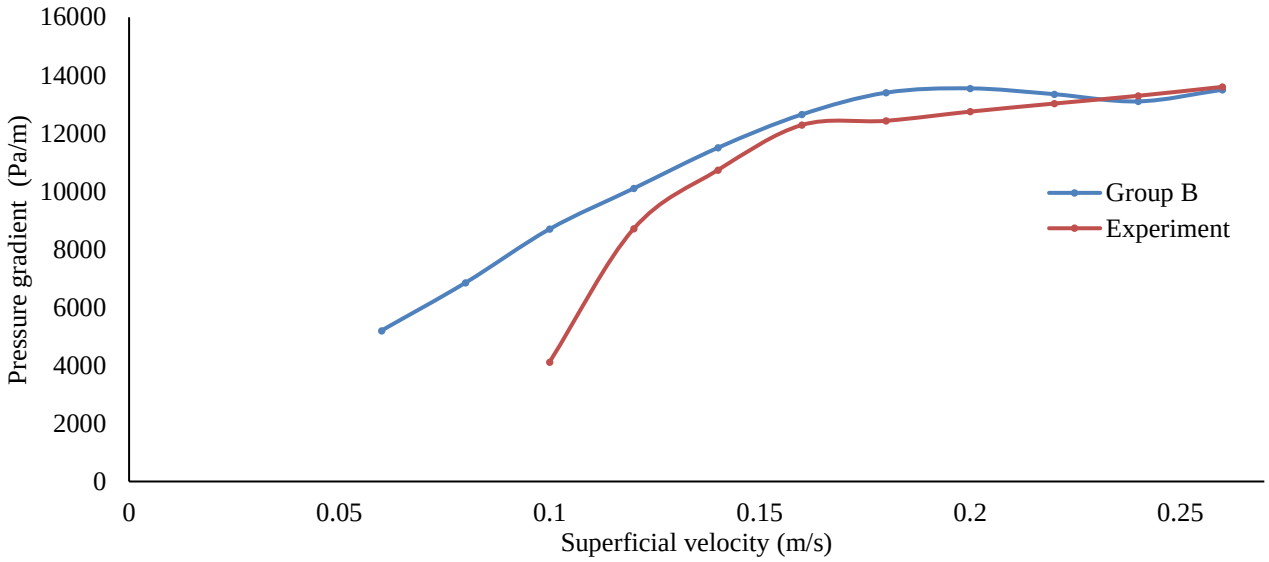

Figure 4. Group-B pressure-gradient variation with the inlet superficial velocity, the experimental result from (Thapa & Halvorsen, 2013).

(Yao *et al.*, 2002). However, the standard "twoPhaseEulerFoam" does not include the cohesive forces.

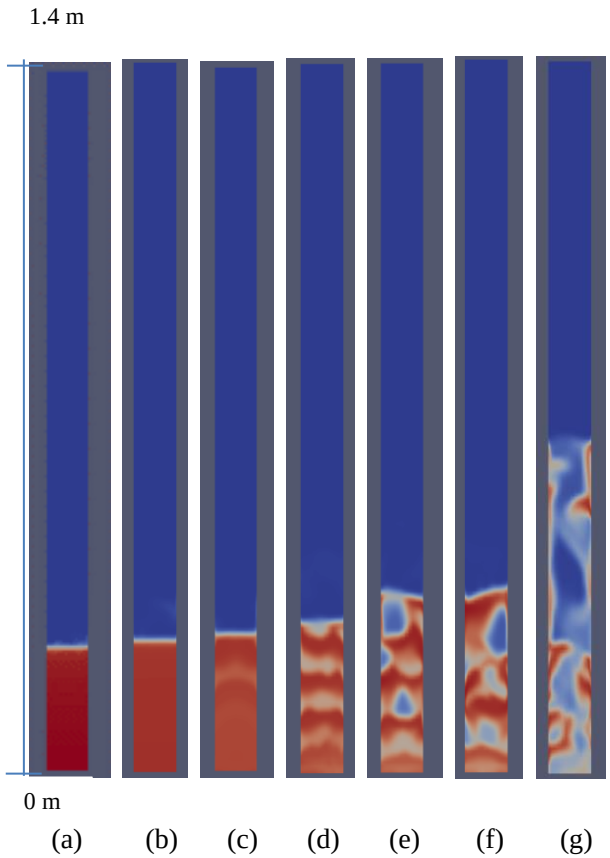

Figure 5. Solid volume fraction with different inlet superficial velocities, Geldart's classification, Group-B, $\rho_s = 2500$ kg/m^3, $d_p = 350$ µm**,** the maximum column height is 1.4 m ; (a) 0.05 m/s, (b) 0.2 m/s, (c) 0.25 m/s, (d) 0.3 m/s, (e) 0.4 m/s, (f) 0.45 m/s, (g) 1.0 m/s

4.4 Group-D

4.4.1 Pressure gradient

Figure 10 shows the pressure gradient variation with the inlet superficial velocity. The minimum fluidization velocity was 1.15 m/s and the pressure gradient in the bed was 2600 Pa.

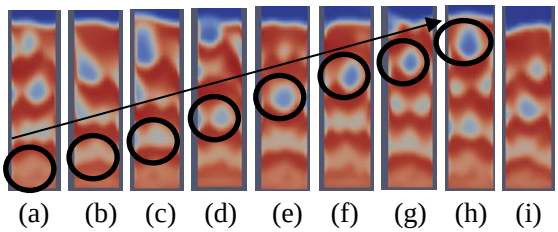

Figure 6. Bubble formation and rise vs. time, $d_p = 350$ µm,$v = 0.35$ m/s; (a) t = 2.5 s, (b) t = 3.0 s, (c) t = 3.5 s, (d) t = 4.0 s, (e) t = 4.5 s, (f) t = 5.0 s, (g) t = 5.5 s, (h) t = 6.0 s, (i) t = 6.5 s

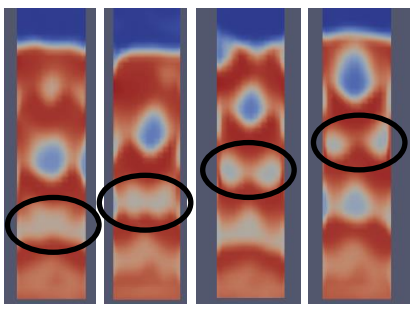

Figure 7. Bubble splitting, $d_p = 350$ µm, $v = 0.35$ m/s; (a) $t = 2.5$ s, (b) $t = 3.0$ s, (c) $t = 3.5$ s, (d) $t = 4.0$ s

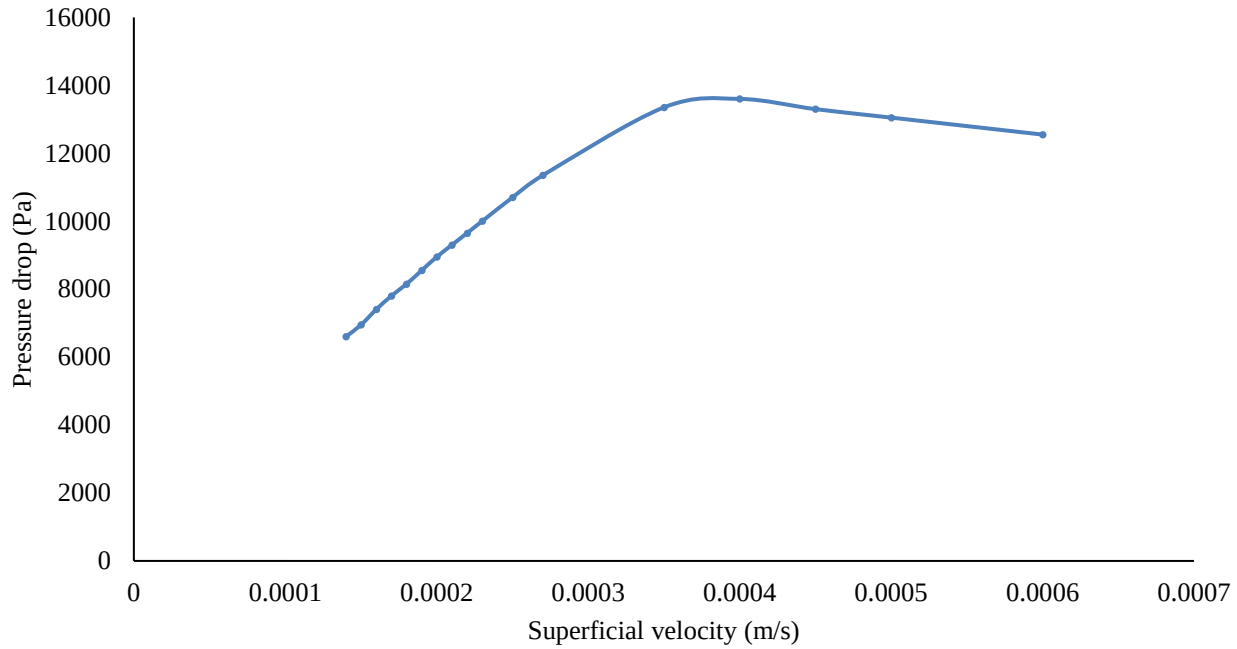

Figure 8. Group-C particles pressure-gradient variation with the inlet superficial velocity

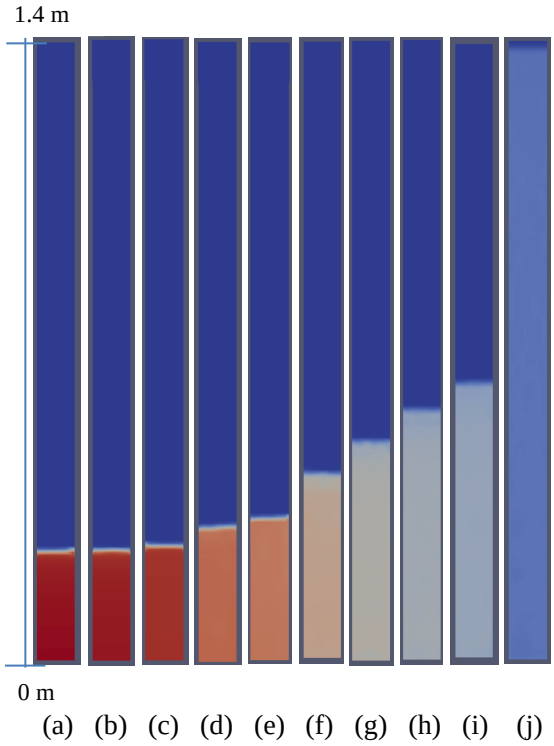

Figure 9. Solid volume fraction, Geldart's classification, Group-C, $\rho_s = 2500\ \mathrm{kg/m^3}$, $d_p = 15\mu\mathrm{m}$, the maximum column height is 1.4 m; (a) 0.00014 m/s, (b) 0.00027 m/s, (c) 0.0004 m/s, (d) 0.0008 m/s, (e) 0.001 m/s, (f) 0.002 m/s, (g) 0.003 m/s, (h) 0.004 m/s, (i) 0.005 m/s, (j) 0.01 m/s after 380 s

4.4.2 Flow regimes

Figure 11 shows solid volume fraction change with increase of the inlet superficial velocity. Flow behavior was similar with Group-B particles. However, bubbles were not stable as for Group-B and they were splitting faster. Back mixing was slower compared to Group-B particles (Geldart, 1972).

4.4.3 Bubbles formation

The shapes of the bubbles changed rapidly. The average size of the bubbles is larger than the average size of Group-B bubbles. The bubbles were very unstable at the top of the bed. There were large openings of bubbles at the top of the bed as shown in Figure 12. The average bubble size was 0.07 m, which was approximately equal to the width of the column ($d_t = 0.082$ m). The calculated average bubble-rise-velocity was 1.04 m/s from Equation-14. However, the simulated average bubble rise velocity was 0.4 m/s. Group-D bubbles rose at lower speed than the inlet superficial velocity. This is due to Group-D bubbles being comparatively larger and this creates higher voidages to rise the gas compared to the other groups.

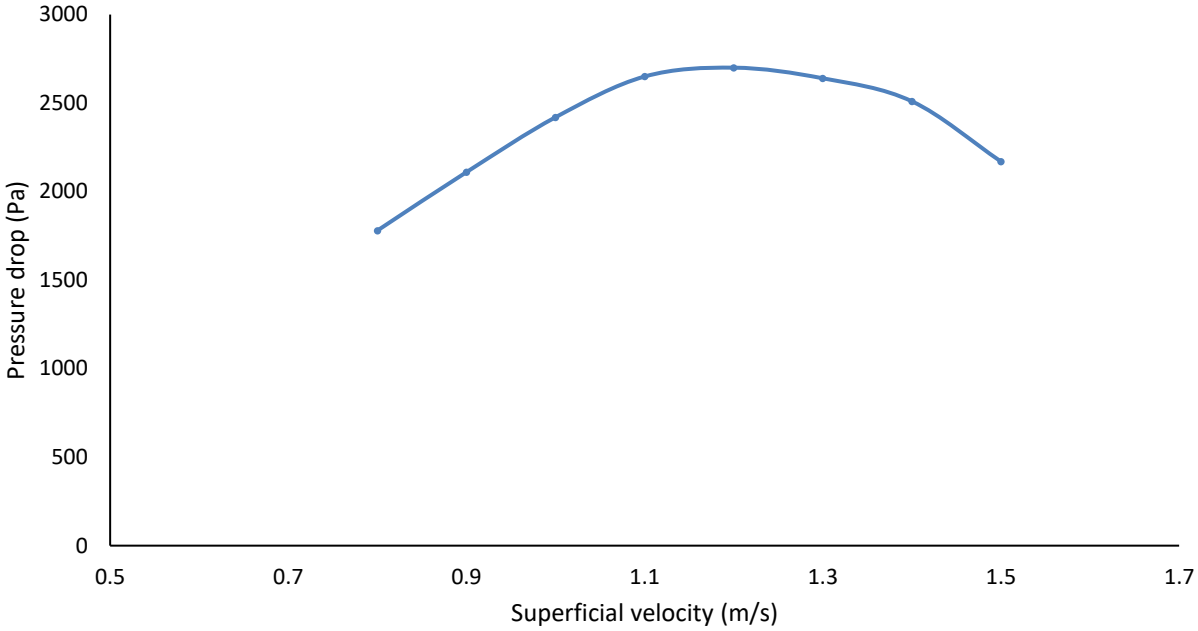

Figure 10. Group-D particle pressure-gradient variation with the inlet superficial velocity

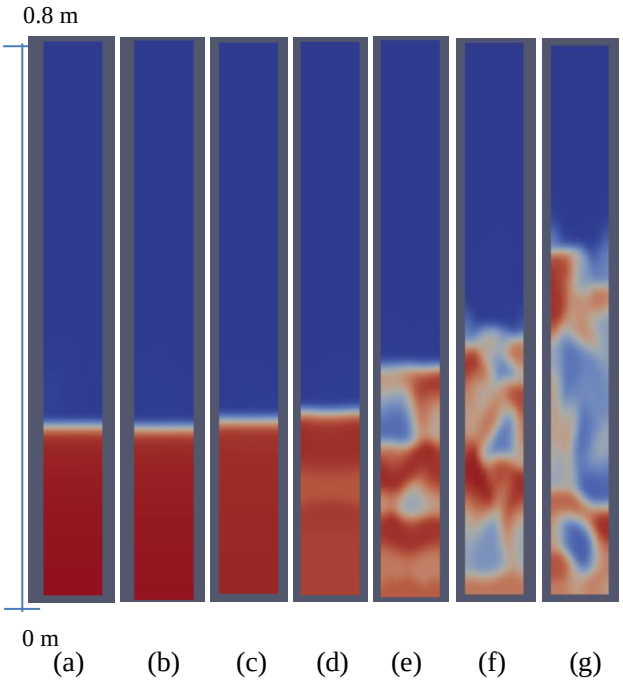

Figure 11. Solid volume fraction after 70 s, Geldart's classification, Group-D, $\rho_s = 2500\ \mathrm{kg/m^3}$, $d_p = 1500\mu\mathrm{m}$, the maximum column height is 0.8 m; (a) 0.8 m/s, (b) 0.9 m/s, (c) 1.1 m/s, (d) 1.3 m/s, (e) 1.5 m/s, (f) 2.0 m/s , (g) 2.5 m/s

5 Comparison of Group-A, B, C, and D

5.1 Bed expansion

Figure 13 shows bed expansion with the inlet superficial velocity for the all four particle groups. The bed expansion factor was defined as $\frac{h}{h_{mf}}$. Here h was the bed height and h_{mf} was the bed height at the minimum fluidization. The expansions were considered until the bubble formation occurred. Group-C particles showed the highest bed expansion ratio, which was 1 to 2.5 times. Group-A particles showed a bed expansion 1 to 2.1 times. Group-B particles showed a bed expansion 1 to 1.2 times. Group-D particles gave lowest bed expansion that was 1 to 1.05 times. Group-C expanded with the smallest velocities and Group-D expanded with the largest velocities.

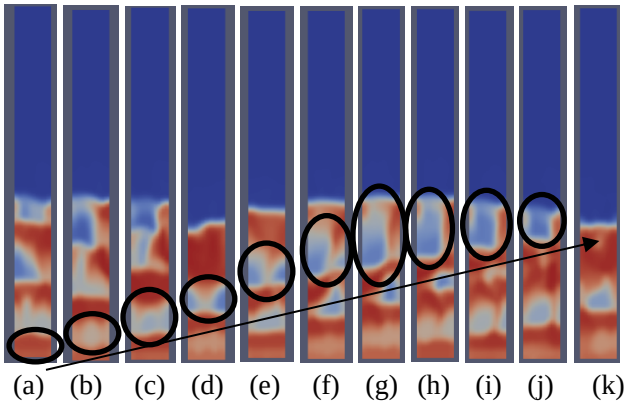

Figure 12. Bubble formation and rise of Group-D particles,$d_p = 1500\mu\mathrm{m}$, $v = 1.6\ \mathrm{m/s}$; (a) t = 1.55 s, (b) t = 1.72 s, (c) t = 1.80 s, (d) t = 1.91 s, (e) t = 2.05 s, (f) t = 2.13 s, (g) t = 2.18 s, (h) t = 2.23 s, (i) t = 2.28 s, (j) t = 2.32 s, (k) t = 2.38 s

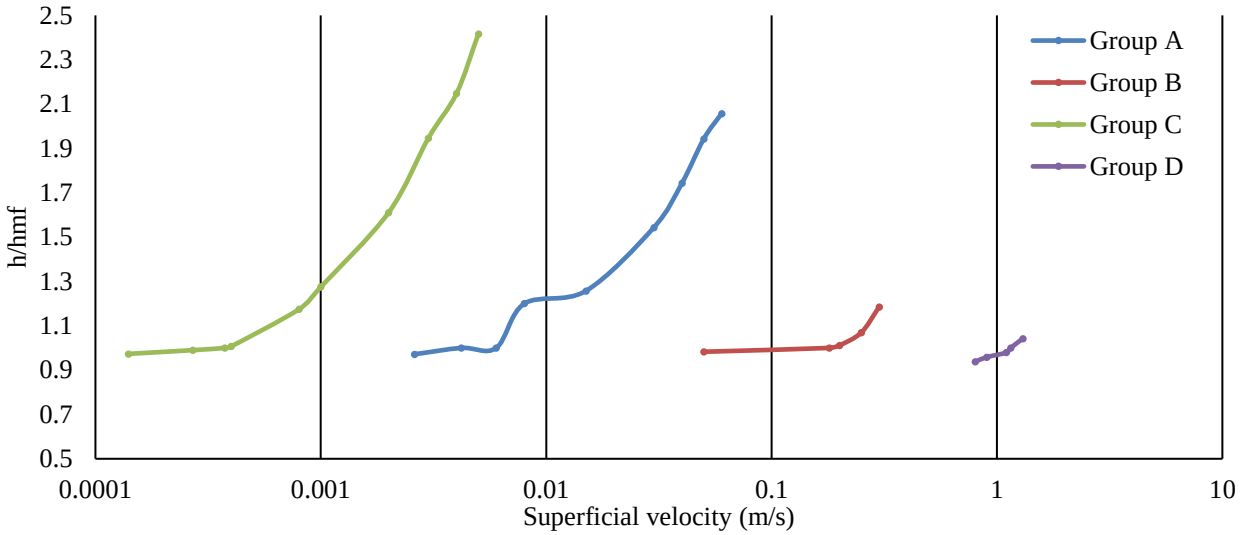

Figure 13. Bed expansion with the inlet superficial velocity for Group-A, B, C and D particles. x-axis is given in log

5.2 Void fraction at the minimum fluidization

The void fraction at the minimum fluidization is an important parameter for many calculations. Table .2 gives minimum fluidization velocity (u_{mf}), bed height at the minimum fluidization (h_{mf}) and void fraction at minimum fluidization (α_{mf}). The minimum allowable void fraction was defined as 0.3564 during the simulations. The void fraction at minimum fluidization was calculated as the average void fraction in a packed bed.

Table 2. Simulated results at minimum fluidization for all the four groups

	Group-A	Group-B	Group-C	Group-D
d_p(μm)	60	350	15	1500
u_{mf}(m/s)	0.006	0.19	0.000375	1.15
h_{mf} (mm)	255	263	256	259
α_{mf}	0.4427	0.4539	0.4467	0.4565

6 Conclusions

Group-A and -C particles show bubble-less bed expansion. Group-C particles show the highest bed expansion ratio and Group-D particles show the lowest bed expansion ratio, respectively 2.5 times and 1.05 times, before bubble formation. A higher average bubble size occurs in Group-D particles than Group-B particles. Group-A and Group-C particles are less prone to mixing than Group-B and Group-D particles due to less bubble formation. Group-C particles show higher flow properties than the others. The minimum fluidization velocities become gradually smaller from Group-D, B, A to C.

Acknowledgement

Economic support from The Research Council of Norway and Statoil ASA through project no. 255348/E30 “Sensors and models for improved kick/loss detection in drilling (Semi-kidd)” is gratefully acknowledged. The authors also gratefully acknowledge the resources for experiments and simulations provided by the University College of Southeast Norway.

References

Alavi S. and Caussat B. (2005). Experimental study on fluidization of micronic powders. *Powder Technology*, *157*(1–3), 114-120. doi:http://dx.doi.org/10.1016/j.powtec.2005.05.017

Crowe C. T., Schwarzkopf J. D., Sommerfeld M. and Tsuji Y. (2011). *Multiphase flows with droplets and particles*: CRC press.

Geldart D. (1972). Types of Gas Fhidization *Powder Technology,*, *7*(1973), 285-292.

Gidaspow D. (1994). *Multiphase flow and fluidization : continuum and kinetic theory descriptions*. Boston: Academic Press.

Horio M and Nonaka A. (1987). A generalized bubble diameter correlation for gas-sold fluidized beds *AIChE Journal*, *33*(11), 1865-1872.

Karimipour S. and Pugsley T. (2010). Study of gas streaming in a deep fluidized bed containing Geldart's Group A particles. *Chemical Engineering Science*, *65*(11), 3508-3517. doi:http://dx.doi.org/10.1016/j.ces.2010.02.045

Kunii D. and Levenspiel O. (1991). *Fluidization engineering* (2. ed.). Boston,Mass.: Butterworth-Heinemann.

Lu B., Wang W. and Li J. (2009). Searching for a mesh-independent sub-grid model for CFD simulation of gas–solid riser flows. *Chemical Engineering Science*,

64(15), 3437-3447. doi:http://dx.doi.org/10.1016/j.ces.2009.04.024

Lu B., Wang W. and Li J. (2011). Eulerian simulation of gas–solid flows with particles of Geldart groups A, B and D using EMMS-based meso-scale model. *Chemical Engineering Science, 66*(20), 4624-4635. doi:http://dx.doi.org/10.1016/j.ces.2011.06.026

Motlagh A. H. A., Grace J. R., Salcudean M. and Hrenya C. M. (2014). New structure-based model for Eulerian simulation of hydrodynamics in gas–solid fluidized beds of Geldart group "A" particles. *Chemical Engineering Science, 120*, 22-36. doi:http://dx.doi.org/10.1016/j.ces.2014.08.042

Pandit J. K., Wang X. S. and Rhodes M. J. (2005). Study of Geldart's Group A behaviour using the discrete element method simulation. *Powder Technology, 160*(1), 7-14. doi:http://dx.doi.org/10.1016/j.powtec.2005.04.044

Pei P., Zhang K., Lu E. and Wen D. (2009). CFD simulation of bubbling and collapsing characteristics in a gas-solid fluidized bed. *Petroleum Science, 6*(1), 69-75. doi:10.1007/s12182-009-0013-0

Rusche H. (2002). *Computational fluid dynamics of dispersed two-phase flows at high phase fractions.* (Doctor of Philosophy), Imperial College London (University of London).

Thapa R. and Halvorsen B. (2013). *Study of Flow Behavior in Bubbling Fluidized Bed Biomass Gasification Reactor Using CFD Simulation.* Paper presented at the The 14th International Conference on Fluidization-From Fundamentals to Products. http://dc.engconfintl.org/fluidization_xiv/69

Wang J., van der Hoef M. A. and Kuipers J. A. M. (2009). Why the two-fluid model fails to predict the bed expansion characteristics of Geldart A particles in gas-fluidized beds: A tentative answer. *Chemical Engineering Science, 64*(3), 622-625. doi:http://dx.doi.org/10.1016/j.ces.2008.09.028

Wang J., van der Hoef M. A. and Kuipers J. A. M. (2011). The role of scale resolution versus inter-particle cohesive forces in two-fluid modeling of bubbling fluidization of Geldart A particles. *Chemical Engineering Science, 66*(18), 4229-4240. doi:http://dx.doi.org/10.1016/j.ces.2011.06.004

Wang X., Rahman F. and Rhodes M. (2007). Nanoparticle fluidization and Geldart's classification. *Chemical Engineering Science, 62*(13), 3455-3461. doi:http://dx.doi.org/10.1016/j.ces.2007.02.051

Yao W., Guangsheng G., Fei W. and Jun W. (2002). Fluidization and agglomerate structure of SiO2 nanoparticles. *Powder Technology, 124*(1–2), 152-159. doi:http://dx.doi.org/10.1016/S0032-5910(01)00491-0

Ye M., van der Hoef M. A. and Kuipers J. A. M. (2005). The effects of particle and gas properties on the fluidization of Geldart A particles. *Chemical Engineering Science, 60*(16), 4567-4580. doi:http://dx.doi.org/10.1016/j.ces.2005.03.017

Zhang K., Brandani S., Bi J. and Jiang J. (2008). CFD simulation of fluidization quality in the three-dimensional fluidized bed. *Progress in Natural Science, 18*(6), 729-733. doi:http://dx.doi.org/10.1016/j.pnsc.2008.02.002

Appendixes

MATLAB code for the FLIC Scheme

Main code

```
%% High resolution, well balance, positivity preserving numerical scheme for
the
modified shallow water equation: trapezoidal non-prismatic channels
% Authors - Prasanna Welahettige and Knut Vaagsaether
% From 2017/07/04 to 2019/05/22
% This code is related to Paper 5 Carreau viscosity model

clear
clc
g = 9.81; % Gravity
L = 3.7; % Total length of the channel, m
dx = 0.01; % step length
x = 0:dx:L;
N = 30000; % number of time steps, N > 30000 gives a steady results for this
case
t = zeros(1, N+1);
t0 = 0; t(1)= t0; % Initial time

%% Geometry
[b, b_half, bP, bN, b_temp] = GeometryNonPrismatic_Rec(x); % bottom width
variation

theta = 70 * pi/180; % trapezoidal angle in radius
k1 = 1/tan(theta); % constant
k2 = 1/sin(theta); % constant

%% Initial conditions
Un = zeros(2, length(x)); % h and hu
U = zeros(2, length(x)); % h and hu of t n+1
h01 = 0.001; % initial condition
V01 = 0.01; % initial condition
A01 = h01*(b +k1*h01);% initial condition, same flow depth
U(1,:) = A01;
U(2, :) = A01*V01; % initial condition

% Inlet boundary elevation
He = 0.3;
xe = 0.1;
L_xe = 1 + xe/dx;
H = elevation(x, dx, xe, He);

%% Gravity angle
alpha_g = 1.7;
alpha = zeros(1, length(x));
alpha(1:L_xe) = 180/pi*atan(He/xe) + alpha_g;
alpha(L_xe+1:end) = alpha_g;
```

```
%% Carreau model
lambda = 0.0095;
n = 0.6443;
eta_inf = 0.00032;
eta_0 = 0.01384;
k = 0.41;
rho = 1336;

%% Inlet condition
h02 = 0.02; % inlet flow depth
V02 = 1.3030;% inlet flow velocity
A02 = h02*(b(1) +k1*h02);% inlet cross sectional area
h = h01*ones(1,length(x)); h(1) = h02;

% To plot
Uplot1 = zeros(N+1, length(x)); % for A
Uplot2 = zeros(N+1, length(x)); % for Q
Uplot3 = zeros(N+1, length(x)); % for h
Uplot1(1,:) = U(1,:);
Uplot2(1,:) = U(2,:)./U(1,:);
Uplot3(1,:) = H + (-b+sqrt((b.^2) + 4*k1.*U(1,:)))/(2*k1);

for i = 1:N

        dt = variableTimeStep_Rc_NP_fast(U, h, dx);

        Un = U;
        hn = h;
        Un(1, 1) = A02; % inlet flow velocity 1 m/s constant in all time
        Un(2, 1) = A02*V02; % inlet flow velocity 1 m/s constant in all time

        %% Pure advection
        %Face flux
        Fn = Flux_Rc_NP_fast(Un(1, :), Un(2, :), b, k1); %Face flux

        % Advection flux
        U_Advection = Pure_Advection(Un, Fn, hn, H, b, bP, bN, b_temp, dt, dx,
        k1);

        %% Source term calling
        S = Source_RK4(U_Advection(1,:), U_Advection(2,:), dt, b, lambda, n,
        eta_inf, eta_0, rho, k1, k2, alpha, k, B, Pi);

        %% Free falling
        S_end = free_falling(U_Advection(1,:), dt);
        S(:,end-4:end) = S_end;
```

```
        U = U_Advection + S;
        h = (-b+sqrt((b.^2) + 4*k1.*U(1,:)))/(2*k1);

        Uplot1(i+1,:) = U(1,:); % A
        Uplot2(i+1,:) = U(2,:)./U(1,:); % u
        Uplot3(i+1,:) = H + (-b+sqrt((b.^2) + 4*k1.*U(1,:)))/(2*k1); % h

        %% Variable time step calling
        t(i+1) = t(i) + dt;
end

%% Movie - Visualize
delay = -10;
figure(1);
h = plot(x, 1000*Uplot3(1,:), 'LineWidth',2);
axis ([x(1), x(length(x)), 0,200])
xlabel('x, [m]'); ylabel('h, [mm]');
%title('Dam-break')
set(h, 'xData', x)
set(gca,'FontSize',12)
counter = 0;

for i = 2:length(Uplot3(:,1))
        t(i);
        set(h, 'ydata', 1000* Uplot3(i,:));
        legend(strcat('t=', num2str(t(i))), 'location', 'northeast');
        pause(delay);
        if mod(i,1000) == 0
        filestem = sprintf('h_%04d', counter);
        print(filestem, '-dpng');
        counter = counter + 1;
        end
end
```

Geometry

```
%% Geometry details

% Trapezoidal open Venturi channel
function [b,b_half, bP, bN, b_temp] = GeometryNonPrismatic_Rec(x)
b=zeros(1,length(x));
        for i = 1:length(x)
                if x(i) <= 2.95
                b(i) = 0.2;
                elseif 2.95 < x(i) && x(i) <= 3.1
                b(i) = 0.2 - (x(i) - 2.95)/1.5;
                elseif 3.1 < x(i) && x(i) <= 3.3
                b(i) = 0.1;
                elseif 3.3 < x(i) && x(i) <= 3.45
                b(i) = 0.1 + (x(i) - 3.3)/1.5;
                elseif 3.45 < x(i) && x(i) <= 3.7
                b(i) = 0.2;
                end
        end
%b left and right values
b_temp = b; b_temp(1)=[]; b_temp(end)=[];
b_temp1 = b; b_temp1(end)=[]; % add two node before and after
b_temp2 = b; b_temp2(1)=[];
b_half = (b_temp1 + b_temp2)/2;
bP = b_half; bP(1) = [];
bN = b_half; bN(end) = [];
end
```

Elevated inlet boundary

```
%% Elevated inlet boundary

function H = elevation(x, dx, xe, He)
H = zeros(1,length(x));
        for i = 1:length(x)
                if x(i) < x(1 + xe/dx)
                H(i) = He - He*x(i)/xe;
                end
        end

end
```

Variable time step

```
%% Variable time step

function VTS = variableTimeStep_Rc_NP_fast(U, h, dx)
        %% Froud number to calculate the wave speed
        g = 9.81;
        k_int1 = h < 10^-8;
        h(k_int1) = 0; % Remove negative values
        Smax = max(abs(U(2,:)./U(1,:)) + sqrt(h.*g)); % Maximum wave
        propagation speed

        %% CFL condition
        CFL = 0.7; % fixed CFL coefficient for variable time steps
        dt = CFL*dx/Smax; % calculate the variable time step
        VTS = dt;
end
```

Fluxes

```
%% Flux function

% Mass flux and momentum flux
function F = Flux_Rc_NP_fast(u1, u2, b, k1) % n is number of step in spatial
        g = 9.81;
        h_temp = -b + sqrt((b.^2) + 4*k1*u1);
        F = [u2; ((u2.^2)./u1) + ((u1.*h_temp/(4*k1)) +
        ((h_temp.^3)/(48*k1^2)))*g]; %
        flux as array of anonymous function
        f1 = F(1,:);
        f2 = F(2,:);
        k_int = u1 < 10^-8;
        f1(k_int) = 0; % Remove negative values
        f2(k_int) = 0;
        F = [f1;f2];
end
```

FLIC scheme

```
%% FLIC scheme for the high order flux

function U = Pure_Advection(Un, Fn, hn, H, b, bP, bN, b_temp, dt, dx, k1)
        UnjP1 = Un; UnjP1(:,1:2) = []; % j+1
        Unj = Un; Unj(:,1) = []; Unj(:,length(Unj)) = []; % j
        UnjN1 = Un; UnjN1(:,length(Un)-1:length(Un)) = []; % j-1
        FnjP1 = Fn; FnjP1(:,1:2) = []; % j+1
        Fnj = Fn; Fnj(:,1) = []; Fnj(:,length(Fnj)) = []; % j
        FnjN1 = Fn; FnjN1(:,length(Fn)-1:length(Fn)) = []; % j-1

        %% Richtmyer scheme
        UnRIP = 0.5*(Unj + UnjP1) + (0.5*dt./dx).*(Fnj - FnjP1); % j+0.5
        UnRIN = 0.5*(UnjN1 + Unj) + (0.5*dt./dx).*(FnjN1 - Fnj); % j-0.5
        FnRIP = Flux_Rc_NP_fast(UnRIP(1,:), UnRIP(2,:), bP, k1 );
        FnRIN = Flux_Rc_NP_fast(UnRIN(1,:), UnRIN(2,:), bN, k1);
        FnRIN(:,1) = Fn(:,1);

        %% Lax-Friedriches
        FnLFP = 0.5*(Fnj + FnjP1) + (0.5*dx/dt).*(Unj - UnjP1); % j+0.5
        FnLFN = 0.5*(FnjN1 + Fnj) + (0.5*dx/dt).*(UnjN1 - Unj); % j+0.5
        FnLFN(:,1) = Fn(:,1);

        %% Higher order
        FnHOP = FnRIP; %higher order j + 05
        FnHON = FnRIN; %higher order j – 05

        %% Lower order
        FnFORCEP = 0.5*(FnLFP + FnRIP);
        FnFORCEN = 0.5*(FnLFN + FnRIN);
        FnLOP = FnFORCEP; % low order schem given by FORCE scheme, j +
        0.5
        FnLON = FnFORCEN; % j - 0.5

        %% Flux-limiter SUPER-BEE calling
        [PhiP, PhiN] = fluxLimiterSB_NonPrismatic_KP_SU3(Un(1,:), Un(2,:), hn,
        H, k1);

        %% FLIC scheme for intercell fluxes
        FnjP = FnLOP + PhiP.* (FnHOP - FnLOP);
        FnjN = FnLON + PhiN.* (FnHON - FnLON);
        FnjN(:,1) = Fn(:,1);

        %% Wall reflection pressure force
        S1 = Source_temp(Un(1,:), bP, bN, b_temp, k1);

        %% Euler approach for consevation equations for pure advection
```

```
        dF = (FnjP - FnjN);
        Un_temp = Un; Un_temp(:,1) = []; Un_temp(:,end) = [];
        U_temp = Un_temp -(dt/dx)*(dF-S1);
        U = [Un(:,1), U_temp, U_temp(:,end)];
end
```

Flux limiter

```
%% Flux limiter - SUPER-BEE flux limiter

% SUPER-BEE flux limiter
% r is the flow parameter, ratio of upwind change to the local change
function [PhiP, PhiN] = fluxLimiterSB_NonPrismatic_KP_SU3(u1, u2, h, H, k1)
        g = 9.81;
        kg1 = (1/2) + (k1*(h.^2)./(6*u1));
        qn = kg1.*(h + H)*g + 0.5*(u2./u1).^2;
        %qn = kg1*h*g + 0.5*u.^2;% Total enrgy is potential energy + kinetic
        energy
        % To avoid expensive for-loop
        qn0 = qn(1) + qn(2) - qn(3);
        qnEnd = qn(end-2) + qn(end-1) - qn(end);
        qn_temp = [qn0, qn, qnEnd];
        qnjN1 = qn_temp; qnjN1(length(qnjN1)-2:length(qnjN1)) = []; % j-1
        qnj = qn_temp; qnj(length(qnj)-1 :length(qnj)) = []; qnj(1) = []; % j
        qnjP1 = qn_temp; qnjP1(length(qnjP1)) = []; qnjP1(1:2) = []; % j+1
        qnjP2 = qn_temp; qnjP2(1:3) = [];
        % delta q
        dqjN = qnj - qnjN1; % dq j-0.5
        dqjP = qnjP1 - qnj; % dq j+0.5
        dqjPP = qnjP2 - qnjP1; % dq j +1.5
        % Left and right
        rnjL = dqjN./dqjP; % r j+0.5 L
        rnjR = dqjPP./dqjP; % r j+0.5 R
        r = [rnjL; rnjR];
        CFL = 0.7;
        phing = (1 - CFL)/(1+CFL);
        phi = zeros(2,length(rnjL));
        Phi_min = zeros(1,length(rnjL));

        for k = 1:2
                for i =1:length(rnjL) % this for loop to make easy the calculation
                        % condition of SUPER-BEE flux limiter
                        if r(k,i) <= 0
                        phi(k,i) = 0;
                        elseif 0 < r(k,i) && r(k,i) <= 1/2
```

```
                    phi(k,i) = 2*r(k,i);
                    elseif 1/2 < r(k,i) && r(k,i) <= 1|| isnan(r(k,i))
                    phi(k,i) = 1;
                    else
                    phi(k,i) = min(2, phing + (1 - phing)*r(k,i));
                    end
                    if k == 2
                    Phi_min(i) = min(phi(1,i),phi(2,i));
                    end
                end
        end
        PhiP = Phi_min; PhiP(1) = [];
        PhiN = Phi_min; PhiN(end) = [];
        PhiN(1) = 1.1;
end
```

Wall reflection pressure force

```
%% Wall reflection effect

function S = Source_temp(u1, bP, bN, b_temp, k1)
        g = 9.81;
        u1_temp = u1;u1_temp(1) = []; u1_temp(end) = [];
        db = (bP-bN);
        S = [zeros(1,length(db));((-b_temp +sqrt((b_temp.^2) +
        4*k1*u1_temp)).^2).*db*g/
        (8*k1^2)];
        k_int = u1_temp < 10^-8;
        s1 = S(1,:);
        s2 = S(2,:);
        s2(k_int) = 0; % Remove negative values
        S = [s1;s2];
end
```

Runge-Kutta 4th order

```
%% Runge-Kutta 4th order explicit for source term splitting
function S_RK4 = Source_RK4(u1, u2, dt, b, lambda, n, eta_inf, eta_0, rho, k1,
k2,
        alpha,k, B, Pi)
        %% call for source
        %f = @Source_Newtonian;
        f = @Source_nonNewtonian_my_laminar;
        K1 = dt*f(u1, u2, b, lambda, n, eta_inf, eta_0, rho, k1, k2, alpha, k, B, Pi);
        K2 = dt*f(u1 + 0.5*K1(1,:), u2 + 0.5*K1(2,:), b, lambda, n, eta_inf, eta_0,
        rho, k1,
```

```
        k2, alpha, k, B, Pi);
        K3 = dt*f(u1 + 0.5*K2(1,:), u2 + 0.5*K2(2,:), b, lambda, n, eta_inf, eta_0,
        rho, k1,
        k2, alpha, k, B, Pi);
        K4 = dt*f(u1 + K3(1,:), u2 + K3(2,:), b, lambda, n, eta_inf, eta_0, rho, k1,
        k2,
        alpha, k, B, Pi);
        S = (1/6)*(K1 + 2*K2 + 2*K3 + K4);
        k_int = u1 < 10^-8;
        s2 = S(2,:);
        s2(k_int) = 0; % Remove negative values
        S_RK4 = [S(1,:); s2];
End
```

External friction

```
%% Manning's friction/wall friction
function S = Source_Newtonian(u1, u2, b, k1, k2, alpha)
        g = 9.81;
        km = 0.012; % Steel smooth
        kn = 1; % unit correction
        S = [zeros(1,length(u1)); g*sin(pi*alpha/180).*u1 -
        (g*(km/kn)^2)*((u2.^2)./u1).*((b +
        (k1/k2)*(-b + sqrt((b.^2)+(4*k1*u1)))))./u1).^(4/3)];
End
```

Internal friction

```
%% Carreau

function S = Source_nonNewtonian_my_laminar(u1, u2, b, lambda, n, eta_inf,
eta_0, rho,
k1, k2, alpha, k)
        % Internal viscous dissipation
        V = u2./u1;
        h = (-b+sqrt((b.^2) + 4*k1.*u1))./(2*k1);
        %kg1 = (1/2) + (k1*(h.^2)./(6*u1));
        Rh = u1./(b.^2 + 2*u1);
        a1 = (b + 2*k2.*h).*2.*V./(Rh.*rho);
        a2 = (1 + (lambda*2*V./Rh).^2).^((n-1)/2);
        s2 = a1.*(eta_inf + (eta_0 - eta_inf).*a2);
        f2 = [zeros(1,length(u1)); s2];
        % call gravity and Newtonian source + Turbulence
        f1 = @Source_Newtonian;
        S = f1(u1, u2, b, k1, k2, alpha) - f2;
End
```

Free falling

```
%% free falling effect

% consider last five computational cells
function S_end = free_falling(u1, dt)
        g = 9.81;
        alpha = 0.7;
        alpha_end = 70 +alpha;
        u1_end = u1(end-4:end);
        f_end = @(u1_end) [zeros(1,length(u1_end));
        g*sin(pi*alpha_end/180)*u1_end]; % No
        friction term and high gravity
        %% Runge-Kutta 4th explicit
        K1_end = dt*f_end(u1_end);
        % K2_end = dt*f_end(u1_end); %+ 0.5*K1_end(1), u2(end) +
        0.5*K1_end(2), b(end));
        % K3_end = dt*f_end(u1_end); %+ 0.5*K2_end(1), u2(end) +
        0.5*K2_end(2), b(end));
        % K4_end = dt*f_end(u1_end); %+ K3_end(1), u2(end) + K3_end(2),
        b(end));
        S_end = K1_end;
end
```

Doctoral dissertation no. 41
2019
—

Transient drilling fluid flow in Venturi channels: comparing 3D and 1D models to experimental data

Dissertation for the degree of Ph.D

—

Prasanna Welahettige

—

ISBN: 978-82-7206-535-4 (print)
ISBN: 978-82-7206-536-1 (online)

usn.no